THE UNIVERSITY *of* EDINBURGH

This thesis has been submitted in fulfilment of the requirements for a postgraduate degree (e.g. PhD, MPhil, DClinPsychol) at the University of Edinburgh. Please note the following terms and conditions of use:

This work is protected by copyright and other intellectual property rights, which are retained by the thesis author, unless otherwise stated.
A copy can be downloaded for personal non-commercial research or study, without prior permission or charge.
This thesis cannot be reproduced or quoted extensively from without first obtaining permission in writing from the author.
The content must not be changed in any way or sold commercially in any format or medium without the formal permission of the author.
When referring to this work, full bibliographic details including the author, title, awarding institution and date of the thesis must be given.

Novel Compact Antenna Designs for Future Wireless Communication Systems

Christian Núñez-Álvarez

THE UNIVERSITY
of EDINBURGH

Thesis submitted in fulfilment of
the requirements for the degree of
Doctor of Philosophy
to the
University of Edinburgh — 2016

Declaration

I declare that this thesis has been composed solely by myself and that it has not been submitted, either in whole or in part, in any previous application for a degree. Except where otherwise acknowledged, the work presented is entirely my own.

Christian Núñez-Álvarez

September 2016

Abstract

Wireless and mobile devices are becoming packed with more applications that require an increasing number of communication technologies as well as a constant desire for size reduction. Ideally, every single communication technology should have a dedicated antenna system. This puts pressure on antenna engineers as the available space for the radiation elements is becoming very limited, particularly for small mobile phones and small cell base stations. Traditionally, reducing the size of the antenna was enough to accommodate these requirements. However, making antennas smaller strongly affects their performance. In order to further shrink a multi-radio transmitting system, antenna reconfiguration provides an option to converge multiple radiating elements into a single one, and hence, save space in wireless and mobile devices.

The creation of novel materials such as carbon nanotubes, graphene and metamaterials, which present extraordinary electrical and mechanical properties, has opened new possibilities within the antenna field. The most interesting properties of these materials are the presence of plasmons in carbon nanotubes and graphene at much lower frequencies than in metals, the ability to tune the surface impedance of graphene by applying a DC voltage bias and the possibility of generating size-independent resonances in metamaterials. These materials are studied here as alternative methods to achieve antenna size reduction and reconfigurability at microwave frequencies.

This thesis presents an initial study of the advantages and disadvantages of designing small and reconfigurable antennas fully made of carbon nanotubes and

graphene at microwave, millimetre wave and terahertz frequencies. Here, the focus is on the trade-offs between the antenna performance and the achievable size reduction and reconfigurability at microwave frequencies. The results show that the resulting low antenna efficiencies do not compensate the small size reduction and reconfigurability of these antennas at such frequencies. This is mainly caused by the large losses suffered in carbon nanotubes and graphene and the low inductive behaviour of these materials at microwave frequencies. Furthermore, carbon nanotubes present extremely high input impedances, which make the antenna matching very difficult, with little reconfigurability due to not being able to actively tune their resistivity and the infeasibility of using plasmons at frequencies for commercial applications (up to 10 GHz). For this reason, three planar hybrid antennas made of a traditional conductor (i.e. copper) and graphene are presented as the main proposed solutions for antenna reconfigurability and size reduction at microwave frequencies.

The first proposed design provides frequency reconfigurability by changing the electrical length of microstrip patch antennas using the variable surface impedance of graphene. However, the resulting antenna efficiencies are low compared to other reconfigurable antennas found in the literature. The second design provides polarization reconfigurability by adding graphene sheets to the truncated corners of a square patch antenna. The resulting antenna efficiencies are improved when compared to the first antenna design. This is achieved because the impact of graphene on the antenna efficiency is reduced due to the use of graphene sheets with smaller size. The final design combines size reduction and frequency reconfigurability. Size reduction is achieved by designing a zeroth order resonant (ZOR) antenna, while frequency reconfigurability is achieved by tuning the surface impedance of graphene. The variable surface impedance of graphene changes the inductive and capacitive behaviour of the ZOR antenna which in turns changes its resonant frequency. The resulting antenna efficiencies are better compared to the first design but worse than in the second design.

Additional features presented by the first and third proposed antenna designs are the ability to tune the reflection coefficient and antenna bandwidth, which might help to reduce the complexity of the matching network; and to select any intermediate resonant frequency between two edge frequencies. The latter property which might be useful to compensate undesired effects in wearable antennas, by selecting appropriate values of the surface impedance of graphene. In addition, an analysis of the power consumed in the proposed reconfigurable antennas is also provided when switching between different values of the surface impedance of graphene. Finally, the proposed antenna designs are also evaluated as fully transparent and flexible reconfigurable antennas which allows integration in scenarios where flexibility and transparency are a requirement or an advantage.

Acknowledgements

I would like to thank my two supervisors, Prof. John S. Thompson and Prof. Rebecca Cheung, for their invaluable support, help, encouragement and guidance throughout my PhD. Thank you for your patience.

I would also like to extend my appreciation to the other students and staff of the Institute for Digital Communications (IDCOM) for their help, feedback and fruitful discussions, and for making my stay at the institute unforgettable. I would also wish to say thanks to the other staff from the University of Edinburgh that have always been kind and helpful to me.

Additional thanks to my financial sponsors, the Engineering and Physical Sciences Research Council (EPSRC) and Agilent/Keysight technologies, for the scholarships and professional experiences carried out during my PhD.

Thanks to all the people that have played football with me. You have gave me lots of well needed breaks.

Special thanks to my family for their countless sacrifices and support that has made everything possible during my whole life. Also to all my friends for your understanding, compression, and also, for many memorable moments.

Last but not least, a big thank you to my wife for the motivation and encouragement during my PhD, and of course, for your endless love. Seeing you always smiling made everything easier.

Contents

List of Tables

List of Figures

Nomenclature

Acronyms

a-Si:H	Hydrogenated amorphous silicon
AC	Alternate current
AgNW/Cu	Hybrid silver nanowires and copper microwires
AMC	Artificial magnetic conductor
BAN	Body area network
CNT	Carbon nanotube
CP	Circular polarization
CRLH TL	Composite Right/Left-handed transmission line
CVD	Chemical vapour deposition
DAB	Digital audio broadcast
DC	Direct current
DNG	Double negative
DVB-H	Digital video broadcast hand-held
EBG	Electromagnetic band gap

ENG	Epsilon negative
ESA	Electronically small antenna
FET	Field effect transistor
FM	Frequency modulation
GNSS	Global navigation satellite system
GPS	Global positioning system
hBN	Hexagonal boron nitrite
HLP	Horizontal linear polarization
IoT	Internet of things
IR	Infra-red
LA	Longitudinal acoustic
LHCP	Left-hand circular polarization
LH TL	Left-handed transmission line
LOS	Line of sight
MEMS	Micro electromechanical systems
MESFET	Metal semiconductor field effect transistor
MIMO	Multiple input multiple output
MNG	Mu negative
MTM LW	Metamaterial leaky wave
MTM	Metamaterial

MWCNT	Multi-wall carbon nanotube
NEMS	Nano electromechanical systems
NLOS	No-line of sight
PAN	Personal area network
PBC	Periodic boundary conditions
PHEMT	Pseudomorphic high electron mobility transistor
PIN	p-type insulator n-type
RFID	Radio-frequency identification
RHCP	Right-hand circular polarization
RH TL	Right-handed transmission line
RIS	Reactive impedance surface
SiC	Silicon carbide
SLG	Single layer of graphene
SWCNT	Single-wall carbon nanotube
TE,TM	Trans-electric and -magnetic modes
THz	Terahertz
TL	Transmission line
UWB	Ultra-wide band
VLP	Vertical linear polarization
WIFI	Wireless fidelity

WiMAX	Worldwide interoperability for microwave access
ZOR	Zeroth order resonant

Variables		**Units**
A	Area of a graphene sheet	m^2
a	Radius of the smallest sphere that entirely encloses an antenna	m
$\hat{\mathbf{a}}_{ant}, \hat{\mathbf{a}}_{inc}$	Wave polarization unitary vectors of an antenna and an incident wave	–
$\acute{x}, \acute{y}$	Driving point location in the cavity mode	m
α	Attenuation constant	Np/m
$\alpha_{X,Y}$	Attenuation of modes X and Y	Np/m
AR	Axial ratio	dB
$\beta(\omega)$	Dispersion relation	rad/m
BW	Operational bandwidth of an antenna	Hz
C	Capacitance of a RC circuit	F
C_{es}, C_Q, C_T	Electrostatic, quantum and total capacitances in CNT	F/m
C_L, C_R	Left-handed and right-handed capacitances in MTM	F
D	Deformation potential in graphene	eV
d	Thickness of a dielectric layer	m

$D(\theta, \phi)$	Directivity of an antenna	–ordB
δ_{eff}	Effective quality factor	–
ϵ_1, ϵ_2	Permittivity of top and bottom substrates	F/m
ϵ_r^d	Relative permittivity of a dielectric layer	–
ε_F	Fermi energy	J
ε_{puddle}	Energy of the electron-hole puddles	J
$\epsilon_1^r, \epsilon_2^r$	Relative permittivity of top and bottom substrate	–
ϵ_r	Relative permittivity of an antenna substrate	–
ϵ_r^{eff}	Effective relative permittivity in the cavity model	–
ε	Carrier energy in graphene	J
$\mathcal{E}(p_z, s)$	Electron dispersion relation in CNT	eV
E_{x0}, E_{y0}	Nominal value of the electric field at the x- and y-axis	V/m
FBW	Fractional bandwidth	–
$F(\pm\mathcal{E}(p_z, s))$	Fermi equilibrium distribution function in CNT	–
$f_d(\varepsilon)$	Fermi-Dirac distribution in graphene	–
f_H	Higher frequency limit	Hz
f_L	Lower frequency limit	Hz

f_{res}	Resonant frequency	Hz
$f_{res}^{X,Y}$	Resonant frequency due to modes X and Y	Hz
f_{ZOR}	Zeroth order resonant frequency	Hz
G	Conductance in CRLH TL	S
$G(\theta, \phi)$	Gain of an antenna	dB
Γ	Phenomenological scattering rate in graphene	s^{-1}
γ	Overlap integral in CNT	eV
γ_p	Plasmon propagation constant in CNT	–
H_{12}	Hamiltonian matrix of electrons in CNT	–
H	Antenna substrate height	m
i	radius of a shell in MWCNT	m
I_D, I_G	D and G peak values from Raman spectroscopy of graphene	–
$i(t)$	Transitional current	A
k_1, k_2	Phase constant in the top and bottom substrates	rad/m
k, k_F, k_p	Free space, Fermi and plasmon phase constants	rad/m
k_p^{TE}, k_p^{TM}	Plasmon phase constant of the TE and TM modes in graphene	rad/m
k_x, k_y	x- and y-projection of the phase constant	rad/s

L	Length of an antenna	m
λ_0	Wavelength in free space	m
λ_{res}	Resonant wavelength	m
ΔL	Additional length due to fringe fields in a patch antenna	m
l_{DS}	Length of a doped semiconductor layer	m
L_K, L_m, L_T	Kinetic, magnetic and total inductances in CNT	H/m
L_R, L_L	Right-handed and left-handed inductances in MTM	H
L_T	Total inducante per unit length of a CNT	H/m
m^*	Carrier mass in graphene	Kg
m_i	Number of conducting channels in CNT	–
M_μ	Permeability ratio	–
m_r	Integer for the radius of a CNT	–
μ_1	Permeability top substrate	H/m
μ_2	Permeability bottom substrate	H/m
μ_c	Chemical potential in graphene	J
$\mu_{c,min}$	Minimum chemical potential in graphene	J
μ_d, μ_t	Defects and total carrier mobility in graphene	Vs/m^2

μ_{DS}	Carrier mobility in a doped semiconductor	$\mathrm{Vs/m^3}$
μ_1^r, μ_2^r	Relative permeability of top and bottom substrates	–
μ_r^{eff}	Effective relative permeability	–
N	Total number of unit cells in CRLH TL	–
n	Charge carrier density in graphene	$\mathrm{m^{-2}}$
N_b	Number of tubes	–
n_d, n_i	Charge carrier density due to defects and impurities in graphene	$\mathrm{m^{-2}}$
n_{DS}	Carrier density in a doped semiconductor	$\mathrm{m^{-3}}$
n_{eff}	Effective index	–
N_ϵ	Permittivity ratio	–
n_m	Resonant mode in a CRLH TL	–
n_R	Refractive index	–
n_r	Integer for the radius of a CNT	–
N_s	Number of shells in MWCNT	–
n_s	Integer counter of a shell in a MWCNT	–
m^{-2}	Carrier inhomogeneity density in graphene	$\mathrm{m^{-2}}$
ω	Angular frequency	rad/s

$\omega_{L,R,se,sh}$	Left-handed, right-handed, series and shunt resonances in CRLH TL	rad/s
$\omega_{X,Y}$	Angular resonant frequency due to modes X and Y in the cavity model	rad/s
p	Length of unit cell in CRLH TL	m
P_{del}	Power delivered to an antenna	W
ϕ	Azimuth angle	radians
PLF	Polarization loss factor	–
η_t, η_r	Total and radiation efficiencies of an antenna	% or dB
P_{loss}	Power lost in an antenna	W
P_{peak}	Peak power consumed	W
P_{rad}	Power radiated by an antenna	W
ψ	Angle between the unitary vectors of the antenna and incident wave polarizations	radians
P_{sim}	Simulated power	W
P_{sup}	Power supplied by a source	W
$p(t)$	Dynamic power consumed	W
$k_{x,y}$	x- and y-projections of the electron quasi-momentum	Kgm/s
p_z	z-projection of the electron's two-dimensional quasi-momentum	Kgm/s

Q	Quality factor of an antenna	–
$Q_{c,d,r,sw}$	Quality factor due to conductor, dielectric, radiation and surface-wave losses	–
Q_T	Total quality factor	–
R	Resistance in CRLH TL	Ω
R	Resistance of a RC circuit	Ω
r	Distance of an observer from an antenna	m
R_{CNT}	Resistance per unit length of a CNT	Ω/m
R_{DS}	Resistance in a doped semiconductor	Ω
RG	Return gain	dB
ρ	Voltage reflection coefficient	–
R_{in}	Input resistance	Ω
r_{inner}	Radius of inner most shell in a MWCNT	m
RL	Return loss	dB
r_{MWCNT}	Total radius of a MWCNT	m
Rs	Surface resistance in graphene	Ω
Rs_{OFF}	Surface resistance for the OFF state	Ω
Rs_{ON}	Surface resistance for the ON state	Ω
r_{SWCNT}	Radius of a SWCNT	m

$S11$	Scattering parameter at port 1	dB
$S21$	Scattering parameter between port 1 and 2	dB
$S22$	Scattering parameter at port 2	dB
s	Chiral angle counter in CNT	–
σ_{AC}	AC surface admittance of graphene	S
σ_{DS}	Conductivity in a doped semiconductor	S/m
σ_s	Surface admittance of graphene	S
σ_{zz}	Total axial admittance of a SWCNT	S
$\Delta\sigma$	Interband admittance of a SWCNT	S
$\tilde{\sigma}_{zz}$	Intraband contributions admittance of a SWCNT	S
$\tilde{\sigma}_{zz}^{armchair}$	Admitance of an armchair CNT	S
$\tilde{\sigma}_{zz}^{chiral}$	Admitance of an chiral CNT	S
$\tilde{\sigma}_{zz}^{zigzag}$	Admitance of a zigzag CNT	S
T	Operational temperature	K
$\tan\delta$	Loss tangent of an antenna substrate	–
τ	Relaxation time in a CNT	s
$\tau_{d,i,p,c}$	Relaxation time due to defects, impurities, phonons and carrier interactions	s

$\tau_{L,S}$	Relaxation time due to long and short range scattering	s
τ_{RC}	Time constant of an RC circuit	s
τ_t	Total relaxation time	s
T_{BG}	Bloch-Grüneisen temperature	K
t_{DS}	Thickness of a doped semiconductor	m
TE_{01}, TM_{01}	First trans-electric and -magnetic mode	–
θ	Elevation angle	radians
$\|\theta_{cv}\|$	Matrix element of the longitudinal velocity in CNT	m/s
θ_{SWCNT}	Chiral angle of a SWCNT	radians
U	Radiation intensity	W/sr
v	Relaxation frequency in CNT	Hz
V_b	Voltage bias	V
V_{drv}	Voltage at the driving point	V
v_f^c	Fermi velocity in a CNT	m/s
V^-	Reflected voltage wave	V
V_0	Peak voltage	V
v_p	Propagation velocity in CNT	m/s
V^+	Incident voltage wave	V
$VSWR$	Voltage standing wave ratio	–

$v(t)$	Transitional voltage	V
$I_{terminals}$	Current at the terminals	A
$V_{terminals}$	Voltage at the terminals	V
$\nu_z(p_z, s)$	Electron velocity in CNT	m/s
W	Width of an antenna	m
w_{DS}	Width of a doped semiconductor layer	m
W_{rad}	Radiation density	W/m^2
W_s	Energy stored in an antenna	J
X, Y	Modes excited along the length and width of a cavity	–
x, y	x- and y- axes	–
X_{in}	Input reactance	Ω
XPD	Cross polarization discrimination	dB
Xs	Surface reactance in graphene	$\Omega/\square$
Y_{shunt}	Shunt conductance in CRLH TL	S
Zs	Surface impedance of graphene	$\Omega/\square$
Zc	Characteristic impedance of a TL	Ω
Z_{in}	Input impedance	Ω
Z_{in}^{TL}	Input impedance of a TL	Ω
Zo	Characteristic impedance of a quarter wavelength transformer	Ω

Z_s	Internal impedance of a source	Ω
Z_{series}	Series resistance in CRLH TL	Ω
Z_s^{max}	Maximum surface impedance in graphene	$\Omega/_{\square}$
$Zs_{ON,OFF}$	Surface impedance for the ON and OFF states	$\Omega/_{\square}$
Z^{TE}, Z^{TM}	Dispersion equation for the TE and TM modes in graphene	–

Constants		**Value**	**Units**
b	Inter-atomic distance between carbon atoms	0.142	nm
c	Speed of light in vacuum	$\approx 3\times10^{8}$	m/s
δ	Distance between shells	0.34	nm
ϵ_o	Permittivity of vacuum	8.8542×10^{-12}	F/m
η_0	Free space impedance	$\approx$376.73	Ω
$\hbar$	Reduced Planck's constant	1.0546×10^{-34}	Js
k_B	Boltzmann constant	1.3806×10^{-23}	J/K
q	Electron charge	1.6022×10^{-19}	C
ρ_m	Mass density of graphene	7.6×10^{-7}	Kg/m^2
R_o	Radius of the interaction potential	$\approx$0.284	nm
v_f^g	Fermi velocity in graphene	$\approx 1\times10^{6}$	m/s
v_{ph}	Sound velocity of LA phonons in graphene	2.1×10^{4}	m/s

Chapter 1

INTRODUCTION

1.1 RESEARCH MOTIVATION

This thesis is motivated by a series of topics and changes in wireless and mobile systems as well as in materials science that will be key for the years to come:

- Wireless and mobile devices are packing more technologies while reducing their sizes.
- Large cells are being substituted by smaller cells.
- Multiple-input-multiple-output technology is becoming a standard technique in wireless and mobile communications.
- Novel materials are opening new lines of research and possibilities.

1.1.1 MULTIBAND OPERATION

With the increasing demand of high data rates [1] and the upcoming of new technologies such as wearable technologies [2], [3] and the internet of things (IoT) [1], [4]–[10], wireless data providers are starting to use newly freed frequency bands in the microwave (up to 10 GHz) and in the millimetre-wave (from 30 GHz

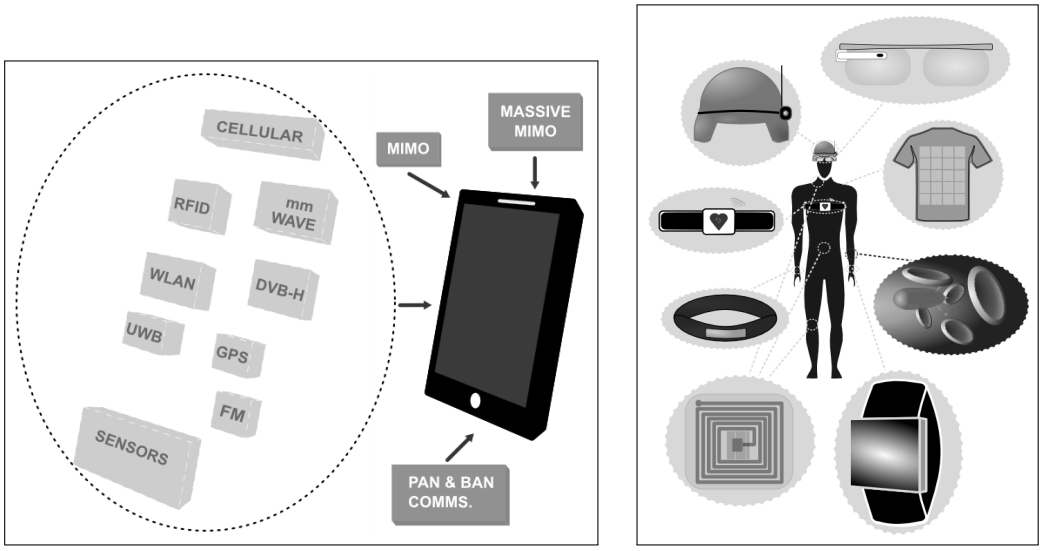

(a) **(b)**

Figure 1.1: In wearable technology, small devices communicate to each other and to a gateway device such as mobile phone, tablet, laptop, etc; forming body/personal area networks (BAN/PAN). Mobile devices (and also wireless devices) struggle to accommodate new technologies due to limited available space.

to 300 GHz) spectrum [1], [6], [9], [11]–[15] where larger portions of bandwidth are availabe. Consequently, future wireless devices might eventually need to operate in a large array of bands spread over a huge spectrum to incorporate the immense number of wireless and mobile services such as 3^{rd} (3G), 4^{th} (4G), 5^{th} (5G) - and beyond - generations of mobile communications, wireless fidelity (WIFI), worldwide interoperability for microwave access (WIMAX), radio frequency identification (RFID), bluetooth, ultra wideband (UWB), global navigation satellite system (GNSS), frequency modulation (FM), digital audio broadcasting (DAB), digital video broadcasting hand-held (DVB-H), and possibly any other millimetre wave (mm-wave) technology that might emerge in the near future, making multiband operation a must.

1.1.2 BASE STATION AND ACCESS POINT EVOLUTION

Traditional long-range base stations and access points are being replaced by smart and short-range micro cells, pico cells and femto cells in order to reduce the power consumption and optimize the data throughput [1], [5], [7], [9], [13], [15]. Small cells translate into small base stations and access points in order to reduce their footprint. Therefore, characteristics such as small size, transparency and reconfigurability might be necessary attributes in the antennas forming those base stations and access points.

1.1.3 ESTABLISHING MULTIPLE ANTENNA SYSTEMS

Multiple-input-multiple-output (MIMO) systems, using two or more antenna in the transmitter and the receiver at the same time, are already a solution being implemented to increase bit rates while decreasing terminal vulnerability to channel fading and multichannel propagation [6], [7], [9], [13], [15]. MIMO systems with space, time and/or polarization diversity are required in order for base stations, access points and wireless/mobile devices to adapt to different link conditions, communication services and number of users, so the guaranteed high data rates are successfully achieved.

1.1.4 THE RISE OF "WONDER" MATERIALS

In the last two decades, new materials such as carbon nanotubes (CNTs), graphene and metamaterials (MTMs) have revolutionised [16]–[18] many fields of science and engineering such as device interconnects, transistors, gas sensors, field emission devices, guided waves, transmission lines, filters, antennas, etc; thanks to their extraordinary electrical properties [19]–[30]. Some of the most important electrical properties in carbon nanotubes and graphene are that they present

ballistic propagation of charge carriers for distances of up to several micrometres [31], plasma frequencies at much lower frequencies than in conventional metals [32]; and variable surface admittance that depends on the radius of the carbon nanotubes and on the applied chemical or electrostatic doping to the graphene sheet. Furthermore, CNTs and graphene are the first quasi-one dimensional and two dimensional materials to be synthesised respectively, making them impossible to see for the human eye and with a huge potential in the nanotechnology field. These properties have caused carbon nanotubes and graphene to be called the wonder materials and researchers predict a great potential to be the backbone for future electronic devices. Likewise, MTMs show some other interesting electrical properties such as the presence of negative permittivity and permeability. This peculiar property has introduced a new concept in transmission lines, called left-handiness, which allows transmission lines, and also antennas, to resonate at left-handed resonances and zeroth order resonances, which are independent of the transmission line or antenna size.

1.2 CHALLENGES

1.2.1 SIZE LIMITATION

The large number of wireless technologies that wireless and mobile devices will need to operate must all fit into any wireless and mobile device. Moreover, because many of the communications technologies will operate at a large array of bands spread over a very wide spectrum, those devices will need to be able to transmit and receive at all those frequencies at any time. Ideally, every communication subsystem should have a dedicated antenna. In addition, implementing MIMO technology requires an increase of the number of antennas at both ends, at the base stations/access points and at wireless/mobile devices. This translates into a pressure to accommodate those large number of antennas in equipment and devices where the available space is already very limited. A solution to this is

to reduce the size of the antenna. The main issue for antenna size reduction is that reducing the size of an antenna is not a matter of technology constraint but is limited by the fundamental physics of wave propagation. Consequently, making antennas smaller strongly affects their performance. In order to further shrink a multi-radio transmitting system, antenna reconfiguration provides an option to converge multiple radiating elements into a single one, and hence, save space. However, again, implementing antenna reconfigurability also affects the performance of the resulting antenna.

1.2.2 TRANSPARENCY AND FLEXIBILITY

Transparency and/or flexibility might be a solution to reduce the footprint of an antenna in small base stations, access points and wearable devices. However, transparent and flexible materials present lower conductivities than conventional non-transparent metals such as copper, aluminium, silver and gold. Although there are some transparent and/or materials that can provide acceptable antenna efficiencies, they cannot, by their own, provide size reduction and/or reconfigurability. Therefore, they still rely on the conventional methods such as micro or nano electromechanical systems (MEMS or NEMS), field effect transistor switches (FET), p-semiconductor isolator n-semiconductor diodes (PIN diodes), varactors and tunable materials to achieve reconfigurability which are not transparent or flexible at all.

1.2.3 CARBON NANOTUBES AND GRAPHENE LIMITATIONS

Although carbon nanotubes and graphene have been successfully implemented in many applications from microwave to optical frequencies, in the antenna field, these materials have been mostly studied, researched and implemented in antennas from infra-red to optical frequencies and little on the microwave

and millimetre wave regime. In addition, carbon nanotubes and graphene are still underdeveloped, specially when compared to other technologies already implemented in the microwave regime, and thus, the potential advantages of using these materials in antennas at such frequencies is unclear.

1.3 OBJECTIVES OF THIS THESIS

To solve all the previous challenges, the aim of the present project is:

- Investigate the electrical limitations of carbon nanotubes and graphene for practical applications in the microwave regime.
- Identify electrical properties of carbon nanotubes, graphene and metamaterials that might be applied and of interest to antennas in the microwave regime.
- Propose, analyse and simulate various antennas where these materials are implemented to achieve size reduction, reconfigurability, transparency and/or flexibility at the microwave regime.
- Provide the advantages, disadvantages and the trade-offs of the proposed antennas made of these materials as well as compare them to other state-of-the-art antennas in the literature.

1.4 NOVEL CONTRIBUTIONS OF THIS THESIS

The novel contributions of this thesis are:

- Two hybrid metal-graphene frequency reconfigurable antennas are designed for WIFI and LTE applications. The hybrid nature of the antenna would allow large changes in the resonant frequency, due to the addition of

the variable surface impedance of graphene, while keeping the antenna efficiencies within reasonable values, due to the main material in the antenna is a good conductor such as copper. In addition, substituting copper for a low resistive transparent conductive film would allow the antenna to be fully transparent. A transparent antenna for WIFI and LTE applications could be used in either mobile and wireless devices or in base stations and access points to allow their integration in scenarios where traditional antennas cannot be implemented because of their visible impact.

- A hybrid metal-graphene polarization reconfigurable antenna and an array based on the same design are designed for DAB/GNSS, different transmission link conditions and antenna orientation. Again, the implementation of graphene would allow to switch between different linear and circular polarizations in order to adapt to each condition and service. Keeping a good conductor such as copper should reduce the losses suffered in the antenna, and hence, provide good antenna efficiencies. Substituting copper for the transparent conductive film would allow transparent polarization reconfigurable antennas that could be implemented in applications where a reduced footprint of the antenna is required such as car windows, product label, solar panels, light panels, etc.

- Two hybrid metal-graphene frequency reconfigurable zeroth order resonant antennas are designed for LTE applications. The characteristic feature of the resonant frequency being independent of the antenna size in zeroth order antennas would provide a substantial antenna size reduction while integrating graphene into the zeroth order antennas would allow for active frequency reconfigurability.

1.5 PUBLICATIONS ARISING FROM THIS THESIS

The work in this thesis has been published in the following papers:

Alvarez, C. N.; Cheung, R. and Thompson, J. S.; "Graphene reconfigurable antennas for LTE and WIFI Systems", 2014 Loughborough Antennas and Propagation Conference (LAPC 2014), 2014, 434-438.

Alvarez, C. N.; Cheung, R. and Thompson, J. S.; "Polarization Reconfigurable Antennas Using Graphene for Microwave Applications", 2015 IEEE International Conference on Ubiquitous Wireless Broadband (ICUWB 2015), 2015, 1-5.

Nunez-Alvarez, C.; Cheung, R. and Thompson, J. S.; "Performance Analysis Of Hybrid Metal-Graphene Frequency Reconfigurable Antennas For The Microwave Regime", IEEE Transactions on Antennas and Propagation. Accepted, awaiting publication.

Nunez-Alvarez, C.; Cheung, R. and Thompson, J. S.; "Performance Analysis Of Hybrid Metal-Graphene Frequency Reconfigurable Zeroth Order Resonant Antennas For Long Term Evolution Applications", IEEE Transactions on Antennas and Propagation. Under second review.

1.6 THESIS STRUCTURE

The remainder of this thesis is structured as follows:

Chapter 2 contains the theory background. First, the antenna concept and the main antenna parameters are defined as well as the limitations of the electrically small antennas and reconfigurable antennas. Second, the definitions of graphene, carbon nanotubes and metamaterials are provided. Moreover, the formulations and characteristics of the admittance of graphene and carbon

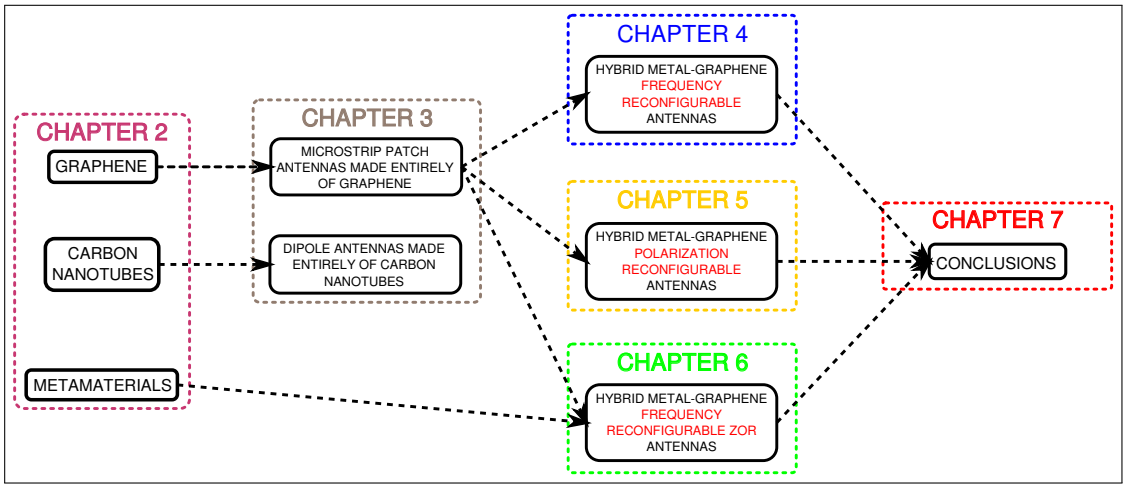

Figure 1.2: Thesis structure.

nanotubes are described. Finally, the equations needed to analyse dipole antennas and microstrip patch antennas fully made of carbon nanotubes and graphene are also provided.

Chapter 3 is a brief chapter where dipole antennas fully made of different configurations of carbon nanotubes and microstrip patch antennas fully made of graphene for different surface impedances are analysed. The dipole antennas and the microstrip patch antennas are designed to resonate at 2.45 GHz, 60 GHz and 110 GHz. The performance study is focused on the trade-off between the achieved size reduction, reconfigurability and radiation efficiency. The work in this chapter motivates the design of hybrid metal-graphene antennas in later chapters.

Chapter 4 presents two hybrid metal-graphene frequency reconfigurable antennas for WIFI and LTE applications. The antennas are based on the microstrip patch antenna. The first design is composed of a main patch made of copper or a hybrid transparent conductive film and two extensions on the radiating edges made of graphene. In this design, frequency reconfigurability is achieved by selecting two extreme values of surface impedance of graphene to simulate ON and OFF states. Switching the graphene extensions translate into larger or shorter lengths of the antenna and hence lower or higher resonant frequencies.

The second design is also composed by a main patch made of either copper or a hybrid transparent conductive film with four slots inserted at each of the four sides where each slot is covered by a graphene sheet. Applying the same technique as in the first design, the surface impedance of graphene is switched between two extreme values to simulate ON and OFF states. In this case, switching the surface impedance of the graphene sheets changes the path of the currents propagating along the antenna making them travel longer or shorter distances and hence resonate at lower or higher frequencies. In addition, there is a section where the limitations of implementing graphene in these designs is studied as well as the power consumed by the antennas. Finally, there is also a comparison between the proposed antennas and other state-of-the-art frequency reconfigurable antennas.

Chapter 5 introduces a hybrid metal-graphene polarization reconfigurable antenna for DAB and GNSS applications. The proposed antenna design is based on a square patch antenna with the four trimmed corners where graphene extensions, in the shape of triangles, are added to substitute the trimmed corners. The main patch is made again of copper or a hybrid transparent conductive film. With only one feeding port, the proposed antenna is able to switch between a linear and two circular polarizations by switching ON and OFF the graphene extensions. Additionally, a two element array composed by the proposed antenna design is presented for applications where polarization diversity is desired. The two antennas are able to switch between two linear polarizations (horizontal and vertical) and two circular polarization (right hand and left hand) at any time. The proposed antenna is compared to other state-of-the-art polarization reconfigurable antennas and the power consumption by the antennas is also provided.

Chapter 6 proposes two hybrid metal-graphene frequency reconfigurable zeroth order resonant antennas for LTE applications. Both antennas are composed of microstrip distributed elements that form left-handed and right-handed inductances and capacitances which determine the zeroth order resonance of both antennas. In the first design, the graphene sheet is added under a microstrip

meander-line while in the second design is added next to a top patch forming a capacitance. In both designs, the surface impedance of graphene is changed to modify the resulting inductances and capacitances of the proposed antenna designs which in turn tunes the zeroth order resonance of the antennas. The analysis includes the study of the performance of the unit cells that form the proposed antenna designs as well as the complete antennas (formed by multiple unit cells). In addition, the power consumption of the proposed designs is studied.

Chapter 7 concludes the thesis with a summary of key concepts, trade-offs and conclusions. It also presents some future work.

Chapter 2

BACKGROUND THEORY

The aim of this thesis is to study the use of novel materials such as graphene, carbon nanotubes and metamaterials in antennas. This chapter provides a comprehensive review of the necessary theory on antennas and the materials implemented in this thesis. The chapter discusses two major topics. The first part deals with the basics of the antenna theory as well as a discussion on electrically small antennas and reconfigurable antennas. The second part introduces the fundamental properties of carbon nanotubes, graphene and metamaterials along with the characterization of antennas fully made of these materials.

2.1 ANTENNA THEORY

2.1.1 DEFINITION OF AN ANTENNA

From the IEEE Standard Definitions of Terms for Antennas, an antenna is defined as "That part of a transmitting or receiving system that is designed to radiate or receive electromagnetic waves" [33]. In other words, antennas allow the wireless transmission of information between electrical devices by generating or harvesting electromagnetic waves. The radiation of electromagnetic waves to free space is accomplished by applying a time oscillating signal at the terminals of the antenna.

The reciprocity theorem in antennas states that if the same antenna is used to transmit as to receive, their characteristics and properties are exactly the same whether it is transmitting or receiving electromagnetic waves [34]–[36].

Many antennas work on the principle of antenna resonance and are hence called resonant antennas. There are only certain frequencies where the resonant antenna enters into resonance, called the resonant frequency f_{res} (Hz), which follows equation (2.1),

$$f_{res} = \frac{c}{\lambda_{res}}, \tag{2.1}$$

where c is the speed of light (m/s) and λ_{res} is the resonant wavelength (m) of the signal to be transmitted or received. Furthermore, one of the antenna dimensions such as the length L (m), width W (m) or height H (m) is commonly set to be a multiple of the wavelength, being most typically around $\lambda_{res}/2$. As observed, the lower the resonant frequency, the larger the resonant wavelength and also the dimensions of the antenna. This is a fundamental principle that has limited most of the antenna designs since the very beginning. However, it is not an unbreakable condition and, as it is explored later in Section 2.1.3 and Section 2.5, it is possible to substantially reduce the antenna size or to even achieve antenna resonances that are completely independent on the antenna size.

2.1.2 ANTENNA PARAMETERS

Any antenna is characterised, first, as a part of an electric circuit by its input impedance, bandwidth and efficiency, and second, as an electromagnetic radiator or receiver by its radiation pattern, directivity, gain and polarization. All of these antenna parameters are briefly defined in this section.

INPUT IMPEDANCE

From the IEEE Standard Definitions of Terms for Antennas, the input impedance of an antenna is defined as “the impedance presented by an antenna at its

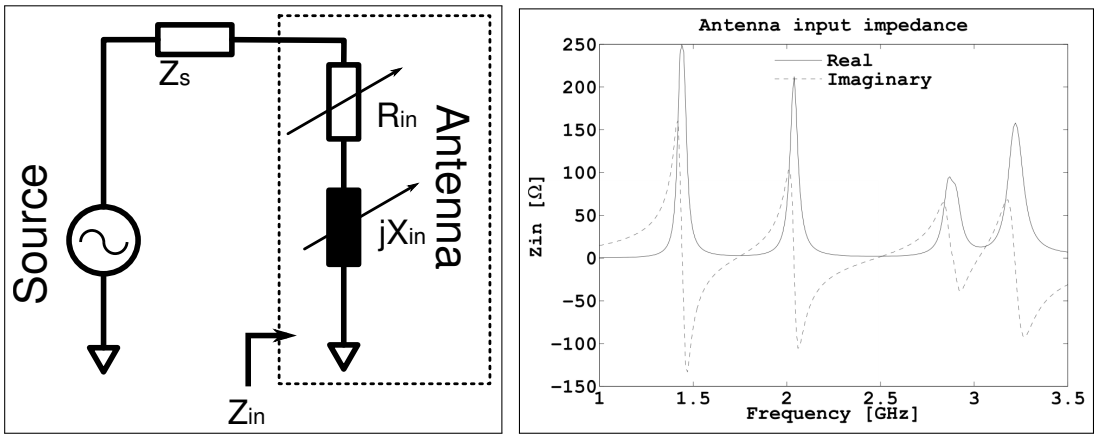

(a) (b)

Figure 2.1: (a) Circuit equivalent of an antenna connected to a source and (b) the frequency variations of its input impedance.

terminals" [33], see Fig. 2.5. The input impedance Z_{in} (Ω) is the circuit equivalent of an antenna which allows one to easily analyse its behaviour when connected to an electrical circuit. It can be also defined as the ratio between the voltage and current presented by the antenna at the terminals

$$Z_{in} = \frac{V_{terminals}}{I_{terminals}} = Rin + jXin, \tag{2.2}$$

where $V_{terminals}$ and $I_{terminals}$ are the voltage (V) and current (A) at the antenna terminals, and Rin (Ω) and Xin (Ω) are the input resistance and reactance of the antenna. The real part of the input impedance represents all the losses suffered in the antenna while the input reactance represents the energy stored in the antenna [34].

REFLECTION COEFFICIENT, RETURN LOSS, ANTENNA BANDWIDTH AND ANTENNA MATCHING

There is always a part of the power generated by the source that is reflected back due to mismatches between the input impedance presented by the antenna Z_{in} and the internal impedance presented by the source Z_s (Ω). The voltage reflection

coefficient ρ (dimensionless) is the parameter that defines the ratio between the reflected voltage V^- (V) wave and the incident voltage wave V^+ (V) and is calculated as [37]

$$\rho = \frac{V^-}{V^+} = \frac{Z_{in} - Z_s}{Z_{in} + Z_s}. \tag{2.3}$$

Knowing that any power supplied by the source P_{sup} (W) that it is not transferred to the antenna is reflected back to the source, then the reflected power P_{ref} (W) can be defined as

$$P_{ref} = P_{sup}\rho^2, \tag{2.4}$$

and the power delivered P_{del} (W) to the antenna is

$$P_{del} = P_{sup}\left(1 - \rho^2\right), \tag{2.5}$$

Here we see that, if the input impedance is the conjugate of the source impedance Z_{in}=Z_s^*, the reflection coefficient is zero ρ=0 and all the power supplied by the source is delivered to the antenna. However, whenever the input impedance is not the conjugate of the source impedance $Z_{in} \neq Z_s^*$, there is some reflection at the terminals of the antenna as $\rho \neq$0 and hence less power is delivered to the antenna and more power is lost due to being reflected back to the source.

The ratio between the power lost due to reflection and the power supplied by the source is commonly called the return gain RG (dB) if expressed in negative values, or return loss RL (dB) if expressed in positive values, and is defined as [37]

$$RG = 20\log|\rho| = -RL = S11. \tag{2.6}$$

where $S11$ (dB) is the scattering parameter at port 1. Fig. 2.2 presents an example of how the return gain of an antenna variates with frequency. The more negative the value of the return gain, the better the matching of the antenna

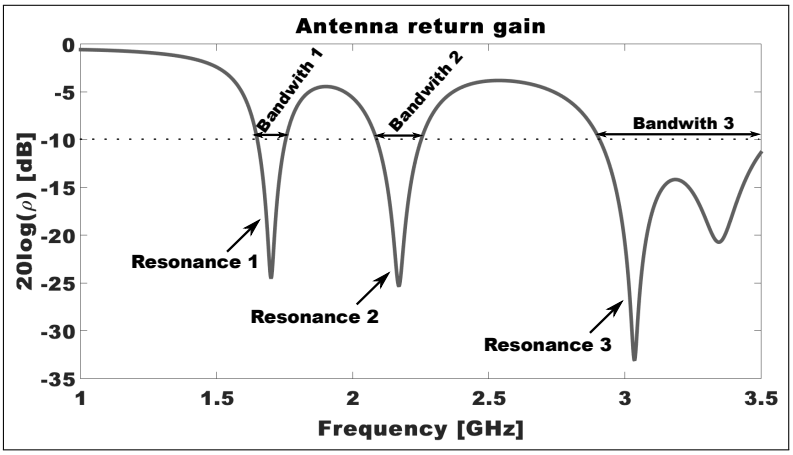

Figure 2.2: Antenna return gain representation, bandwidth and resonances.

to the source, and hence, the more power is transferred from the source to the antenna.

The antenna bandwidth BW (Hz) is defined as "The range of frequencies within which the performance of the antenna conforms to a specified standard with respect to some characteristic" [33]. In other words, it is the range of the frequencies where the antenna can be assumed to satisfy a given requirement. The antenna bandwidth might be limited by impedance restrictions or by radiation characteristics; and it is always defined by the application where the antenna is designed to be implemented. If the antenna is required by an application to guarantee that it receives a certain amount of power from the source, then, as seen earlier in this subsection, the acceptable antenna bandwidth is defined by setting a minimum or maximum value of the reflection coefficient ρ, return loss RL, or even antenna efficiency, and it is called impedance bandwidth [34]. On the other hand, if the application specifies the way the antenna must radiate, then it is categorised as pattern bandwidth where parameters such as gain, side lobe level, beam-width, polarization and beam direction, are the limiting factors [34]. Fig. 2.2 also shows an example of the antenna bandwidth, or range of frequencies, where the return gain satisfy a specific minimum value, in this case RG$\leq$-10 dB.

Depending on the type of the antenna, it might happen that the condition

$Z_{in} = Z_s^*$ is not satisfied, and hence, there is a mismatch between the components. In such cases, it is necessary to introduce a matching network between the antenna and the source [34]. This matching network is designed to smooth the impedance transition between the source and the antenna. This is achieved by forcing the input impedance of the transmission line Z_{in}^{TL} (Ω), when the antenna is acting as a load, to be equal to the internal impedance of the source. The matching network could be a section of transmission lines or passive elements such as resistors, capacitors and inductors.

RADIATION PATTERN, DIRECTIVITY, GAIN AND EFFICIENCY

The radiation pattern is defined in the IEEE Standard Definitions of Terms for Antennas as "The spatial distribution of a quantity that characterizes the electromagnetic field generated by an antenna" [33]. It is sometimes also called the antenna pattern. If an observer is placed at a determined distance, or radius r, and angle (θ,ϕ), elevation and azimuth angles (radians) respectively, from the antenna, the radiation pattern indicates the amount of radiation that the observer will receive at that particular point. It the same process is repeated for all the possible angle values, the resulting graphical or mathematical function is the radiation pattern. Likewise, it also indicates how much electromagnetic radiation the antenna will receive from the same observer if, in this case, the observer was radiating electromagnetic waves instead of receiving them.

The radiation pattern has the characteristic of possessing lobes. Radiation pattern lobes are volumetric components of the radiation pattern where the electromagnetic radiation is relatively stronger compared to their surrounding space. In addition, depending on the direction and relative strength when compared to each other, they can be classified as the major (or main) lobe, side lobes and back lobes. The main lobe determines the direction of the strongest

[1]By Timothy Truckle [Public domain], via Wikimedia Commons `https://en.wikipedia.org/wiki/File:Sidelobes_en.svg`

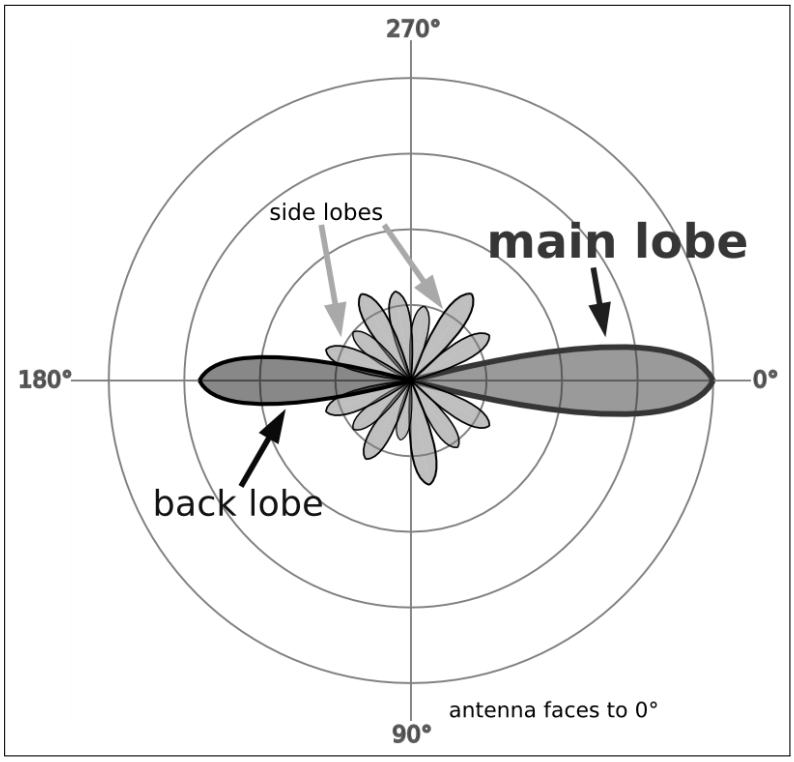

Figure 2.3: Different radiation patern lobes[1].

electromagnetic radiation, the side lobes are weaker lobes compared to the main lobe and the back lobe is always found in the opposite direction of the main lobe. Furthermore, depending on the configuration of these lobes, the radiation patterns can be classified into three different patterns such as isotropic, omnidirectional and directional radiation patterns [34], [36].

An antenna possessing an isotropic radiation pattern is defined as "A hypothetical, lossless antenna having equal radiation intensity in all directions" [33]. Hence, the radiation pattern of an isotropic antenna is a perfect sphere with value one at each angle because it radiates and receives exactly the same amount of electromagnetic radiation at any angle. Isotropic radiation patterns are used as reference for the other types of radiation patterns. Isotropic antennas are only possible as a mathematical concept and cannot be physically implemented [34].

An omnidirectional antenna is defined as "An antenna having an essentially non-directional pattern in a given plane of the antenna and a directional pattern

in any orthogonal plane" [33], or in other words, an omnidirectional antenna presents similar radiation along a wide range of angles and at least a null in a particular angle. Omnidirectional radiation patterns are a particular case of directional radiation patterns.

A directional antenna is defined as "An antenna having the property of radiating or receiving electromagnetic waves more effectively in some direction[s] than others" [33]. A directive antenna accentuate the radiation at some angles at expenses of attenuating at some others. A key property of such antennas is the directivity of an antenna D or $D(\theta, \phi)$ (dimensionless or in dB) which is "The ratio of the radiation intensity in a given direction from the antenna to the radiation intensity averaged over all directions" [33]. Therefore, the larger the radiation at a particular angle compared to the isotropic case the larger the directivity is at that angle.

There are two definitions for efficiency. The first one is the radiation efficiency η_r and it is defined as "The ratio of the total power radiated by an antenna to the net power accepted by the antenna from the connected transmitter" [33]. This efficiency definition refers to how much power is radiated from the power delivered to the antenna by the source. The radiation efficiency η_r (%) is calculated as

$$\eta_r = \frac{P_{rad}}{P_{del}} 100 = \frac{P_{rad}}{P_{rad} + P_{loss}} 100, \tag{2.7}$$

or in decibels as

$$\eta_r = 10 \log_{10} \left(\frac{P_{rad}}{P_{rad} + R_{loss}} \right). \tag{2.8}$$

where P_{loss} is the power lost (W) in the antenna and P_{rad} is the power radiated (W). The higher the losses in the antenna the lower the radiation efficiency. The second definition is called the realized radiation efficiency or total radiation efficiency η_t (% or dB) and it is defined as "The radiation efficiency of an antenna reduced by its impedance mismatch factor" [33]. In this case, the resulting

efficiency η_t considers all the possible losses, including the loss from the power reflected back to the source and is obtained as

$$\eta_t = \frac{P_{rad}}{P_{sup}} 100 = \frac{P_{rad}\left(1-\rho^2\right)}{P_{del}} = \eta_r \left(1-\rho^2\right) 100, \tag{2.9}$$

or in decibels as

$$\eta_t = 10 \log_{10} \left(\eta_r \left(1-\rho^2\right)\right). \tag{2.10}$$

If there is no mismatch between the source and the antenna ρ=0, the total antenna efficiency is equal to the radiation efficiency η_t=η_r.

Similar to the directivity, the gain of an antenna G or $G(\theta, \phi)$ (dimensionless or in dB) is defined as "The ratio of the radiation intensity in a given direction to the radiation intensity that would be produced if the power accepted by the antenna were isotropically radiated" [33]. The definition is very similar to the one provided for the directivity but in this case the reference power is the power accepted by the antenna (the power measured at the terminals of the antenna) instead of the power radiated. This means that the gain accounts for the radiation efficiency η_r of the antenna. There is a relation between the gain and directivity of an antenna. This relation is expressed in dimensionless units as

$$G(\theta, \phi) = \eta_r D(\theta, \phi). \tag{2.11}$$

or in decibels as

$$G(\theta, \phi) = \eta_r + D(\theta, \phi). \tag{2.12}$$

As observed, the gain and directivity are very similar parameters but not equal. However, in the case where the antenna is lossless, the radiation efficiency is one η_r=1 (dimensionless) or zero η_r=0 dB, and thus, they are exactly the same.

POLARIZATION

In antenna theory the direction at which the electric and magnetic fields point to is important and is defined by the polarization of the electromagnetic wave. Sufficiently far away from the antenna, any electromagnetic wave propagating in a medium can be modelled as a plane wave. Consequently, the polarization of an antenna is defined as "In a given direction from the antenna, the polarization of the wave transmitted by the antenna" [33]. The polarization of an antenna determines the polarization of the plane wave that can be transmitted to free space, as well as, the polarization of the plane wave that the antenna is able to receive. If an antenna has a different polarization to the plane wave that it is trying to receive, it will reduce the ability to receive the energy from that particular plane wave. In a two antenna system where one antenna transmits and another receives, the polarization of both antennas must either be equal or as close as possible, otherwise, they might not be able to communicate at all due to the loss from polarization mismatch.

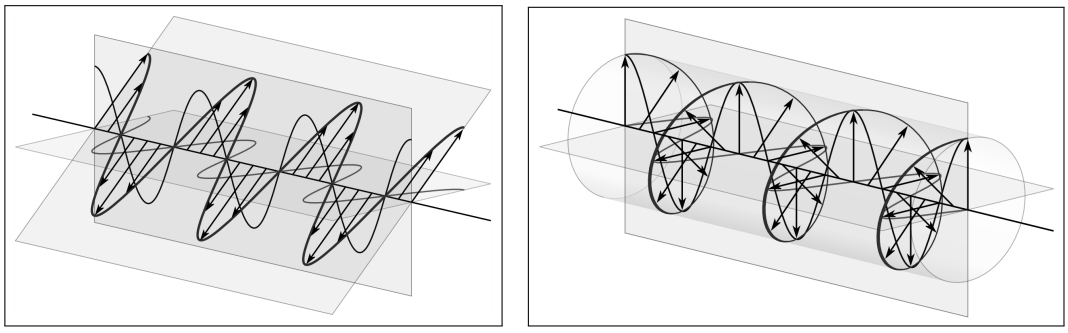

(a) **(b)**

Figure 2.4: Graphical representation of different electromagnetic polarizations (a) linear polarizations[2] and (b) circular polarizations[3].

There are three types of polarization, linear, circular and elliptical, see Fig. 2.4. However, in reality, the linear and the circular polarization are special cases of the elliptical polarization [33]. An electromagnetic wave presents a linear polarization when its electric field (and consequently also the magnetic field) is directed always along the same line at any point in space and time, or in other words, is always parallel to the same axis [34]. In addition, if a ground plane is defined, linear polarization can be divided into horizontal and vertical if the electric field propagates in parallel or perpendicular to the ground plane, respectively. An electromagnetic wave has a circular polarization when the direction of its electric field follows a circular pattern as a function of time [34]. Depending on the orientation of the rotation, the circular polarization can be split into right-hand or left-hand if the rotation is clockwise or anti-clockwise, respectively. The axial ratio (AR) (dB) is a parameter that measures the ratio between these two components and can be calculated as [34]

$$AR = 20\log_{10}\left(\frac{E_{x0}}{E_{y0}}\right) \quad \text{if } E_{x0} > E_{y0}, \tag{2.13}$$

$$AR = 20\log_{10}\left(\frac{E_{y0}}{E_{x0}}\right) \quad \text{if } E_{x0} < E_{y0}, \tag{2.14}$$

$$\tag{2.15}$$

where E_{x0} and E_{y0} are the nominal values of the electric field (V/m) at the axes x and y. Therefore, the axial ratio is useful to determine what type of polarization a plane wave has depending on its value. If AR=0 dB, then the plane wave posses a circular polarization as both components have the same weight. On the other hand, if AR=∞ dB, then, the plane wave is linearly polarised as the minor component is zero and the total electric field is the result of only one of the

[2]By Dave3457 derivative work: RJB1 [Public domain], via Wikimedia Commons `https://commons.wikimedia.org/wiki/File%3ALinearly_Polarized_Wave.svg`

[3]By Dave3457 (Own work) [Public domain], via Wikimedia Commons `https://commons.wikimedia.org/wiki/File%3ACircular.Polarization.Circularly.Polarized.Light_With.Components_Left.Handed.svg`

components. For all the other remaining AR values, the plane wave is considered to be elliptically polarized.

Another efficiency factor to consider comes from the mismatch between the antenna polarization and a plane wave polarization. Any antenna generates an electromagnetic wave with a specific polarization, and from the reciprocity theorem, any antenna is only able to harvest an electromagnetic wave that have the same polarization as the antenna. This is because the electric field is only able to excite a resonating current in the antenna if the wave is received at a specific angle of polarization. The polarization loss factor (PLF) (dimensionless) accounts for the mismatch between the antenna polarization and the plane wave polarization, and defined as [34]

$$PLF = |\hat{\mathbf{a}}_{ant} \cdot \hat{\mathbf{b}}_{inc}|^2 = |\cos\psi|^2, \tag{2.16}$$

where $\hat{\mathbf{a}}_{ant}$ (dimensionless) and $\hat{\mathbf{b}}_{inc}$ (dimensionless) are the unitary vectors of the antenna and incident wave polarizations and $||$ is the absolute value. As observed, the PLF depends directly on the angle ψ (radiants) between the two unitary vectors $\hat{\mathbf{a}}_{ant}$ and $\hat{\mathbf{a}}_{inc}$. If the angle is ψ=0 or ψ=$n\pi$ radiants (for n=1,2,3,...), there is no polarization mismatch and all the energy from the wave is coupled to the antenna. On the other hand, if the angle is ψ=$n\pi/2$ radiants (for n=1,3,5,...) then no coupling exists between the incident wave and the antenna and consequently no energy is harvest from the plane wave. In this later case, the plane wave presents an orthogonal polarization with regard to the antenna polarization. In addition, in a system of two or more antennas, where one or more is transmitting and one or more is receiving, it is vital to guarantee as much as possible the alignment of their polarizations for an efficient communication.

2.1.3 THE ELECTRICALLY SMALL ANTENNA

Traditionally, the size of an antenna is determined by the wavelength of the electromagnetic wave to be transmitted or received, being half of the wavelength

or larger the most ideal size. However, smaller antenna designs are possible at the expense of deteriorating other important antenna parameters such as the antenna bandwidth, gain and efficiency [38]. This trade-off dictates the maximum reduction of a radiating system for a specific set of antenna restrictions. The quality factor Q is commonly used to characterise the performance of antennas as it provides an indication of the power radiated by the antenna and the energy stored in the antenna.

The quality factor Q (dimensionless) of antennas that excite either one of the transmagnetic TM_{01} or the transelectric TE_{01} modes for linearly polarised antennas, or both modes at the same time for circularly polarized antennas, can be calculated as [39], [40]

$$Q = \frac{1}{ka} + \left(\frac{1}{ka}\right)^3, \tag{2.17}$$

for the linearly polarised case, and as

$$Q = \left[\frac{2}{ka} + \left(\frac{1}{ka}\right)^3\right], \tag{2.18}$$

for the circular polarised case, where $k{=}2\pi f/c$ is the wavenumber or phase constant (rad/m) of the electromagnetic wave and a is the radius (m) of the smallest sphere that encloses entirely the antenna. Note that the term "electrically small antenna" refers to antennas that are much smaller in size to the wavelength. Typically, an antenna is electrically small if it occupies a volume that it is enclosed within a sphere of radius $a \leq \lambda/2\pi$ [41], [42]. This gives a ratio of $ka \leq 1$ which means that electrically small antennas have large values of quality factor. Large values of quality factor Q translates into more energy stored in the antenna and less being radiated. This dramatically affects the achievable antenna bandwidth and gain. In [43] the quality factor Q analysis is extended to any type of antenna polarization.

QUALITY FACTOR AND BANDWIDTH LIMITATIONS

In [44], a practical and realistic relation between the quality factor and the fractional bandwidth of an electrically small antenna is defined

$$FBW \approx \frac{1}{Q}\frac{VSWR-1}{\sqrt{VSWR}}, \tag{2.19}$$

where FBW is the fractional bandwidth (dimensionless) expressed as

$$FBW = \frac{f_H - f_L}{\sqrt{f_h f_L}}, \tag{2.20}$$

where f_H and f_L are the high- and low-edge frequencies (Hz) defining the bandwidth [45]; and $VSWR$ is the voltage standing wave ratio (dimensionless)

$$VSWR = \frac{1+|\rho|}{1-|\rho|}. \tag{2.21}$$

As it is seen, the higher the quality factor, the lower the fractional bandwidth, and consequently, electrically small antennas are expected to have very narrow bandwidths. Additional formulations in [45], based on Fano's and Wheeler's principles, provide other approximations depending on the number of tuned circuits.

QUALITY FACTOR AND GAIN LIMITATIONS

Harrington demonstrated in [43] that the gain of the antenna is dependent on the size of the antenna

$$G = (ka)^2 + 2\,(ka)\,. \tag{2.22}$$

Consequently, electrically small antennas are also expected to have small values of gain.

2.1.4 THE RECONFIGURABLE ANTENNA

A reconfigurable antenna is designed in a manner that it is possible to manually or automatically (via software) change its resonant frequency, operational bandwidth, radiation pattern, and/or polarization to adapt to different services, system requirements and environments. This is achieved by switching, via mechanical or electrical actuation, the current path propagating along the element, changing their geometrical shapes, tuning their feeding network or modifying their physical dimensions [46].

Mechanical switching is mostly performed by Micro or Nano Electromechanical systems (MEMS or NEMS) depending on the device scale. MEMS (NEMS) are basically very small switches formed by two plates separated, OFF state, a certain distance to each other with a dielectric between them. Then, the plates are electrostatically attracted via an applied voltage to the other until they touch, ON state.

Electrical switching is mainly carried out by transistor based technology such as Metal Semiconductor Field Effect Transistor (MESFET), Pseudomorphic High Electron Mobility transistor (PHEMT); or by diode-based technology such as the P-type Insulator N-type diode (PIN diode). In most of the cases, the switching is achieved when changing charge carrier concentrations by applying a direct current (DC) voltage bias or light (mostly infra-red IR) so an electrical path is created through the switch.

Varactors are diodes added to any part of the antenna where its capacitance varies with the applied control voltage [46], [47]. Tunable materials are the latest solution being considered for reconfigurable antennas. They are materials where electrical, magnetic and/or mechanical properties are tuned by applying external excitations such as thermal, electric, magnetic or light bias.

In this thesis, graphene, carbon nanotubes and metamaterials are investigated as alternative methods to obtain antenna size reduction and reconfigurability. In

the next sections, these materials are defined and analysed for the implementation in antennas.

2.2 GRAPHENE

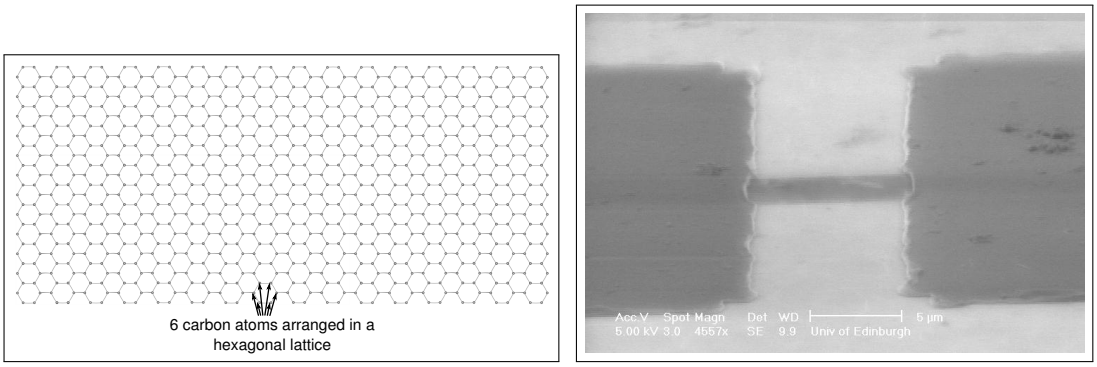

(a) **(b)**

Figure 2.5: Graphene: (a) graphical representation of a graphene sheet and (b) actual picture of a graphene sheet[4].

Graphene is a flat mono-atomic layer of Carbon atoms distributed in a two-dimensional honeycomb-like lattice through sp2 bonding [22], [48]–[51]. Graphene sheets can be very narrow (a few atoms width) and up to several centimetres length [52] while being just one atom thick, making graphene the first "two dimensional" material. Electrons/holes behave as massless relativistic particles, called Dirac fermions, as their energy-momentum is linear, instead of being quadratic, and at the specific Dirac point their energy (or energy gap between the conduction and valence band) is exactly zero making graphene a zero-gap semiconductor or semi-metal [22], [49]–[51]. This phenomena translates into some extraordinary electronic properties theoretically predicted by [53] and measured much later by [18], such as the fact that the surface admittance of graphene can

[4]Graphene resonator made at the Scottish Microelectronics Centre (SMC), courtesy of Prof. Rebecca Cheung.

be tuned by applying and electrostatic field via a DC voltage bias. In addition, an unbiased pristine single layer of graphene (SLG) only absorbs 2.3% [54], [55] of the visible light spectrum and measurements of mechanical strength conclude that it is able to support breaking forces of up to 42 N/m with Young's modulus of 1 TPa and intrinsic strength of 130 GPa [56] while being extremely light (0.77 mg/m^2) at the same time.

2.2.1 ADMITTANCE PROPERTIES OF GRAPHENE

The surface admittance of graphene σ_s (S) can be evaluated considering quantum mechanics and statistics such as the quantum mechanical Fermi-Dirac statistics, the Pauli principle and the Drude-Sommerfield model [57]–[59]. This results in a surface admittance expressed in a Kubo-like formula (based on the current-current correlation function) that accounts for the quantum nature and interband effects in graphene and is calculated as [59]–[61]

$$\sigma_s = \frac{jq^2}{\pi\hbar^2(\omega - j2\Gamma)}\left[\int_0^\infty \varepsilon(\frac{\partial f_d(\varepsilon)}{\partial\varepsilon} - \frac{\partial f_d(-\varepsilon)}{\partial\varepsilon})d\varepsilon - \int_0^\infty \frac{f_d(-\varepsilon) - f_d(\varepsilon)}{(\omega - j2\Gamma)^2 - 4(\varepsilon\hbar)^2}d\varepsilon\right], \tag{2.23}$$

where q is the electron charge (C), Γ=$1/2\tau_t$ is the phenomenological scattering rate (s^{-1}), τ_t is the relaxation time (s), $\hbar$ is the reduced Planck's constant (Js), ε is the carrier energy (J), T is the operational temperature (K), ω=$2\pi f$ is the angular frequency (rad/s) and $f_d(\varepsilon)$ is the Fermi-Dirac distribution (dimensionless) computed as equation (2.24)

$$f_d(\varepsilon) = \frac{1}{e^{(\varepsilon-\mu_c)/k_BT} + 1} \tag{2.24}$$

where μ_c is the chemical potential (J), or Fermi energy ε_F (J), and k_B is the Boltzmann constant (J/K). This approximation provides the isotropic surface longitudinal admittance of graphene valid at any frequency (from DC to optical frequencies) and in the absence of magnetic field (no Hall conductivity is present)

[60]. In equation (2.23), the first integral is determined by intraband interactions and the second one is due to interband contributions.

For the range of frequencies considered here, $2\pi f \ll \tau_t^{-1}$ where f is up to 110 GHz and τ <1ps, the intraband contributions are dominant and the resulting surface admittance can be simplified, if Γ (and hence τ_t) is assumed to be independent of the energy ε, as [61]

$$\sigma_{AC} = \frac{-jq^2 k_B T}{\pi\hbar^2(\omega - j\tau_t^{-1})}\left(\frac{\mu_c}{k_B T} + 2\ln(e^{-\frac{\mu_c}{k_B T}} + 1)\right), \tag{2.25}$$

where the resulting surface admittance is still dependent on the chemical potential μ_c, relaxation time τ_t, operational temperature T and operational frequency ω. In graphene, the chemical potential μ_c is related to the carrier density n (m^{-2}) as [22], [24]

$$n = \frac{2}{\pi(\hbar v_f^g)^2}\int_0^\infty \varepsilon[f_d(\varepsilon - \mu_c) - f_d(\varepsilon + \mu_c)]d\varepsilon \simeq \frac{(\mu_c/\hbar v_f^g)^2}{\pi}, \tag{2.26}$$

where $v_f^g = 1 \times 10^6$ is the Fermi velocity (m/s) in graphene. The value of n can be dynamically modified via the electric field effect shown in Fig. 2.6, where a direct current (DC) voltage is applied between a graphene sheet and a heavily doped semiconductor to vary the number of charge carriers n in the graphene sheet. The change of n follows equation (2.27)

$$n = \frac{\epsilon_o \epsilon_r^d V_b}{dq}, \tag{2.27}$$

where ϵ_o is the vacuum permittivity (F/m), V_b is the DC voltage bias (V), d is the thickness (m) and ϵ_r^d is the relative permittivity of the dielectric separating the graphene sheet and the back gate material (a p or n doped semiconductor) [18], [24].

Nonetheless, one might gain the impression that any value of the surface impedance of graphene $Zs{=}\sigma_{AC}^{-1}$ ($\Omega/_\square$) can be achieved by applying a sufficiently large or small value of V_b. Unfortunately, this is not possible due to scattering

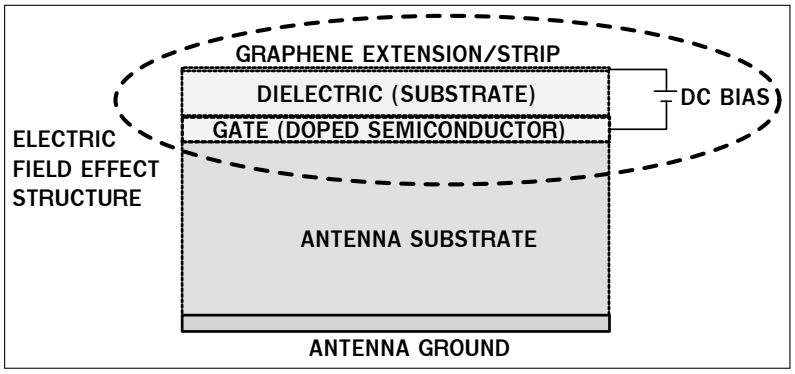

Figure 2.6: Example of an electric field effect structure added to a patch antenna.

mechanisms present in graphene that will limit Zs to lie between a minimum and a maximum achievable values for very low and very high voltages V_b. Therefore, it is important to understand the physics involved in the variable admittance phenomenon and its limitations to enable realistic surface impedances and the associated voltages V_b to be considered in the design of reconfigurable antennas in this thesis. This is discussed in detail in the next section.

2.2.2 SCATTERING MECHANISMS IN GRAPHENE

For a simplistic evaluation, τ_t in equation (2.25) might be considered constant and independent of the carrier density n and hence the surface admittance is only proportional to n [18]. However, this is not always the case. The relaxation time τ_t, and consequently also the carrier mobility, are almost always dependent on the charge carrier density n. This is due to the fact that for different values of n, there are different scattering mechanisms that ultimately determine the surface admittance value in (2.25) [22], [62]. The Matthiessen rule, equation (2.28), determines the overall relaxation time for any carrier density n and temperature T [24],

$$\frac{1}{\tau_t} = \left(\frac{1}{\tau_d} + \frac{1}{\tau_i}\right) + \left(\frac{1}{\tau_p} + \frac{1}{\tau_c}\right) = \left(\frac{1}{\tau_L}\right) + \left(\frac{1}{\tau_S}\right), \tag{2.28}$$

where each τ_x is due to a single scattering mechanism such as defects (τ_d),

impurities (τ_i), phonons (τ_p) and carrier-carrier (τ_c) interaction. Furthermore, scattering mechanisms in graphene might be classified into two main groups, long range scattering (τ_L) and short range scattering (τ_S) as shown in equation (2.28). The main difference between them is their dependence on n and T. Note that, in graphene, the relaxation time τ_t and the carrier mobility μ_t (m^2/Vs) are related to the carrier density n by the Drude's model conductivity equation [22], [24], [63]–[66] as

$$\tau_t = \frac{\mu m^*}{e} = \frac{\mu_t \hbar \sqrt{\pi n}}{e v_f^g}, \tag{2.29}$$

where m^* is the carrier mass in graphene (Kg).

LONG RANGE SCATTERING EFFECTS

To start with, defects in graphene might be caused by topological defects (i.e. Stone-Wales defects), vacancies, interstitial atoms, substitutions of non Carbon atoms/molecules, grain boundaries, edge defects and inter-facial roughness (or wrinkles/ripples) [22], [24]. Localized defects cause moving carriers to be scattered within the crystal lattice and also a slight modification of the local energy bands (even create a bandgap or displace the Dirac Point at that location) [22], [67]. The relaxation time for graphene due to these effects follows the equation (2.30) [51], [68], [69].

$$\tau_d \simeq \frac{\mu_d \hbar \sqrt{n\pi}}{q v_f^g} [ln(k_F R_o)]^2 = \frac{\sqrt{n\pi}}{n_d v_f^g} [ln(k_F R_o)]^2, \tag{2.30}$$

where μ_d is the carrier mobility (m^2/Vs) due to defects, n_d is the defect density (m^{-2}), k_F is the Fermi wavevector (rad/m) and R_o is the radius of the interaction potential ($\sim$ 0.284 nm). The value of n_d might be empirically obtained by the equation (2.31) [49], [51], [70].

$$n_d(m^{-2}) \sim \frac{1,8 \times 10^{26}}{\lambda^4} \frac{I_D}{I_G} \tag{2.31}$$

where λ is the wavelength of the excitation source (in nm), and I_D and I_G are the D and G peak values obtained from graphene's Raman spectroscopy, respectively.

The relaxation time τ_d has a $\sqrt{n}$ dependency on the number of charged carriers, and consequently, it is considered to contribute to the long range relaxation time τ_L [51], even though they are short-range processes [51], [71]. Defects might be reduced, or even completely removed, through better synthesis techniques, improved patterning processes, dry transfers, thermal and ohmic annealing and substrate engineering [49], [51], [72]–[74]. For example, chemical vapour deposition (CVD) grown graphene is more sensitive to these defects than mechanically ex-foliated graphene, but a proper selection of the target substrate, better transfer process and post-annealing help to drastically reduce them [75], [76].

Another scattering source comes from impurities trapped in the surface of graphene, and/or at the interface between graphene and the substrate (see Fig. 2.6); and even inside the substrate itself [22], [51]. They cause the charge carriers propagating in graphene to be scattered from Coulomb forces [49], [51]. Its associated relaxation time is defined by equation (2.32)

$$\tau_i \simeq \frac{\mu_i \hbar \sqrt{n\pi}}{q v_f^g} = \frac{10\sqrt{n\pi}}{\pi n_i v_f^g}, \tag{2.32}$$

where n_i is the impurity density (m^{-2}). In this case, n_i is commonly obtained from experimental measurements of the conductivity when Coulomb scattering is dominant. The resulting τ_i is again proportional to $\sqrt{n}$ and hence it is also classified as long-range scattering effect (τ_L) [51]. Similarly to defect based scattering, impurities might be reduced by improved transfer methods, annealing and substrate engineering [49], [51], [77]–[85]. Moreover, in [71] the authors predict that reducing a couple of orders of magnitude the impurity density (from 10^{16} m^{-2} to 10^{14} m^{-2}) should provide carrier mobilities as high as $\sim$20 m^2/Vs, which would be then limited by scattering caused by phonons as discussed next.

SHORT RANGE SCATTERING EFFECTS

Carrier-phonon scattering is caused by collisions between the charge carriers and the atomic nuclei that are moving in the crystal lattice due to, for instance, thermal vibrations [51]. They are acoustic or optical whether the phonons move in phase or out of phase, respectively [58], [86]. Unlike defects and impurities (where they are either fully intrinsic or extrinsic), they might depend on both graphene's internal properties and the surrounding environment. Longitudinal acoustic (LA) phonons are considered here to be dominant as optical phonons in graphene have too high energies (∼0.1-0.2 eV) to affect the material at room temperature [62], [87], and any other phonons (i.e. extrinsic optical, polar, remote oxide, flexural and remote inter-facial phonons) caused by the environment can be substantially reduced or even completely removed by substrate engineering or by suspending the graphene sheet in air [62], [88]. In fact, LA phonons are often considered to be the ultimate mechanism that will limit graphene device performance in the future, once the other scattering effects are drastically reduced or completely removed [62], [88]. Their relaxation time is expressed in equation (4.11), as long as the temperature T is well above the Bloch-Grüneisen temperature T_{BG} ($T \gg T_{BG}$) [62],

$$\tau_p = \frac{\mu_p \hbar \sqrt{n\pi}}{q v_f^g} = \frac{4\hbar^2 \rho_m v_{ph}^2 v_f^g}{\sqrt{n\pi} D^2 k_B T}, \tag{2.33}$$

where D is the deformation potential (eV), $\rho_m = 7.6 \times 10^{-7}$ is the two dimensional mass density of graphene (Kg/m^2), $v_{ph} = 2.1 \times 10^4$ is the sound velocity of LA phonons in graphene (m/s) and T_{BG} is the Bloch-Grüneisen temperature (K) defined as

$$T_{BG} = \frac{2\hbar k_F v_{ph}}{k_B}. \tag{2.34}$$

In this case, the relaxation time depends on the carrier density as $1/\sqrt{n}$ so it contributes to the short range relaxation time (τ_S). The operational temperature

plays an important role and can reduce or increase considerably the surface impedance of graphene due to phonons.

Finally, carrier-carrier interactions do not provide substantial losses in graphene at room temperature with finite charge carrier densities and in the diffusive regime [89]. Under these conditions, other scattering processes, specially LA phonons, would be dominant over any carrier-carrier collisions so that its contribution can be neglected. Therefore this effect is not considered in this thesis for the relaxation time equation in (2.28).

2.2.3 MAXIMUM AND MINIMUM Zs

At room temperature (295 K), the maximum surface impedance (or minimum surface admittance) in the low electric field-effect carrier density regime is limited by thermally excited carriers [90], and electron-hole puddles caused by charged impurities [91]. As observed from the surface admittance equation in (2.25), the Kubo formalism already takes into account the thermally excited carrier densities as it is temperature dependent. However, the energy of the electron-hole puddles needs to be determined to set the minimum achievable surface admittance. The energy of the electron-hole puddles ε_{puddle} (J), or the lowest possible chemical potential level $\mu_{c,min}$ (J), follows equation (2.35)

$$\varepsilon_{puddle} = \mu_{c,min} = \hbar v_f^g \sqrt{\pi \tilde{n}}, \tag{2.35}$$

where $\tilde{n}$ is the carrier density (m^{-2}) variations - carrier inhomogeneity density - caused by the electron-hole puddles which forces the minimum carrier density n to be greater than or equal to this value $n_{min} \geq \tilde{n}$. It is important to mention that defects n_d and impurities n_i are the main cause of the electron-hole puddles $\tilde{n}$ present in graphene sheets and reducing their densities should decrease their effect.

Fig. 2.7 shows a typical example of how the total relaxation time τ_t is dominated at different charge carrier densities n by long-range and short-range

relaxation times (τ_L and τ_S respectively). The total relaxation time is computed from equation (2.28) by selecting different values of n (from $1{\cdot}10^{16}$ m^{-2} to $1{\cdot}10^{18}$ m^{-2}), where τ_L and τ_S are obtained by setting $\mu_t = \mu_L$ =2 m^2/Vs in equation (2.29); D=18 eV and T=295 K are used in equation (4.11) to evaluate τ_p. The range of simulated values for n here is selected in order to visually demonstrate the differences. It is firstly observed that as the carrier density n is increased (for instance raising the DC bias voltage) the long-range scattering times increase as defects and impurities contribute less to the scattering of carriers. Conversely, the short-range scattering time drops to lower values for high carrier densities as LA phonons start to dominate scattering.

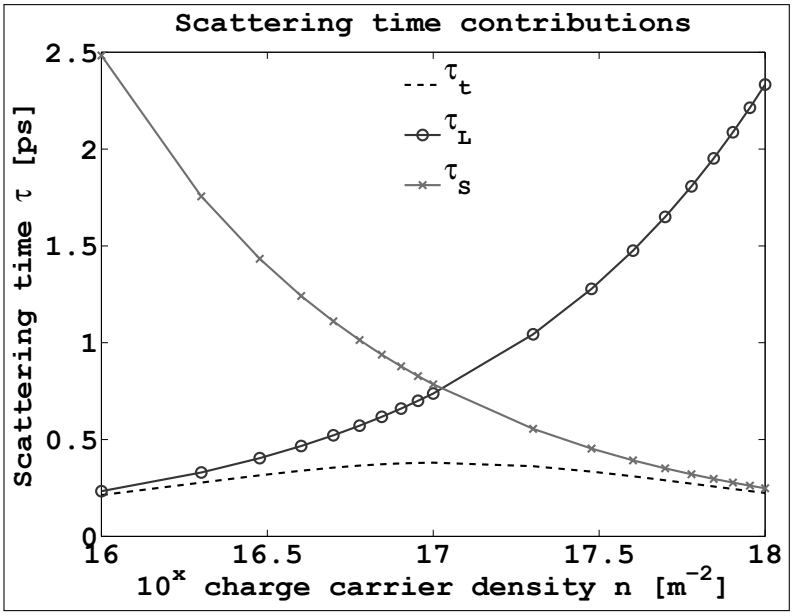

Figure 2.7: The total relaxation time (τ_t) is dominated by different relaxation times.

As expected, for low n values, the relaxation time is dominated by defects and impurities while for high densities it is the LA phonons that are the limiting factor. If the resulting total relaxation time τ_t is used to calculate the total surface impedance Zs - from equation (2.25) - for different values of charged carrier density n, the resulting total Zs also follows the same behaviour as τ_t. Consequently, there is a trade-off between the graphene material quality (defined

by setting either a value of τ_L or μ_L, or by independent values of n_d and n_i), the maximum applied V_b needed (which directly depends on required carrier density n), the deformation potential D, the operating temperature T and the maximum and minimum values of Zs achievable.

2.2.4 MICROSTRIP PATCH ANTENNAS FULLY MADE OF GRAPHENE

In this thesis, graphene-based antennas are implemented in planar structures, like the microstrip patch antenna, due to its two dimensional nature. This section provides the equations necessary to evaluate the performance of microstrip patch antennas fully made of graphene.

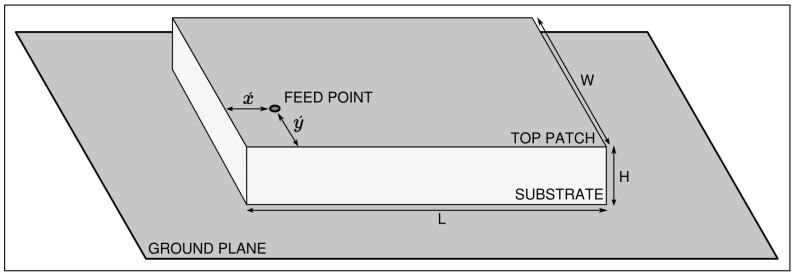

Figure 2.8: Graphical representation of a microstrip patch antenna.

The radiation efficiency (dB) of a microstrip patch antenna fully made of graphene is calculated following the cavity model in [92], see Fig. 2.8, as

$$\eta_r = 10 \log \left(\frac{1}{\delta_{eff} Q_r} \right), \tag{2.36}$$

where

$$\delta_{eff} = \frac{1}{Q_T} = \frac{1}{Q_d} + \frac{1}{Q_c} + \frac{1}{Q_r} + \frac{1}{Q_{sw}}, \tag{2.37}$$

where Q_d is the dielectric loss, Q_c is the conductor loss, Q_r is the radiation loss and Q_{sw} is the surface wave loss. The dielectric loss Q_d is directly determined by the loss tangent tanδ (dimensionless) of the substrate

$$Q_d = \frac{1}{\tan\delta}. \tag{2.38}$$

The conductor loss Q_c (dimensionless) is caused by power dissipated as heat in the antenna due to the finite admittance of the material used

$$Q_c = \frac{1}{2}\eta_0\mu_r\left(\frac{kH}{Zs}\right), \tag{2.39}$$

where H=0.02c/f_{res} (m) is the substrate hight set to satisfy the validation of the cavity model [92], η_0≈376.73 Ω is the free space impedance, μ_r is the relative permeability (dimensionless) of the antenna substrate and Zs is the surface impedance of graphene, see equation (2.25). In this case, Zs is obtained from equation (2.25). The radiation loss Q_r considers the energy that it is stored within the antenna and not radiated to free space. It is computed as

$$Q_r = \frac{2\omega W_s}{P_{rad}}, \tag{2.40}$$

where W_s is the energy (J) stored in the antenna. W_s is calculated as

$$W_s = \frac{\epsilon_0\epsilon_r LWV_{drv}^2}{8H}, \tag{2.41}$$

where V_{drv} is the driving point voltage (V), ϵ_r is the relative permittivity of the substrate, L is the length (m) of the antenna and W is the width (m) of the antenna. The antenna width is calculated as

$$W = \frac{c\sqrt{\frac{2}{\epsilon_r+1}}}{2f_{res}}. \tag{2.42}$$

The antenna length is calculated to resonate at the specific resonant frequencies of interest f_{res} as

$$L = \frac{c}{2f_{res}\sqrt{\epsilon_r^{eff}}} - 2\Delta_L, \tag{2.43}$$

where

$$\epsilon_r^{eff} = \frac{\epsilon_r + 1}{2} + \frac{\epsilon_r - 1}{2\sqrt{1 + \frac{12H}{W}}}, \tag{2.44}$$

is the effective relative permittivity (dimensionless) due to the fringing fields and

$$\Delta_L = 0.412H \frac{\left(\epsilon_r^{eff} + 0.3\right)\left(\frac{W}{H} + 0.264\right)}{\left(\epsilon_r^{eff} + 0.258\right)\left(\frac{W}{H} + 0.8\right)}, \tag{2.45}$$

is the additional length (m) due to the fringing fields. The power radiated by the microstrip antenna is

$$P_{rad} = \frac{V_0^2 A \pi^4}{23040}\left[(1-B)\left(1 - \frac{A}{15} + \frac{A^2}{420}\right) + \frac{B^2}{5}\left(2 - \frac{A}{7} + \frac{A^2}{189}\right)\right], \tag{2.46}$$

with

$$A = \left(\frac{\pi L}{\lambda}\right)^2, \tag{2.47}$$

where λ=c/f, being f any frequency (Hz) and

$$B = \left(\frac{2W}{\lambda}\right)^2. \tag{2.48}$$

Finally, the surface wave loss Q_{sw} (dimensionless) accounts for the amount of power lost by waves propagating on the surface of the substrate. It is computed as

$$Q_{sw} = Q_r \left(\frac{\epsilon_r^{hed}}{1 - \epsilon_r^{hed}}\right), \tag{2.49}$$

where

$$\epsilon_r^{hed} = \frac{P_r^{hed}}{P_r^{hed} + P_{sw}^{hed}}, \tag{2.50}$$

$$P_r^{hed} = \frac{\left(k_0 H\right)^2 \left(80\pi^2 \mu_r^2 c_1\right)}{\lambda_0^2}, \tag{2.51}$$

$$c_1 = 1 - \frac{1}{n_1^2} + \frac{2}{5n_1^4}, \tag{2.52}$$

$$n_1 = \sqrt{\epsilon_r \mu_r}, \tag{2.53}$$

and where

$$P_{sw}^{hed} = \frac{\eta_0 k_0^2}{8} \frac{\epsilon_r \left(x_0^2 - 1\right)^{3/2}}{\epsilon_r(1 + x_1) + k_0 H \sqrt{x_0^2 - 1}\,(1 + \epsilon_r^2 x_1)}, \tag{2.54}$$

$$x_1 = \frac{x_0^2 - 1}{\epsilon_r - x_0^2}, \tag{2.55}$$

$$x_0 = 1 + \frac{-\epsilon_r^2 + \alpha_0\alpha_1 + \epsilon_r\sqrt{\epsilon_r^2 - 2\alpha_0\alpha_1 + \alpha_0^2}}{(\epsilon_r^2 - \alpha_1^2)}, \tag{2.56}$$

$$\alpha_0 = \sqrt{\epsilon_r - 1}\tan\left(k_0 H\sqrt{\epsilon_r - 1}\right), \tag{2.57}$$

$$\alpha_1 = -\left[\frac{\tan\left(k_0 H\sqrt{\epsilon_r - 1}\right) + \frac{k_0 H\sqrt{\epsilon_r - 1}}{\cos^2\left(k_0 H\sqrt{\epsilon_r - 1}\right)}}{\sqrt{\epsilon_r - 1}}\right]. \tag{2.58}$$

Following the same procedure as in [92], the cavity model also provides a method for calculated the input impedance of a microstrip patch antenna as

$$Z_{in} = \sum_{X=0}^{\infty}\sum_{Y=0}^{\infty} \frac{j\omega\alpha_{X,Y}}{\omega_{X,Y}^2 - (1 - j\delta_{eff}\omega^2)}, \tag{2.59}$$

where X and Y are the modes (dimensionless) excited in the cavity, $\omega_{X,Y}$ is the angular resonant frequency (rad/s) for each mode X and Y obtained from

$$\omega_{X,Y} = 2\pi f_{res}^{X,Y} = \frac{1}{n_{eff}}\sqrt{\left(\frac{X\pi}{L}\right)^2 + \left(\frac{Y\pi}{W}\right)^2}, \tag{2.60}$$

where n_{eff} is the effective electromagnetic refractive index equal to $\sqrt{\epsilon_r^{eff}\mu_r^{eff}}$ where ϵ_r^{eff} and μ_r^{eff} are the effective relative permittivity and permeability of the antenna substrate respectively; and $\alpha_{X,Y}$ (Np/m) is calculated as

$$\alpha_{X,Y} = \frac{H\delta_X\delta_Y}{LW\epsilon_0\epsilon_r}\cos^2\left(\frac{X\pi\acute{y}}{L}\right)\cos^2\left(\frac{Y\pi\acute{x}}{W}\right)\mathrm{sinc}^2\left(\frac{XY\pi\omega_p}{2L}\right), \tag{2.61}$$

where $\acute{y}$ (m) and $\acute{x}$ (m) are the coordinates of the driving point.

An interesting electrical property of graphene is that it can support surface plasmons at much lower frequencies than conventional metals, see Section 2.4. These are surface waves guided along the boundary of the graphene sheet and the surrounding material (i.e. free space if suspended) or between two substrates with permittivities $\epsilon_1{=}\epsilon_1^r\epsilon_0$ (F/m) and $\epsilon_2{=}\epsilon_2^r\epsilon_0$ (F/m), and permeabilities $\mu_1{=}\mu_1^r\mu_0$ (H/m) and $\mu_2{=}\mu_2^r\mu_0$ (H/m) for the top and bottom substrates respectively. These surface waves can propagate as transverse-electric (TE) or transverse-magnetic (TM). Their dispersion equations are [61]

$$Z^{TE}(k_p^{TE},\omega) = M_\mu^2 p_1 + p_2 + j\sigma_s\mu_2 = 0, \tag{2.62}$$

for the TE wave and

$$Z^{TM}(k_p^{TM},\omega) = N_\epsilon^2 p_1 + p_2 + \frac{\sigma_s p_1 p_2}{j\omega\epsilon_1} = 0, \tag{2.63}$$

for the TM wave, where $M_\mu^2{=}\mu_2/\mu_1$, $N_\epsilon^2{=}\epsilon_2/\epsilon_1$, $p_1{=}\sqrt{k_p^2-k_1^2}$, $p_2{=}\sqrt{k_p^2-k_2^2}$, k_1 and k_2 are the phase constants (rad/m) in substrates top and bottom respectively and k_p is the plasmon phase constant (rad/m). These two dispersion equations provide the conditions for the TE or TM waves to propagate along a graphene sheet placed between two substrates. Likewise, if $M{=}1$, $\mu_1^r{=}\mu_2^r{=}\mu^r$ and $\epsilon_1^r{=}\epsilon_2^r{=}\epsilon^r$ then the plasmon phase constants for the TE and TM can be obtained as [61]

$$k_p^{TE} = k\sqrt{\mu^r\epsilon_1^r - \left(\frac{(\epsilon_1^r-\epsilon_2^r)+\sigma_s^2\eta_0^2(\mu^r)^2}{2\sigma_s\eta_0}\right)^2}, \tag{2.64}$$

and

$$k_p^{TM} = k\sqrt{\mu^r\epsilon_1^r - \left(\frac{2\sigma_s\eta_0}{(\epsilon_1^r-\epsilon_2^r)+\sigma_s^2\eta_0^2(\mu^r)^2}\right)^2}. \tag{2.65}$$

The formulations provided in this section will be used in Chapter 3 to evaluate the use of graphene in microstrip patch antennas to provide antenna size reduction

by exciting plasmon waves and antenna reconfigurability by changing the surface impedance of graphene.

2.3 CARBON NANOTUBES

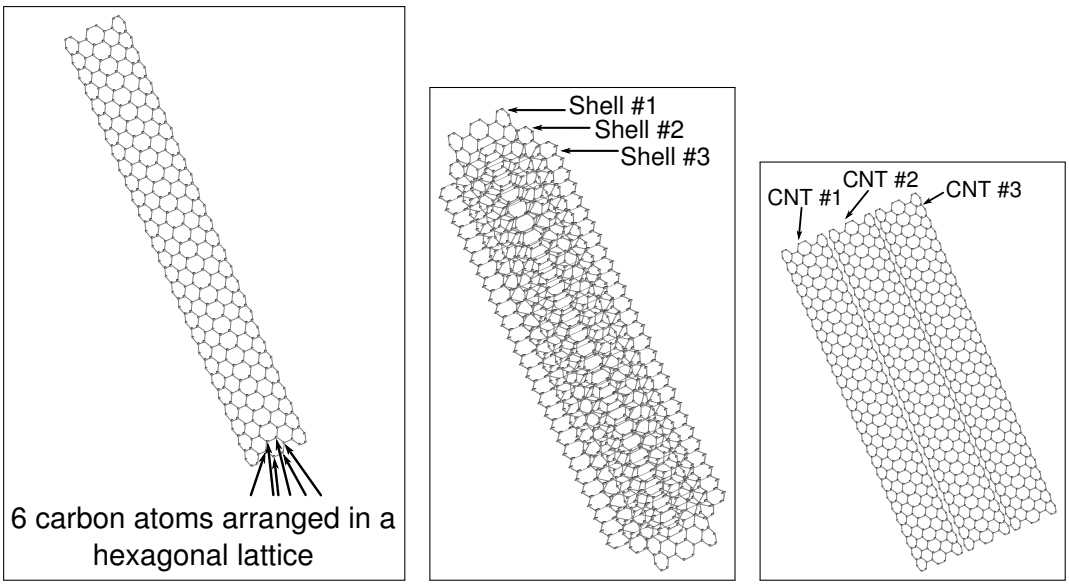

(a) **(b)** **(c)**

Figure 2.9: Graphical representation of different carbon nanotubes (CNTs) configurations (a) single-wall carbon nanotube (SWCNT), (b) multi-wall carbon nanotube (MWCNT) and (c) carbon nanotube bundle.

Carbon nanotubes (CNTs) are basically hollow tubes composed of carbon atoms forming a single-atom thick shell along an axis. Firstly synthesized by S. Ijima in 1991 [16], they are seen as "rolled up" graphene sheets, although they are grown from porous substrates where carbon atoms are deposited or injected via arc discharge, laser ablation and chemical vapour deposition (CVD), among others [93].

In general, their radii varies from 0.3 nm to several nanometres [94] and their length can be up to a few centimetres [95]. It is this aspect ratio that makes carbon nanotubes so interesting in nanotechnology (a quasi "one dimensional" material).

CNTs offer a very wide range of thermal, electrical and mechanical properties such as ballistic conduction of a few micrometers [96] and Young modulus of 1-1.3 TPa [97], [98]. Furthermore, CNTs can be synthesized into single-wall carbon nanotubes (SWCNTs) and multi-wall carbon nanotubes (MWCNTs), which basically consist of multiple concentric SWCNTs. MWCNTs can have radii from 1 nm to 50 nm. Additionally, SWCNTs and MWCNTs might be arranged into bundles of dozens or even hundreds of nanotubes.

2.3.1 ADMITTANCE OF CARBON NANOTUBES

Following a quantum-mechanical analysis of the effective permittivity of the carbon nanotube, the total axial admittance σ_{zz} (S) of a single-wall carbon nanotube is [99]

$$\sigma_{zz} = \tilde{\sigma}_{zz} + \Delta\sigma, \tag{2.66}$$

where $\tilde{\sigma}_{zz}$ is the admittance (S) evaluated following a semi-classical approximation of the motion of π-electrons under the effect of an electromagnetic field and $\Delta\sigma$ accounts for the interband contributions

$$\Delta\sigma = \frac{jq^2\,(\omega + jv)}{2\pi^2\hbar r_{SWCNT}} \sum_s \int_{1stBZ} \frac{1}{\mathcal{E}(p_z,s)} |\theta_{CV}(p_z,s)|^2 \frac{F[-\mathcal{E}(p_z,s)] - F[\mathcal{E}(p_z,s)]}{\hbar^2(\omega + jv)^2 - 4\mathcal{E}^2(p_z,s)} dp_z, \tag{2.67}$$

where $v{=}1/\tau$ is the relaxation frequency (Hz), r_{SWCNT} is the radius (m) of the SWCNT, $s{=}[1,2,3,...,m_r]$ is the counter for the chiral angle, m_r is an integer that sets the radius of the SWCNT, $1stBZ$ refers to the first Brillouin zone, $\mathcal{E}(p_z,s)$ is the electron dispersion relation (eV), $F(\pm\mathcal{E}(p_z,s))$ is the Fermi equilibrium distribution function (dimensionless), p_z is the z-projection of the electron's two-dimensional quasi-momentum $\mathbf{p}$ (Kgm/s) tangential to the SWCNT surface and $|\theta_{cv}|$ is the matrix element of the longitudinal velocity (m/s)

$$|\theta_{cv}| = \hbar^{-1}\left|\Im\left[\sqrt{H_{12}^{*}/H_{12}}\partial H_{12}/\partial p_z\right]\right|, \tag{2.68}$$

where H_{12} is the Hamiltonian matrix of electrons in a hexagonal lattice [100]

$$H_{12} = \begin{pmatrix} 0 & H_{12}(k_x, k_y) \\ H_{12}^{*}(k_x, k_y) & 0 \end{pmatrix} \tag{2.69}$$

with [101]

$$H_{12}(k_x, k_y) = -\gamma_1 e^{j\frac{b}{\hbar}p_x} - \gamma_2 e^{-j\frac{b}{\hbar}\left(\frac{1}{2}p_x - \frac{\sqrt{3}}{2}p_y\right)} - \gamma_3 e^{-j\frac{b}{\hbar}\left(\frac{1}{2}p_x + \sqrt{3}p_y\right)}, \tag{2.70}$$

where $\gamma_1 = \gamma_2 = \gamma_3 = \gamma$ are the overlap integrals (eV), $k_{x,y}$ are the x- and y-projections of the phase constant (rad/m) and $p_{x,y}$ are the x- and y-projections of the electron quasi-momentum $\mathbf{p}$ (Kgm/s).

In the microwave and infra-red frequencies, the $\tilde{\sigma}_{zz}$ contribution is dominant, and thus in this thesis, $\tilde{\sigma}_{zz}$ is the only admittance considered for carbon nanotubes. The general solution for the admittance of carbon nanotubes $\tilde{\sigma}_{zz}$ following the semi-classical approximation and assuming homogeneous distribution of the electromagnetic field (h=0) depends on the type of the SWCNT obtained. Depending on how the carbon nanotube is "rolled up" from an equivalent graphene sheet, the resulting nanotube presents different chiral angle which in turn defines its electrical behaviour [101]

$$\theta_{SWCNT} = \tan^{-1}\left(\frac{\sqrt{3}n_r}{2m_r + n_r}\right), \tag{2.71}$$

where m_r and n_r are the dual indices that represents multiple integers of the atomic distance between adjacent carbon atoms. Likewise, following the configuration of m_r and n_r the resulting radius of the SWCNT is obtained as [101]

$$r_{SWCNT} = \frac{\sqrt{3}}{2\pi}b\sqrt{m_r^2 + m_r n_r + n_r^2}, \tag{2.72}$$

where b=0.142 nm is the inter-atomic distance between carbon atoms in graphene. Depending on the chiral angle, the resulting CNTs can adopt different electronic behaviours [101]. A CNT is a zig-zag SWCNT when n_r=0 and for any value of m_r. On the other hand, a CNT is an armchair SWCNT when n_r=m_r and for any value fo m_r. Finally, a CNT is a chiral SWCNT when $0< n_r \neq m_r$.

Zig-zag SWCNTs are metallic if m_r is multiple of 3 but form a semiconductor otherwise. The full expression of $\tilde{\sigma}_{zz}$ for zig-zag SWCNTs is [101]

$$\tilde{\sigma}_{zz}^{zigzag} = -\frac{j2q^2}{\sqrt{3}\pi\hbar m_r b\,(\omega + jv)} \sum_{s=1}^{m_r} \int_{-2\pi\hbar/3b}^{2\pi\hbar/3b} \nu_z^2(p_z, s) \frac{\partial F}{\partial \mathcal{E}} dp_z, \tag{2.73}$$

where

$$\nu_z(p_z, s) = \frac{\partial \mathcal{E}(p_z, s)}{\partial p_z}, \tag{2.74}$$

$$\mathcal{E}(p_z, s) = \pm\gamma \sqrt{1 + 4\cos\left(\frac{3bp_z}{2\hbar}\right)\cos\left(\frac{\pi s}{m_r}\right) + 4\cos^2\left(\frac{\pi s}{m_r}\right)}, \tag{2.75}$$

$$F = \frac{1}{1 + e^{\frac{\mathcal{E}(p_z,s)}{k_B T}}}, \tag{2.76}$$

are the electron velocity (m/s), the electron dispersion (eV) in zig-zag SWCNTs and the Fermi equilibrium distribution function respectively. For small radius values $m_r \leq$60 and metallic zig-zag SWCNTs, equation (2.73) is reduced to [99]

$$\tilde{\sigma}_{zz}^{zigzag} \simeq j\frac{2\sqrt{3}q^2\gamma}{m_r\pi\hbar^2(\omega + jv)}, \tag{2.77}$$

Armchair SWCNTs are always metallic and the general expression for their admittance $\tilde{\sigma}_{zz}$ is [101]

$$\tilde{\sigma}_{zz}^{armchair} = -\frac{j2q^2}{3\pi\hbar m_r b\,(\omega + jv)} \sum_{s=1}^{m_r} \int_{-2\pi\hbar/3b}^{2\pi\hbar/3b} \nu_z^2(p_z, s) \frac{\partial F}{\partial \mathcal{E}} dp_z, \tag{2.78}$$

where now

$$\mathcal{E}(p_z, s) = \pm\gamma\sqrt{1 + 4\cos\left(\frac{\pi s}{m_r}\right)\cos\left(\frac{\sqrt{3}bp_z}{2\hbar}\right) + 4\cos^2\left(\frac{\sqrt{3}bp_z}{2\hbar}\right)}. \quad (2.79)$$

Note that the only difference between equation (2.73) and (2.78) is the $\sqrt{3} \Leftrightarrow 3$ change and different electron dispersion relation $\mathcal{E}(p_z, s)$. Again, for small radii m_r <50, equation (2.78) can be reduced to

$$\tilde{\sigma}_{zz}^{armchair} \simeq j\frac{2q^2\gamma}{m_r\pi\hbar^2(\omega + jv)}. \quad (2.80)$$

Finally, chiral SWCNTs can also be either metallic or a semiconductor if $2m_r + n_r$ is multiple of 3 or not, respectively. The approximate admittance $\tilde{\sigma}_{zz}$ for chiral SWCNTs is [99]

$$\tilde{\sigma}_{zz}^{chiral} \simeq j\frac{2\sqrt{3}q^2\gamma}{\pi\hbar^2\sqrt{m_r^2 + m_r n_r + n_r^2}(\omega + jv)}. \quad (2.81)$$

Note that equation (2.81) converts to equation (2.77) for n_r=0 and to equation (2.80) for m_r=n_r.

2.3.2 DIPOLE ANTENNAS FULLY MADE OF CARBON NANOTUBES

Carbon nanotubes can be implemented into dipole antennas, see Fig. 2.10, due to their cylindrical nature. In this section, the important parameters of the radiation efficiency and plasmon phase constant are presented for antenna dipoles made of SWCNTs, MWCNTs and bundles of SWCNTs and MWCNTs.

The radiation efficiency η_r (dB) of a carbon nanotube dipole can be calculated as [102]

$$\eta_r = 10\log\left(\frac{P_{rad}}{P_{rad} + P_{loss}}\right), \quad (2.82)$$

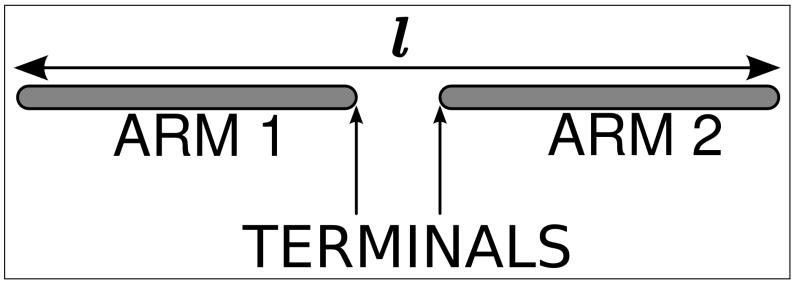

Figure 2.10: Graphical representation of a dipole antenna.

where P_{rad} (W) is the power radiated by the carbon nanotube dipole (SWCNT, MWCNT or SWCTN and MWCNT bundle dipole) and P_{loss} (W) is the power lost as heat in the carbon nanotube. The power radiated is calculated by integrating the radiation intensity over a sphere surrounding the carbon nanotube dipole

$$P_{rad} = \int_0^{2\pi} \int_0^{\pi} U \sin\theta d\theta d\phi, \tag{2.83}$$

where U=$W_{rad}r^2$ is the radiation intensity (W/sr) and W_{rad} is the radiation density (W/m^2) calculated as

$$W_{rad} = \left(\frac{k}{\gamma_p}\right)^2 \frac{(V_0/Z_c)^2 \eta}{8\pi^2 r^2} \left[\sin\theta \frac{\cos\left(\frac{kl}{2}\cos\theta\right) - \cos\left(\frac{\gamma_p l}{2}\right)}{1 - \left(\frac{k}{\gamma_p}\right)^2 \cos^2\theta}\right]^2, \tag{2.84}$$

where γ_p is the plasmon propagation constant and V_0 is the maximum voltage (V) in the antenna

$$V_0 = \frac{V_{terminals}}{2\cosh\left(\gamma_p \frac{l}{2}\right)}, \tag{2.85}$$

where l=$2v_p/f_{res}$ is the length (m) of the dipole (assumed to be a $\lambda/2$ dipole) and Z_c is the characteristic impedance (Ω) of the transmission line and the antenna made of carbon nanotube. The resulting radiation density from a dipole made of carbon nanotubes is different to the well known radiation density from a common metallic material (i.e. copper) as it accounts for the plasmon effect (k/γ_p)

produced in the carbon nanotubes, see Section 2.4. The plasmon propagation constant is obtained from

$$\gamma_p = \alpha + jk_p = \sqrt{(R_{CNT} + j\omega L_T)(j\omega C_T)}, \tag{2.86}$$

where α is the attenuation constant (Np/m), R_{CNT} (Ω/m) is the resistance per unit length in carbon nanotubes, L_T (H/m) and C_T (F/m) are the total inductance and capacitance per unit length present in carbon nanotubes and ω is the angular frequency (rad/s). The plasmon phase constant k_p can be calculated alternatively as

$$k_p = \frac{2\pi f_{res}}{v_p}. \tag{2.87}$$

The velocity of propagation v_p (m/s) is calculated as

$$v_p = \frac{1}{\sqrt{L_T C_T}}. \tag{2.88}$$

The total inductance is the series addition L_T=L_K+L_m of the kinetic inductance L_K (H/m) and the magnetic inductance L_m (H/m). The magnetic inductance can be calculated as [103]

$$L_m = \frac{\mu_0 \epsilon_0}{C_{es}}, \tag{2.89}$$

where C_{es} is the electrostatic capacitance (F/m) between the carbon nanotube and the ground plane which is calculated from [102]

$$C_{es} = \frac{\pi \epsilon_r \epsilon_0}{\log\left(\frac{sep}{dia}\right)}, \tag{2.90}$$

where ϵ_r is the relative permittivity of the surrounding material, *sep* is the separation (m) between the two carbon nanotubes forming the transmission line and the dipole and dia=$2r_{SWCNT}$ is the diameter (m) of the carbon nanotubes (assumed here to be SWCNT). On the other hand, the total capacitance is the

parallel addition C_T=1/((1/C_Q)+(1/C_{es})) of the quantum capacitance C_Q (F/m) and the electrostatic capacitance C_{es} (F/m).

Going back to equation (2.84), the characteristic impedance of the transmission line and the dipole made of carbon nanotubes is

$$Z_c = \sqrt{\frac{R_{CNT} + j\omega L_T}{j\omega C_T}}. \tag{2.91}$$

Finally, the power lost as heat in the antenna P_{loss} is calculated from the voltage $V_{terminal}$ (V) and current $I_{terminal}$ (A) at the terminals of the dipole as

$$P_{loss} = \frac{1}{2}\Re(V_{terminal} I_{terminal}*), \tag{2.92}$$

where

$$I_{terminal} = \frac{V_0}{Z_C} \sinh\left(\gamma_p \frac{l}{2}\right). \tag{2.93}$$

The equations presented above apply for the SWCNT, MWCNT, SWCNT bundle and MWCNT bundle dipole antennas. However, for each case, the calculation of R_{CNT}, L_K and C_Q must be adapted to the different CNT cases. For the case of SWCNT dipole antennas, the resistance per unit length is calculated from [104] as

$$R_{CNT} = \Re\left(\frac{1}{2\pi r_{SWCNT}\sigma_{SWCNT}}\right). \tag{2.94}$$

where σ_{SWCNT} is the admittance (S) of the SWCNT obtained from equations (2.73), (2.78) and (2.81). The kinetic inductance is extracted from [104] as

$$L_K = \frac{\Im(\frac{1}{2\pi r_{SWCNT}\sigma_{SWCNT}})}{\omega}, \tag{2.95}$$

and the quantum capacitance is calculated as [102]

$$C_Q = \frac{2q^2}{2\pi\hbar v_f^c}, \tag{2.96}$$

where v_f^c is the Fermi velocity (m/s) in carbon nanotubes calculated as

$$v_f^c = \frac{3\gamma b}{2\hbar}. \tag{2.97}$$

For the multi-wall carbon nanotube dipole antennas formed by N_s number of shells, the values of R_{CNT}, L_K and C_Q must account for the effect of having multiple concentric shells (n_s=2,3,4,...,N_s). Following [103], [105], the value of R_{CNT} is calculated as

$$R_{CNT} = \left[\sum_{i=1}^{ss} \frac{2m_i}{\Re(2\pi i \sigma_{SWCNT}(i))} \right], \tag{2.98}$$

where i is the radius (m) of the n_s shell, ss=r_{inner}+δN_s (m) is the total radius of the MWCNT, r_{inner} is the radius (m) of the inner most shell, δ=0.34×10^{-9} (m) is the inter-shell distance, m_i is the number of channels of a shell of radius i and $\sigma_{SWCNT}(i)$ is the admittance of the shell (SWCNT) with radius i. The number of channels per shell of radius i is calculated as

$$m_i = \begin{cases} 2/3 & i < 3\text{nm} \\ K_1 i + K_2 & i > 3\text{nm} \end{cases} \tag{2.99}$$

where K_1=122×10^{-6} m^{-1} and K_2=0.425. The value L_K is calculated similarly as R_{CNT}

$$L_K = \left[\sum_{i=1}^{s} \frac{2m_i}{\Im(2\pi i \sigma_{SWCNT}(i)/\omega)} \right]. \tag{2.100}$$

Finally, the value of C_Q is obtained from

$$C_Q = \Lambda N + \Xi r_{inner} + \Upsilon, \tag{2.101}$$

where Λ=2.56×10^{-11} (F/m), Ξ=7.525×10^{-2} (F/m^2) and Υ=9.887×10^{-11} (F/m).

Similar to the MWCNT case, grouping a number N_b of SWCNT and MWCNT to form dipole antennas also affects the resulting per unit lengths of the resistance,

kinetic inductance and quantum capacitance as the resulting bundle can be considered as mmultiple SWCNT and MWCNT in parallel. In order to consider this effect, in the bundle cases, the R_{CNT}, L_K and C_Q is calculated following the equations (2.94), (2.95) and (2.96) for the SWCNT bundle case and equations (2.98), (2.100) and (2.101) for the MWCNT bundle case. The only difference is that the resulting values of R_{CNT} and L_K are now divided by the number of tubes in the bundle N_b (R_{CNT}/N_b and L_K/N_b) and the resulting C_Q is now multiplied by N_b ($C_Q N_b$) to account for the aggregation effect [106], [107].

The formulations provided in this sections will be used in Chapter 3 to evaluate dipole antennas made entirely of carbon nanotubes in order to achieve antenna size reduction from plasmon frequencies.

2.4 PLASMONS

A Plasmon is a quantization of a collective oscillation of charges within a medium due to a perturbation in a plasma equilibrium [86]. An exciting property of CNTs and graphene is that plasmon resonant frequencies are observed at much lower frequencies than in conventional metals. This means that a signal propagating along CNTs and graphene has a much shorter wavelength than in a conventional medium, e.g. free space. As a result, antennas made of CNTs and graphene can resonate at considerably smaller dimensions for the same frequencies as larger antennas made from conventional materials would do. In CNTs and graphene, the plasmon wavelengths can be up to several tens of times shorter than in free space.

2.5 METAMATERIALS

Metamaterials (MTM) are artificial materials made of the repetition of smaller elements that present unusual electromagnetic properties not found in nature [30],

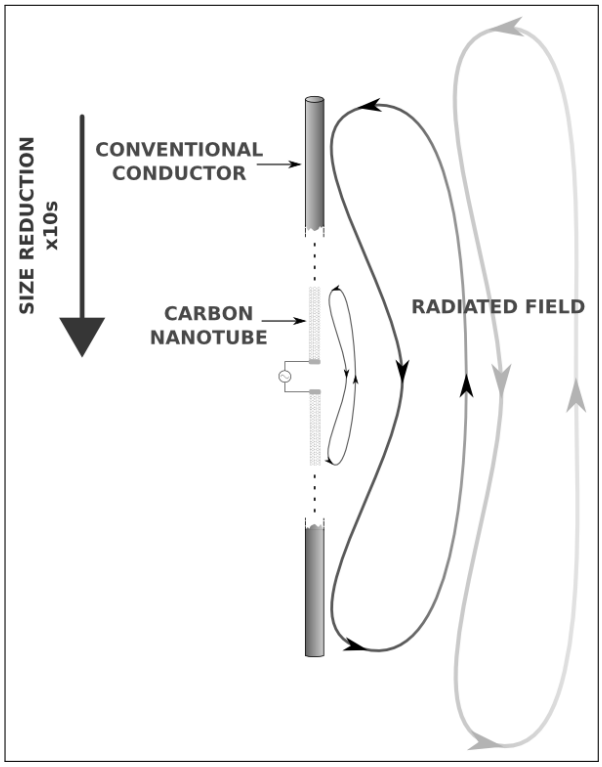

Figure 2.11: Graphical representation of size reduction in carbon nanotubes dipoles due to plasmon resonances.

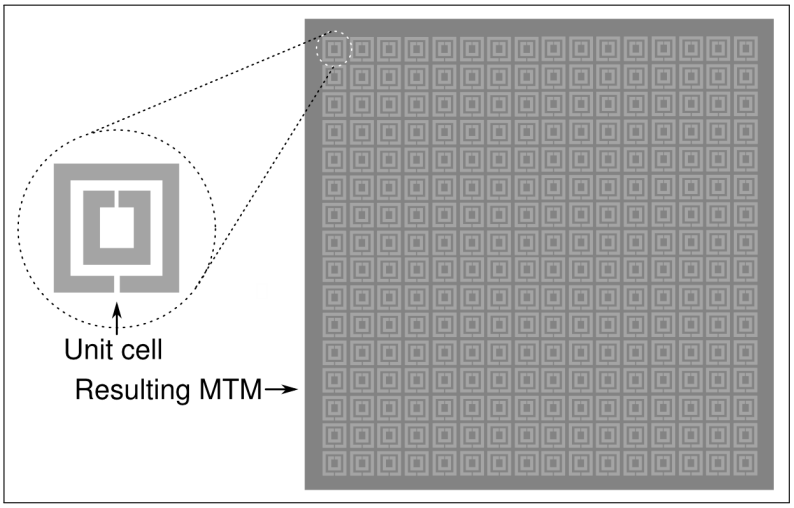

Figure 2.12: Graphical representation of a metamaterial and the unit cell that forms it.

see Fig. 2.12. Among their most interesting properties, MTMs can be synthesised to be frequency selective surfaces that filter signals with specific frequencies or present zero reflection phase such as the electromagnetic band gap (EBG), the reactive impedance surface (RIS) and the artificial magnetic conductors (AMC) [108]. Furthermore, MTMs can also be materials with negative permittivities or permeabilities, or both simultaneously [19], [29].

Taking advantage of the negative permittivity and/or permeability found in metamaterials, transmission lines made by these materials provide different refractive index $n_R=\sqrt{\epsilon_r \mu_r}$ at different frequencies. For instance, electromagnetic waves propagating in a pure imaginary refractive index experience phase velocities moving in an opposite direction to the the wave velocity, or group velocity [30]. When this phenomenon occurs, the resulting electromagnetic waves are said to be propagating in a left-handed transmission line (LH TL). Because it is not possible to obtain pure LH TLs, due to parasitic capacitances and inductances, real metamaterial transmission lines are composite right/left-handed transmission lines (CRLH TL) where at some frequencies the transmission line acts as a right-handed transmission line (RH TL), or as a classical transmission line, while at other frequencies acts as a pure LH TL.

2.5.1 COMPOSITE RIGHT/LEFT-HAND TRANSMISSION LINE BASED ANTENNAS

CRLH TL can be applied to the antenna field to produce antennas that have right-hand, left-hand and zeroth order resonances. Interestingly, zeroth order resonances are independent of the antenna size. This means a zeroth order resonant antenna of any dimension could resonate at any desired frequency. However, increasing the size of the antenna will increase the antenna gain, bandwidth, etc; as seen in section 2.1.3. The CRLH TL based antenna can be modelled using a unit cell equivalence formed by a resistance R (Ω) and a conductance G (S) representing the losses in the antenna, a right-hand inductance

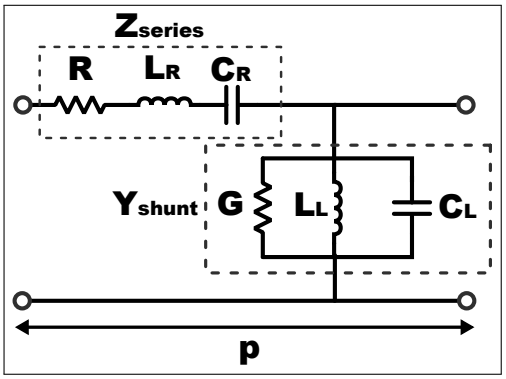

Figure 2.13: Circuit model of a CRLH TL unit cell.

L_R (L), a right-handed capacitance C_R (F), a left-handed inductance L_L (L) and a left-handed capacitance C_L (F) as shown in Fig. 2.13 [30].

Additionally, the same unit cell can also be modelled as a series impedance Z_{series} (Ω) and a shunt conductance Y_{shunt} (S)

$$Z_{series} = R + j\left(\omega L_R - \frac{1}{\omega C_L}\right), \tag{2.102}$$

$$Y_{shunt} = G + j\left(\omega C_R - \frac{1}{\omega L_L}\right). \tag{2.103}$$

Consequently, the dispersion relation $\beta(\omega)$ (rad/m) of a CRLH TL antenna can be extracted by applying the periodic boundary conditions (PBCs) related to the Bloch-Floquet theorem as [30]

$$\beta(\omega) = \frac{1}{p}\cos^{-1}\left(1 - \frac{1}{2}\left(Z_{series}Y_{shunt}\right)\right) = \frac{1}{p}\cos^{-1}\left(1 - \frac{1}{2}\left(\frac{\omega_L^2}{\omega^2} + \frac{\omega^2}{\omega_R^2} - \frac{\omega_L^2}{\omega_{se}^2} - \frac{\omega_L^2}{\omega_{sh}^2}\right)\right), \tag{2.104}$$

where p is the length of the unit cell (m) and

$$\omega_L = \frac{1}{\sqrt{C_L L_L}}, \tag{2.105}$$

$$\omega_R = \frac{1}{\sqrt{C_R L_R}}, \tag{2.106}$$

$$\omega_{se} = \frac{1}{\sqrt{C_L L_R}}, \tag{2.107}$$

$$\omega_{sh} = \frac{1}{\sqrt{C_R L_L}}, \tag{2.108}$$

are the resonances due to the right-handed ω_R (rad/s), the left-handed ω_L (rad/s), the series ω_{se} (rad/s) and the shunt ω_{sh} (rad/s) contributions respectively. From the dispersion relation of the CRLH TL antenna in equation (2.104), an open- or short-ended resonator based on the CRLH TL presents resonances whenever the following condition is satisfied [109]

$$\beta_{n_m}(\omega) = \frac{n_m \pi}{l} = \frac{n_m \pi}{Np} \qquad \text{for } n_m = 0, \pm 1, \pm 2, ..., (N\text{-}1); \tag{2.109}$$

where n_m is the resonant mode, l is the total length of the CRLH TL structure (m) and N is the number of cascade unit cells. Therefore, the higher the number of unit cells placed in cascade the higher the number of negative and positive resonances.

Zeroth order resonant antennas are evaluated in more detail in Chapter 6 where the two proposed antenna designs are based on this type of metamaterial-based antenna.

2.6 CONCLUSIONS

In this chapter, the basic theory on antennas and the materials implemented in this thesis have been presented. The definition of antennas and their main parameters have been introduced and explained. Likewise, the electrical properties of graphene, carbon nanotubes and metamaterials have been provided in detail. Finally, the formulations that allow to analyse microstrip patch antennas entirely made of graphene, dipole antennas entirely made of carbon nanotubes and metamaterial based antennas have also been described. Specifically, the formulations provided for the graphene and carbon nanotube antennas used to analyse the antenna efficiencies, size reduction and reconfigurability in the next chapter.

Chapter 3

PERFORMANCE EVALUATION OF ANTENNAS ENTIRELY MADE OF CARBON NANOTUBES AND GRAPHENE

This chapter studies whether antennas entirely made of carbon nanotubes or graphene can provide advantageous features such as antenna size reduction and reconfigurability at microwave and millimetre wave frequencies. This is carried out, at three resonant frequencies 2.45 GHz, 60 GHZ and 110 GHz, by analysing dipole antennas entirely made of single-wall carbon nanotubes (SWCNTs), multi-wall carbon nanotubes (MWCNTs) and groups of SWCNTs and MWCNTs, called bundles, with different nanotube radii, number of shells and number of tubes. Likewise, microstrip patch antennas entirely made of graphene are also simulated at the same resonant frequencies but for different surface impedances of graphene.

3.1 INTRODUCTION

Carbon nanotubes and graphene might accommodate plasmon waves at much lower frequencies that conventional metals [110]. Additionally, graphene posses the ability to dynamically change its surface impedance by changing the charge carrier density via chemical doping or DC voltage bias. Plasmon waves propagating in carbon nanotubes and graphene are slower waves compared to waves propagating in free space. Consequently, these plasmon wavelengths are considerably smaller than in free space. This is particularly interesting for antennas because antennas operating at plasmon frequencies could have considerably smaller sizes than conventional antennas made with other materials, and consequently, could substantially save space in future wireless and mobile devices. In addition, the variable surface impedance of graphene, specially the imaginary part, might provide reconfigurability in antennas. Reconfigurable antennas can perform the same operation as multiple antennas designed for different applications but occupying much less space, and thus, also could reduce the antenna footprint in future devices. Some research on the performance of antennas entirely made of carbon nanotubes and graphene have been realised in [32], [102]–[105], [111]–[122] for microwave, millimetre wave, terahertz (THz), infra-red and optical frequencies. The aim of this chapter is to provide a conclusive analysis of the performance, trade-offs and achievable reconfigurability of antennas entirely made of carbon nanotubes and graphene at specifically microwave and millimetre wave frequencies. This chapter intends to serve as a stepping stone for the following chapters of this thesis.

The key concepts discussed in this chapter can be summarized as follows:

- Determine whether antennas entirely made of carbon nanotubes can provide considerable size reduction with reasonable radiation efficiency for microwave and millimetre wave applications.

- Determine whether antennas entirely made of graphene can provide recon-

figurability and size reduction with reasonable radiation efficiency for microwave and millimetre wave applications.

The chapter is structured as follows, section 3.2 will study antennas entirely made of different configurations of carbon nanotubes, while section 3.3 will deal with antennas entirely made of graphene for different charge carrier densities. Finally, section 3.4 will finish the chapter with some key conclusions.

3.2 DIPOLE ANTENNAS ENTIRELY MADE OF CARBON NANOTUBES

In this section, a summary of the main conclusions obtained from simulated carbon nanotubes as dipole antennas is provided. For the detailed analysis of carbon nanotubes as dipole antennas, see Apendix 3.2. In Appendix 3.2 the performance of dipole antennas made of SWCNT, MWCNT and bundles is simulated following an equivalent transmission line approximation where the special condition of the admittance of carbon nanotubes is taken into account [102]. Special interest is paid to the radiation efficiency and size reduction trade-offs.

From the evaluation in Appendix 3.2, it is concluded that SWCNT dipoles are not acceptable for antenna applications at the frequencies of interest due to their extremely low antenna efficiencies. The reason is, although carbon nanotubes have considerably lower resistance per unit lengths R_{CNT} than for other nanotube materials with same dimensions (i.e. copper), the resistance per unit length found in SWCNT is still excessively high for antenna applications.

In the case of MWCNTs dipoles, it might be considered for antenna applications where some size reduction is desired at the expense of low efficiency. For example, for a large number of shells and at f_{res}=60 GHz and f_{res}=110 GHz, the radiation efficiencies converge to reasonable values but they are still below the target value of $\eta_r \geq$-10 dB.

In the case of CNT bundles, it is shown that even with a large number of SWCNTs in a bundle, the resulting radiation efficiency is still far below the target value of $\eta_r \geq$-10 dB. Consequently, there is not a single case where SWCNTs could potentially be used for antenna applications at the frequencies of interest. In contrast, for the MWCNT bundle case, radiation efficiencies of around -10 dB can be achieved with as little as two tubes of MWCNTs with 151 shells at 60 GHz and 110 GHz, or with fifty tubes of MWCNTs with 151 shells at 2.45 GHz. As a result, it is possible to find an optimum value of N_b for MWCNTs that might satisfy the minimum radiation efficiency of some commercial applications. However, by improving the radiation efficiency, the ratio between k_p and k is drastically reduced and little to no size reduction is obtained when acceptable values of radiation efficiency are achieved. This is an important drawback because one of the main reasons for using carbon nanotubes antennas is the ability to enable significant reduction of the antenna size. Consequently, even in the cases where MWCNTs bundles could be used, it might still not justify the lower antenna performance compared to antennas made of other metallic materials (i.e. copper).

Finally, dipoles made of carbon nanotubes present a very high input impedance (on the order of kΩ) which makes them impossible to match to conventional source impedances of 50 Ω and 75 Ω. Consequently, it is unlikely for them to be of any use at microwave and millimetre wave bands as long as the standard internal impedances of radio-frequency sources are set to 50 Ω or 75 Ω.

3.3 MICROSTRIP PATCH ANTENNAS ENTIRELY MADE OF GRAPHENE

In this section, the performance of microstrip patch antennas made of a single layer of graphene is evaluated by following the cavity model [92], where the special condition of the surface impedance of graphene is taken into consideration. In here, the interest is on the radiation efficiency and frequency reconfigurability

trade-off. First, the initial considerations and set up are defined in subsection 3.3.1. Later, the simulated results are discussed in subsection 3.3.2.

3.3.1 EVALUATED ANTENNAS

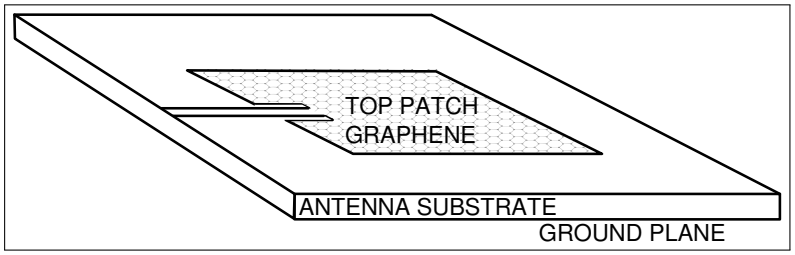

Figure 3.1: Graphical representation of a microstrip patch antenna where the top patch is entirely made of graphene.

Due to the planar nature of graphene, microstrip patch antennas entirely made of graphene are studied here at f_{res}=2.45 GHz, f_{res}=60 GHz and f_{res}=110 GHz, see Fig. 3.1. The antennas are evaluated by calculating their radiation efficiency as well as the achievable frequency reconfigurability.

The radiation efficiency η_r (dB) is calculated following the cavity model in [92] as, see equation (2.36) in Chapter 2 for a detailed explanation,

$$\eta_r = 10 \log \left(\frac{1}{\delta_{eff} Q_r} \right), \tag{3.1}$$

where Q_r (dimensionless) accounts for radiation losses and δ_{eff} (dimensionless) includes all the losses in the microstrip antenna. To evaluate the frequency reconfigurability, the reflection coefficient $S11$ (dB) is calculated for different surface impedances of graphene. In order to do so, the graphene microstrip patch antenna input impedance is matched to a 50 Ω source for a specific value of the surface impedance of graphene. Then, the surface impedance of graphene is changed by adjusting the charge carrier density n. The cavity model also provides a method for calculating the input impedance z_{in} (Ω of a microstrip patch antenna as

$$Z_{in} = \sum_{X=0}^{\infty}\sum_{Y=0}^{\infty} \frac{j\omega\alpha_{XY}}{\omega_{XY}^2 - (1 - j\delta_{eff}\omega^2)}, \tag{3.2}$$

It is expected to have small input impedances due to the relatively large surface impedances of graphene. Consequently, a $\lambda/4$ transmission line section (transformer) with a characteristic impedance $Z_0 \approx 23$ (Ω) is placed between the driving point and the source. The resulting input impedance seen from the source is then

$$Z_{in}^{\lambda/4} = \frac{Z_0^2}{Z_{in}}, \tag{3.3}$$

Finally, the $S11$ is extracted as

$$S11 = \left| 10 \log \left(\frac{Z_{in}^{\lambda/4} - Z_0}{Z_{in}^{\lambda/4} + Z_0} \right) \right|. \tag{3.4}$$

The plasmon phase constants for the TE and TM can be obtained as [61], see equations (2.64) and (2.65) in Chapter 2 for a detailed explanation,

$$k_p^{TE} = k\sqrt{1 - \left(\frac{(1 - \epsilon_2^r) + \sigma_{graphene}^2 \eta_0^2}{2\sigma_s \eta_0} \right)^2}, \tag{3.5}$$

and

$$k_p^{TM} = k\sqrt{1 - \left(\frac{2\sigma_s \eta_0}{(1 - \epsilon_2^r) + \sigma_{graphene}^2 \eta_0^2} \right)^2}, \tag{3.6}$$

However, it is important to highlight that the TE and TM surface plasmon waves must fulfil the condition of their dispersion wave equations [61], see equations (2.62) and (2.63) in Chapter 2 for a detailed explanation,

$$Z^{TE}(k_p^{TE}, \omega) = M_\mu^2 p_1 + p_2 + j\sigma_s \mu_2 = 0, \tag{3.7}$$

for the TE wave and

$$Z^{TM}(k_p^{TM}, \omega) = N_\epsilon^2 p_1 + p_2 + \frac{\sigma_s p_1 p_2}{j\omega\epsilon_1} = 0, \tag{3.8}$$

in order to propagate on the graphene layer in the boundary between the antenna substrate and free space.

3.3.2 RESULTS

In here, the radiation efficiency η_r and the tunable resonant frequency ($S11$ variations) are simulated for different charge carrier densities n for three different frequencies f_{res}=2.45 GHz, f_{res}=60 GHz and f_{res}=110 GHz. The voltage applied to the driving point is V_0=1 V. The coordinates of the driving point are $\acute{y}$=0 m and $\acute{x}$=W/2 m. In here, only the trans-magnetic mode TM_{10} is considered (the antenna resonance is proportional to the length L of the antenna), so P=1 and Q=0. The antenna substrate is Polystyrene (PS) with ϵ_r=3.1 and tanδ=0.0002 [123], with a substrate height H=0.02c/f_{res} m in order to satisfy the limits of application of the cavity model. The values of Zs for the microstrip antenna are set by the surface conductance of graphene in equation (2.25) of chapter 2, as Zs=σ_{AC}^{-1}. As for carbon nanotube antennas, an acceptable radiation efficiency for commercial applications would be $\eta_r \geq$-10 dB.

Fig. 3.2 represents the variation of the resulting radiation efficiency and reflection coefficient by changing the charge carrier density for a microstrip patch antenna made of graphene at 2.45 GHz. The obtained radiation efficiency is close to, but still lower than, the minimum value for the frequency of interest. Furthermore, the achieved variations in the resonant frequency are negligible. On the other hand, the graphene antenna does provide a method for dynamically tuning the antenna to the source (dynamic antenna matching) by changing the values of n. This also affects the operational bandwidth (BW), and hence, it is theoretically possible to select any value of BW by selecting a proper value of n. However, due to the low radiation efficiency and the negligible changes in the resonant frequencies, this solution is only suitable for applications where variable antenna matching and bandwidth is desired at the expense of low radiation efficiency. For f_{res}=60 GHz, see Fig. 3.3, very similar results are obtained. The

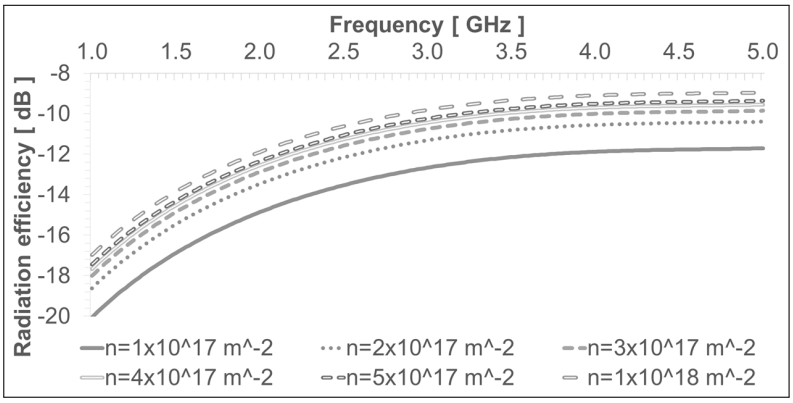

(a)

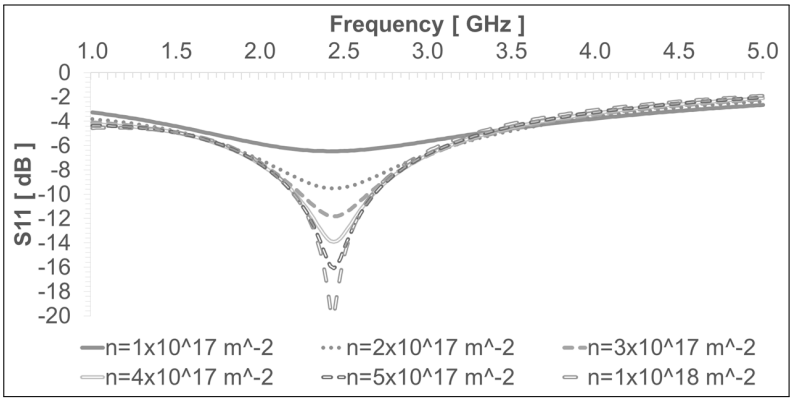

(b)

Figure 3.2: Microstrip patch antenna made of graphene for 2.45 GHz applications, (a) Radiation efficiency and (b) tunable reflection coefficient for different charge carrier densities n (m^{-2}).

radiation efficiencies are still below the minimum value for virtually no changes in the resonant frequencies.

In Fig. 3.4, the results obtained for the reflection coefficient $S11$ show that, although not substantial, some changes in the resonant frequencies are possible by changing the values of n. However, the radiation efficiencies are still below the minimum value of acceptable radiation efficiency ($\eta_r \geq$-10 dB). As a result, graphene could potentially be used for applications at 110 GHz where small changes in the resonant frequency, antenna matching and bandwidth is required (e.g. for wearable antennas) but at the expenses of low antenna efficiencies.

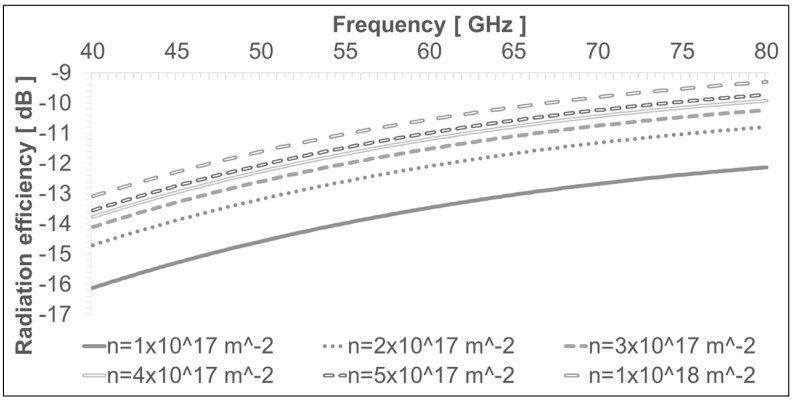

(a)

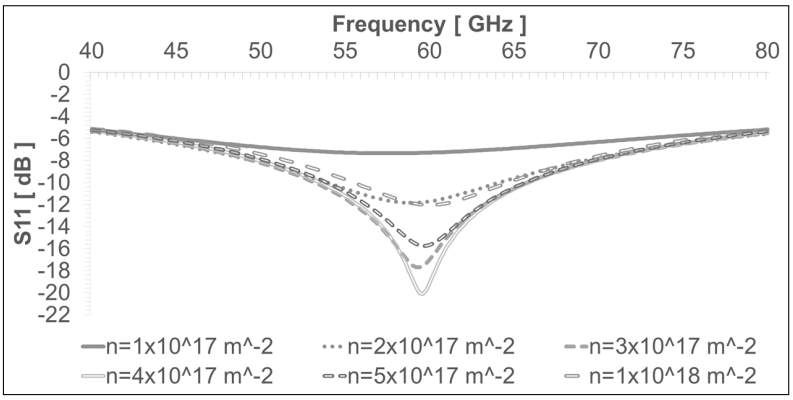

(b)

Figure 3.3: Microstrip patch antenna made of graphene for 60 GHz applications, (a) Radiation efficiency and (b) tunable reflection coefficient for different charge carrier densities n (m^{-2}).

Finally, Fig. 3.5 shows the results of the dispersion equations for the trans-electric (TE) and trans-magnetic (TM) guided waves propagating along the Polystyrene/graphene/free space boundary, as well as their plasmon phase constant values (k_p^{TE} and k_p^{TM}) normalized to the free space phase constant k. Note that the values shown in Fig. 3.5 are either 0 or 1. These values indicate whether the conditions Z^{TE} and Z^{TM} in equations (3.7) and (3.8) are satisfied (0) or not satisfied (1). As observed, a TE guided wave cannot propagate because the result is not zero, see equation (3.7), while a TM guided wave may or may not be excited and propagate as its result is zero, see (2.63). In case a TM guided wave

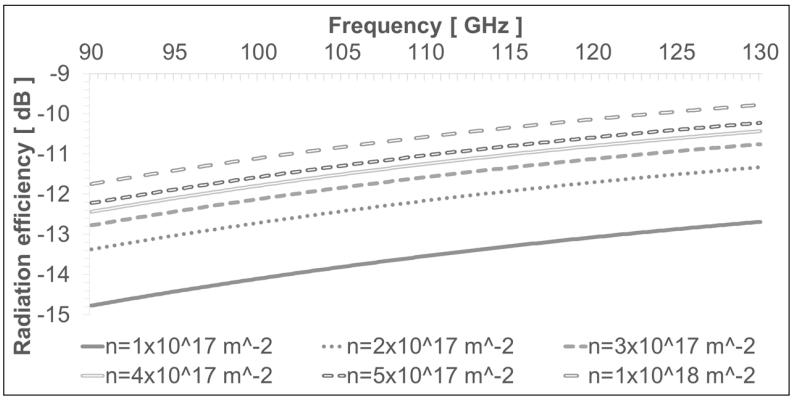

(a)

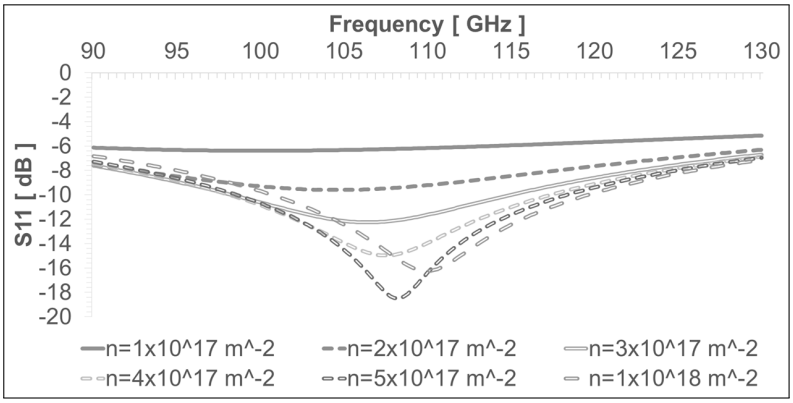

(b)

Figure 3.4: Microstrip patch antenna made of graphene for 110 GHz applications, (a) Radiation efficiency and (b) tunable reflection coefficient for different charge carrier densities n (m^{-2}).

becomes excited and is able to propagate in graphene, the k_p^{TM}/k ratio is near one, meaning that the resulting wave has a wavelength close to the wavelength of the same wave propagating in free space. Therefore, for the frequencies of interest, no TE or TM surface plasmon waves can be excited and hence no size reduction can be achieved.

This does not mean that graphene cannot be used in conventional antenna applications at these frequencies. It means that the graphene plasmons are not excited and hence cannot be used for substantial size reduction at these frequencies as in carbon nanotubes. The reason is found in the admittance of

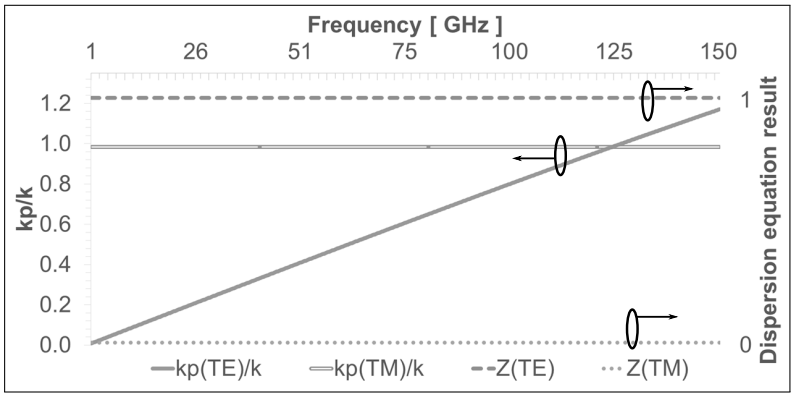

Figure 3.5: Ratio between surface plasmon phase constant and free space constant for the TE and TM guided waves (solid lines), and dispersion equation results for the TE and TM guided waves (dashed lines), for a charge carrier density of n=5$\times 10^{17}$ m^{-2}.

graphene at these frequencies. In order to excite a TE surface plasmon wave, the susceptance of graphene should be positive. This condition only occurs when the interband contributions are dominant (in the THz and infra-red regime). On the other hand, in order to have a TM surface plasmon wave with $k_p^{TM}/k \gg 1$, the susceptance of graphene must be negative, a condition which is satisfied at the frequencies of interest here, but at the same time, the graphene sheet must be placed between two substrates with extremely high relative permittivities ϵ_1^r and ϵ_2^r (whose ratio is in the order of hundreds). However, this can also be achieved by traditional means in antennas made of other metallic materials as the excited waves that contribute to the radiation are strongly confined in high permittivity substrates, and hence, graphene is not required.

3.4 CONCLUSIONS

This chapter has studied the suitability of antennas entirely made of carbon nanotubes and graphene for size reduction and/or reconfigurability at 2.45 GHz, 60 GHz and 110 GHz. It is concluded that:

- Dipole antennas entirely made of either single SWCNTs or MWCNTs could potentially provide a substantial size reduction but are not efficient at all. Conversely, dipole antennas made of SWCNT and MWCNT bundles could provide reasonable radiation efficiencies but at the expense of achieving little to no size reduction versus conventional metal antennas.

- Microstrip antennas entirely made of graphene are close to the desired minimum radiation efficiency of $\eta_r \geq$-10 dB but provide little frequency reconfigurability and no size reduction.

Although the admittance of carbon nanotubes cannot be tuned, carbon nanotubes might still be implemented in nano-communications at THz and infra-red frequencies, due to their great size reduction ability provided by the plasmon phenomenon, if large source impedances and characteristic impedances become the standard. However, for microwave and millimetre wave, the high input impedance of carbon nanotubes dipoles might present an unbridgeable challenge. On the other hand, antennas entirely made of graphene present more conventional input impedances. In addition, graphene can be an interesting solution for THz and infra-red frequencies due to the ability to present surface plasmons that can be tuned by changing the charge carrier densities. However, the variable surface conductance of graphene could still be used in the microwave regime. This is because at such frequencies, the surface conductance of graphene does change considerably. In such case and in order to obtain reasonable radiation efficiencies, graphene antennas cannot be made entirely of graphene but in combination with other metallic materials (i.e. copper) so that the ohmic losses are substantially reduced while still providing a high degree of reconfigurability. For this reason, chapters 4 to 6 propose hybrid metal-graphene reconfigurable antennas. Specifically, in Chapter 4, a hybrid antenna made of copper and graphene is proposed and evaluated as a frequency reconfigurable antenna for WIFI and LTE applications.

Chapter 4

HYBRID METAL-GRAPHENE FREQUENCY RECONFIGURABLE ANTENNAS

This chapter studies, analyses and discusses the performance, limitations and trade-offs of implementing graphene in planar frequency reconfigurable antennas for wireless and mobile applications. This is carried out by proposing and simulating two antenna designs where graphene is introduced to provide frequency reconfigurability to cover some WIFI and LTE bands. It examines the two proposed antennas as well as the field-effect structure where the variable surface impedance of graphene is achieved. Additionally, the results are compared to other state-of-the-art frequency reconfigurable antennas that implement other switching technologies.

4.1 INTRODUCTION

Frequency reconfigurable antennas are now used for multiple applications in the microwave [124]–[140], millimetre wave [141]–[146], theraherz (THz) [147], [148], infrared [149], [150], and even in the optical domain [151]–[156]. Although frequency reconfigurability is not a new concept, it is only recently that it has been extensively implemented in telecommunications. Frequency reconfigurable antennas are particularly important in wireless and mobile devices due to the strong space constraints in these devices. A single frequency reconfigurable antenna can provide operation at multiple bands where usually multiple individual antennas would be needed, and hence, save space. Commonly, frequency reconfigurable antennas are achieved by integrating micro electromehanical systems (MEMS), nano electromehanical systems (NEMS), field-effect transistors (FET), p-type insulator n-type (PIN) diodes, varactors or tunable materials. In [131], a frequency reconfigurable antenna is achieved by manually placing and removing two copper tapes on the longitudinal radiating edges which increases or reduces the electrical size of the antenna. In a similar fashion, graphene is implemented here in two novel designs as a tunable material to achieve frequency reconfigurability by also changing the electrical size of the antenna.

Graphene frequency reconfigurable antennas are being mostly studied for infrared and THz frequencies as it can significantly reduce size and provide high antenna reconfigurability at such frequencies [121], [157]–[165]. As large area samples of graphene (in the order of several centimetres) grown by chemical vapour deposition (CVD) have been successfully synthesised [52], it is viable to realize devices for microwave applications made of graphene. However, antennas fully made of graphene are expected to have low antenna efficiencies with very little reconfigurability at microwave frequencies [121], [157]. For this reason, the antenna designs proposed here are hybrid metal-graphene frequency reconfigurable antennas where the impact of the high ohmic losses of graphene is reduced while providing substantial antenna reconfigurability. In [166], the

concept and analysis of hybrid metal-graphene antennas was introduced for THz frequencies. In [167], a hybrid graphene-metal for millimetre wave applications has been investigated and in [168], [169] graphene has been implemented as a radio frequency (RF) switch in frequency reconfigurable antennas in the microwave. In contrast, this chapter carries out a feasibility study of using graphene as a tunable material for hybrid metal-graphene antennas in the microwave regime.

Additionally, a single layer of graphene only absorbs 2.7% of visible light, making graphene an interesting material for transparent antennas in the microwave regime. Transparent antennas can be integrated in places where traditional non-transparent conductive materials (i.e. copper or aluminium) cannot be used such as car and building windows, solar panels (particularly useful in satellites), electronic displays, product labels and light panels. Traditionally, transparency in antennas is achieved by implementing thin-film transparent conductors, meshed conductors or a hybrid combination of both [170]–[180]. Graphene has already been implemented in transparent antennas for microwave applications as a multilayer structure or as a part of a hybrid transparent conductive film to improve the mechanical and electrical properties of the transparent antenna [181], [182]. However, frequency reconfigurable transparent antennas still rely on traditional switching technologies (i.e. MEMS, PIN diodes, varactors, FET switches and tunable materials) that might present little or no transparency. Thus, graphene is proposed here as a solution for enabling frequency reconfigurability in transparent antennas for microwave applications without compromising their transparency.

The novel contributions presented in this chapter can be summarized as follows:

- Analyse and simulate two possible hybrid metal-graphene reconfigurable antenna designs to cover WIFI (2.4 GHz, 3.6 GHz and 5 GHz) and LTE (1.8 GHz , 2.1 GHz , 2.6 GHz and 3.6 GHz) frequency bands.

- Present the advantages and disadvantages of using graphene in reconfigurable antennas at microwave frequencies as well as system limitations such

as the selection of suitable dielectric-semiconductor layers for the DC voltage bias and the power consumption.

The chapter is structured as follows, section 4.2 will define the system limitations and trade-offs of using graphene in the two proposed antenna designs, then, section 4.3 will describe the proposed antenna designs and the scenario set up. Afterwards, the simulation results will be presented and discussed in section 4.4. Finally, section 4.5 will finish the chapter with key conclusions.

4.2 SYSTEM LIMITATIONS

In this section, three critical issues are discussed related to the implementation of graphene, and the field-effect structure, in antennas for frequency reconfigurability. In subsection 4.2.1, there is a discussion of the trade-offs between suspending graphene on air or laying it on a dielectric/substrate, see Fig. 4.1, and in case of depositing graphene on a substrate, to select a suitable dielectric/substrate material that could provide the best performance. Afterwards, a brief analysis of the effect of adding the heavily doped semiconductor to the antenna structure is found in subsection 4.2.2. Finally, the instantaneous power consumption expression, when a graphene sheet is switched between large or small surface impedances, is derived in subsection 4.2.3. These points are important for supporting later the selection of the parameters in section 4.3 as well as the power consumed by the proposed antennas in section 4.4.

4.2.1 SUSPEND GRAPHENE IN AIR OR LAY IT ON A SUBSTRATE?

Traditionally, suspending graphene in air provides better performance than over substrates [78]. However, large electric fields and narrow distances d between the gate semiconductor and graphene sheet, see Fig. 4.1, are needed to induce high

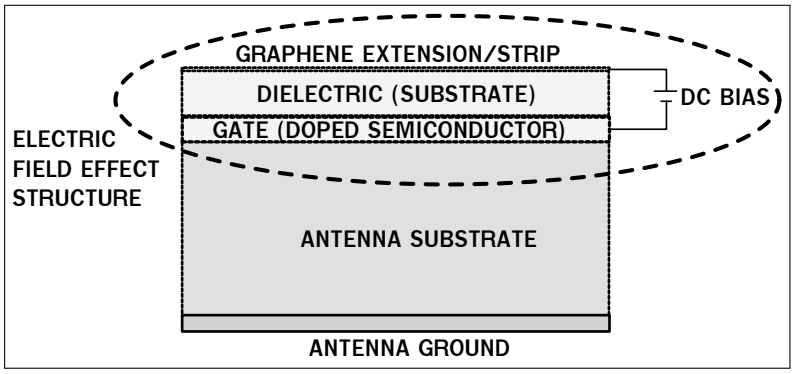

Figure 4.1: Example of an electric field effect structure added to a patch antenna.

carrier density n values with reasonably low voltages V_b values. This might not be possible to achieve for suspended graphene without compromising its structural integrity [56], [78]. Consequently, only graphene laid on a substrate acting as a dielectric (Fig. 4.1) is considered from now on.

Recently, mobilities similar to suspended graphene have been obtained for graphene on hexagonal Boron Nitride (hBN) [81] [83] [75]. This is an excellent substrate for graphene because it is flat, possesses a similar crystal structure to graphite (reduced lattice mismatch) and provides large optical phonon energies and band gap [183]. Additionally, CVD grown graphene has also been successfully transferred to hBN substrates providing qualities close to exfoliated graphene [76]. However, at the time of writing, this has been only achieved for very small areas of graphene. However, in this chapter, it is assumed that a large area of graphene sheet could be deposited onto hBN substrates following, for instance, the dry method described in [76] in the near future.

4.2.2 DOPED SEMICONDUCTOR EFFECT

Heavily doped semiconductors can potentially provide reasonably good values of conductivity, specially in the microwave regime. From the general Drude's formula of conductivity, the conductivity of a doped semiconductor σ_{DS} (S/m) is

$$\sigma_{DS} = n_{DS} q \mu_{DS}, \tag{4.1}$$

where q is the electron charge (C), n_{DS} (m^{-3}) and μ_{DS} (m^{-2}/Vs) are the free carrier density and mobility of the doped semiconductor respectively. Therefore, by substantially raising the free carrier density n_{DS} (assuming the electron mobility μ_{DS} is kept the same) the conductivity of the doped semiconductor is also highly increased. To compensate this effect, a low carrier mobility μ_{DS} should be selected. As shown later in this chapter in Table 4.2, the number of free carrier densities needed in graphene are n_{ON}=5·10^{17} m^{-2} for the ON state and n_{OFF}=6·10^{14} m^{-2} for the OFF state. Consequently, The required free carrier density n_{DS} in the doped semiconductor can be obtained as

$$n_{DS} \geq \frac{(n_{ON} - n_{OFF})}{t_{DS}}, \tag{4.2}$$

where t_{DS} (m) is the thickness of the doped semiconductor layer. Note that, to reach this relation, the length l_{DS} (m) and the width w_{DS} (m) of both, the graphene layer and the doped semiconductor, are assumed to be the same. From equations (4.1) and (4.2), the total resistance of the doped semiconductor R_{DS} can be calculated as

$$R_{DS} \leq (\sigma_{DC})^{-1} \frac{l}{w t_{DS}} = \frac{l}{(n_{ON} - n_{OFF})\, w_{DS} q \mu_{DS}}. \tag{4.3}$$

For the size of the graphene sheets considered in this chapter, see Tables 4.3 and 4.4, and to obtain resistances R_{DS} on the order of kΩ or larger, the required electron mobility should be μ_{DS} ≤0.02 m^{-2}/Vs. Heavily doped silicon carbride (SiC) [184] or hydrogenated amorphous silicon (a-Si:H) [185] can meet these requirements and be used as the heavily doped semiconductors in Fig. 4.1 without a noticable impact on the antenna performance. Alternatively, the graphene layer could be self-biased. In [186], the authors produced a field-effect structure composed by two doped graphene monolayers at THz frequencies.

There, the authors applied one or two DC voltage bias to control independently the conductivity of each of the doped graphene layers. Applying a similar procedure here but at microwave frequencies would allow one to substitute the heavily doped semicondcutor in Fig. 4.1 for another doped graphene layer with low quality (low electron mobility) and hence reduce undesired effects on the antenna performance.

4.2.3 DC INSTANTANEOUS POWER IN BIASED GRAPHENE

Finally, another important system limitation is set by the power consumed. In the field effect configuration, Fig. 4.1, the graphene sheet and the heavily doped semiconductor might be modelled as a parallel plate capacitor. Although the DC power consumption in capacitors is negligible due to electrical isolation, there is still movement of induced charges between the plates every time the DC bias voltage V_b is changed. This movement of charges creates a temporary current and therefore power is dissipated in any resistance present in the circuit as ohmic losses. In a Resistor-Capacitor (RC) circuit, the time needed for the capacitor to achieve the final carrier density n is proportional to the time constant $\tau_{RC} = RC$ (s) [187]. In the particular case considered here, τ_{RC} must be set as low as possible so it is suitable for WIFI and LTE applications. The capacitance C (F) created between the graphene sheet and the doped semiconductor is defined in equation (4.4) [187]

$$C = \frac{\epsilon_r^d \epsilon_o A}{d}, \tag{4.4}$$

where ϵ_r^d is the relative permittivity of the dielectric, ϵ_o is the permittivity of vacuum (F/m), A is the area of the graphene sheet and the doped semiconductor ($l \times w$, assumed to be the same) (m^2), and d the separation distance between the graphene and the semiconductor (m). Hence, the resulting capacitance C is

dictated, in one hand, by the parameters ϵ_r^d and d in equation (2.27) (see equation (2.27) in Chapter 2 for more details) as low V_b values are desired, and on the other hand, by the dimensions of the graphene sheets used.

$$n = \frac{\epsilon_o \epsilon_r^d V_b}{dq}, \tag{4.5}$$

The value of the resistor R (Ω) is extracted from the required τ_{RC} and C values. The dynamic power $p(t)$ (W) consumed by the circuit depends on the transitional current and voltage on the resistor R - $i_R(t)$ and $v_R(t)$ - as equation (4.6) shows

$$p(t) = v_R(t) i_R(t) = \frac{V_b^2}{R} e^{\frac{-2t}{\tau_{RC}}}. \tag{4.6}$$

Hence, combining the relation of $\tau_{RC} = RC$ with equations (4.5),(4.4),(4.6) the peak power is defined as (4.7)

$$P_{peak} = p(0) = \frac{n^2 q^2 dA}{\epsilon_o \epsilon_r^d \tau_{RC}}. \tag{4.7}$$

This is the maximum power that the circuit might consume at the instant of changing the value of V_b. As observed in Fig. 4.2a, a fast switching time causes a large current in the system and more power is consumed during a short amount of time. In contrast, a longer waiting time reduces the maximum power consumed during the charging-discharging time. The value at P_{peak} can be further decreased by reducing the thickness d of the dielectric, see Fig. 4.2b, using a larger ϵ_r^d, see Fig. 4.2c, or having smaller area of graphene sheets, see Fig. 4.2d. This would additionally reduce the required V_b. However, these parameters are not easily modified as d depends on current technology constraints, ϵ_r^d on the properties of the target dielectric substrate and A on the target application.

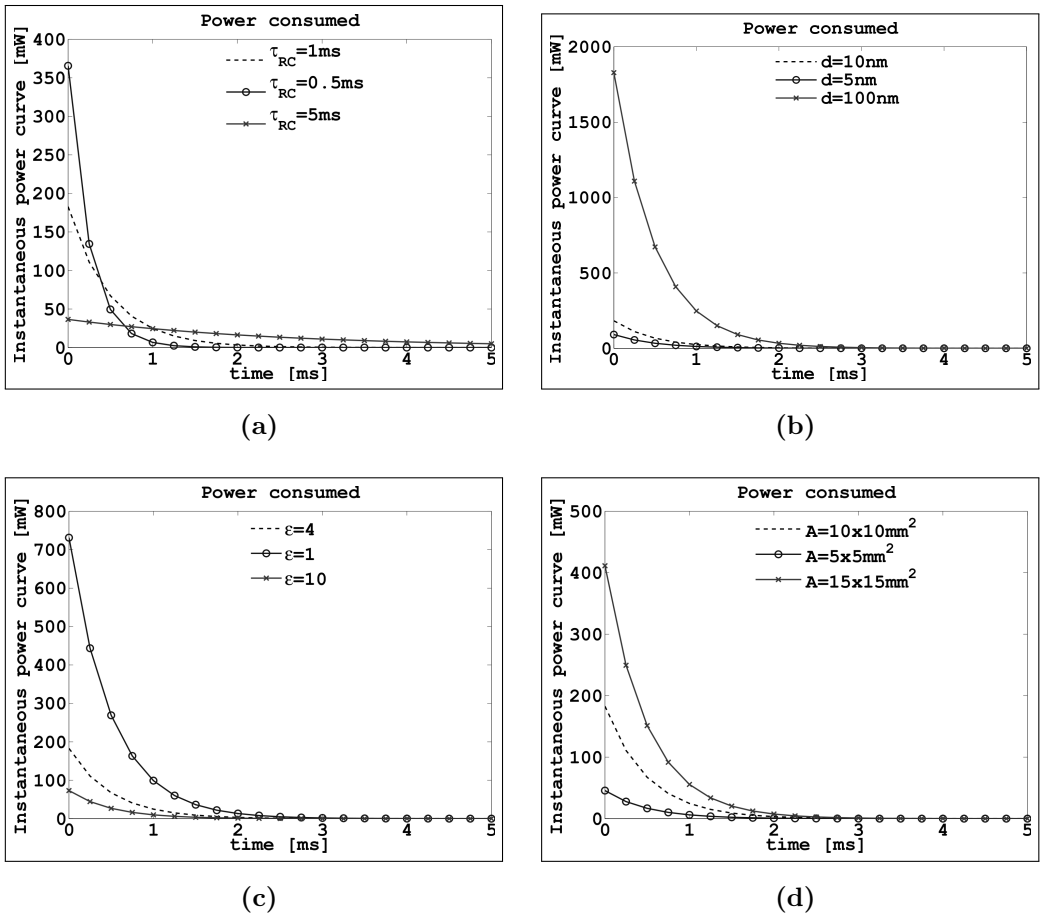

Figure 4.2: Time representation of consumed instantaneous power in the resistor following equation (4.6). Common values are τ=1 ms, d=10 nm, ϵ_r^d=4 and A=100 mm^2. A charging cycle for different settings of a) time constants, b) dielectric thickness, c) dielectric relative permittivity and d) graphene sheet areas.

4.3 PROPOSED ANTENNA DESIGNS

Following the cavity model, the resonant frequency for a rectangular patch antenna is given by (4.8) [34], see equation (2.60) for more details,

$$f_{res}^{X,Y} = \frac{c}{2\pi n_{eff}} \sqrt{\left(\frac{X\pi}{L_{main}}\right)^2 + \left(\frac{Y\pi}{W}\right)^2}, \tag{4.8}$$

where c is the speed of light (m/s), n_{eff} is the effective electromagnetic refractive index; X and Y are a multiple of the half-period of the time-varying

electromagnetic field propagating along each dimension of the structure; L_{main} (m) and W (m) are the physical dimensions of the antenna. Therefore, modifying any of the dimensions of the antenna at a particular time (L_{main} and W) causes a switch of the operational frequency for that particular mode (X and Y). A solution to dynamically affect the length and/or width of the antenna is to stop or allow current to propagate to certain parts of the structure or to divert it to cause it to travel longer distances. This is done by adding graphene sheets to the structure which allow or impede current to flow when these are activated or deactivated, hence changing the behaviour of the antenna.

In order to demonstrate the use of graphene in frequency reconfigurable antennas, two main designs are studied:

- A rectangular microstrip antenna with extensions made of graphene added at the edges, Fig. 4.3.
- A rectangular microstrip antenna with inserted strips made of graphene, Fig. 4.4.

The first design (Fig. 4.3) aims to increase or decrease the physical length of the structure in the ON or OFF state respectively, while the second one (Fig. 4.4) diverts the current propagating along the antenna so the effective length is larger or shorter than the physical length in the OFF or ON state respectively. The DC voltage bias (V_b) could be applied directly through the feeding port if a common value of V_b is desired for all the graphene extensions/strips so that it activates and deactivates them all at the same time. That would save the necessity of adding a DC bias circuit. However, inserting a gap between the main patch and the extensions/strips provides a solution to avoid a common DC bias voltage throughout the antenna and allows individual control to activate and deactivate single extensions/strips. Consequently, different DC voltage bias (i.e. Vb_1 and Vb_2) should be applied through individual DC vias lines to each of the required graphene sheets. Figs. 4.3 and Fig. 4.5 include an example of how the

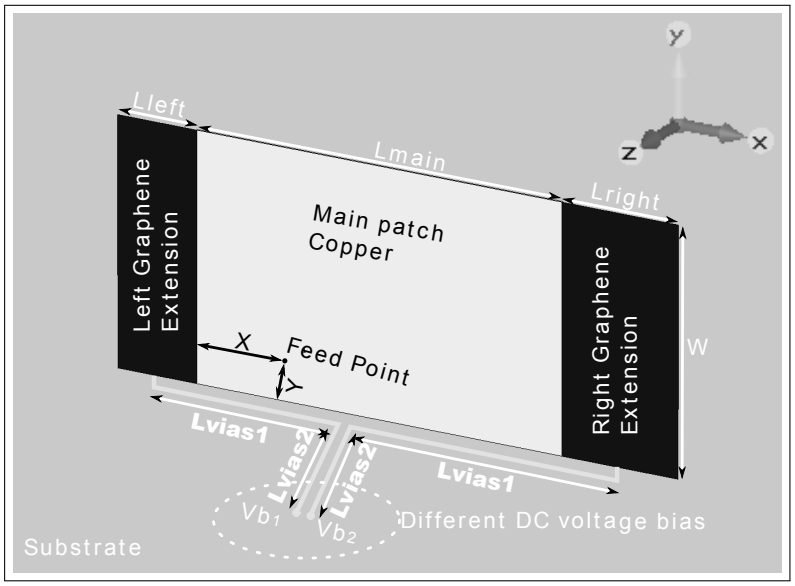

Figure 4.3: Graphical representation of the frequency reconfigurable antenna for WIFI applications.

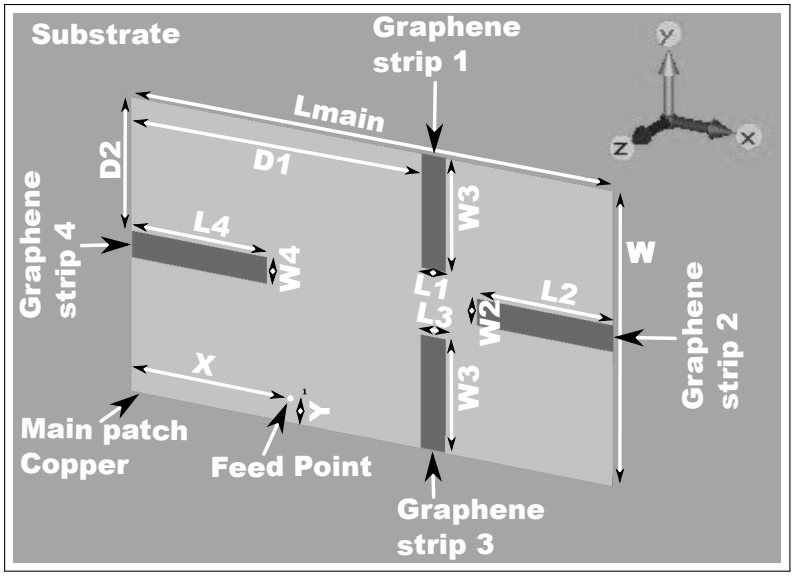

Figure 4.4: Graphical representation of the frequency reconfigurable antenna for LTE applications.

DC vias lines could be implemented. Note that for the field-effect structure in Fig. 4.5, and consequently neither the DC vias in Fig. 4.3, is not included in the simulations due to its extremely small thickness (in the nanometre scale).

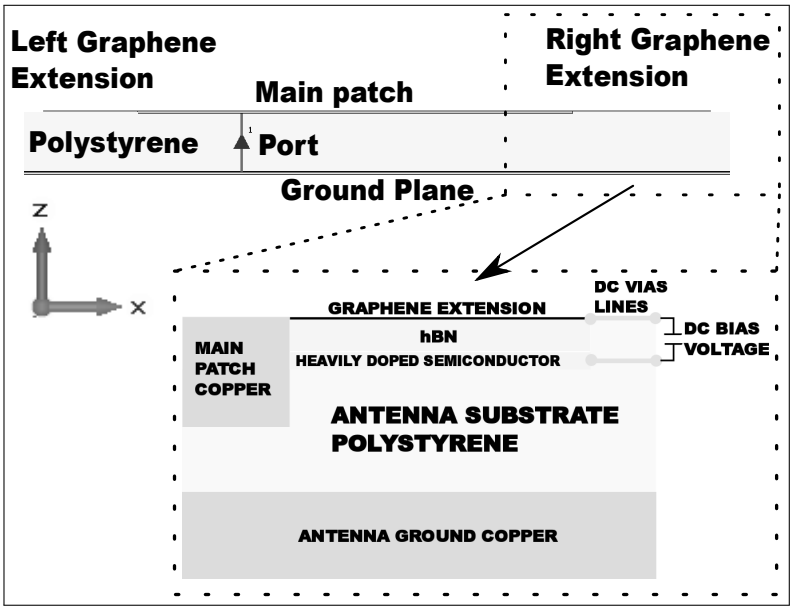

Figure 4.5: Graphical representation of zoomed view of the tuning structure for WIFI design (x-z plane) in Fig. 4.3.

The values of Zs_{ON}, Zs_{OFF} and the general set up values for the simulations are defined next.

4.3.1 ELECTRIC FIELD EFFECT CONFIGURATION

For the values shown in Table 4.1, it is firstly assumed that the time between switching from one operating frequency to another does not have to be fast (on the order of 1 millisecond). This is within a reasonable assumption considering handover interruption times in LTE-advanced (60 ms) [188]. The switching time is defined as the time needed for the voltage between the graphene sheet and the semiconductor to rise from 50% of the final value to the 90% [46]. Secondly, the thickness d of the dielectric can be reduced up to a few nanometres which is technologically available nowadays [189]. Finally, the ϵ_r^d for hBN is obtained from [189].

Table 4.1: Selected general parameters

τ_{RC} [ms]	1
Switching time [ms]	1.6
d [nm]	10
ϵ_r^d for hBN	4

4.3.2 SIMULATED Zs_{ON} AND Zs_{OFF} VALUES

In order to obtain practical values of the ON and OFF state surface impedances Zs_{ON} and Zs_{OFF}, realistic values of τ_S, τ_L and $\tilde{n}$ are needed. Additionally, a high OFF/ON ratio (Zs_{OFF}/Zs_{ON}) is also desired. The values of surface impedance for the ON and OFF states, Zs_{ON} and Zs_{OFF} respectively, in Table 4.2 are obtained from equation (4.9), which is a slightly modified version of equation (2.25) in Chapter 2 which includes the relaxation time effect in equation (2.28) in also Chapter 2,

$$Zs \approx \frac{j\pi\hbar^2(2\pi f(\tau_L\tau_S) - j(\tau_L + \tau_S))}{q^2(\tau_L\tau_S)[\mu_c + 2k_BT\ln(e^{-\frac{\mu_c}{k_BT}} + 1)]}, \tag{4.9}$$

where τ_L accounts for all the long range scattering effects and can be calculated as [18], [22], [65]

$$\tau_L = \frac{\mu_L m^*}{q} \simeq \frac{\mu_L\hbar\sqrt{n\pi}}{qv_f^g}, \tag{4.10}$$

where μ_L is the electron mobility (m^2/Vs) and m^* is the carrier mass (Kg) in graphene. The value of τ_S is calculated as in equation (4.11) by just considering the LA phonon contribution, considered in this chapter to be the dominant scattering mechanism at room temperature [62], [88], [89],

$$\tau_S = \frac{\mu_p\hbar\sqrt{n\pi}}{qv_f^g} = \frac{4\hbar^2\rho_m v_{ph}^2 v_f^g}{\sqrt{n\pi}D^2k_BT}, \tag{4.11}$$

where D is the deformation potential (eV), $\rho_m = 7.6 \times 10^{-7}$ is the two dimensional mass density of graphene (Kg/m^2) and $v_{ph} = 2.1 \times 10^4$ is the sound

velocity of LA phonons in graphene (m/s). The precise deformation potential D value is still discussed, but some experimental values have been obtained in the literature and D ∼18 eV seems to be a common and accepted value for graphene over a substrate [62]. However, it might theoretically have a large range of possible values between 4 eV and 30 eV as found in graphite and carbon nanotube materials [190]. The value of μ_c is directly obtained by substituting equation (4.12), see equation (2.26) in Chapter 2 for more details, into equation (4.5)

$$\mu_c \simeq \hbar v_f^g \sqrt{n\pi}. \tag{4.12}$$

The Zs_{ON} value is found by increasing the charge carrier density n until saturation is reached as LA phonon scattering becomes dominant and at the same time the voltage V_b is not too high (22.7 V). On the other hand, the value for Zs_{OFF} is obtained by setting the minimum achievable chemical potential equal to the energy of the electron-hole puddles ($\mu_{c,min} = \varepsilon_{puddle}$) in equation (4.13), see equation (2.35) in Chapter 2 for more details,

$$\varepsilon_{puddle} = \mu_{c,min} = \hbar v_f^g \sqrt{\pi \tilde{n}}. \tag{4.13}$$

The carrier inhomogeneity density $\tilde{n}$=6×10^{14} m^{-2} is obtained from [76]. The value of μ_L is also extracted from reference [76]. V_b values are calculated using equation (4.5) by considering selected values of ϵ_r^d and d in Table 4.1, and n values in Table 4.2. Although the resulting V_b values might be too large for implementation in low voltage devices, e.g. mobile phones, the values can be reduced in the future by using thinner dielectrics with higher relative permittivity once the technology is available. For the OFF state, the resulting V_b values are near 0 V due to having very low inhomogeneity density $\tilde{n}$.

Finally, for all the scenarios evaluated in Section 4.4 the antenna substrate selected is Polystyrene (PS) with ϵ_r=2.4 and tanδ=0.0002 [123]. The antenna substrate thickness (H) is set to 2.1 mm as the space available in mobile devices

Table 4.2: Selected surface impedance Zs values

Set	1		2		3	
State	ON	OFF	ON	OFF	ON	OFF
n [m^{-2}]	$5{\cdot}10^{17}$	$6{\cdot}10^{14}$	$5{\cdot}10^{17}$	$6{\cdot}10^{14}$	$5{\cdot}10^{17}$	$6{\cdot}10^{14}$
V_b [V]	22.72	$\sim$0	22.72	$\sim$0	22.72	$\sim$0
μ_L [m^2/Vs]	2.7		2.7		2.7	
D [eV]	4		18		18	
T [K]	295		295		4.2	
Zs_{ON} [$\Omega/\square$]	6+j0.3	2580+j6	34+j0.3	2580+j6	5+j0.1	3840+j9

is very limited. In the next section, the proposed antenna designs are simulated and analysed.

4.3.3 IMPEDANCE UNCERTAINTY ANALYSIS

As seen in equation (4.9), the surface impedance Z_s of graphene depends on various factors such as the DC voltage bias V_b, the electron mobility μ_L, the operational temperature T and the deformation potential D. The effect of reducing the operational temperature and deformation potential on the surface impedance of graphene has already been calculated in Table 4.2 and their impact on the antenna efficiency is shown later in section 4.4. In this section, an impedance uncertainty analysis is carried out to show how small changes in the ideal DC voltage bias and the expected electron mobility might affect the final surface impedance of graphene. To do so, the variation in the surface impedance of graphene is calculated via partial derivatives of the surface impedance over the variation in the values of V_b and μ_L.

The resulting surface impedances of graphene for the ON and OFF states can be calculated as

$$\hat{Z}s_{ON} = Zs_{ON} + \Delta Zs_{ON}\Big|_{\Delta V_{ON}} + \Delta Zs_{ON}\Big|_{\Delta \mu_L}, \tag{4.14}$$

$$\hat{Z}s_{OFF} = Zs_{OFF} + \Delta Zs_{OFF}\Big|_{\Delta V_{OFF}} + \Delta Zs_{OFF}\Big|_{\Delta \mu_L}, \tag{4.15}$$

where Zs_{ON} and Zs_{OFF} are the expected values from Set 2 in Table 4.2 and

$$\Delta Zs_{ON}\Big|_{\Delta V_{ON}} = \frac{\partial Zs_{ON}}{\partial \hat{V}_{ON}} \hat{V}_{ON}, \tag{4.16}$$

$$\Delta Zs_{OFF}\Big|_{\Delta V_{OFF}} = \frac{\partial Zs_{OFF}}{\partial \hat{V}_{OFF}} \hat{V}_{OFF}, \tag{4.17}$$

$$\Delta Zs_{OFF}\Big|_{\Delta \mu_L} = \frac{\partial Zs_{ON}}{\partial \hat{\mu}_L} \hat{\mu}_L, \tag{4.18}$$

are the partial derivatives of Zs_{ON} and Zs_{OFF} over the actual DC voltage bias applied for the ON and OFF state, $\hat{V}_{ON}$ and $\hat{V}_{OFF}$, and the actual electron mobility of the graphene sample $\hat{\mu}_L$.

The actual values of the applied DC voltage bias, $\hat{V}_{ON}$ and $\hat{V}_{OFF}$, depend on the power supply accuracy. The values of $\hat{V}_{ON}$ and $\hat{V}_{OFF}$ evaluated here a found as

$$\hat{V}_{ON,OFF} = V_b^{ON,OFF} + (V_b^{ON,OFF}) * 0.05\% + 10mV, \tag{4.19}$$

where the accuracy values, 0.05% and 10 mV, have been obtained from the datasheet of the power supply model E3634A 200W Power Supply [191]. Therefore, the actual DC voltage bias for the ON and OFF state are set between the theoretical values of V_b found in Set 2 of Table 4.2 and the values $\hat{V}_{ON,OFF}$ obtained in equation (4.19) when V_b is also from Set 2 in Table 4.2. On the other hand, the values of the electron mobility in the graphene samples are expected to be between 2.7 and 4.5 m^2/Vs [76].

The resulting surface impedances of graphene for the ON and OFF states are $\hat{Z}s_{ON}$=30+j0.2 $\Omega/\square$ and Zs_{OFF}=974+j2.8 $\Omega/\square$, respectively. As observed, the

value for the ON state does not change considerably due to that the change in the DC voltage bias for the ON state is negligible and that increasing the electron mobility decreases the surface impedance, which is desired for the ON state. However, the surface impedance for the OFF state does change drastically due to the DC voltage bias for the OFF state is a very small value and the power supply accuracy rises the final V_b value. In addition, increasing the electron mobility, again, decreases the surface impedance, which for the OFF state is not desired. In any case, the change in the surface impedance of graphene between the ON and OFF state is still relatively large and hence still valid for the desired operation. Later in section 4.4 the impact of these new surface impedance values on the antenna performance is shown.

4.4 RESULTS

The results here are obtained from the transient solver (time domain solver) in the CST Microwave Studio 2015. The graphene sheets have been defined as solid sheets with thickness equal to zero and simulated as ohmic sheet surface impedances. The excitation is a discrete port with 50 Ω port impedance. The efficiencies calculated from CST follow equation (4.20);

$$\eta_t = \left(\frac{P_{rad}}{P_{sim}}\right) \times 100 \tag{4.20}$$

where η_t is the total antenna efficiency (%), P_{rad} is the power being radiated by the antenna (W) and P_{sim}=0.5 W is the power generated by the excitation signal.

4.4.1 WIFI SCENARIO

The following scenario evaluates the first design to cover three bands in WIFI (2.4 GHz, 3.6 GHz and 5 GHz), see Fig. 4.3. The extensions are activated and deactivated to change the resonant frequencies between 2.4 GHz and 3.6 GHz.

In this scenario, the TM_{11} mode is used as the antenna is fed in a corner which allows an extra resonance at 5 GHz by adjusting the width of the main patch W. See Table 4.3 for the antenna dimensions.

Table 4.3: Set up parameters for WIFI scenario, see Fig. 4.3

$Lmain$ [mm]	W [mm]	$Lleft$ [mm]	$Lright$ [mm]	X [mm]	Y [mm]
23	14.7	5	7.3	5.5	2

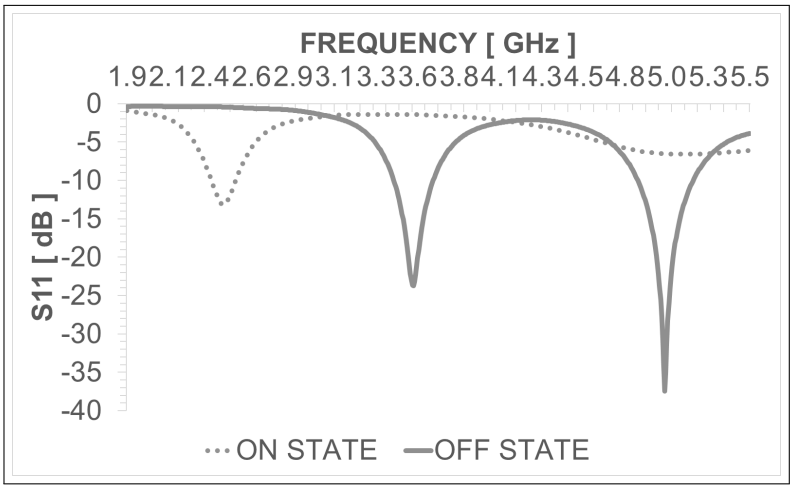

Figure 4.6: Reflection coefficient for the WIFI design with the extensions activated (dotted line) and with the extensions deactivated (solid line).

Fig. 4.6 provides the reflection coefficient ($S11$) parameters for the WIFI scenario. When the extensions are deactivated (OFF state), the resonant frequencies are found at 3.6 GHz and 5 GHz. On the other hand, when the extensions are activated (ON state), the lower resonant frequency changes from 3.6 GHz to 2.4 GHz. Thus the activation and deactivation of the extensions is required to switch between these two resonant frequencies.

In order to confirm that the activation/deactivation of the graphene extensions do change the antenna behaviour, Fig. 4.7 provides the surface current distribution along the main patch and the graphene extensions for frequencies 2.4 GHz, 3.6 GHz and 5 GHz, when the graphene extensions are either activated or

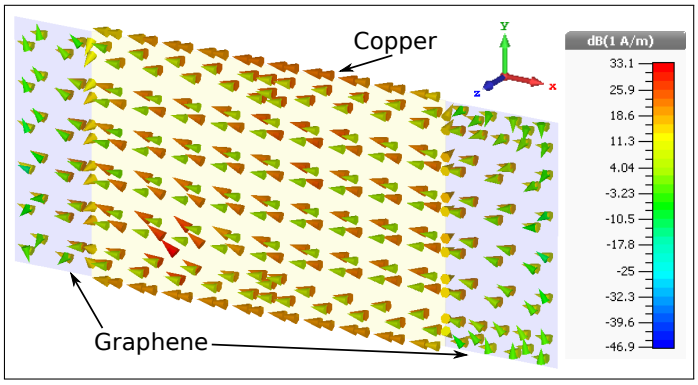

(a)

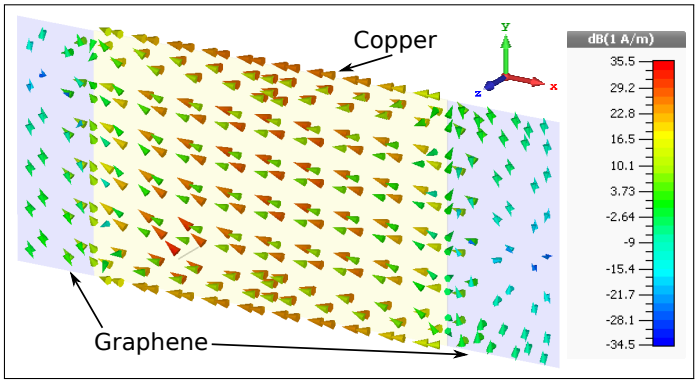

(b)

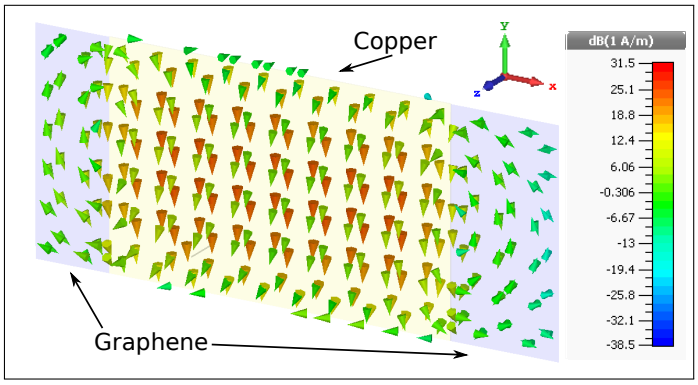

(c)

Figure 4.7: Surface current density on the WIFI antenna at (a) 2.4 GHz, (b) 3.6 GHz and (c) 5 GHz.

deactivated respectively. As expected, when the graphene extensions are on the OFF state - at 3.6 GHz, little current is allowed to propagate along the exten-

sions. In contrast, when the graphene extensions are in the ON state - at 2.4 GHz, substantially more current is able to propagate along the extensions and contribute to the electromagnetic radiation. This effectively changes the resonant length of the antenna and hence its resonant frequency.

Fig. 4.8 shows the radiation patterns at 2.4 GHz , 3.6 GHz and 5 GHz, when the graphene extensions are activated and deactivated respectively. As observed, all the radiation patterns are similar in shape to a balloon and close to the characteristics for a typical square patch antenna, showing that the graphene extensions have little effect on the shape of the radiation pattern. The obtained antenna gains are -3.4dB, 1.3 dB and 5.2 dB at 2.4 GHz, 3.6 GHz and 5 GHz respectively.

The antenna efficiencies extracted from the WIFI design are shown in Fig. 4.9. The antenna efficiencies η_t (solid line) show that when the antenna radiates at 2.4 GHz, η_t is lower than at any of the other two frequencies because of the graphene extensions attenuating the currents that contribute to radiation at that frequency. The power lost on graphene is about 337 mW which is a 67% of the total loss. When the graphene extensions are deactivated, in theory, the presence of the graphene extensions should have an equal effect at 3.6 GHz and 5 GHz, but their respective antenna efficiencies are not the same. An explanation might be that at 3.6 GHz, the graphene sheet must stop as much as possible any current propagating to the extensions. The better the graphene extensions achieve that, the less power is lost in the graphene material and the more is radiated. On the contrary, at 5 GHz there are some currents propagating on the extensions, see Fig. 4.7c. However, whether these currents are attenuated or not does not strongly affect the antenna efficiency but the antenna matching at that frequency, see Fig. 4.6. In addition, the antenna efficiencies obtained when considering the surface impedances from the impedance uncertainty $\hat{Z}s_{ON,OFF}$ (dotted line) show that there is a small improvement at 2.4 GHz compared to the theoretical values $Zs_{ON,OFF}$, but a decrement in the performance for the 3.6 GHz and 5 GHz

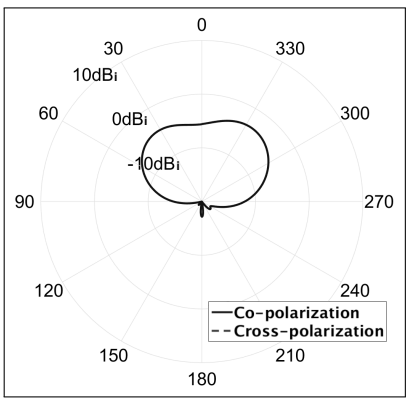

(a) E Plane (x-z plane)

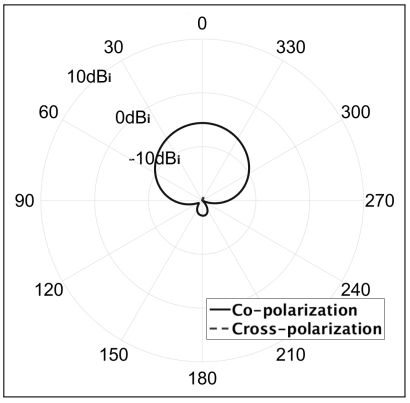

(b) H plane (y-z plane)

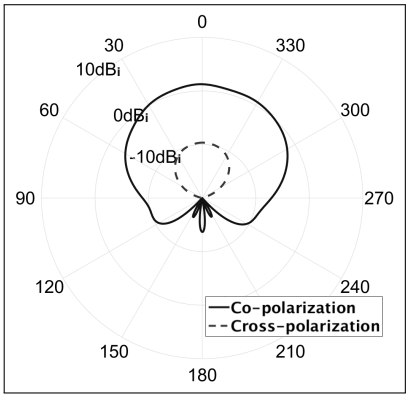

(c) E Plane (x-z plane)

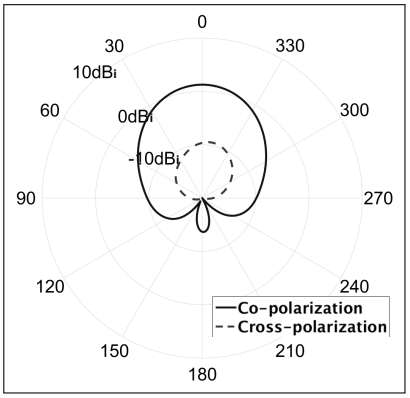

(d) H plane (y-z plane)

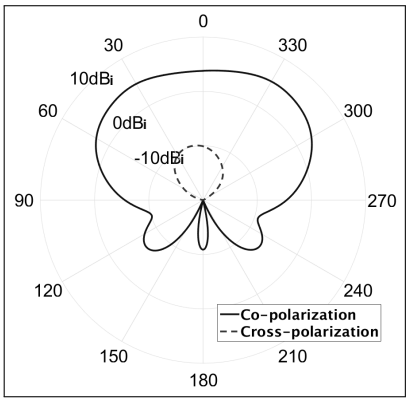

(e) E Plane (y-z plane)

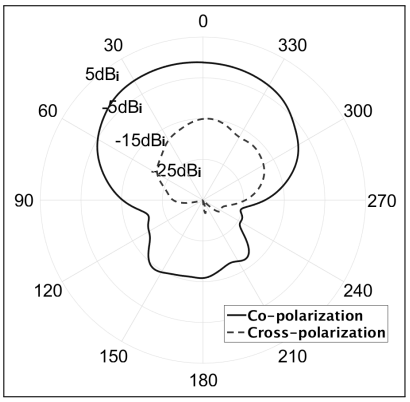

(f) H plane (x-z plane)

Figure 4.8: Radiation patterns of the WIFI antenna at (a)-(b) 2.4 GHz, (c)-(d) 3.6 GHz and (e)-(f) 5 GHz.

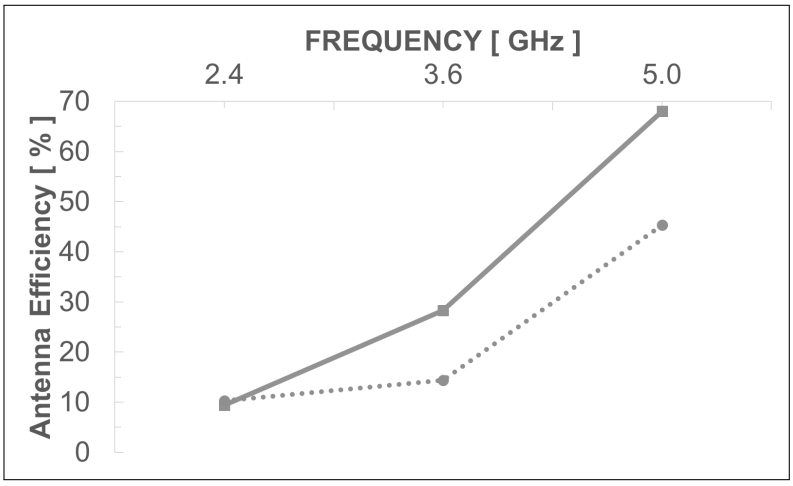

Figure 4.9: Antenna efficiencies of the WIFI design, solid line: from $Zs_{ON,OFF}$ values, dotted line: from $\hat{Z}s_{ON,OFF}$ values.

frequencies. In any case, it is demonstrated that the WIFI design proposed here is able to cover the target bands but the antenna efficiency at 2.4 GHz might be too low.

To demonstrate the impact of the surface impedance on the ON state (2.4 GHz), the same antenna is evaluated but now Zs_{ON}=6+j0.3 $\Omega/_{\square}$ (set 1 in Table 4.2) instead of Zs_{ON}=34+j0.3 $\Omega/_{\square}$ (set 2 in Table 4.2) by assuming that the deformation potential D is improved from D=18 eV to D=4 eV. The resulting value of η_t changes from 9.4% to 35.5% as the the power lost in graphene has been reduced from 337 mW to 253 mW at 2.4 GHz. This shows how important is to reduce the graphene surface impedance for the ON state Zs_{ON} in order to have reasonable antenna efficiencies. Unfortunately, the lower limit of Zs_{ON} depends on the deformation potential D which is yet not fully determined from experimental studies, and consequently, variations when defining this parameter strongly affects the final performance.

EFFECT OF THE DC BIAS LINES ON THE ANTENNA EFFICIENCY

In this section, the DC bias lines shown in Fig. 4.3 are added in the simulation analysis to observe the effect on the antenna efficiency. Note that, the tuning structure in Fig. 4.5 is still not simulated here due to the extremely small thickness of the layers. Therefore, only copper strips are added to simulate some bias lines that could provide different DC voltage bias to the graphene and doped semiconductor. The size of the added lines are Lvias1=5 mm, Lvias=5 mm and 100 μm thick. The resulting antenna efficiencies are 8%, 25% and 32% at 2.4 GHz, 3.6 GHz and 5 GHz respectively. As expected, the values obtained with the DC bias lines are smaller than the ones without the DC bias lines, see Fig. 4.9, at all the resonant frequencies. Additional simulations are carried out where the values of Lvias1 and Lvias2 are changed. The results concluded that decreasing the value of Lvias1 further reduced the antenna efficiency at 2.4 GHz but increased at the other two resonant frequencies. Likewise, when increasing Lvias2 all the antenna efficiencies were reduced. Therefore, the addition of the DC bias lines affects the antenna efficiency, and consequently, an optimum configuration and size of the DC bias lines is required when building the physical prototypes of the antennas.

TUNABLE BANDWIDTH AND ANTENNA MATCHING

Here, the antenna matching and operational bandwidth is studied when different surface resistances Rs are selected. Note that by changing the Rs, the surface reactance Xs of the surface impedance - $Zs = Rs + jXs$ - is also slightly changed but has no impact on the final result. As observed in Fig. 4.10, this allows to improve the antenna matching and tune the operational bandwidth BW. For instance, at 2.4 GHz, the value of the reflection coefficient goes from -8.7 dB to -13.2 dB by just selecting Rs=51 $\Omega/_{\square}$ or Rs=31 $\Omega/_{\square}$ respectively, see Fig. 4.10. This effect is also reproduced for the 3.6 GHz and 5 GHz frequencies. Consequently, the control of the input impedance, and hence the reflection

coefficient, might help to reduce the complexity of the antenna matching network in future reconfigurable antennas made partially of graphene. The operational bandwidth can be tuned from a maximum all the way down to 0 MHz, which means not having the condition $S11 \leq$-10 dB, by again selecting a proper Rs, see Fig. 4.11. Having control of the operational bandwidth might allow graphene reconfigurable antennas to adapt to diverse communication technologies that might operate at the same frequency. The resulting antenna efficiencies are close to each other, however, the best efficiencies are again found when both Rs_{ON} and Rs_{OFF} are minimum and maximum respectively.

TUNABLE RESONANT FREQUENCY

Since intermediate values of the graphene surface impedance between Zs_{ON} and Zs_{OFF} can be selected, it is theoretically possible to select any resonant frequency between the two edge frequencies limited by these values. To show an example of this, Fig. 4.12 shows the reflection coefficient of the WIFI antenna design, Fig. 4.3, for four different values of Rs. Both extension lengths have been shrunk to L_{left}=L_{right}=3 mm to keep a good matching of the antenna over the range of operating frequencies. In this case, the four different values of Rs provide four different resonant frequencies, see Fig. 4.12. Interestingly, the antenna efficiency η_t for the two extreme values Rs=70 $\Omega/_{\square}$ and Rs=2580 $\Omega/_{\square}$, see Fig. 4.13, are now better than the ones obtained in the WIFI scenario for Rs_{ON}=34 $\Omega/_{\square}$ and Rs_{OFF}=2580 $\Omega/_{\square}$, see section 4.4.1. Clearly, shorter graphene extensions cause less ohmic losses but smaller changes in the resonant frequencies since now the lower resonant frequency is 3 GHz instead of 2.4 GHz. For the intermediate resonant frequencies, the antenna efficiencies are worse compared to the two edge frequencies. The cause is that as more and more current is allowed to propagate to the extensions (by reducing the Rs), the current is being substantially attenuated due to large values of Rs. The ability to select any resonant frequency within a specific range might prove very useful in wearable

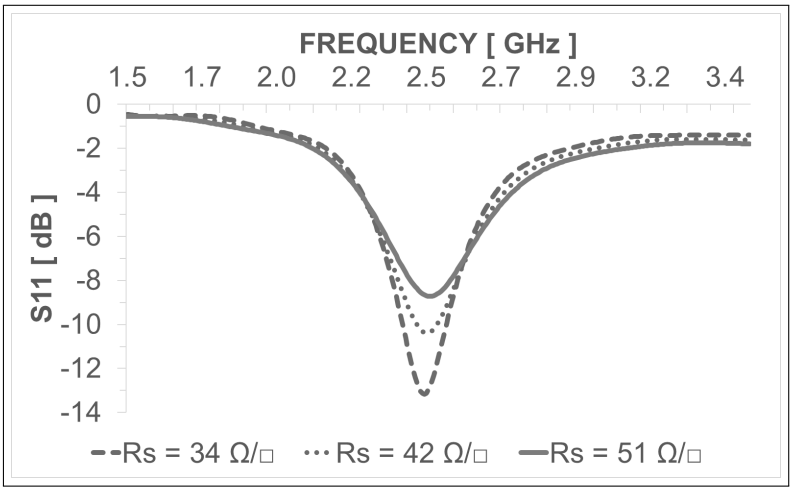

(a)

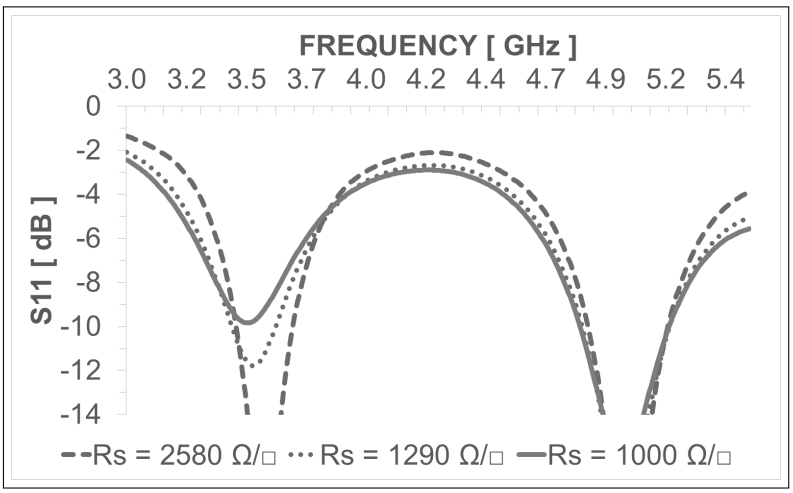

(b)

Figure 4.10: Reflection coefficient for the WIFI antenna with variable BW for the (a) ON state and (b) OFF state.

applications, where streching and bending affects the resonant frequency of the antenna among other parameters.

For instance, in [192], the authors studied the performance of wearable antennas made of graphene ink from 1 GHz to 5 GHz. Their obtained gains, between 0.2 dB and -1 dB, were similar or lower to the ones obtained here, see section 4.4.1. The resonant frequency, bandwidth and gain of the antennas under their study were slightly affected at different bending and twisting cases. Because

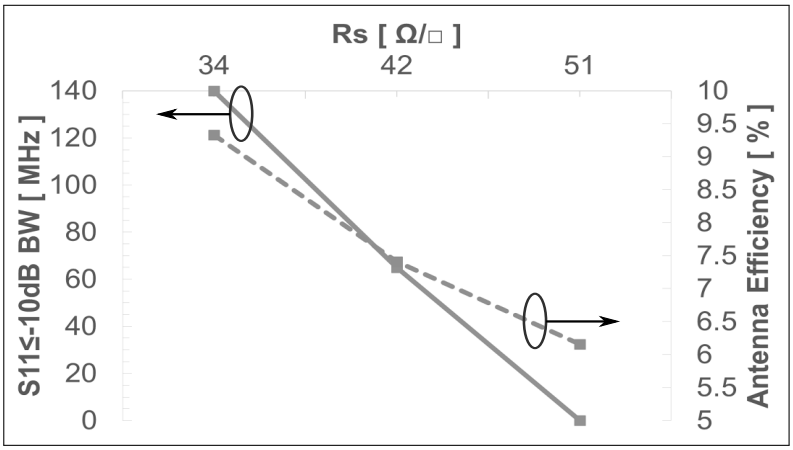

(a)

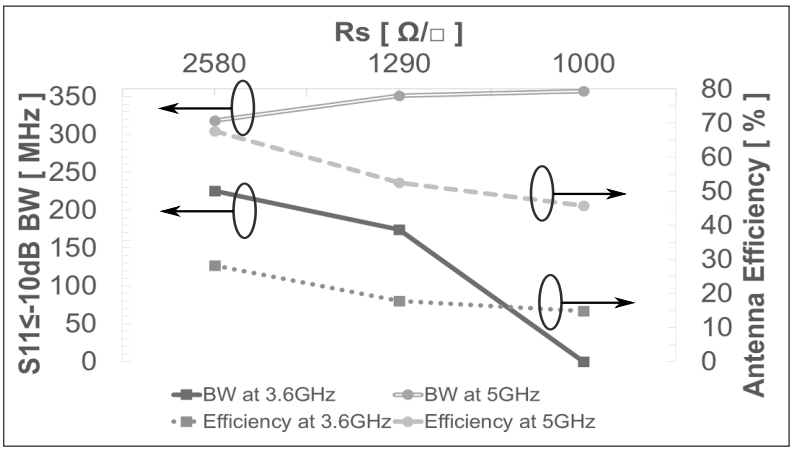

(b)

Figure 4.11: Bandwidth and antenna efficiency variation for different values of Rs at a) 2.4GHz and b) 3.6GHz and 5GHz.

the graphene ink cannot provide reconfigurability by itself, using graphene as in the proposed antennas might produce enough reconfigurability to compensate for the side effects observed in the graphene ink case.

FREQUENCY RECONFIGURABILITY FOR TRANSPARENT ANTENNAS AND IN LOW TEMPERATURE APPLICATIONS

As a single layer of pristine graphene is 97.7% transparent to visible light, graphene could be implemented in fully transparent antennas. Here, the WIFI

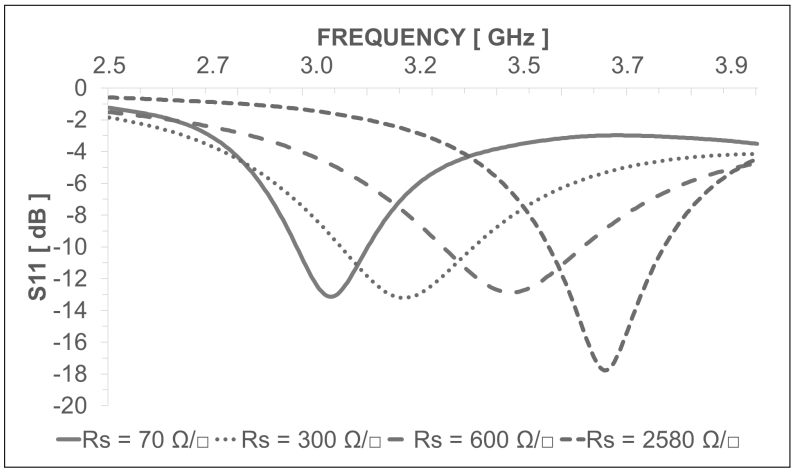

Figure 4.12: Reflection coefficient for the WIFI design with intermediate Rs values selected.

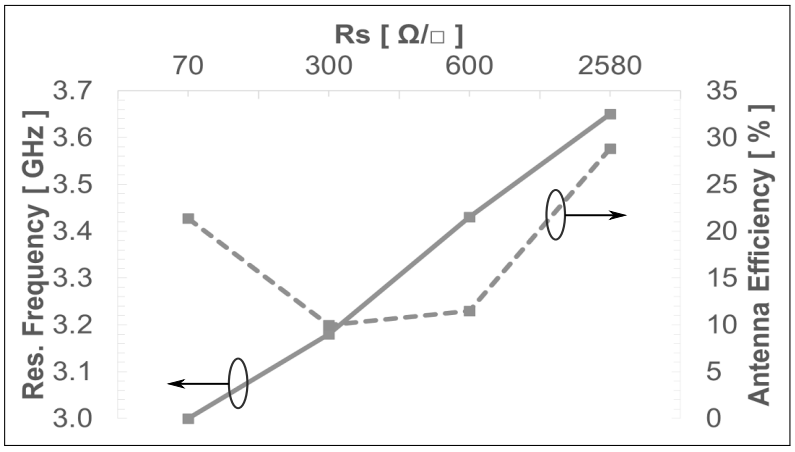

Figure 4.13: Resonant frequency and antenna efficiency variation as Rs changes.

design is analysed as a full transparent solution. To do so, the copper used in the main patch and ground plane is substituted by a hybrid transparent conductive film composed by mesoscale and nanoscale silver and copper nanowires (AgNW/Cu) produced in [193]. This conductive film provides 92% transparency in the visible light and a surface resistance of Rs=0.36 $\Omega/_{\square}$. The antenna dimensions are kept the same as in Table 4.3. The ON and OFF state surface impedances selected, Zs_{ON} and Zs_{OFF}, are from the set 2 in Table 4.2 as it is assumed to operate at room temperature. The full transparent WIFI antenna

is still able to switch between the desired frequencies of 2.4 GHz, 3.6 GHz and 5GHz. Fig. 4.14 shows the antenna efficiencies for the fully transparent antenna at room temperature. The values obtained are lower than when copper is implemented, see Fig. 4.9. However, this is expected as the conductivity of the transparent film AgNW/Cu is lower than copper and therefore additional ohmic losses are introduced. In fact, transparent antennas found in the literature have lower antenna efficiencies, from 6.4% up to 85% for transparencies of around 81% to 90%, than their counterparts made of non-transparent materials with better conductivity (i.e. made of copper) [174], [175], [177], [178]. This shows that a hybrid graphene-AgNW/Cu antenna with a minimum transparency of 92% can be a potential solution to provide frequency reconfigurability to full transparent antennas.

Additionally, the surface impedance of graphene is temperature dependent. Decreasing the operational temperature results in a much lower surface impedance for the ON state Rs_{ON} and a much larger surface impedance for the OFF state Rs_{OFF}, see set 3 in Table 4.2. Now, the WIFI design is simulated again with the AgNW/Cu transparent film as the main patch and ground plane but, in this case, the surface impedances for the ON and OFF state are selected from the set 3 in Table 4.2. Fig. 4.14 shows the antenna efficiency for the fully transparent antenna at T=4.2K. The extracted antenna efficiencies are now higher than the previous full transparent antenna at room temperature and even higher than when copper is used in the main patch and ground plane. This is due to the ratio Rs_{OFF}/Rs_{ON} when the operational temperature is 4.2K (set 3 in Table 4.2) is larger compared to the ratio for the non-transparent (i.e. copper) and the full transparent antenna at room temperature (set 2 in Table 4.2). Increasing this ratio improves the antenna efficiency as there are less ohmic losses in the ON state and more current is stop in the OFF state. This demonstrates that graphene could be a suitable solution to provide frequency reconfigurability to antennas that need to operate at very low temperatures with reasonable antenna efficiencies such as in space applications.

This is specially important because other switching technologies such as MEMS, PIN diodes and FET switches might struggle to work at such low temperatures and hence graphene might be an interesting alternative solution.

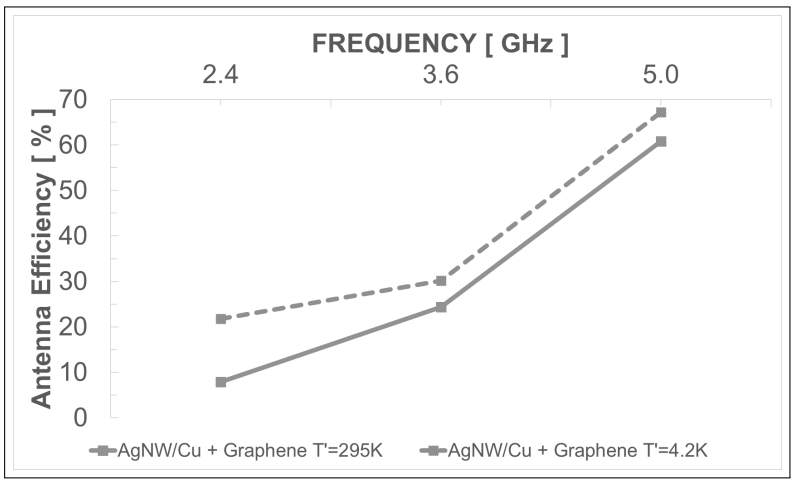

Figure 4.14: Resonant frequency and antenna efficiency variation as Rs changes.

4.4.2 LTE SCENARIO

The second design, Fig. 4.4, covers four bands of LTE (1.8 GHz, 2.1 GHz, 2.6 GHz and 3.6 GHz) by switching ON and OFF different graphene strips. This scenario also uses the TM_{11} mode for radiating. The values of Zs_{ON} and Zs_{OFF} are assigned from the Set 2 in Table 4.2. See Table 4.4 for the structure dimensions.

Table 4.4: Set up parameters for LTE scenario, see Fig. 4.4

$Lmain$ [mm]	W [mm]	$L1$ [mm]	$W1$ [mm]	$L2$ [mm]	$W2$ [mm]	$L3$ [mm]
39	22	2	8.5	11	2	2
$W3$ [mm]	$L4$ [mm]	$W4$ [mm]	$D1$ [mm]	$D2$ [mm]	X [mm]	Y [mm]
8.5	11	2	23.5	10	12.5	1

Fig. 4.15 provides the $S11$ parameters for the LTE scenario. When all four graphene strips are activated, the antenna operates efficiently at 2.1 GHz and 3.6 GHz. Conversely, when all four strips are deactivated, the antenna switches now to 1.8 GHz operation. Finally, when strips 2 and 4 are OFF and strips 1 and 3 are ON, the antenna achieves good matching at 2.6 GHz. Ideally, the antenna should switch between the four desired bands by switching ON or OFF all four strips at the same time. Unfortunately, when the four strips are deactivated the secondary frequency is found to be slightly over 2.6 GHz. This is because deactivating strips 1 and 3 affects the resonance at 2.6 GHz.

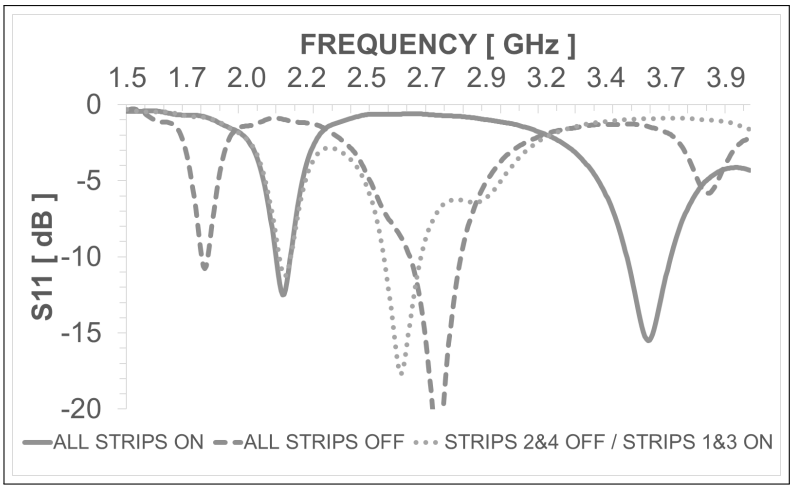

Figure 4.15: Reflection coefficient for the LTE design with all strips activated (solid line), all strips deactivated (dashed line), and with strips 2 and 4 deactivated and strips 1 and 3 activated (dotted line).

The surface current densities have been simulated to show the effect of the graphene strips on the behaviour of the antenna. Fig. 4.16 and Fig. 4.17 show the current distributions along the main patch and the graphene strips at 1.8 GHz, 2.1 GHz, 2.6 GHz and 3.6 GHz; where pairs of graphene strips are activated and deactivated (Fig. 4.4). When the graphene strips 1 and 3, Fig. 4.16b, and strips 2 and 4, Fig. 4.17b, are set to the ON state the current is allowed to propagate through the strips. However, when the graphene strips are set to the OFF state,

Fig. 4.16a and Fig. 4.17a, the currents are not allowed to propagate through the strips but are diverted around them. That makes the currents travel longer paths and therefore the antenna resonances are found at lower frequencies.

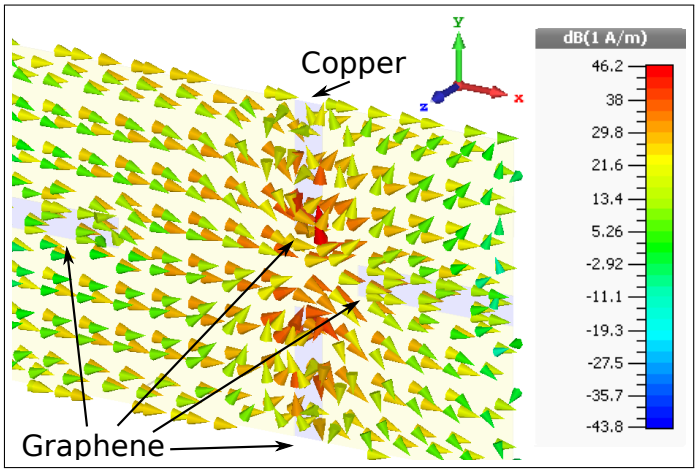

(a)

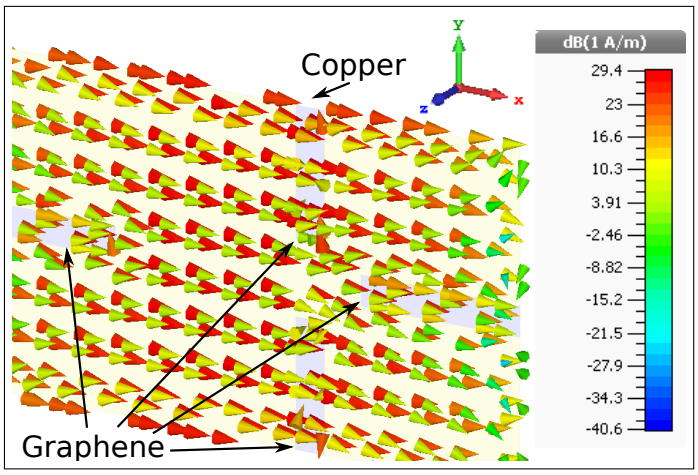

(b)

Figure 4.16: Surface current density in the LTE antenna at (a) 1.8 GHz and (b) 2.1 GHz.

Fig. 4.18 and Fig. 4.19 show the radiation patterns at 1.8 GHz, 2.1 GHz, 2.6 GHz and 3.6 GHz; where again the graphene strips activated and deactivated. The resulting radiation patterns are again similar in shape to a balloon and close to a typical square patch antenna, as previously observed in the WIFI scenario.

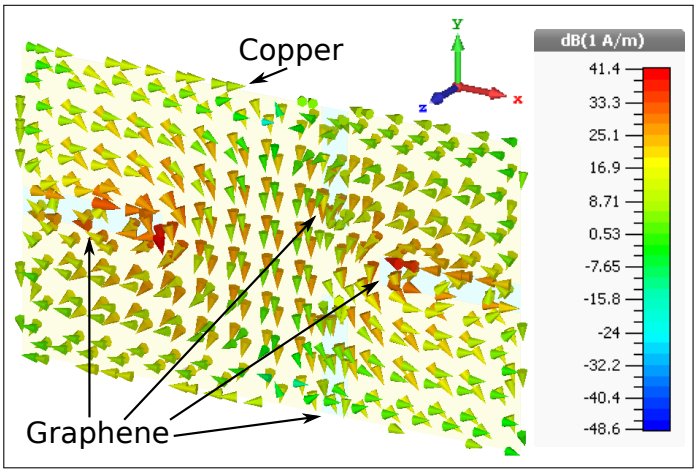

(a)

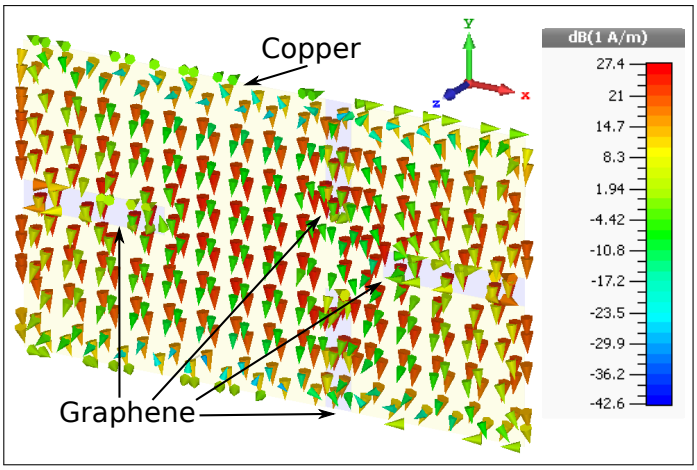

(b)

Figure 4.17: Surface current density in the LTE antenna at (a) 2.6 GHz and (b) 3.6 GHz.

Thus, the addition of the graphene strips seems to not strongly affect the shape of the radiation pattern. The resulting antenna gains are -1.6 dB, -0.7 dB, -3.3 dB and 3.9 dB at 1.8 GHz, 2.1 GHz, 2.6 GHz and 3.6 GHz respectively.

The efficiency results obtained are shown in Fig. 4.20. The worst efficiency is found at 2.6 GHz due to a large change of frequency being forced - from 3.6 GHz to 2.6 GHz. This is because, on one hand, the losses due to the graphene strips and diversion of currents, and in the other hand, at 2.6 GHz the resulting

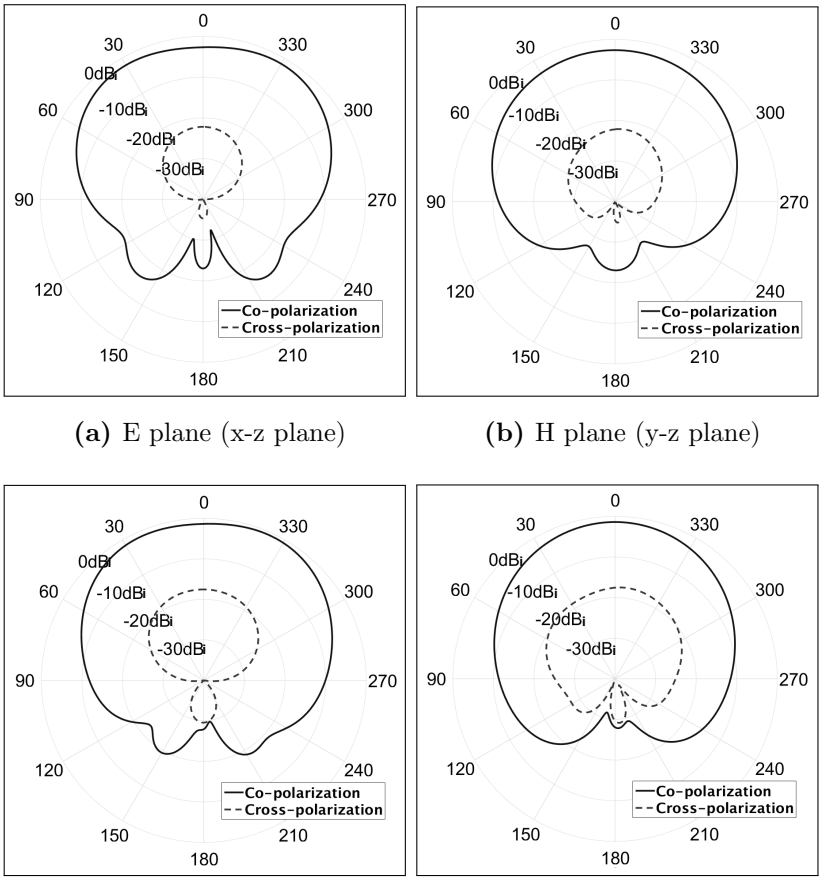

(a) E plane (x-z plane) **(b)** H plane (y-z plane)

(c) E plane (x-z plane) **(d)** H plane (y-z plane)

Figure 4.18: Radiation patterns of the LTE antenna at (a)-(b) 1.8 GHz and (c)-(d) 2.1 GHz.

physical size of the antenna is much smaller than the optimum half-wavelength, consequently, the antenna does not radiate well.

INDIVIDUAL GRAPHENE STRIP SWITCHING

In the LTE design, in order to change the resonant frequencies, pairs of strips are accordingly switched ON and OFF. However, it could be possible to individually activate or deactivate any of strips independently and hence achieve intermediate resonant frequencies. Fig. 4.21 presents the results for individually switching graphene strips 1 and 3, where the widths of strips 1 and 3 were changed from

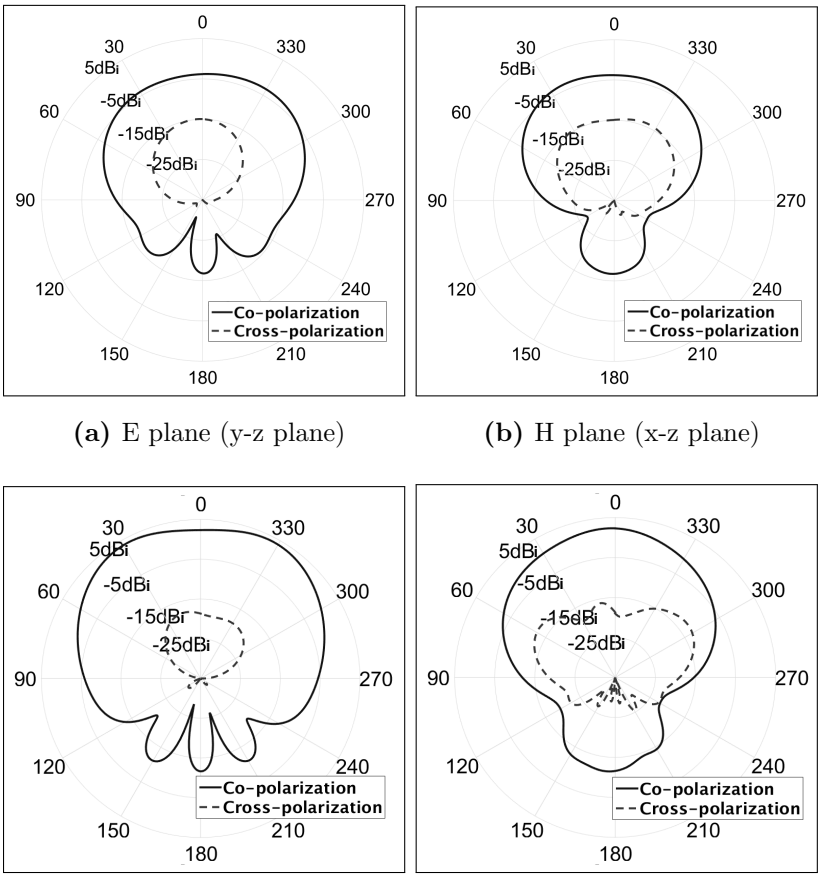

(a) E plane (y-z plane) **(b)** H plane (x-z plane)

(c) E plane (y-z plane) **(d)** H plane (x-z plane)

Figure 4.19: Radiation patterns of the LTE antenna at (a)-(b) 2.6 GHz and (c)-(d) 3.6 GHz.

$W1$=$W3$=8.5 mm to $W1$=9.5 mm and $W3$=7.5 mm. As shown, if both graphene strips are on the ON state, the antenna is radiating at 2.1 GHz, as in the previous LTE configuration. But, if strip 1 is now individually changed to the OFF state while strip 3 is kept on the ON state, the resonance changes to 1.92 GHz. On the contrary, if strip 3 is the one changed to the OFF state and the strip 1 is kept on the ON state, the obtained resonant frequency is now 2.01 GHz. Finally, if both are switched to the OFF state, then the antenna resonates to 1.8 GHz as in the previous scenario. The efficiencies for the two extra resonant frequencies achieved here - 1.92 GHz and 2.01 GHz - are found to be 11% and 15.5% respectively, in

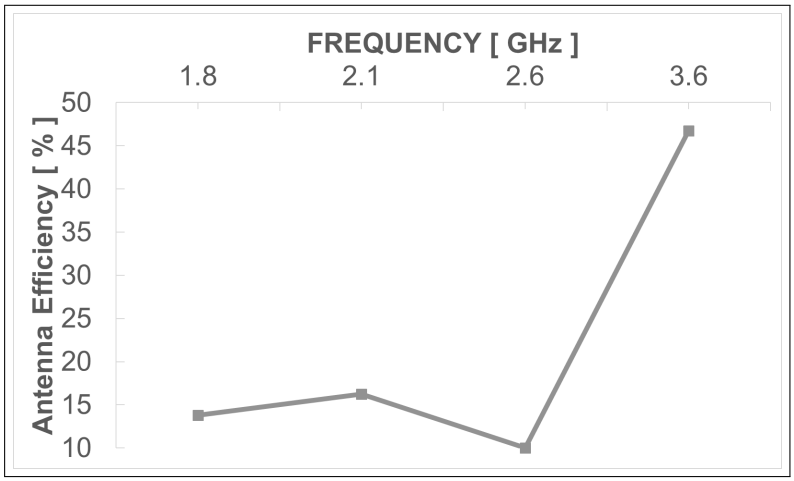

Figure 4.20: Antenna efficiencies of the LTE design.

the same order as for 1.8 GHz. Therefore, frequency reconfigurable antennas made partially of graphene extensions/strips could provide as many resonant frequencies as combinations of activating/deactivating graphene sheets without causing a drop in the the antenna efficiency.

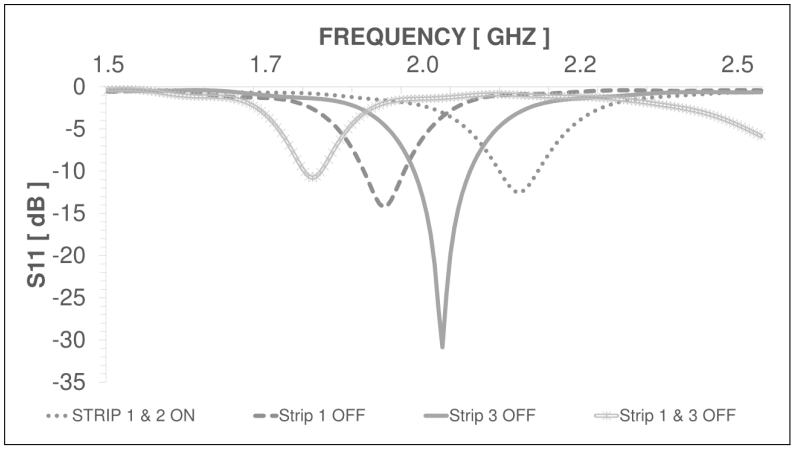

Figure 4.21: Reflection coefficient for the LTE design with strips 1 and 3 activated (dotted line), strip 1 deactivated and strip 3 activated (dashed line), strip 2 deactivated and 1 activated (solid line) and strip 1 and 3 deactivated (double solid line).

4.4.3 PERFORMANCE COMPARISON

Here, the results obtained from the proposed WIFI and LTE antennas are compared to some other planar frequency reconfigurable antennas found in the literature. In [133], an anular slot antenna is configured to switch between two operating frequencies by integrating MEMS. In [138], a planar inverted-F antenna (PIFA) covers some commercial mobile phone bands by implementing multiple PIN-diodes. In [139], a patch antenna with a varactor loaded slot can operate at any frequency within a specific range by applying different DC voltages. Finally, in [137], a microstrip patch antenna with a stub connected through an optical switch can switch between two frequencies by illuminating the optical switch with a laser. Table 6.5 summarizes the comparison.

As observed from Table 6.5, the antenna efficiencies obtained when using graphene are lower compared to any of the other switching technologies in the low and high limits. This is expected as graphene is still a material under developement. Moreover, graphene is used here as part of the radiating structure which does not add extra weight or space. However, in the other papers, the RF switches are elements added to the structure that do not contribute to radiation and increase the weight and volume of the antenna. In the case of using optical switches, it also increases the complexity and power consumption of the feeding system. As shown in this section, implementing graphene in antennas can provide the ON/OFF behaviour similar to MEMS, PIN-diode and optical switches. In addition, it provides the continous frequency selection found in antennas loaded with varactors with the extra feature of bandwidth selection. Therefore, using graphene converges multiple modes of operation into a single solution. Additionally, graphene can easily operate at mm-wave and THz regime where conventional switches will perform poorly or even not work at all.

Table 4.5: Comparison of different reconfigurable antennas

Reference	Technology	Frequencies Covered	Antenna Efficiency
This work: WIFI design	Graphene	2.4 GHz, 3.6 GHz and 5 GHz	9.4 to 68%
This work: LTE design	Graphene	1.8 GHz, 2.1 GHz, 2.6 GHz and 3.6 GHz	10% to 46.8%
[133]	MEMS	2.4 GHz and 5.2 GHz	90% to 92%
[138]	PIN-diode	0.7 GHz, 0.85/0.9 GHz, 1.8/1.9 GHz and 2.3/2.5 GHz	52.1% to 85.4%
[139]	Varactor	continuous from 3.24 GHz to 4.35 GHz	38% to 90%
[137]	Optical switch	0.875 GHz and 1.01 GHz	No data provided

4.4.4 SWITCHING POWER CONSUMPTION

Table 4.6 and 4.7 provide the peak power consumed (P_{peak}) for all the scenarios evaluated in this paper when switching from one operating frequency to another due to the change of required values of charge carrier density n. For example, when switching between 2.4 GHz and 3.6 GHz in the WIFI design as the graphene extensions are activated or deactivated respectively. It is important to highlight here that the power consumption happens during a very short period of time - t $\ll$ switching time - and quickly drops to zero. So in normal use, hybrid metal-graphene reconfigurable antennas have very low power consumption. The total

power shown is calculated by using equation (4.7) where the dielectric thickness d, the relative permittivity ϵ_r^d and the time constant τ_{RC} are set using the values in Table 4.1. Specific values such as the charge carrier density n and the physical area of graphene A are extracted from Tables 4.2, 4.3 and 4.4. Note that, in the evaluated scenarios there are from two to four graphene sheets being fed and the total power consumed is the addition of the power consumed by each individual sheet as it switches ON or OFF.

Table 4.6: P_{peak} values for WIFI based designs

WIFI (Section 4.4.1)	n [m^{-2}]	A [mm^2]	P_{peak} [mW]
Zs_{ON}= 34+j0.3 [$\Omega/\square$]	$5{\cdot}10^{17}$	180.8	330.6
Zs_{ON}= 6+j0.3 [$\Omega/\square$]	$5{\cdot}10^{17}$	180.8	330.6
Tunable BW and $S11$ (Section 4.4.1)	n [m^{-2}]	A [mm^2]	P_{peak} [mW]
Rs_{ON}= 34 [$\Omega/\square$]	$5{\cdot}10^{17}$	180.8	330.6
Rs_{ON}= 42 [$\Omega/\square$]	$1.8{\cdot}10^{17}$	180.8	42.8
Rs_{ON}= 51 [$\Omega/\square$]	$1.05{\cdot}10^{17}$	180.8	14.6
Tunable $f_{resonant}$ (section 4.4.1)	n [m^{-2}]	A [mm^2]	P_{peak} [mW]
Rs_{ON}= 70 [$\Omega/\square$]	$5.7{\cdot}10^{16}$	88.2	2.1
Rs_{ON}= 300 [$\Omega/\square$]	$8.5{\cdot}10^{15}$	88.2	0.0466
Rs_{ON}= 600 [$\Omega/\square$]	$3.9{\cdot}10^{15}$	88.2	0.0098

From Table 4.6 and 4.7 it is observed that the peak power consumption substantially decreases as the physical dimensions of the graphene sheets reduce. For example, when the area of the extensions of the WIFI design is reduced from 180.8 mm^2 to 88.2 mm^2, or when only strips 1 and 3 are turned ON - total area of 34 mm^2 - instead of all the strips ON - total area 78 mm^2 - in the LTE design, the value of P_{peak} is reduced. This is another reason for implementing graphene in hybrid metal-graphene antennas instead of full graphene antennas. Likewise, low values of charge carrier density n also help to reduce the power

consumed. Interesting results are obtained for the tunable resonant frequency scenario in Table 4.6 (Subsection 4.4.1) where very low peak power consumptions are obtained - 2.1 mW, 46.6 μW and 9.8 μW - for changes in the resonant frequency of up to 650 MHz. Likewise, relaxing the values for the ON state surface impedance (Zs_{ON}) seems to be also beneficial on the point of view of power consumption. For example, in the tunable bandwidth and matching scenario, selecting the Rs_{ON}=51 $\Omega/\square$ instead of Rs_{ON}=34 $\Omega/\square$ reduces the neccessary carrier density significantly and hence the peak power consumption drops by more than 20 times, from 330.6 mW to 14.6 mW.

Table 4.7: P_{peak} values for LTE based designs

LTE scenario (4.4.2)	n [m^{-2}]	A [mm^2]	P_{peak} [mW]
All Zs_{ON}= 34+j0.3 [$\Omega/\square$]	$5{\cdot}10^{17}$	78	142.6
Strips 1-3 Zs_{ON}= 34+j0.3 [$\Omega/\square$]	$5{\cdot}10^{17}$	34	62.2
Individual Strip 4.4.2)	**n [m^{-2}]**	**A [mm^2]**	**P_{peak} [mW]**
Strip 1 Zs_{ON}= 34+j0.3 [$\Omega/\square$]	$5{\cdot}10^{17}$	19	34.7
trip 3 Zs_{ON}= 34+j0.3 [$\Omega/\square$]	$5{\cdot}10^{17}$	15	27.4

It is also worth to analyse the impact of the deformation potential D and operational temperature values in the power consumption. As seen in the WIFI section, see section 4.4.1, the antenna efficiency can be greatly improved by assuming Zs_{ON}=6+j0.3 $\Omega/\square$ due to a much better achievable deformation potential D=4 eV. However, if instead of dropping the value of Zs so much, it is enough to have Zs_{ON}=34+j0.3 (assuming that the antenna efficiency obtained is acceptable), then, the required charge carrier density n to achieve that value would be n=7×10^{16} m^{-2} instead of n=5×10^{17} m^{-2} (an order of magnitude lower). This reduction in the n would cause a reduction of the peak power consumption from 330.6 mW to just 6.6 mW, a factor of 50 times less. Exactly the same conclusion is extracted for the case of very low temperature. As a result, there is a trade off between in one hand a required antenna performance, such as achievable

frequency reconfigurability and/or antenna efficiency; and on the other hand, the allowed switching power consumption. It is possible to greatly improve one aspect at the expense of increasing the other.

4.5 CONCLUSIONS

This chapter has analysed the performance of using graphene in frequency reconfigurable antennas in the microwave regime via the simulation of two hybrid metal-graphene antennas for WIFI and LTE applications. It has been demonstrated that:

- Graphene, as a material with tunable surface impedance, allowed large frequency reconfigurability - up to 1.2 GHz change - with additional tunability of the antenna matching - up to 20 dB improvement - and bandwidth - up to 225 MHz increase.
- The proposed antennas can achieve high degree of reconfigurability in terms of changing operational frequency but at the expense of lower antenna efficiencies - between 9.4% and 68%.
- Although very low power consumption is achieved during normal operation, moderate values of the instantaneous peak power ($\leq$ 330.6 mW) are present during the switching process which only occurs during very short time periods ($\leq$ 1.6 ms).

Reducing the area of the graphene sheets would substantially improve the instantaneous peak power values. This might be of special interest in millimetre wave applications where the size of the graphene sheets is expected to be much smaller than in microwave applications. Additionally, choosing higher values of surface impedances for the ON state (Zs_{ON}) would also reduce the power consumed at the expense of reducing the antenna efficiency. Results showed that the higher the ratio between Zs_{OFF} and Zs_{ON}, and the lower the value of

Zs_{ON}, the higher the antenna efficiencies that are achieved. Unfortunately, the lower limit of Zs_{ON} depends on the deformation potential D which is yet not fully determined from experimental studies, and consequently, variations when defining this parameter strongly affects the final performance. For instance, an improvement of the antenna efficiency, from 9.4% to 35.5%, is achieved in the WIFI scenario by selecting D=4 eV instead of D=18 eV. Alternatively, one can reduce the thickness d and increase the relative permittivity ϵ_r^d of the dielectric placed between the graphene sheet and the doped semiconductor, but this solution is limited by current material synthesis and processing techniques, and will only become possible as technology improves.

In Chapter 5, a polarization reconfigurable antenna made of a hybrid metal-graphene combination is proposed and evaluated for DAB, GNSS, different link conditions and arbitrary antenna orientation.

Chapter 5

HYBRID METAL-GRAPHENE POLARIZATION RECONFIGURABLE ANTENNAS

This chapter studies, analyses and discusses the performance, limitations and trade-offs of implementing graphene in planar polarization reconfigurable antennas for wireless and mobile applications. Here, two antenna systems are proposed and simulated. The first system is composed of a single element while the second system is composed of a two element array. In this chapter, graphene is implemented to switch between different linear and circular polarizations. The first design switches between digital audio broadcast (DAB) and global navigation satellite system (GNSS) such as Galileo and the second design is able to adapt to different channel conditions for any communication technology operating at 2.4 GHz. The performance results are compared to other state-of-the-art polarization reconfigurable antennas that implement other switching technologies.

5.1 INTRODUCTION

In general, any communication system can operate using any polarization, but in practice, some polarizations are preferred to others for particular applications. In many terrestrial broadcasting (i.e. DAB), wireless (i.e. WIFI, RFID, Bluetooth) and mobile communications (i.e. GSM, UMTS, LTE) linear polarization is widely, but not exclusively, used as the proportion of electromagnetic radiation coupled is higher and the position of the antennas are assumed to be known. In contrast, circular polarization is mainly used for satellite-to-earth communications (i.e. GNSS) due to the Faraday rotation effect present in the ionosphere [194]. However, in bad communication link conditions such as rich multipath environments, circular polarization can also be used as it is more robust than linear polarization in such conditions. For instance, in no-line-of-sight (NLOS) conditions, the multipath effects are reduced by using circular polarization instead of linear polarization, which is more sensitive to depolarization caused by reflections and refractions [194]. Furthermore, if the antennas are aligned on the same axis, linear polarization (either horizontal or vertical) is desired, while when they are not aligned, circular polarization is preferred as it is independent of the antennas' alignment.

Polarization diversity [195]–[198] is another method used to reduce undesired effects due to channel fading as electromagnetic waves with different polarizations suffer different channel scattering and hence their associate fading are statistically independent [194], [196]. Consequently, polarization reconfigurable antenna arrays are capable of adapting to different environment/link conditions [196]. Additionally, using orthogonal polarizations in antenna arrays reduces the size of the system as radiating elements that work at orthogonal polarizations suffer much less mutual coupling, and thus, they can be located closely together. [194].

There are already many planar polarization reconfigurable antennas and antenna arrays in the literature that use traditional switching technologies such as MEMS [199], [200], FET switches [201]–[203], PIN diode [204]–[215], varactors

[216], [217] and tunable materials [218] for reconfigurability. In [204], the authors proposed a single-fed square patch antenna with its four corners slightly separated from the top patch. These corners are activated and deactivated via PIN-diodes which allow the selection of linear and circular polarizations. Similarly, this chapter will analyse the use of the variable surface impedance of graphene as a potential method to switch between different polarizations at microwave frequencies. The proposed microstrip antennas are made of copper or a hybrid transparent film where graphene sheets are placed on the space left by the truncated corners. Potential applications of transparent polarization reconfigurable antennas and arrays might be found in vehicular communication systems, access points and base stations integrated in building windows for indoor and outdoor communications, substitution of visible cellular base stations, product labels, etc. To the best of the author's knowledge, there are no reports in the literature of polarization reconfigurable antennas made fully or partially of graphene for any range of frequencies (i.e. microwave to THz frequencies).

The novel contributions presented in this chapter can be summarized as follows:

- Analyse and simulate a proposed hybrid metal-graphene polarization reconfigurable antenna that switches between linear polarization for DAB applications at 1.45-1.5 GHz and circular polarization for GNSS applications at 1.55-1.6 GHz.

- Analyse and simulate a proposed two element array of hybrid metal-graphene polarization reconfigurable antennas that switches between linear polarization and circular polarization at 2.4-2.45 GHz for any antenna orientation and link condition.

- Present the advantages and disadvantages of using graphene in polarization reconfigurable antennas at microwave frequencies as well as the power consumption.

The remainder of the chapter is structured as follows: Section 5.2 will describe the proposed hybrid antenna designs and system configuration. Section 5.3 will present the results obtained, the hybrid antenna performance compared to other polarization reconfigurable antennas in the literature and the power consumed. Finally, Section 5.4 will summarise some conclusions.

5.2 PROPOSED ANTENNA DESIGNS

Standard microstrip patch antennas present linear polarization if a single feed and no patch modifications are implemented. However, it is possible to obtain circular polarization by exciting two orthogonal modes (i.e. TM_{01} and TM_{10}) with a 90° phase difference [34]. Commonly, two orthogonal modes with the necessary phase difference can be excited by using one or two feeds. When using two feeds, one of the feeds is directly applied into one edge of the patch while the second feed, containing a 90° power divider, is applied to another edge of the patch. Using a double feed prevents the necessity of adding modifications to the patch. On the other hand, if only a single feed is desired, modifications such as changing the patch shape, patch dimensions or inserting slots into the patch are required for the 90° phase difference. Forcing the length L and the width W of the patch to be slightly different or trimming opposite corners are two of the most common methods for achieving 90° phase difference. Here, the trimmed corners of a patch antenna are substituted by graphene sheets in order to switch between different polarizations.

In order to demonstrate the use of graphene in polarization reconfigurable antennas, two main antenna designs are studied:

- A single polarization reconfigurable antenna based on a square patch antenna with corners truncated made of graphene.5.1a.

- A two element array based on the first design 5.1b.

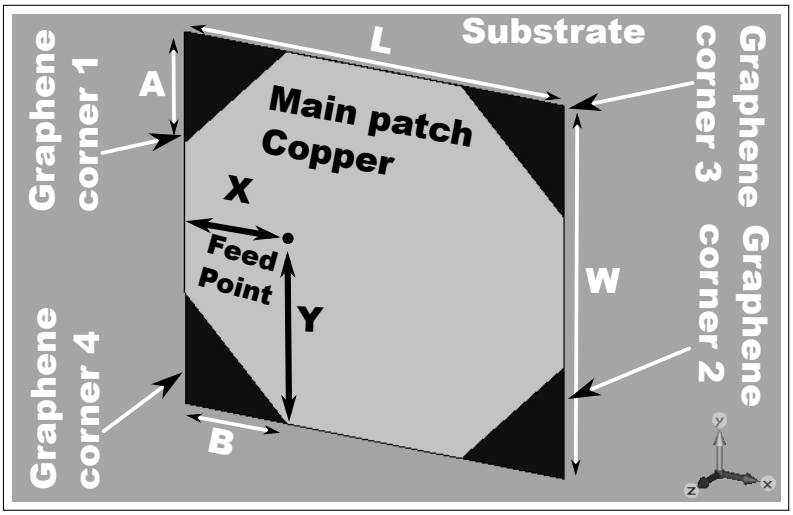

(a)

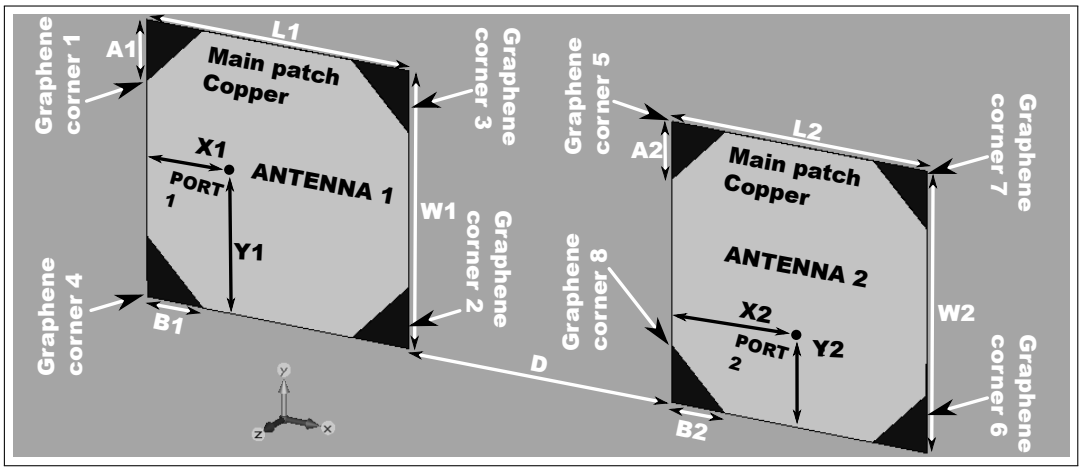

(b)

Figure 5.1: Graphical representation of polarization reconfigurable antennas for a) Scenario 1: DAB+GNSS applications and b) Scenario 2: Known-unknown antenna orientation and LOS-NLOS LINK applications.

The first antenna design aims to switch between horizontal linear polarization (HLP), right-hand circular polarization (RHCP) and left-hand circular polarization (LHCP) by switching ON and OFF different pairs of corners made of graphene. This design allows operation of two radio frequency systems that use completely different polarizations. Likewise, the second antenna system aims to

switch between vertical linear polarization (VLP), HLP, RHCP and LHCP. By switching between different linear and circular polarizations, the system is able to work under different link conditions such as known or unknown orientation of the antennas and/or in line-of-sight (LOS) or non-line-of-sight (NLOS) cases. The advantage of the second design compared to the first design is that because there are two elements, it is possible to have more than one type of polarization at the same time. This feature might be of special interest for applications where polarization diversity is desired to improve the channel capacity [219] or where full duplex simultaneous transmission and reception is desired [220]. The surface impedance of the graphene corners in both designs are controlled by applying DC voltage bias through DC vias lines. A similar bias circuit as in Chapter 4, see Fig. 6.5 in Chapter 4, could be implemented here. As in Chapter 4, this bias circuit is not simulated here due to the extremely small dimensions of the bias structure (in the order of nanometres). Note that in scenario 2, antenna 1 and antenna 2 are fed with different ports, port 1 and port 2. Therefore, the antennas do not produce an array factor gain because the two antennas are not fed simultaneously with the same signal. It might be possible to work as an antenna array in the cases where both antennas produce the same polarization by actively connecting both ports together, and thus acting as a single port. However, that would disable the polarization diversity necessary for MIMO systems. In any case, scenario 2 can provide both methods of operation if required.

5.2.1 ELECTRIC FIELD EFFECT CONFIGURATION

Table 5.1 summarizes the selected values for the electric field effect structure that could be used to switch between different surface impedances of graphene. The hexagonal Boron Nitride (hBN) material is chosen again as the dielectric layer in Fig. 6.5 with ϵ_r^d=4 [189]. In addition, the same thickness, d=10 nm, for the hBN layer is selected to obtain reasonable values of DC voltage bias V_b. However, in this chapter, the switching time can be relaxed because fast switching is not

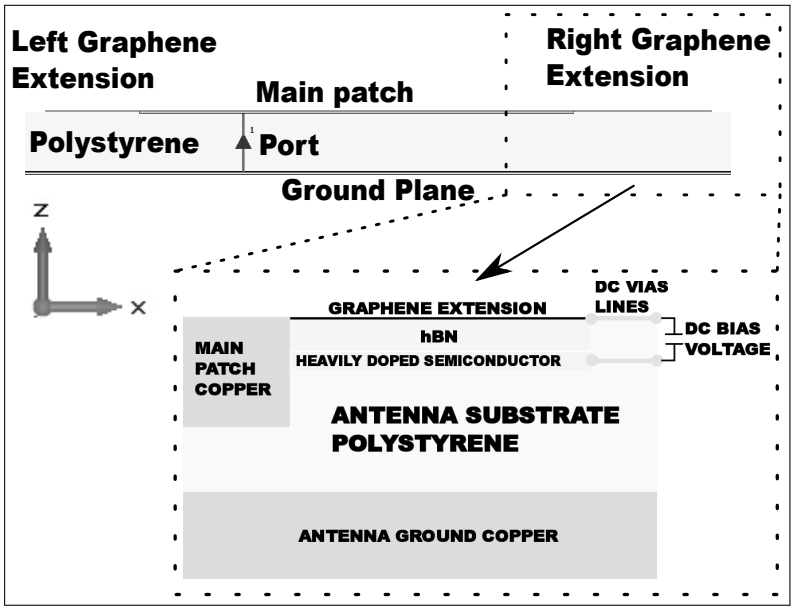

Figure 5.2: Graphical representation of zoomed view of the tuning structure (x-z plane).

required for the applications considered here. Therefore, a switching time of 1 second is selected.

Table 5.1: Selected general parameters

τ_{RC} [s]	0.625
Switching time [s]	1
d [nm]	10
ϵ_r^d for hBN	4

5.2.2 SIMULATED Zs_{ON} AND Zs_{OFF} VALUES

Following the same procedure as in Chapter 4, the values of sheet resistances used here for the ON and OFF states (Rs_{ON} and Rs_{OFF} respectively) in Table 5.2 are obtained from equation (5.1).

$$Zs \approx \frac{j\pi\hbar^2(2\pi f(\tau_L\tau_S) - j(\tau_L + \tau_S))}{q^2(\tau_L\tau_S)[\mu_c + 2k_BT\ln(e^{-\frac{\mu_c}{k_BT}} + 1)]}, \tag{5.1}$$

As can be seen, the values are exactly the same as the values found in the table for sets 1 and 2 in Table 4.2 Chapter 4. These values are selected again for this chapter because they represent a practical case. In addition, for all the scenarios evaluated in Section 5.3 the antenna substrate selected is Polystyrene (PS) with a relative permittivity ϵ_r=2.4 and tangent loss tanδ=0.0002 [123]. The antenna substrate thickness (H) is set to 5 mm as the space available for most wireless devices is very limited. In the next section, the proposed antenna designs are simulated and analysed.

Table 5.2: Selected surface impedance Zs values

Set	1		2	
State	ON	OFF	ON	OFF
n [m^{-2}]	5·10^{17}	6·10^{14}	5·10^{17}	6·10^{14}
V_b [V]	22.72	∼0	22.72	∼0
μ_L [m^2/Vs]	2.7		2.7	
D [eV]	4		18	
T [K]	295		295	
Zs_{ON} [Ω/□]	6+j0.3	2580+j6	34+j0.3	2580+j6

5.3 RESULTS

The results presented in this section are divided into scenario 1 and scenario 2. Scenario 1 discusses the results obtained from the simulations of the single polarization reconfigurable square patch antenna with graphene extensions in the corners. Scenario 2 discusses the simulation results of the two element array polarization reconfigurable antenna with graphene extensions in the corners. The

antennas have been designed in order to obtain the required polarization for each application (i.e. HLP, VLP, RHCP or LHCP). The axial ratio (AR) is used here as the main indicator that the proper polarization is achieved. The AR is obtained as (5.2) [34]

$$AR = \frac{Ex}{Ey} \text{ or } \frac{Ey}{Ex}, \tag{5.2}$$

where Ex and Ey are the electric field components on the x- and y- axis respectively. Ideally, the AR needed for an antenna to radiate with a circular polarization (CP) is AR=0 dB as this corresponds to the two components of the electric field (Ex and Ey) being equal. However, an AR within 3 dB of this value is still accepted as CP [36]. In contrast, linear polarization is achieved when the AR is as high as possible since it means that the electric field is being propagated only on one of the axes.

The results here are obtained from the transient solver (time domain solver) in the CST Microwave Studio 2015. The graphene sheets have been defined as infinitesimally thin solid sheets and simulated as ohmic sheet surface impedances. The excitation is a discrete port with 50 Ω port impedance. The efficiencies calculated from CST follow equation (5.3);

$$\eta_t = \left(\frac{P_{rad}}{P_{sim}}\right) \times 100 \tag{5.3}$$

where η_t is the total antenna efficiency (%), P_{rad} is the power being radiated by the antenna (W) and P_{sim}=0.5 W is the power generated by the excitation signal.

5.3.1 SCENARIO 1: DAB-GNSS SOLUTION

The following scenario considers a single polarization reconfigurable antenna to cover Digital Audio Broadcasting (DAB) at 1.45-1.5 GHz and a global navigation satellite systems (GNSS) such as Galileo and GPS, at 1.55-1.6 GHz, Fig. 5.1a.

Activating or deactivating certain pairs of the graphene corners allows one to switch between different polarizations. Linear polarization is achieved when all the extensions are ON. Right-hand circular polarization (RHCP) is set when only extensions 1 and 2 are OFF while left-hand circular polarization (LHCP) is produced when only extensions 3 and 4 are OFF. The surface impedance values for the ON and OFF states, Zs_{ON} and Zs_{OFF} respectively, are selected from the set 2 in Table 5.2. See Table 5.3 for the antenna dimensions. Note that the four graphene corners have the same dimensions. The conductor used for the ground plane and the top patch is copper.

Table 5.3: Set up parameters for scenario 1, see Fig. 5.1a

L [mm]	W [mm]	A [mm]	B [mm]	X [mm]	Y [mm]
52	47	14	14	7	23.5

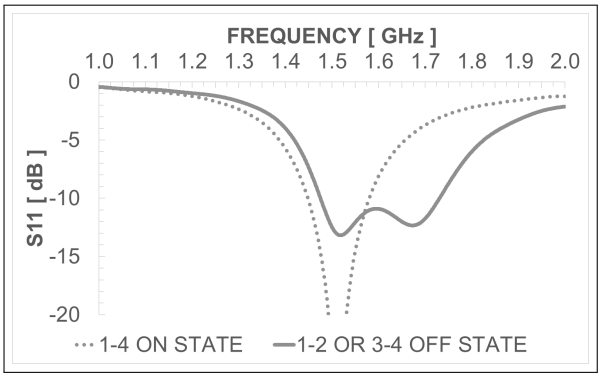

Figure 5.3: Reflection coefficient for scenario 1 with graphene corners 1-4 activated (dotted line) and with the graphene corners 1-2 or 3-4 deactivated (solid line) .

Fig. 5.3 provides the values of the reflection coefficient for scenario 1. As observed, when all the graphene corners are activated, the obtained values for the S11 parameter are S11$\leq$-10 dB for the frequencies of interest, between 1.45 GHz and 1.5 GHz, and hence, the antenna is suitable for DAB applications. On the other hand, when either the graphene corners 1 and 2 or 3 and 4 are deactivated, the resonant frequency moves slightly to higher frequencies to guarantee that

the return coefficient values are S11≤-10 dB for the frequencies used by GNSS operating at 1.55 GHz to 1.6 GHz.

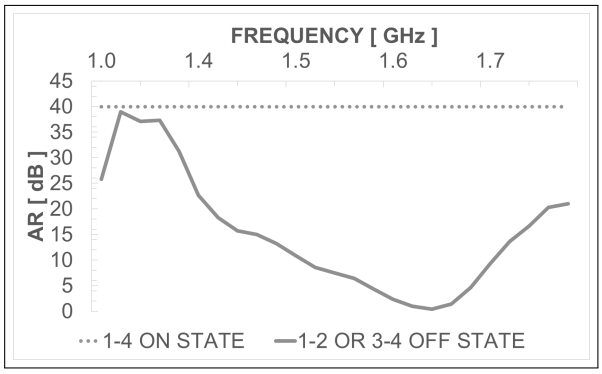

Figure 5.4: Axial ratio for scenario 1 with graphene corners 1-4 activated (dotted line) and with graphene corners 1-22 or 3-4 deactivated (solid line) .

Fig. 5.4 shows the axial ratio (AR) for scenario 1 when all the graphene corners are in the ON state and when either graphene corners 1 and 2 or 3 and 4 are in the OFF state. When all the graphene corners are activated, the resulting axial ratio is AR=40 dB. Here, the important point is not the number itself but that the axial ratio is very large. That is the condition necessary to accept that the antenna polarization is purely linear. On the other hand, when either pairs of graphene corners 1 and 2 or 3 and 4 are deactivated (while the others activated), the resulting axial ratio is kept as AR≤3 dB for the range of frequencies of interest, between 1.55 GHz and 1.6 GHz, thus the antenna polarization can be considered circular. These results confirm that the antenna polarization changes between linear polarization and circular polarization when activating and deactivating certain pairs of graphene corners.

The axial ratio figure is useful to provide information about the type of polarization but it does not provide information about whether the orientation of the polarization is HLP, VLP, RHCP, or LHCP. In order to demonstrate that activating and deactivating certain pairs of graphene corners will change the polarization of the antenna between HLP, RHCP and LHCP, Fig. 5.5, Fig. 5.6

and Fig. 5.7 show the surface currents for the antenna. In turn, they show the cases when all the graphene corners are activated, when 1 and 2 are deactivated while 3 and 4 are activated; and when 3 and 4 are deactivated while 1 and 2 are activated, respectively. Following the changes of direction of the surface current, it is also possible to follow the changes in the electric and magnetic field orientation. For instance, if the surface current flows from the left side to the right side of the patch it means that the voltage on the left side is larger than the voltage on the right side (i.e. positive voltage in the left side and negative voltage in the right side). A positive voltage creates electric field lines driving from the ground plane to the top patch (from negative to positive Z-axis) while a negative voltage creates electric field lines that go from the top patch down to the ground plane (from positive to negative Z-axis). Likewise, these electric field lines are extended to the edges of the top patch in the x-y plane. These extended electric field lines go from the left side to the right side of the antenna. Afterwards, when the surface currents change orientation so do the electric field lines and hence the electric field lines now go from right to left. Consequently, showing how the surface currents propagate on the top patch, allows direct identification of the antenna polarization.

In Fig. 5.5, all the graphene corners are activated. The surface currents are represented for four different phase-times (0°, 90°, 180° and 270°) to show how current propagation evolves during a wave cycle. For all the phase-times, the surface currents propagate following the x-axis in a linear fashion. Having the surface currents propagating linearly means that the electric field lines are excited along the x-axis as well. The electric field is radiated along the positive values of the Z-axis.

In Fig. 5.6, the graphene corners 1 and 2 are OFF while the corners 3 and 4 are kept ON. The surface currents are also represented for four different phase-times (0°, 90°, 180° and 270°). In this case, it is observed that at phase=0°, most of the surface current propagates diagonally from the bottom left corner to the upper

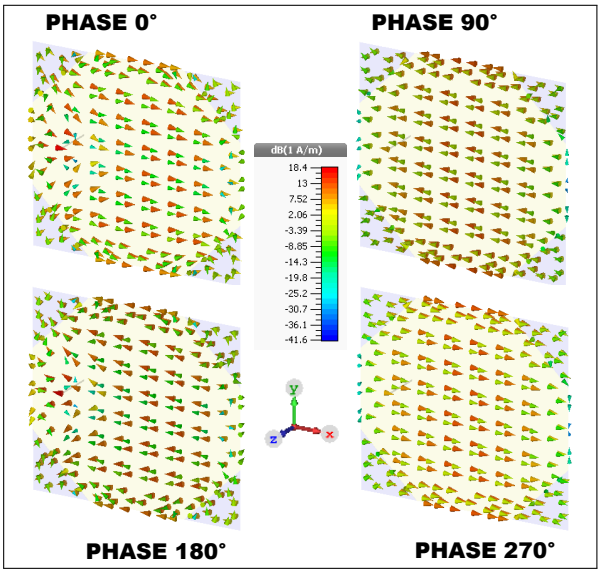

Figure 5.5: Surface current of the antenna when graphene corners 1-4 are activated for different current phases.

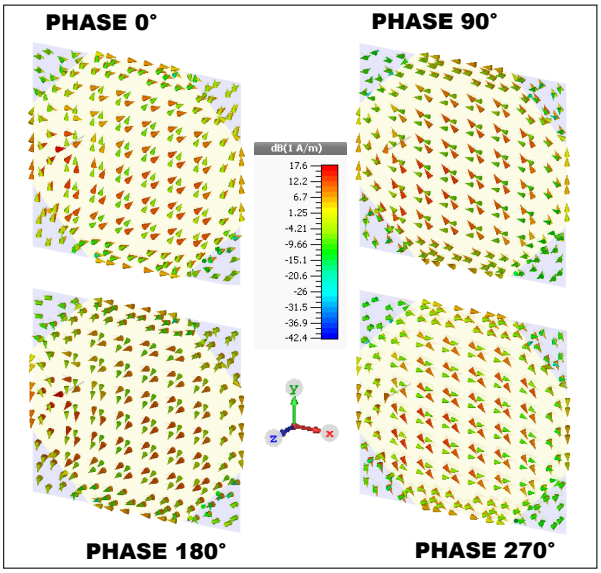

Figure 5.6: Surface current of the antenna when graphene corners 1-2 are deactivated for different current phases.

right corner. Afterwards, at phase=90°, the surface currents propagate diagonally from the bottom right corner to the upper left corner, then from the upper right corner to the bottom left corner (phase=180°) and finally from the upper left

corner to the bottom right corner. Consequently, it is observed that the surface currents follow an anti-clockwise rotation. This anti-clockwise rotation produces a right-handed circular polarization of the electric field along the x-y plane when radiating towards the positive values of the Z-axis.

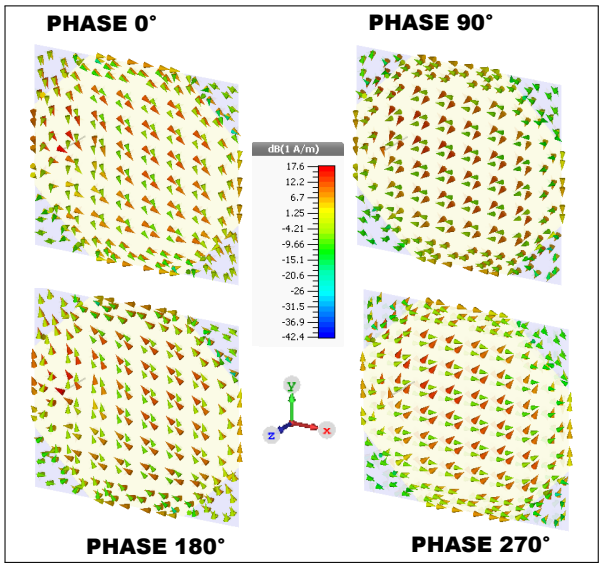

Figure 5.7: Surface current of the antenna when graphene corners 3-4 are deactivated for different current phases.

In Fig. 5.7, the graphene corners 3 and 4 are deactivated while the corners 1 and 2 are kept activated. In this case, the surface currents follow a clockwise rotation along the x-y plane. Consequently, the resulting electric field rotates with a left-handed circular polarization in the x-y plane and propagates along the Z-axis. From these figures it is shown that by switching ON and OFF certain graphene corners, the antenna design is able to cover the required linear polarization for the DAB applications and choose between right-handed or left-handed circular polarizations for the GNSS applications.

Figs. 5.8, 5.9 and 5.10 show the x-z and y-z planes of the radiation patterns for the antenna at different polarizations. As observed in Fig. 5.8, the radiation patterns for the linear polarization are similar to the radiation patterns commonly found in rectangular microstrip patch antennas, and hence, the addition of the

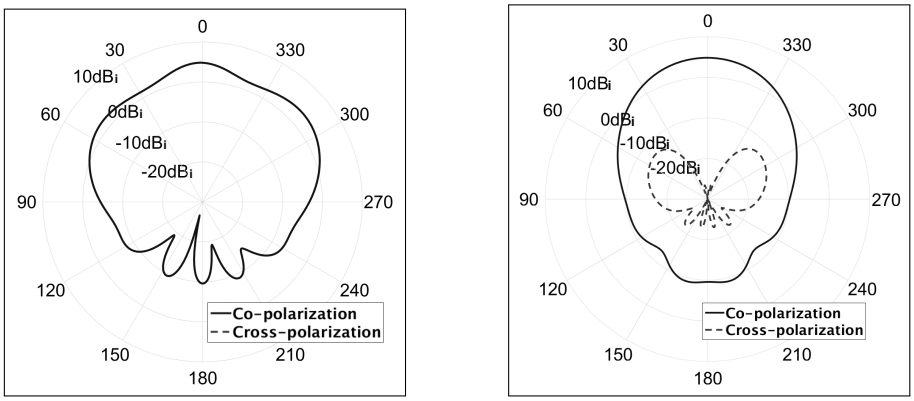

Figure 5.8: Radiation patterns for the antenna when graphene corners 1-4 are activated for a) x-z plane and b) y-z plane.

graphene corners does not seem to affect the radiation patterns of the antenna when operating with linear polarization. In Fig. 5.9 and Fig. 5.10, the radiation patterns shown are for when the graphene corners 1 and 2 are deactivated (RHCP) and when the graphene corners 3 and 4 are deactivated (LHCP) respectively. All four radiation patterns are very similar to each other and to a common rectangular microstrip patch antenna radiation patterns. Therefore, the activation and deactivation of the graphene corners does not significantly change the radiation patterns of the proposed antenna operating circular polarizations. The antenna gains are 4.8 dB, 5.5 dB and 5.5 dB for the HLP, the RHCP and the LHCP cases respectively. Interestingly, the cross-polarization discrimination (XPD), which is the difference in the magnitude between the co-polar (desired polarization) and cross-polar (undesired polarization), is -109 dB and -31.8 dB for the linear polarization and the circular polarizations at θ=0° respectively. The θ angle is found between the x-z and y-z axes, which means that the antenna is able to highly discriminate between desired and undesired polarizations. This feature is important when the target application needs a high purity polarized electromagnetic wave.

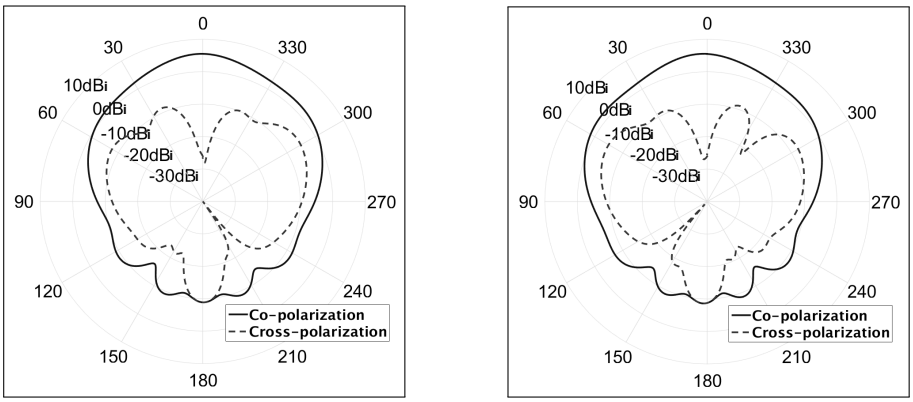

(a) **(b)**

Figure 5.9: Radiation patterns for the antenna when graphene corners 1 and 2 are deactivated for a) x-z plane and b) y-z plane.

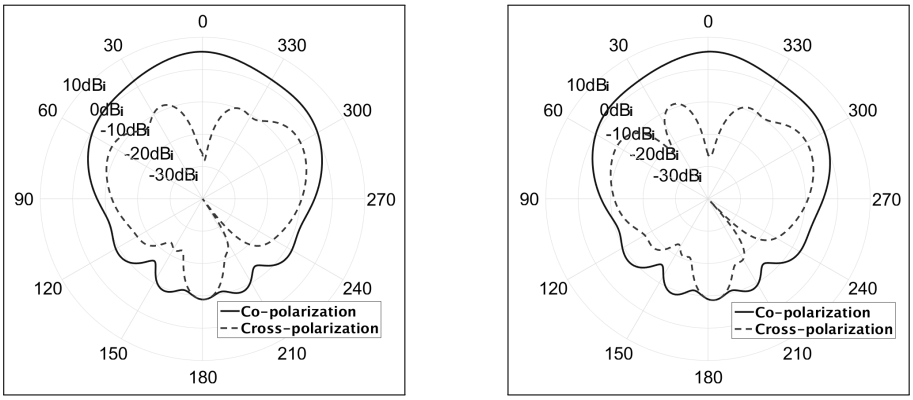

(a) **(b)**

Figure 5.10: Radiation patterns for the antenna when graphene corners 3 and 4 are deactivated for a) x-z plane and b) y-z plane.

The antenna efficiencies obtained from the simulations are 59.2%, 61.4% and 61.4% for the HLP, RHCP and LHCP respectively. These antenna efficiencies are reasonably good for polarization reconfigurable antennas because the losses suffered in graphene are low as small size graphene sheets are used in the corners compared to the total size of the top patch made of copper. The power lost in graphene represents the 36.4%, 30.4% and 30.4% of the simulated power for the

HLP, RHCP and LHCP cases respectively. Furthermore, the antenna efficiencies can be further increased if the surface impedance of the graphene sheets are changed from set 2 to set 1 in table 5.2. The set 1 values provide a lower surface impedance for the ON state Zs_{ON} which causes lower losses when current propagates on the graphene corners. The antenna presents very similar reflection coefficients, axial ratio values, surface currents and radiation patterns but the new resulting antenna efficiencies are now 78.5%, 74% and 74% for the HLP, RHCP and LHCP cases respectively. These antenna efficiencies are higher, around 10% to 20% more, than when set 2 is used, and closer to standard values of antenna efficiencies for non reconfigurable antennas.

DAB-GNSS TRANSPARENT ANTENNA

As in chapter 4, graphene can take advantage of its high transparency in the visible light regime to be implemented in transparent polarization reconfigurable antennas. Here, the conductor for the ground plane and top patch is now substituted by a hybrid transparent conductive film composed by mesoscale and nanoscale silver and copper nanowires (AgNW/Cu) as in Chapter 4. This conductive film provides 92% transparency in the visible light and a surface resistance of Rs=0.36 $\Omega/_{\square}$ [193]. The dimensions are kept the same as in Table 5.3. The selected ON and OFF state surface impedances are from set 2 in Table 5.2. The resulting reflection coefficients, axial ratio values, surface currents and radiation patterns are approximately the same as when copper is used. The main difference is the resulting values of the antenna efficiencies which are now 56.5%, 58% and 58%. Although the new antenna efficiencies are slightly lower than when copper is used, they are still reasonably good for polarization reconfigurable antennas. Therefore, graphene is a viable option to provide polarization reconfigurability in transparent antennas.

5.3.2 SCENARIO 2: KNOWN-UNKNOWN ANTENNA ORIENTATION AND LOS-NLOS LINK CONDITION SOLUTION

Here, the second scenario simulates a two element array based on the same design as in scenario 1, Section 5.3.1, to cover any wireless technology such as wireless fidelity (WIFI), radio frequency identification (RFID) or Bluetooth working at 2.4 GHz, Fig. 5.1b. As in scenario 1, activating and deactivating certain pairs of the graphene corners allows one to switch between different polarizations. When all graphene corners are ON, both antennas produce linear polarization but with opposite orientation as antenna 1 produces horizontal polarization (HLP) while antenna 2 radiates with vertical polarization (VLP). In this manner, both linear polarizations are covered by the system. When graphene corner pairs 1-2 and/or 7-8 are OFF, RHCP is achieved in antenna 1 and/or 2 respectively. In contrast, when graphene corner pairs 3-4 and/or 5-6 are OFF, LHCP is produced in antenna 1 and/or 2 respectively. This allows the system to cover both circular polarizations at the same time. Likewise, switching the corresponding graphene corner pairs, it is also possible to achieve the same circular polarization in both antennas at the same time. Therefore, with a two element array, the system is able to operate with up to two different polarizations HLP, VLP, RHCP and LHCP simultaneously. The surface impedance values for the ON and OFF states are taken from set 2 in Table 5.2. Copper is the conductor used for the ground and the top patch. See Table 5.3 for the antenna dimensions. Note that the four graphene corners of each antenna have the same dimensions. The distance D between the two antennas have been optimized to minimize the mutual coupling between the two antennas while keeping the array surface small. Moreover, due to the number of possible combinations of activating and deactivating graphene corners, and hence polarizations, and in order to not extend excessively the length of this chapter, many of the results for the reflection coefficients, axial ratio values,

surface currents and radiation patterns are not included because they are exactly the same or very similar to each other, and hence, only the most significant results for some of the combinations will be shown next.

Table 5.4: Set up parameters for scenario 2, see Fig. 5.1b

$L1$ [mm]	$W1$ [mm]	$L2$ [mm]	$W2$ [mm]	$A1$ [mm]	$B1$ [mm]	$A2$ [mm]
37.2	36.2	35.8	36.5	8	8	7.5
$B2$ [mm]	$X1$ [mm]	$Y1$ [mm]	$X2$ [mm]	$Y2$ [mm]	D [mm]	
7.5	5	18.1	17.9	7.5	37.2	

Fig. 5.11a and Fig. 5.11b present the reflection coefficients for port 1 in antenna 1 and port 2 in antenna 2 respectively. The results are for when antenna 1 and antenna 2 are operating in HLP and VLP respectively; and when both antennas are operating at LHCP. From Fig. 5.11a and Fig. 5.11b, it is observed that both antennas resonate at 2.4 GHz for the different polarizations, thus, the system is suitable for applications that use different polarizations at such frequency. The return coefficient values for both antennas, S11 and S22, are very similar. The small differences are due to the slightly different dimensions of the antennas and the position of the feeds, see Table 5.4. These differences are implemented to compensate the mutual coupling between antennas so that the desired return loss for both antennas and for all the polarizations is achieved.

An interesting analysis is to compare how the mutual coupling between the antennas is affected by selecting different polarizations at each antenna. For this reason, Fig. 5.12a and Fig. 5.12b give the isolation coefficient (S21) between port 1 and port 2 when selecting the same or different polarizations at both antennas at the same time. Fig. 5.12a shows the isolation coefficient for combinations where at least one of the antennas operates with a linear polarization. The best isolation value is found when both antennas work at a linear polarization. In this

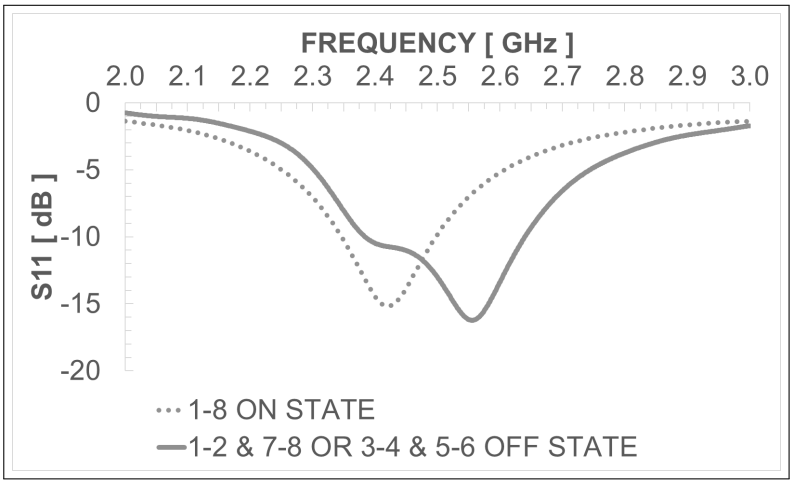

(a)

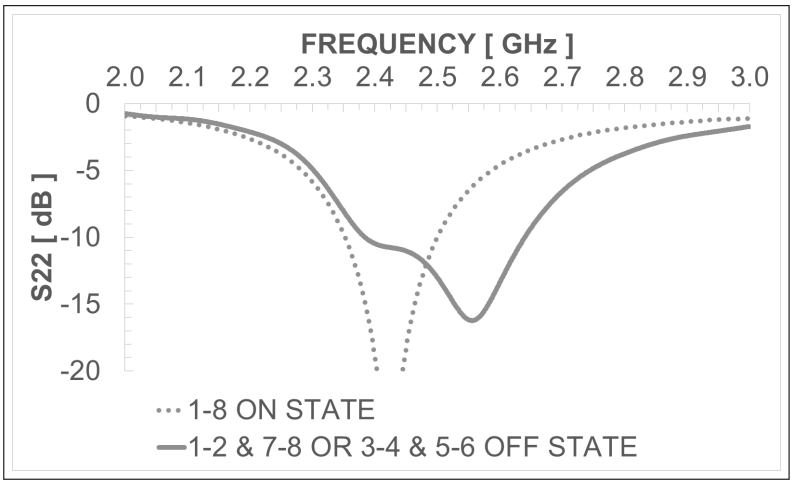

(b)

Figure 5.11: Reflection coefficients for scenario 2 with graphene corners 1-8 activated (dotted line) and with graphene corners 3-6 deactivated (solid line) in a) port 1 and b) port 2.

case, antenna 1 operates as HLP while antenna 2 operates as VLP. Because these polarizations are orthogonal, the induced currents of one antenna do not affect the other antenna very much. The other combinations, which include at least one circular polarization, provide poorer isolation values. The reason for that is that circular polarization is a combination of time varying weighted vertical and

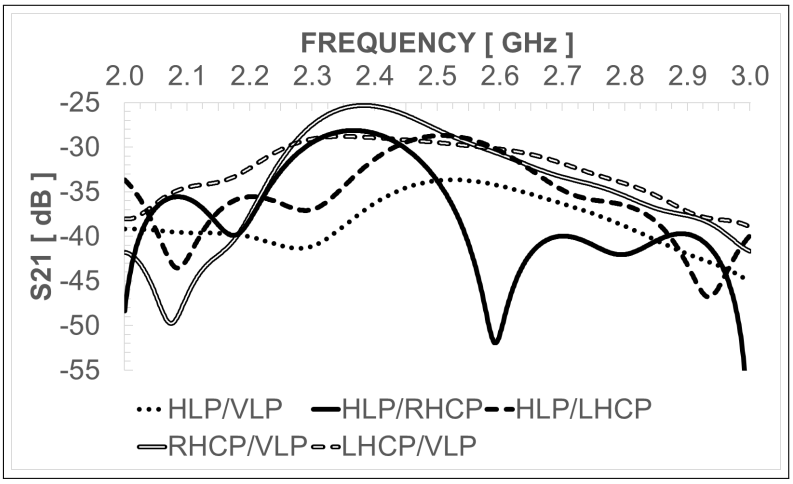

(a)

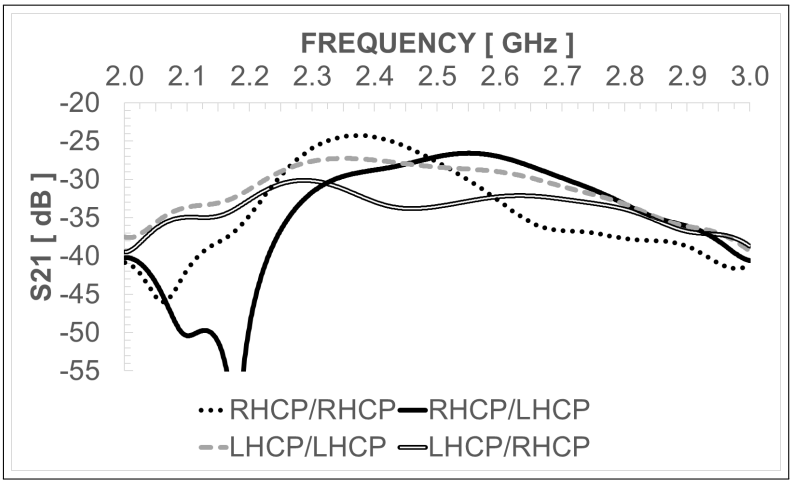

(b)

Figure 5.12: Isolation coefficient for scenario 2 when a) at least one of the antennas is linearly polarized and b) none of the antennas is linearly polarized.

linear polarizations. Consequently, an antenna operating in circular polarization can induce linearly polarized currents into the other antenna and vice versa.

Fig. 5.12b presents the isolation values obtained when both antennas operate with circular polarizations. Theoretically, when both antennas have the same circular polarization, either RHCP-RHCP or LHCP-LHCP, the isolation should be low because currents following the same orientation are induced in both antennas. On the other hand, when the antennas have orthogonal circular

polarizations, RHCP-LHCP or LHCP-RHCP, the isolation values should be high because the induced currents from one antenna cannot propagate well into the other antenna. As observed in Fig. 5.12b, the best isolation values are obtained for the case LHCP-RHCP and for RHCP-LHCP as expected, however, the RHCP-LHCP combination does not perform as well as the LHCP-RHCP combination. The reason for this discrepancy might be found in small details such as the feed point location and slightly different antenna dimensions. In antenna 1, the feed point is closer to the centre of the patch than in the second antenna. Also, antenna 1 is slightly longer but narrower than antenna 2. This causes the induced currents from one antenna to the other to not resonate well. These same differences between the two antennas also cause a reasonably good isolation between the two antennas when they have the same polarization, see LHCP-LHCP and RHCP-RHCP combinations in Fig. 5.12b. A good isolation might be desired for applications where polarization diversity is desired such as in MIMO systems and full duplex transmission and simultaneous reception or in antenna arrays. In those cases, the antennas should be designed to have slightly different dimensions and feed point location.

To further analyse how the different polarizations in one antenna affect the other, Figs. 5.13, 5.14, 5.15 and 5.16 present the surface current propagating on both antennas when antenna 1 is radiating. In the first case, Fig. 5.13 shows how the surface currents generated by port 1 propagate horizontally in antenna 1 and how induced currents in antenna 2 also propagate horizontally with a much smaller magnitude. Although the same surface currents propagate in both antennas, the induced currents on antenna 2 do not affect much the performance of antenna 2 because of the feed placement. The feed point of port 2 is located exactly in the middle of the longitudinal side of the antenna and any horizontally polarized current induced in antenna 2 finds a zero voltage distribution at that point. Therefore, these induced currents generate a negligible current in port 2

due to the extremely low voltage at that point. This is the reason for the good isolation values obtained in Fig. 5.12a for this combination.

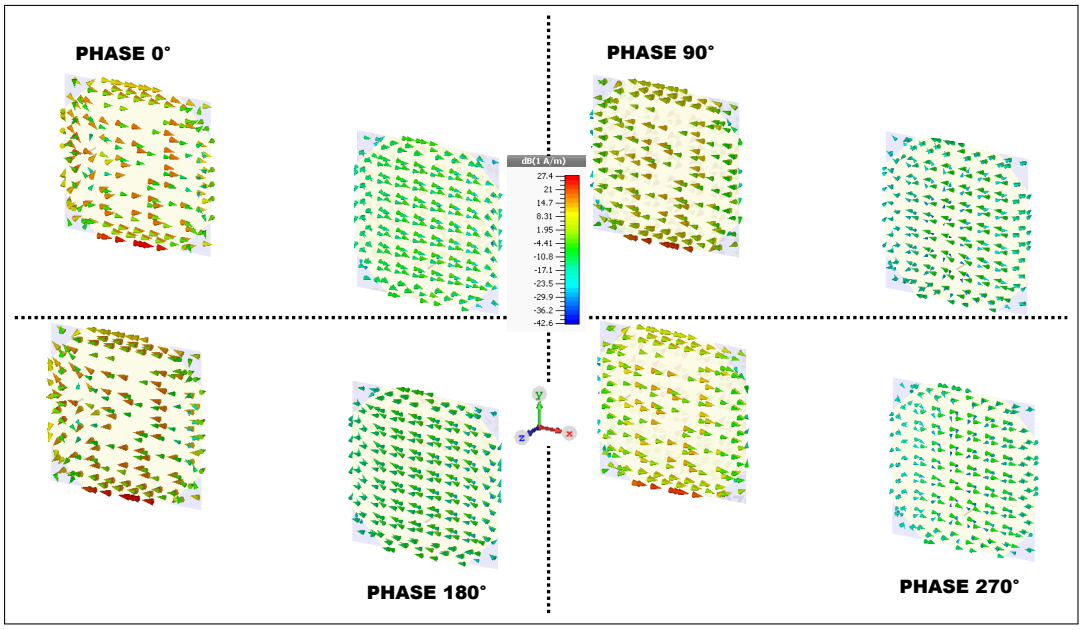

Figure 5.13: Surface currents on antenna 1 and antenna 2 when antenna 1 radiates and graphene corners 1-8 are activated for different current phases.

On the other hand, when antenna 1 produces a circular polarization (Fig. 5.15, 5.14 or Fig. 5.16), the induced surface currents in antenna 2 follow approximately the same distribution of the surface currents in antenna 1 generated by port 1. In this case, the voltage distribution in antenna 2 does not present a zero at the feed point of port 2 and some current is introduced in port 2 from the induced surface currents. This is the reason the isolation values found in circular polarizations are lower than when both antennas use a linear polarization, see Fig. 5.12a and Fig. 5.12b. The only case of circular polarization where the induced currents from antenna 1 do not generate currents in port 2 is when orthogonal polarizations are excited in both antennas, see Fig. 5.16, as they are out of phase.

Figs. 5.17 and 5.18 show the radiation patterns in antenna 1 when antenna 1 has HLP and antenna 2 VLP; and when antenna 1 has LHCP while antenna 2 has RHCP respectively. The resulting radiation pattern for all the combinations are

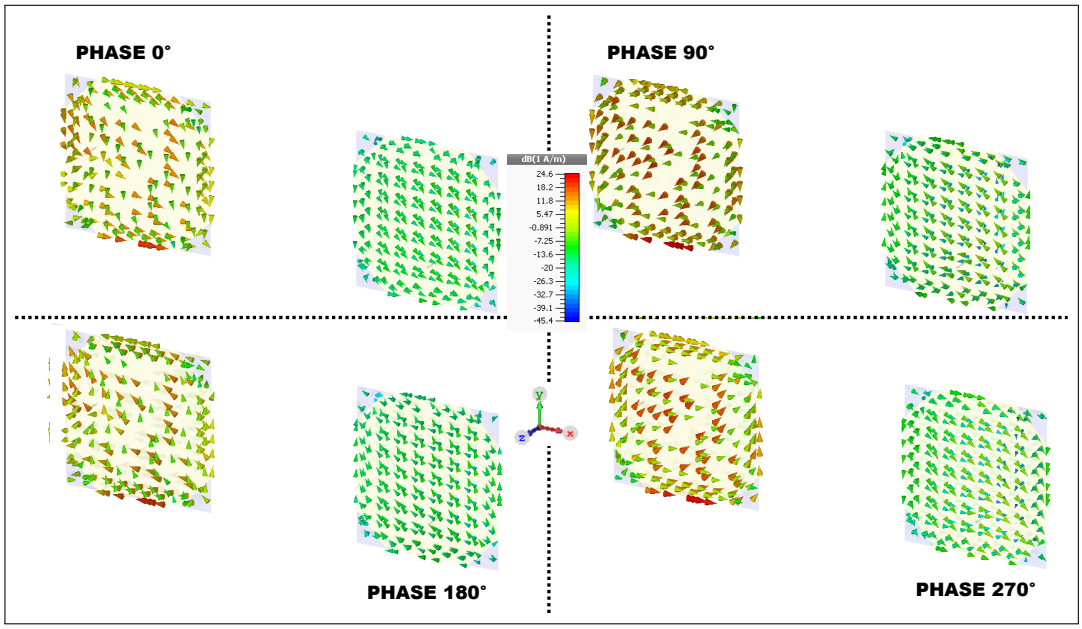

Figure 5.14: Surface currents on antenna 1 and antenna 2 when antenna 1 radiates and graphene corners 3-4 are deactivated for different current phases.

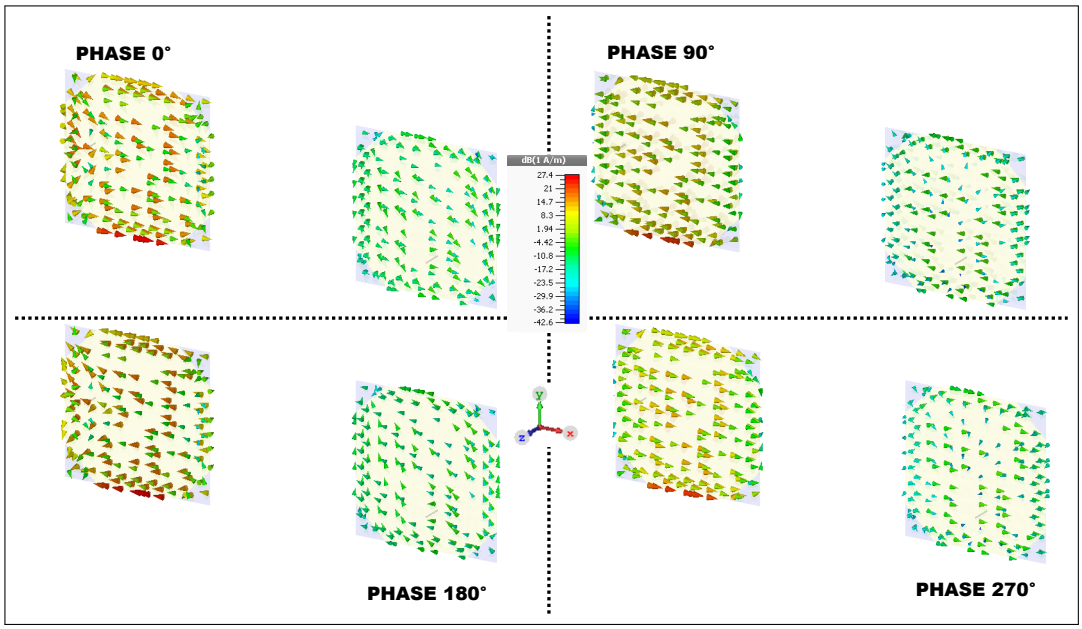

Figure 5.15: Surface currents on antenna 1 and antenna 2 when antenna 1 radiates and graphene corners 7-8 are deactivated for different current phases.

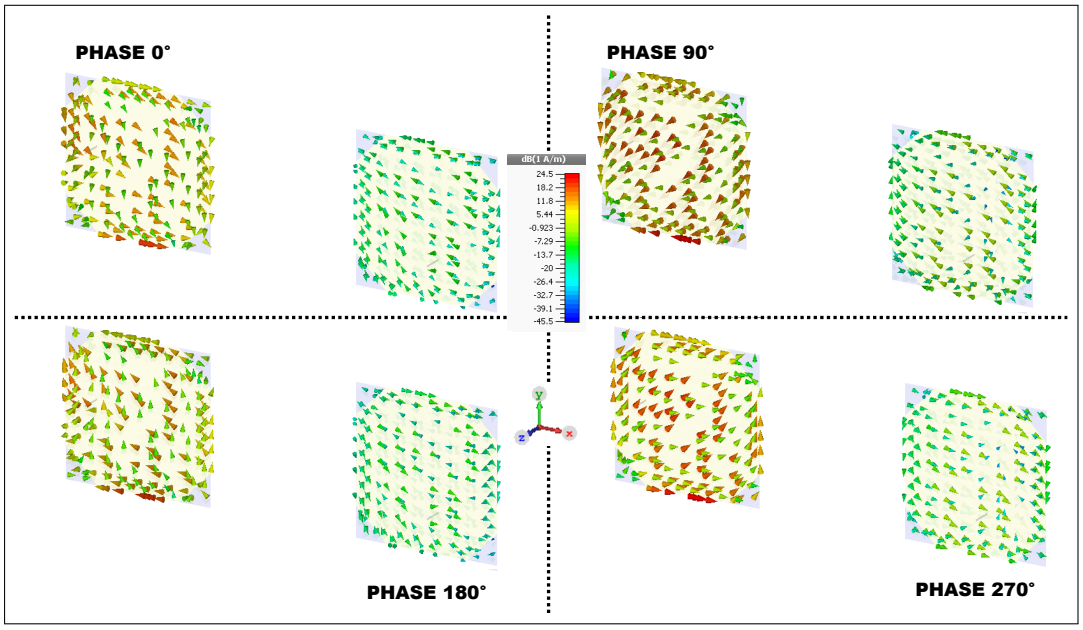

Figure 5.16: Surface currents on antenna 1 and antenna 2 when antenna 1 radiates and graphene corners 3-4 and 7-8 are deactivated for different current phases.

similar in shape to the radiation patterns found commonly in microstrip antennas. However, there is a slight tendency of the radiation pattern, specially the cross-polarized pattern in Fig. 5.18, to be oriented towards the side where the other antenna is. This is a side effect of the mutual coupling between elements in arrays. Nevertheless, the deviation suffered is not substantial. The simulated antenna gains are 6.3 dB and 6.2 dB for antenna 1 and 2 operating both with linear polarization respectively; and 5.2 dB and 5.7 dB for antenna 1 and antenna 2 operating with circular polarization respectively. The remaining antenna gains are around the same values. In addition, the obtained cross-polarization discrimination (XPD) when both antennas generate linear polarizations is high, between -35.3 dB, in a similar fashion to the results obtained for scenario 1. However, the XPD when both antennas radiate orthogonal circular polarizations is -10.5 dB which is a substantial reduction compared to the results in scenario 1. This is caused by the presence of the graphene corners when they are activated. Although the surface impedance of the ON state is low Zs_{ON}=34+j0.3 $\Omega/\square$,

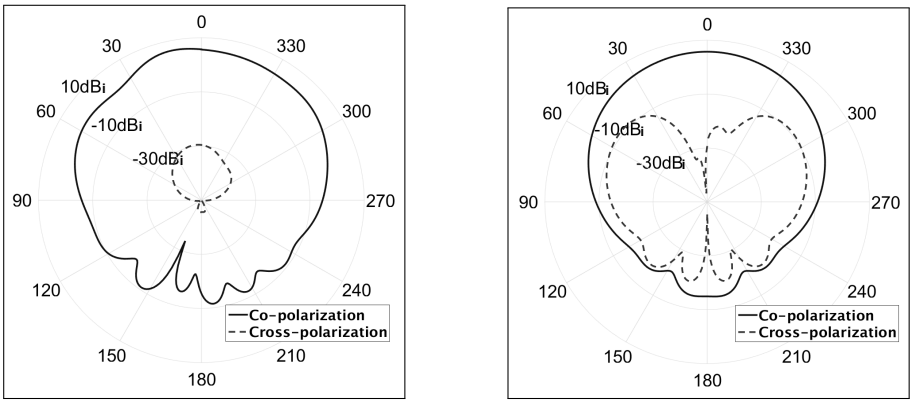

Figure 5.17: Radiation patterns for the antenna when graphene corners 1-8 are activated for a) x-z plane and b) y-z plane.

there are still some currents that do not propagate well on the activated graphene corners and hence are not purely polarized which affects the XPD. In order to increase the cross-polarization discrimination, lower values of surface impedance for the ON state should be applied. For instance, the same simulation is carried out but now with lower surface impedance for the ON state. This is done by selecting the values from set 1 in Table 5.2 for Zs_{ON} and Zs_{OFF}. The XPD obtained in this case is -11.8 dB, which is more than 1 dB of improvement. Thus, it is expected that if the surface impedance for the ON state is further reduced, the XPD should be further improved.

The antenna efficiencies obtained for the scenario 2 are 64.6% and 71.6% for antenna 1 and 2 operating with linear polarization respectively; and 59.3% and 65.3% for antenna 1 and 2 when operating circular polarization respectively. The antenna efficiencies obtained for the antennas when they radiate a circular polarization are slightly lower than for linear polarization. This is because with circular polarization operation, the S11 and S22 parameters are worse compared to linear polarization operation, see Fig. 5.11. Nevertheless, the variation of

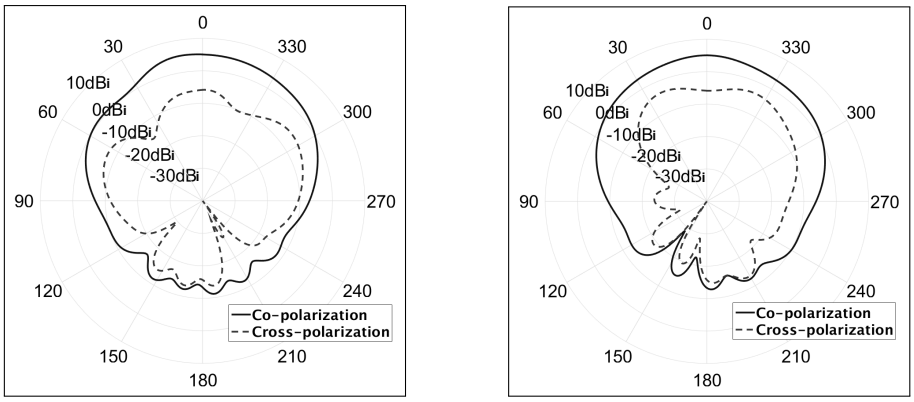

Figure 5.18: Radiation patterns for the antenna when graphene corners 3-6 are deactivated for a) x-z plane and b) y-z plane.

the antenna efficiency is not substantial and can be assumed that the antennas perform similarly with any polarization.

5.3.3 ANTENNA PERFORMANCE COMPARISON

The results obtained from scenario 1 are compared here to other planar polarization reconfigurable antennas found in the literature. In [204], a single-feed square patch antenna is able to switch between HLP, RHCP and LHCP by activating the corners with PIN-diodes. In [209], a single-feed square patch antenna with inserted slots in the ground (close to the corners of the top patch) is able to switch between linear polarization and both circular polarizations by integrating PIN-diodes in the slots. In [214], a two element planar monopole antenna is able to operate a linear polarization and both circular polarization by switching the phase difference of the feeding network with PIN-diodes. Table 5.5 summarizes the comparison.

As observed from Table 5.5, the proposed antenna in scenario 1 performs very similarly to other antennas found in the literature. The proposed antenna is able to switch between three different polarizations as with the other antennas found

Table 5.5: Comparison of different polarization antennas

Reference	Polarizations Covered	Antenna Gain	XPD
This work: scenario 1	LP and RH/LHCP	4.8 to 5.5 dB	-109 to -31 dB
[204]	LP and RH/LHCP	5.2 to 5.3 dB	-17 dB to No data
[209]	LP and RH/LHCP	5.8 to 6.4 dB	-30 to No data
[214]	LP and RH/LHCP	2.2 to 0.6 dB	-17 dB to -15 dB

in the literature. The obtained antenna gain values are very close to the antennas in references [204], [209] and even better than in reference [214]. In addition, the cross-polarization discrimination (XPD) values are also better than in the other references for all the polarizations. Note that, in references [204], [209], there is no data about the XPD values for circular polarizations.

5.3.4 SWITCHING POWER CONSUMPTION

Table 5.6 provides the peak power consumed (P_{peak}) for all the scenarios evaluated in this paper when switching from one polarization to another due to the change of required values of charge carrier density n. The total power shown is calculated by using equation (5.4), see Section 4.2.3 in Chapter 4 for a detailed analysis of the equation,

$$P_{peak} = p(0) = \frac{n^2 q^2 dA}{\epsilon_o \epsilon_r^d \tau_{RC}}. \tag{5.4}$$

where the dielectric thickness d, the relative permittivity ϵ_r^d and the time constant τ_{RC} are set using the values in Table 5.1. Specific values such as the charge carrier density n and the physical area of graphene A are extracted from Tables 5.2, 5.3 and 5.4. Note that, in the evaluated scenarios, there are four to eight graphene corners being fed and the total power consumed is the addition

of the power consumed by each individual corner as it switches between ON and OFF.

Table 5.6: P_{peak} values for scenario 1 and 2 designs

Scenario 1	n [m^{-2}]	A [mm^2]	P_{peak} [mW]
Zs_{ON}= 34+j0.3 [$\Omega/\square$]	$5{\cdot}10^{17}$	392	1.14
Zs_{ON}= 6+j0.3 [$\Omega/\square$]	$5{\cdot}10^{17}$	392	1.14
Scenario 2	**n [m^{-2}]**	**A [mm^2]**	**P_{peak} [mW]**
Zs_{ON}= 34+j0.3 [$\Omega/\square$]	$5{\cdot}10^{17}$	240.5	0.7

From Table 5.6 it is observed that the peak power consumption is reasonably small due to a slow switching time. Allowing a longer time for charging the graphene sheets causes less current because the flow of the charge carriers is lower than for a faster switching time. Again, for scenario 2, the peak power consumed is smaller than when larger areas are used (i.e. scenario 1).

5.4 CONCLUSIONS

This chapter has presented and analysed the use of graphene in polarization reconfigurable antennas for two application-oriented scenarios. Results from both scenarios demonstrate that:

- Antennas made partially of graphene can switch between the linear polarization required for DAB and the circular polarization required for a GNSS.
- A two element array can switch between any possible polarization at the same time to adapt to changing environments such us rich multipath channels (i.e. indoor), random orientation of the antennas or when the antennas operate in LOS or NLOS conditions.
- Very low power consumption is possible due to the implementation of small graphene sheets and slower switching times.

The antenna efficiency results showed that using graphene to switch between polarizations does not strongly affect the performance of the antenna since the area of graphene needed is much smaller than the total area of the antenna. This translates into graphene being a very promising method to provide polarization reconfigurable antennas that at the same time could be integrated in environments where transparency and/or flexibility is a requirement. Specially, graphene can be suitable for polarization reconfigurable antennas and arrays at millimetre wave frequencies where antenna sizes are small and they might be integrated in structures such as windows, cars, solar panels, product labels, etc. In addition, improving the sheet resistance of the ON state from Rs_{ON}=34+j0.3 $\Omega/_{\square}$ to Rs_{ON}=6+j0.3 $\Omega/_{\square}$ slightly increased the antenna efficiency by about 10% to 20%. Consequently, these antenna designs do not require very low sheet resistance to work efficiently.

In the next chapter, Chapter 6, the idea of making a reconfigurable antenna as a combination of a conventional metal (i.e. copper) and graphene is also applied to ZOR antennas for frequency reconfigurability to cover two LTE bands.

Chapter 6

HYBRID METAL-GRAPHENE FREQUENCY RECONFIGURABLE ZOR ANTENNAS

This chapter studies, analyses and discusses the performance, limitations and trade-offs of implementing graphene in planar frequency metamaterial reconfigurable antennas for mobile applications. In order to demonstrate the concept, two electrically small zero order resonant (ZOR) antenna designs are proposed and simulated where graphene provides frequency reconfigurability to cover two LTE bands. The investigation in this chapter includes the analysis and study of the two proposed unit cells that form the proposed ZOR antennas as these unit cells can be applied not only to antennas but to other electromagnetic applications such as filters, transmission lines, lenses, etc. In addition, a performance comparison with other state-of-the-art ZOR antennas is provided in this chapter.

6.1 INTRODUCTION

Traditionally, the resonance of an antenna has a direct dependence on the dimensions of the antenna itself where the lower the operating frequency, the larger the size of the antenna dimensions. This forces the designers of mobile devices to reserve enough space to accommodate the required number of antennas in wireless and mobile devices. Alternatively, it is possible to reduce the size of the antenna. However, this reduces the antenna performance and narrows the operational bandwidth. In order to overcome such constraints, frequency reconfigurable metamaterial antennas might be a potential solution for future wireless devices.

Metamaterials (MTM) can be used in the antenna field as additional elements to improve the antenna performance such as MTM loads and metasurfaces; or as electromagnetic resonators themselves such as the composite right/left-handed transmission line (CRLH TL) based antennas [221]. For instance, metamaterial loadings as the epsilon-negative (ENG) [222]–[225], the mu-negative (MNG) [226]–[229] and the double negative (DNG) [230]–[233] have been integrated in electrically small antennas (ESAs) to compensate downgraded antenna performance due to the size reduction. Metasurfaces like the artificial magnetic conductors (AMC), the electromagnetic band gap (EBG) and the reactive impedance surface (RIS) structures have been studied and implemented in [234]–[240] to reduce surface wave propagation, provide zero reflection phase and shrink antenna size while maintaining or improving the antenna performance.

The CRLH TL based antenna is a metamaterial transmission line characterised by presenting simultaneous left-hand (L_L and C_L) and right-hand (L_R and C_R) inductive and capacitive components that support negative (-1^{st}, -2^{nd}, ...), zeroth (0^{th}) and positive (1^{st}, 2^{nd}, ...) order resonant modes [30]. The metamaterial leaky wave (MTM LW) antenna is an interesting application of the CRLH TL antenna because it provides radiation pattern scanning as well as miniaturization [241]–[245]. However, the interest in this chapter is on the zeroth order (0^{th})

resonance of the CRLH TL antenna, also called zeroth order resonant (ZOR) antenna. The most valuable characteristic of the ZOR antennas is that they are size independent and hence can substantially save space in wireless and mobile devices without suffering degradation in the antenna performance due to size reduction. For example, in [246]–[253], ZOR structures are formed by using printed planar equivalent capacitance and inductance components such as interdigital capacitors, meanderlines, parallel plates, stubs, etc; while in [254]–[258] mushroom-like structures are used as unit cells. In contrast, in [259], [260] chip capacitors and inductors are implemented to achieve ZOR antennas. Additionally, ZOR antennas can be made reconfigurable if their inductive and capacitive components can be actively tuned. Frequency reconfigurable ZOR antennas have been achieved by using varactors [261]–[263], PIN diodes [264]–[266] and MEMS implementations [267]. In a similar manner, the variable surface impedance of graphene is utilized here as a tunable material to create frequency reconfigurable ZOR antennas by actively changing the capacitive and inductive behaviour of ZOR antennas. To the best of the author's knowledge, there are no reports in the literature of frequency reconfigurable metamaterial antennas made fully or partially of graphene for any range of frequencies (i.e. microwave to THz frequencies).

The novel contributions of this chapter can be summarized as follows:

- Investigate the use of the variable surface impedance of graphene to tune the capacitive and inductive components of ZOR antennas in the microwave regime.

- Analyse and simulate two possible hybrid metal-graphene frequency reconfigurable ZOR antenna designs to cover LTE (1.8 GHz and 2.1 GHz) frequency bands.

- Provide design trade-offs between graphene sheet dimensions, reconfigura-

bility, antenna efficiency and power consumption in hybrid metal-graphene frequency reconfigurable ZOR antennas.

The chapter is structured as follows, Section 6.2 will define the proposed unit cells and antenna designs followed by the simulation results in Section 6.3, while Section 6.4 will close the chapter with some conclusions.

6.2 PROPOSED ANTENNA DESIGNS

As discussed in Section 2.5.1 in Chapter 2, the composite right/left-handed transmission line (CRLH TL) is a metamaterial transmission line that supports negative, positive and zeroth order resonances as its refractive index can be negative or positive depending on the operational frequency. In this chapter, it is of interest to operate with the zeroth order resonance of the CRLH TL to create antennas.

When solving equations (6.1) and (6.2) for n_m=0 (zeroth order), see equations (2.104) and (4.8) in Chapter 2 for a detailed explanation,

$$\beta(\omega) = \frac{1}{p}\cos^{-1}\left(1 - \frac{1}{2}\left(Z_{series}Y_{shunt}\right)\right) = \frac{1}{p}\cos^{-1}\left(1 - \frac{1}{2}\left(\frac{\omega_L^2}{\omega^2} + \frac{\omega^2}{\omega_R^2} - \frac{\omega_L^2}{\omega_{se}^2} - \frac{\omega_L^2}{\omega_{sh}^2}\right)\right), \quad (6.1)$$

$$\beta_n(\omega) = \frac{n_m\pi}{l} = \frac{n_m\pi}{Np} \qquad \text{for } n_m\text{=}0,\pm1,\pm2,...,(N\text{-}1); \quad (6.2)$$

there are two possible solutions that fulfil the condition, or in other words, there are two possible values for the zeroth order resonant frequency. In such a case, the zeroth order resonant frequency is calculated from equation (6.3) by either the series resonant frequency ω_{se} if the structure is left short-ended, or the shunt resonant frequency ω_{sh} if left open-ended. Importantly, when n=0, the zeroth order resonant frequency becomes independent of the physical length of

the antenna and it is only determined by the values of C_L and L_R in the case of the short-ended case or C_R and L_L in the case of the open-ended case.

$$\omega_{se} = \frac{1}{\sqrt{C_L L_R}}, \quad \omega_{sh} = \frac{1}{\sqrt{C_R L_L}}, \tag{6.3}$$

Although the ZOR antenna centre frequency is independent of the size of the structure, in practice, it is limited by the space p, see equations (2.104) and (4.8), required by the components C_R, C_L, L_R and L_L. These capacitances and inductances can be implemented by using surface mounted technology (SMT) chip components or distributed components [30], such as microstrip interdigital capacitors, parallel plate capacitors, meander lines, among others. In this chapter, the variable surface impedance of graphene is proposed as a method to actively change the capacitive C_R and inductive L_L behaviour of open-ended ZOR antennas and hence change their resonant frequency.

The two proposed ZOR antennas are constructed from two unit cells:

- Two patches separated by a gap and connected to ground via a meanderline and a cylindrical vias where graphene is placed under the meanderline, Fig. 6.1.
- Two patches separated by a gap where a graphene sheet is placed next to the second patch and connected to ground via a meanderline and a cylindrical vias, Fig. 6.2.

The proposed unit cells are based on microstrip distributed capacitances and inductances where two microstrip patches are separated by a gap and followed by a meander line connected to ground via a cylindrical solid bias. The values C_{pat1}, C_{pat2}, L_{pat1} and L_{pat2} are the capacitances generated between the two top patches and the ground plane, and the inductances present in the two top patches, respectively. Additionally, R_{pat1} and R_{pat2} are the losses in the conductors forming the top patches. C_{gap}, C_{dis1} and C_{dis2} are the capacitances generated by the

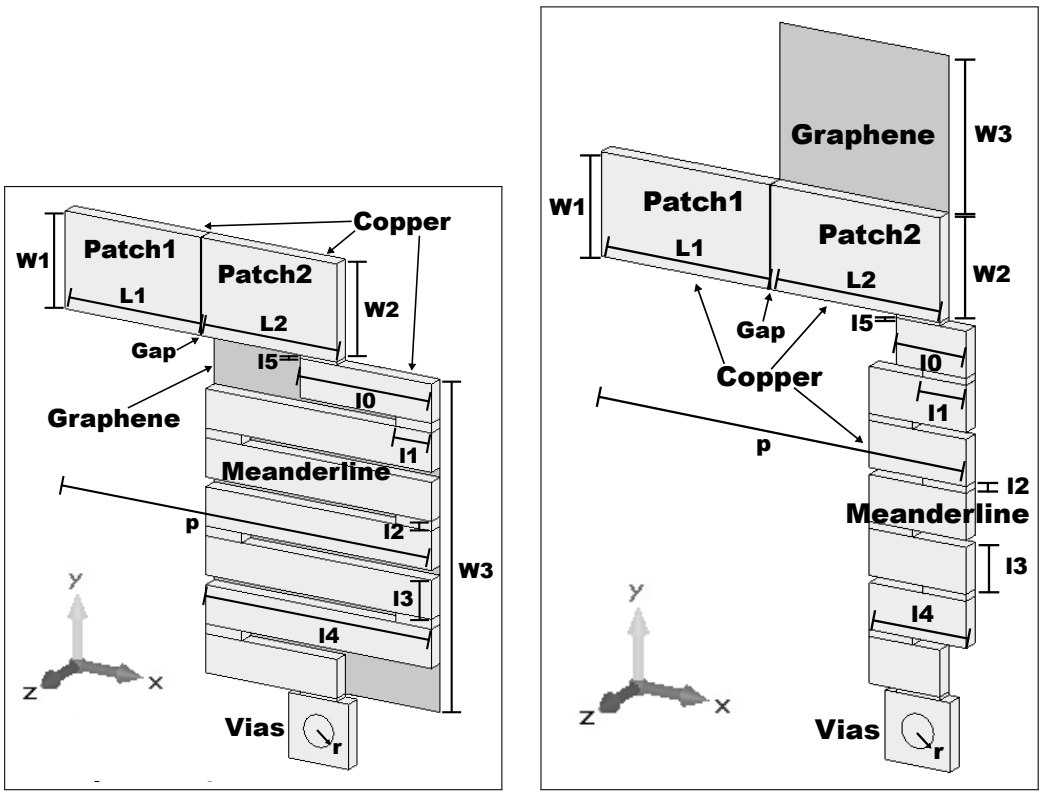

Figure 6.1: The two proposed unit cell designs, a) Unit cell 1: graphene laid under the meander line, b) Unit cell 2: graphene laid next to patch 2.

discontinuity (or separation) between the two top patches. L_{mea}, C_{mea} and R_{mea} are the inductance, capacitance and resistance of the meander line. L_{vias} is the inductance of the solid vias, where the resistance of the bias is assumed to be negligible. Finally, the G_{sub} is the conductance of the substrate. In the first unit cell design, Fig. 6.1a, a graphene sheet is laid under the meander line, while in the second design, Fig. 6.1b, a graphene sheet is laid next to one of the microstrip patches. The two unit cells achieve tunable C_R and L_L values by changing the surface impedance Zs of graphene which causes the inductive behaviour of the meander line in Fig. 6.2a and the capacitive behaviour in Fig. 6.2b to change. However, the variation of the surface impedance of the graphene sheets also affects the capacitive C_{mea} and resistive R_{mea} contributions

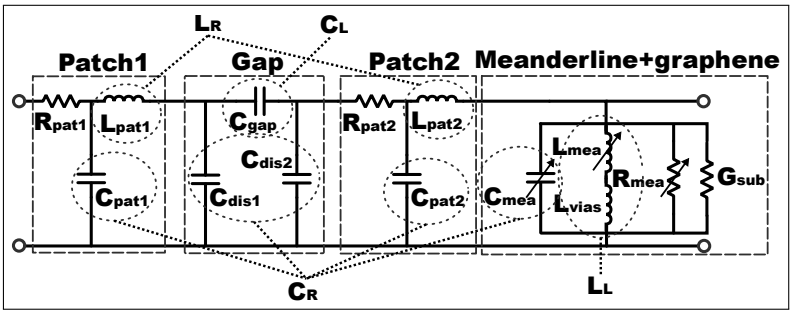

(a)

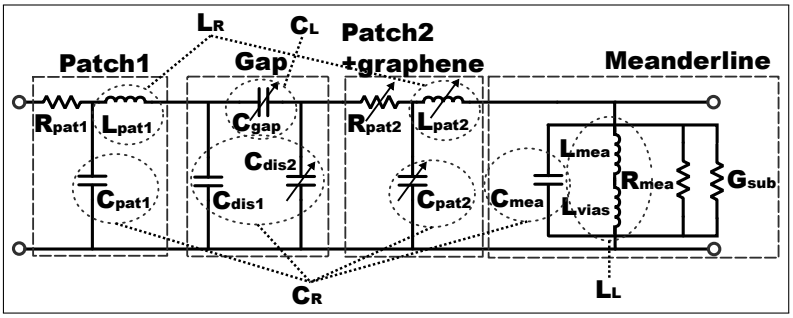

(b)

Figure 6.2: Equivalent electrical circuit of the two proposed unit cell designs, a) Unit cell 1: graphene laid under the meander line, b) Unit cell 2: graphene laid next to patch 2.

of the meander line, the inductive L_{pat2} and resistive R_{pat2} contributions of the parallel plate, and the capacitances C_{gap} and C_{dis2} of the gap between the patches. Consequently, the theoretical variable ZOR resonant frequency f_{ZOR} (Hz) for the unit cells is calculated as

$$f_{ZOR} = \frac{\omega_{sh}}{2\pi} = \frac{1}{2\pi\sqrt{C_R L_L}}, \tag{6.4}$$

where, by extracting the equivalent Π and T networks via S parameters analysis as in [30], the right-hand capacitance and the left-hand inductance might be approximated as

$$C_R \approx C_{pat1} + C_{pat2} + C_{dis1} + C_{dis2} + C_{mea}, \tag{6.5}$$

and

$$L_L \approx L_{mea} + L_{vias}. \tag{6.6}$$

The two proposed ZOR antenna designs are shown in Fig. 6.3 and Fig. 6.4. They are composed of 3 unit cells (N=3) each. Antenna design 1 is formed by the unit cell 1 with graphene laid under the meander line, and antenna design 2 is formed by the unit cell 2 with graphene laid next to the patch 2. Additionally in Fig. 6.5, there is a proposed method to bias the graphene sheets in the proposed antennas. Note that the field-effect structure shown in Fig. 6.5 is not simulated here as the thickness of the hBN and doped semiconductor layers are extremely small (in the order of nanometres). Note that, the antennas are fed by proximity coupling to a microstrip section to reduce the inherent high input impedances of the ZOR antennas for a wide range of frequencies. This generates additional series, $C_{feed,gap}$, and parallel, $C_{feed,dis1}$ and $C_{feed,dis2}$, capacitances between the feed antennas. Particularly important are the additional $C_{feed,dis1}$ and $C_{feed,dis2}$ capacitances as they slightly modify the ZOR resonant frequency f_{ZOR} when added into equation (6.5).

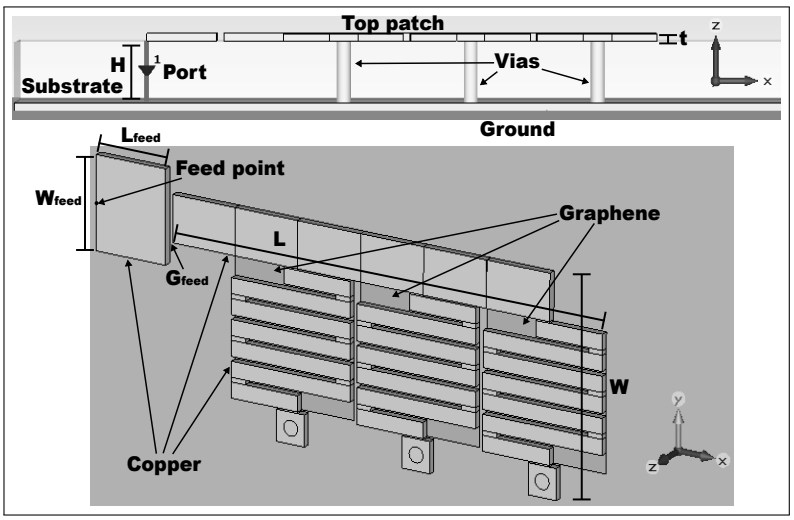

Figure 6.3: Frequency reconfigurable ZOR antenna Design 1: plan and 3D views of graphene laid under the meander line.

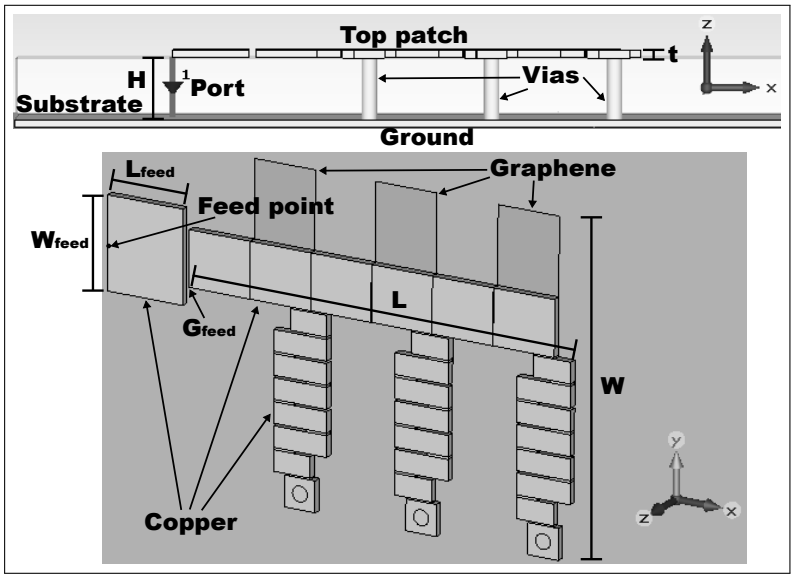

Figure 6.4: Frequency reconfigurable ZOR antenna Design 2: plan and 3D views of graphene laid next to patch 2.

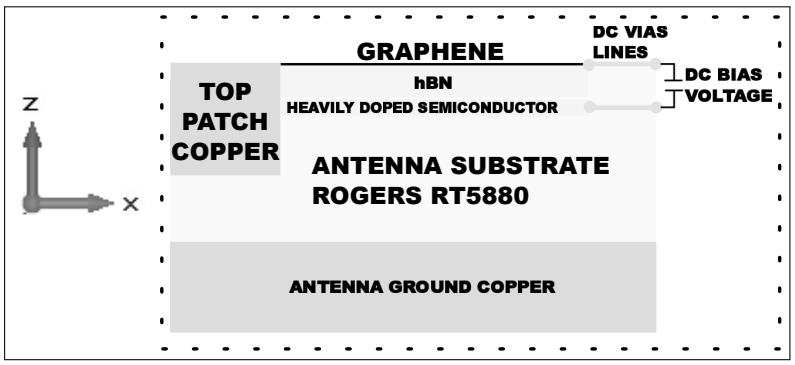

Figure 6.5: An example of a possible bias structure

6.2.1 ELECTRIC FIELD EFFECT CONFIGURATION

As in Chapters 4 and 5, the surface impedance of the graphene sheets integrated in the unit cells, see Fig. 6.1, and hence in the proposed antennas, see Fig. 6.3 and Fig. 6.4, can be tuned by a field-effect structure as in Fig. 6.5. For the dielectric layer, the hexagonal Boron Nitride (hBN) material is chosen again with ϵ_r^d=4 [189] due to the good performance provided by graphene when placed on top of hBN. In addition, the same thickness, d=10 nm, for the hBN layer is

selected to obtain reasonable values of DC voltage bias V_b. As in chapter 4, the switching time is selected again to be fast because switching between different frequency bands must be faster than LTE handover times (60 ms) [188]. Table 6.1 summarizes the selected values for the tuning structure.

Table 6.1: Selected general parameters

τ_{RC} [ms]	1
Switching time [ms]	1.6
d [nm]	10
ϵ_r^d for hBN	4

6.2.2 SIMULATED Zs_{ON} AND Zs_{OFF} VALUES

Similar to Chapters 4 and 5, the values of the surface impedance for the ON and OFF states are selected to be practical values. Following the same procedure as in Chapter 4, the values of sheet resistances used here for the ON and OFF states (Rs_{ON} and Rs_{OFF} respectively) in Table 6.2 are obtained from equation (6.7),

$$Zs \approx \frac{j\pi\hbar^2(2\pi f(\tau_L\tau_S) - j(\tau_L + \tau_S))}{q^2(\tau_L\tau_S)[\mu_c + 2k_BT\ln(e^{-\frac{\mu_c}{k_BT}} + 1)]}. \tag{6.7}$$

As observed, the values are exactly the same as for set 2 and 3 in Table 4.2 in Chapter 4. The antenna substrate used is the Rogers RT5880 with a relative permittivity ϵ_r=2.2 and a loss tangent tanδ=0.0009 [268]. The thickness H of the substrate is set to 4 mm to optimise the ratio between size reduction and efficiency of the antenna, and at the same time, can still fit into current mobile and wireless devices, e.g. mobile phones, tablets, etc.

Table 6.2: Selected surface impedance Zs values

Set	2		3	
State	ON	OFF	ON	OFF
n [m^{-2}]	$5{\cdot}10^{17}$	$6{\cdot}10^{14}$	$5{\cdot}10^{17}$	$6{\cdot}10^{14}$
V_b [V]	22.72	$\sim$0	22.72	$\sim$0
μ_L [m^2/Vs]	2.7		2.7	
D [eV]	18		18	
T [K]	295		4.2	
Zs_{ON} [$\Omega/\square$]	34+j0.3	2580+j6	5+j0.1	3840+j9

6.3 RESULTS

The results section is structured as follows, first, in subsection 6.3.1, the impact of graphene on the unit cells is computed. Second, in subsection 6.3.2, the two proposed antenna designs shown in Figs. 6.3 and 6.4 are evaluated. In subsection 6.3.3, some antenna design trade-offs are analysed. In addition, some intermediate values of Zs are simulated for frequency selection in subsection 6.3.4. In subsection 6.3.5, a performance comparison is made to other designs found in the literature. Finally, in subsection 6.3.6, the power consumed by the two proposed unit cells and antennas is computed.

The simulation results are obtained from the computer simulation technology (CST) microwave studio 2015. In the simulations, the excitation is modelled as a discrete port with an internal impedance of Z=50 Ω. The graphene sheets are modelled as ohmic sheet surface impedance with real and imaginary impedances. The antenna efficiency η_t (%) provided is calculated as

$$\eta_t = \left(\frac{P_{rad}}{P_{sim}}\right) \times 100, \tag{6.8}$$

where P_{rad} is the power radiated by the antenna and P_{sim} is the power

simulated (0.5 W). Therefore, the antenna efficiency also considers the mismatch losses between the feed and the antenna.

6.3.1 IMPACT OF GRAPHENE ON THE MEANDER LINE AND TOP PATCHES

In this subsection, the two proposed unit cells with integrated graphene sheets are simulated. The proportion of capacitance and inductance reconfigurability provided by varying the surface impedance of graphene is studied. In addition, the losses caused by the introduction of the graphene sheets are also analysed.

As shown in Fig. 6.2, it is expected that changing the surface impedance of graphene should change the inductive and capacitive behaviour of some of the elements that compose the unit cells. Fig. 6.6 shows the two configurations used to compute the inductance and capacitance variation when Zs is changed for different lengths of the graphene sheets Gl. The inductance and capacitance values are obtained from network analysis by modifying the graphene sheet lengths, Gl in Fig. 6.6, when it is activated (ON) and deactivated (OFF). The values of the surface impedances of graphene for the ON state and OFF state are selected from set 2 in Table 6.2. The conductor used for the ground plane and the meanderline, patches and vias is copper. Table 6.3 provides the physical dimensions of the unit cells.

The results in Fig. 6.7 show the difference between the variation in the inductance ΔL and capacitance ΔC values when the graphene sheets are activated (ON) and deactivated (OFF). Both values ΔL and ΔC are calculated as the difference between the inductance and capacitance values generated when the graphene sheet is deactivated and the inductance and capacitance values generated when the graphene sheet is activated. These inductance and capacitance variations between ON/OFF states will cause the antenna resonant frequency to change as they change the values of the left-handed inductance L_L and the right-handed capacitance C_R. In the case where graphene is laid under the meander

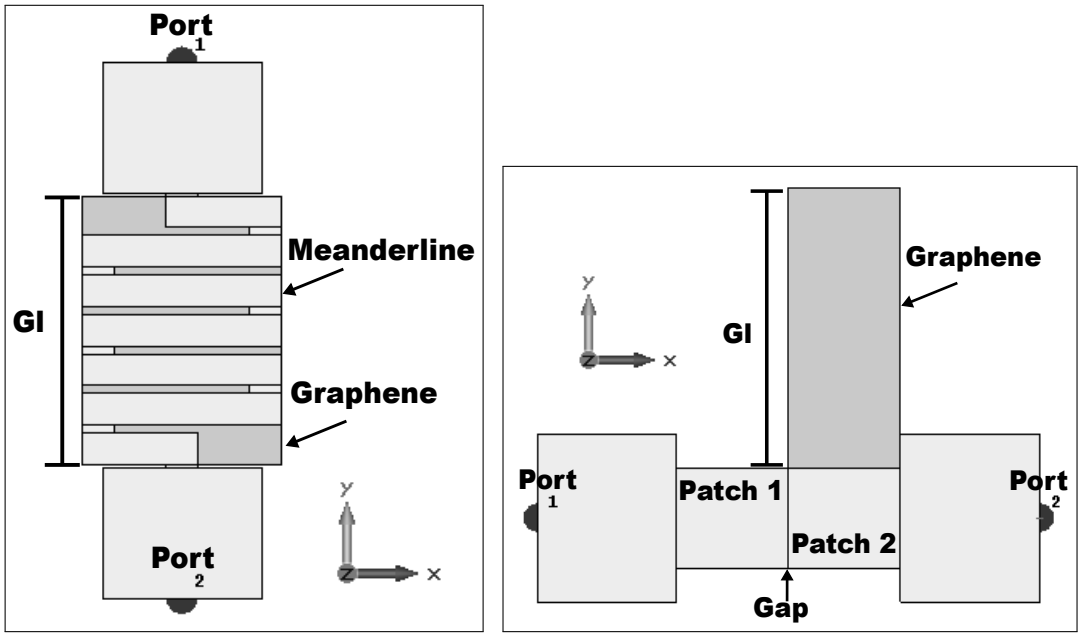

(a) (b)

Figure 6.6: Inductance and capacitance computation of a) graphene under the meander line and b) graphene next to the second patch.

Table 6.3: Unit cells dimensions, in millimetre (mm)

Unit cell 1, Fig. 6.1a			
$W1 = W2 = 3$	$L1 = L2 = 4.5$	$l0 = 4.35$	$l1 = 1.2$
$l2 = 0.3$	$l3 = 1.2$	$l4 = 7.5$	$l5$=0.1
$Gap = 0.01$	$r = 0.5$	$W3 = 10.2$	p=12.16
Unit cell 2, Fig. 6.1b			
$W1 = W2 = 3.6$	$L1 = L2 = 4$	$l0 = 2.425$	$l1 = 1.35$
$l2 = 0.15$	$l3 = 1.35$	$l4 = 3.5$	$l5$=0.1
$Gap = 0.01$	$r = 0.5$	$W3 = 5$	p=9.08

line, the result in Fig. 6.7a indicates that both components, ΔL and ΔC, change when the length of the graphene sheet is varied. Specifically, when the graphene sheet becomes longer, from Gl=2.7 mm to Gl=10.2 mm, ΔL increases from ΔL=-0.27 nH to ΔL=0.96 nH. The reason is that, ideally when the graphene sheet is

deactivated, most of the current must propagate through the meander line and consequently it has a large inductance. However, when the graphene sheet is activated, some current is now diverted to propagate through the graphene sheet instead of going all the way through the meander line. As the inductance of a meander line depends on the number of turns and the length of the turns (among other parameters), the longer the graphene sheet is the shorter the path of the current that needs to propagate through the meander line, and consequently, the lower the resulting inductance. On the contrary, the difference on the capacitance values ΔC decreases, from ΔC=0.15 pF to ΔC=0.02 pF, becoming almost negligible for the longest graphene sheet. As a result, as the graphene sheet becomes longer, the change in the resonant frequency becomes dominated by the change of its inductance instead of the capacitance. Note that, the ΔC values are not large enough to provide a substantial change in the resonant frequency, and hence, it is necessary to base the change of the resonant frequency in the unit cell 1 on the modification of the inductance values ΔL.

In the second case, Fig. 6.7b shows the results for the unit cell 2 when the graphene sheet is attached to the second top patch. As the graphene sheet becomes larger, from Gl=0.5 mm to Gl=10 mm, the capacitance difference ΔC also becomes larger, from ΔC=-0.11 pF to ΔC=-0.43 pF. The reason is that when the graphene sheet is deactivated, negligible current propagates through the graphene sheet and therefore it does not contribute to the parallel capacitance between the top patches and the ground plane. Consequently, it does not matter how large the graphene sheet is. However, when the graphene sheet is activated, some current propagates through the graphene sheet which then contributes to the total capacitance. Thus, the larger the area of the graphene is, the larger the capacitance it generates. In this case, the variation of the capacitance is negative because the capacitance generated when the graphene sheet is deactivated is lower than when the graphene sheet is activated. Regarding the inductance change, it does not follow a perfect linear change but it can be seen that in general the

difference also decreases for longer graphene sheets. Nevertheless, in this case, the inductance change is not important as it only contributes to the right-handed inductance L_R and consequently it does not change the resonant frequency, see equation (6.4). Therefore, the main contribution to the change in the ZOR frequency for the unit cell 2 comes from the capacitance variations ΔC as this affects the right-handed capacitance C_R.

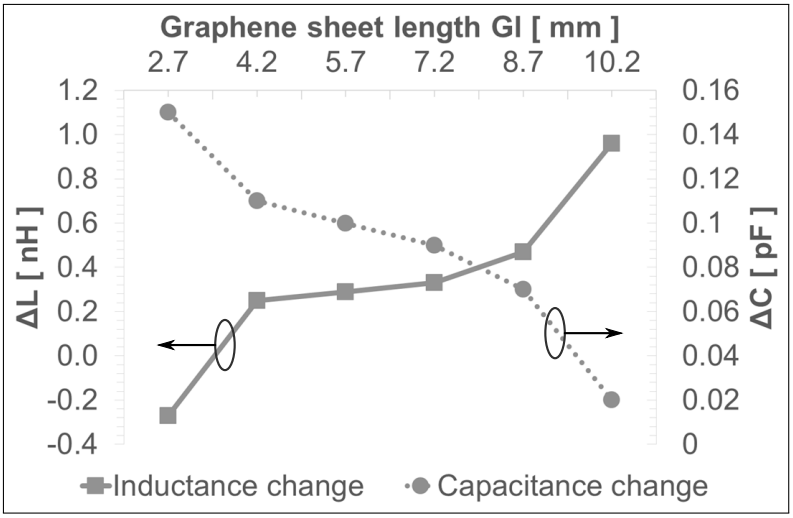

(a)

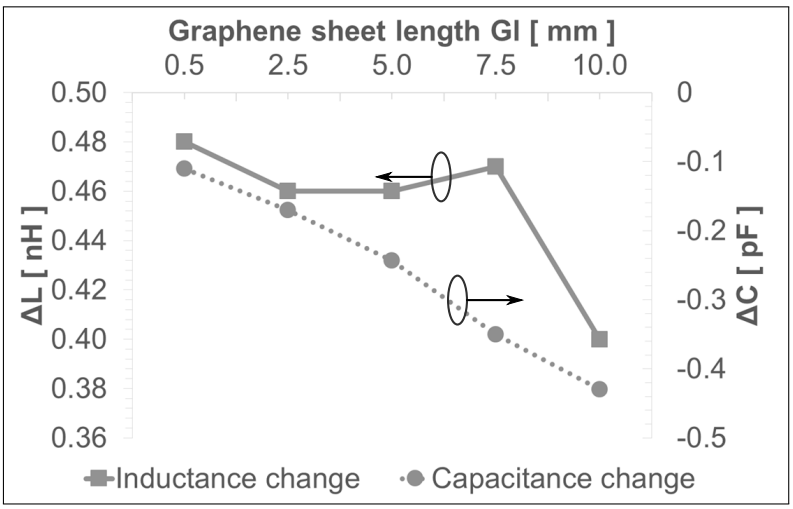

(b)

Figure 6.7: Inductance and capacitance variations of a) graphene under the meander line and b) graphene next to the patch 2.

From the inductance and capacitance results it seems that large changes in resonant frequencies are possible by implementing long graphene sheets. However, it is also important to consider the losses. In Fig. 6.8 the losses due to the presence of graphene when it is activated (ON) and deactivated (OFF) are shown for both cases. Unfortunately, it indicates that the longer the graphene sheet is, the larger the losses are. Consequently, there is a trade-off between the maximum resonant frequency switch and the maximum acceptable losses due to the use of graphene. Additionally, comparing both designs when the graphene sheets are activated, using a graphene sheet under the meander line provides lower ohmic losses for long lengths of graphene sheets - 29.2mW as compared to 66.8 mW for graphene next to the second patch. On the other hand, when the length of the graphene sheet is shorter, as well as when the graphene sheet is deactivated (OFF), both designs perform similarly. The reason for this is that when graphene is placed under the meanderline it provides an alternative path for the current to propagate when switched to the ON state. However, there is still some current propagating on the meander line which experiences low resistance. Therefore, the total losses are low. In contrast, in the case where graphene is placed next to the second top patch, in order to have an effect on the capacitance, some current needs to propagate directly on the graphene sheet when activated. Because the surface impedance of that graphene sheet is high, the current propagating on the graphene sheet suffers larger power losses.

6.3.2 PERFORMANCE OF THE FREQUENCY RECONFIGURABLE ZOR ANTENNAS

In this subsection, the two proposed antennas formed by the two proposed unit cells are simulated. The two ZOR antennas are designed to switch between the LTE bands of 1.8 GHz and 2.1 GHz. It is expected that activating and deactivating the graphene sheets should provide enough change in the capacitive C_R and inductive L_L behaviour of the antennas to change the zeroth order

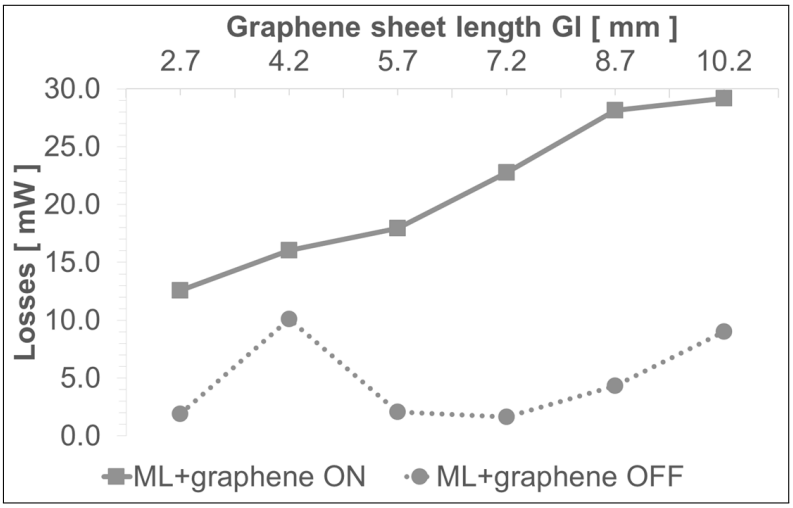

(a)

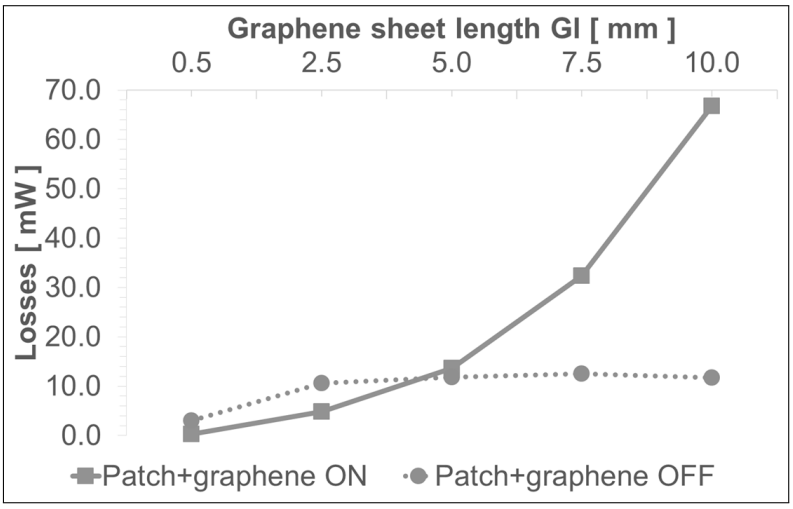

(b)

Figure 6.8: Losses due to graphene in a) graphene under the meander line (ML+graphene) and b) graphene next to the patch 2 (Patch+graphene).

resonant frequencies. The values of the surface impedance of graphene selected are from set 2 in Table 6.2. Again, the main conductor is copper. Table 6.4 gives the physical dimensions of the proposed antennas.

Fig. 6.9 shows the reflection coefficient values of the two antennas when graphene is activated (ON) and deactivated (OFF). In the antenna design 1, when graphene is activated, the resonant frequency is set to 2.1 GHz while when

Table 6.4: Antenna dimensions, in millimetre (mm)

Common for both designs			
$H = 4$	$t = 0.5$	$W_{feed} = 6$	$L_{feed} = 5$
Design 1, Fig. 6.3			
$W = 15.4$	$L = 30.18$	$G_{feed} = 0.2$	
Design 2, Fig. 6.4			
$W = 21.15$	$L = 25.1$	$G_{feed} = 0.45$	

deactivated it changes to 1.8 GHz. Likewise, in the antenna design 2, when graphene is activated, the resonant frequency is found at 1.8 GHz while when deactivated it moves to 2.1 GHz. Additionally, Fig. 6.10 and 6.11 show the surface current distribution on the two antennas when the graphene sheets are activated and deactivated. In the case of the antenna design 1, Fig. 6.10, the change in how the current propagates is difficult to appreciate due to the overlap of the meander line on the graphene sheet. However, it is still possible to note how the current follows the turns of the meander line when the graphene sheet is OFF, Fig. 6.10a, and how it follows a more straight path when the graphene sheet is ON, Fig. 6.10b. For the antenna design 2, when the graphene sheets are deactivated, little current propagates on the graphene sheets. In contrast, when the graphene sheets are activated some current now propagates on the graphene sheets which effectively changes the inductive and capacitive behaviour of the antenna.

In a CRLH TL based antenna, the order of resonance is identified by looking into the electric field distribution at the particular frequencies of interest. When the CRLH TL based antenna is operating at its zeroth order resonance, the electric field lines in the enclosed volume that surrounds the antenna are all pointing to the same direction as the wavelength is infinite. This condition is recognized for both designs at both resonant frequencies as Fig. 6.12, Fig. 6.13, Fig. 6.14 and

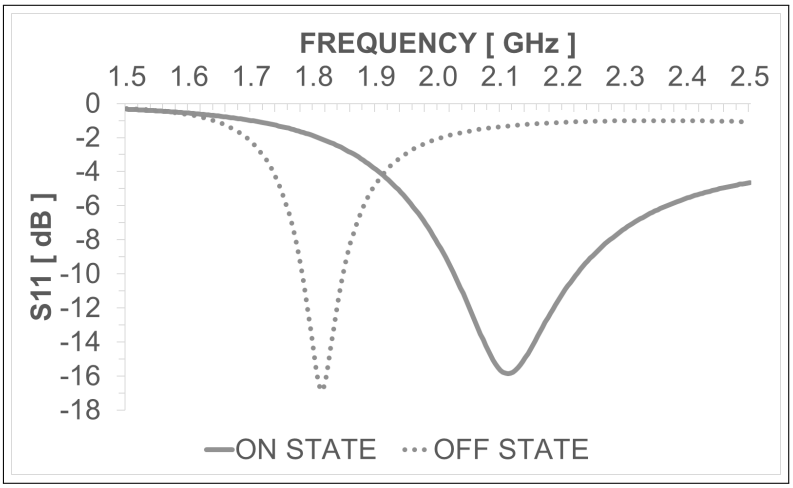

(a)

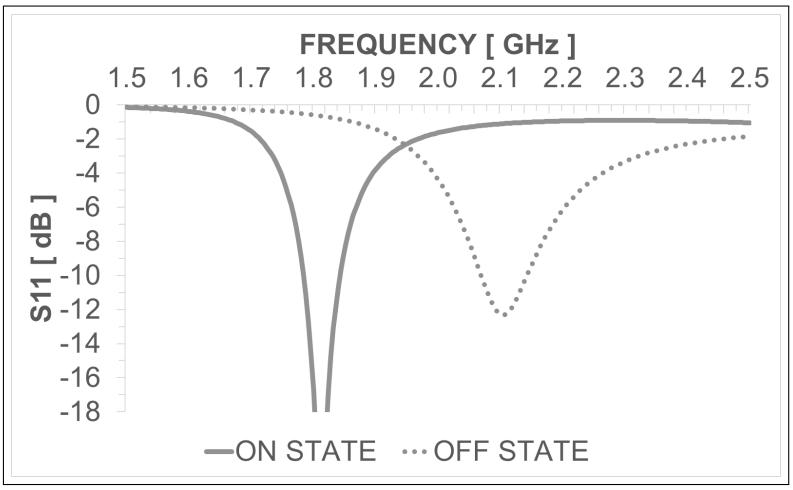

(b)

Figure 6.9: Reflection coefficients for the ON and OFF states, a) Design 1 b) Design 2.

Fig. 6.15 demonstrate. In Fig. 6.12 and Fig. 6.14 the electric field lines between the ground plane and the top patches are uniformly all pointing to the same direction (upwards). Similarly, in Fig. 6.13 and Fig. 6.15, the electric field lines are shown for the X-Z plane. Here, it is clearly seen that the electric field lines go from the ground plane to the top patch within the antenna substrate. All the lines point to the same direction. Therefore, it is confirmed that both antennas are operating at the zeroth order resonance (0^{th}).

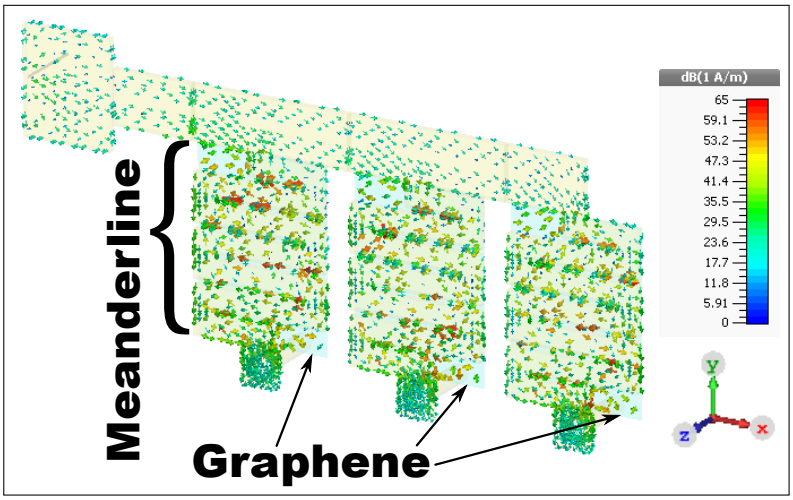

(a)

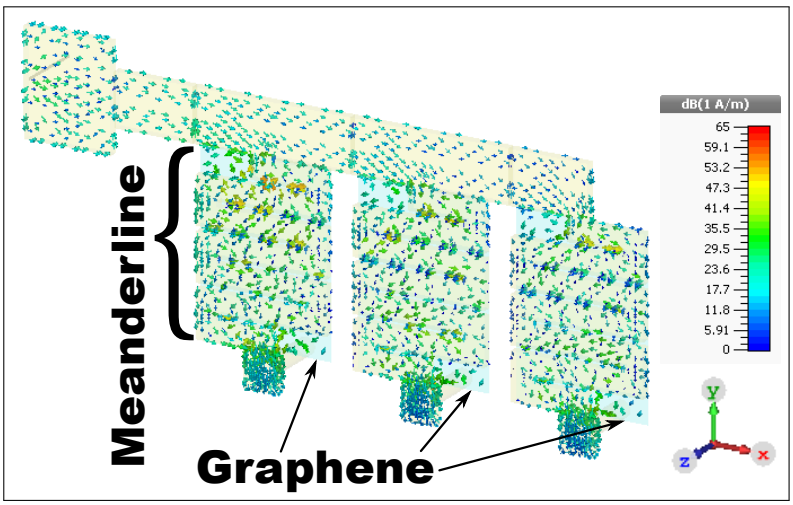

(b)

Figure 6.10: Surface current distribution for antenna design 1 at a) 1.8 GHz and b) 2.1 GHz.

Furthermore, the radiation patterns obtained in Fig. 6.16 and in Fig. 6.17 are of similar shape of a common microstrip antenna and switching ON and OFF the graphene sheets seems to not strongly affect the resulting radiation patterns. However, the radiation patterns are not symetric due to a shorter ground plane in one of the sides of the antenna. The extracted gains for the antenna design 1 are -0.2 dB and -3 dB at 1.8 GHz and 2.1 GHz respectively; and -0.8 dB and 0.6 dB

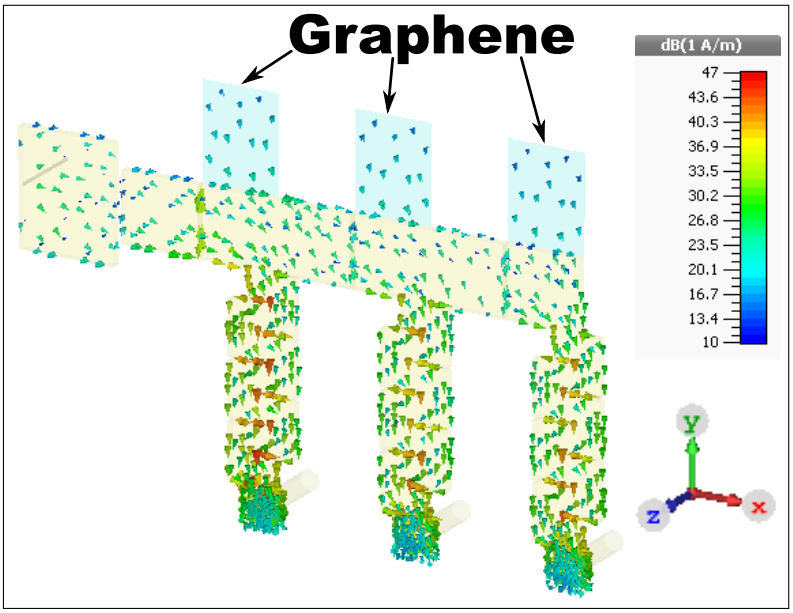

(a)

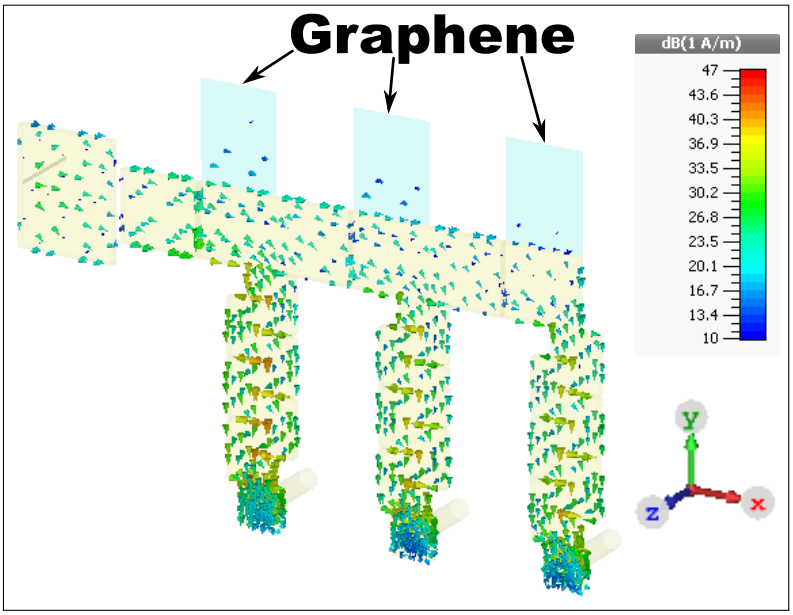

(b)

Figure 6.11: Surface current distribution for antenna design 2 at a) 1.8 GHz and b) 2.1 GHz.

at 1.8 GHz and 2.1 GHz respectively for the antenna design 2. All the presented results confirm that by switching the surface impedance of the graphene sheets

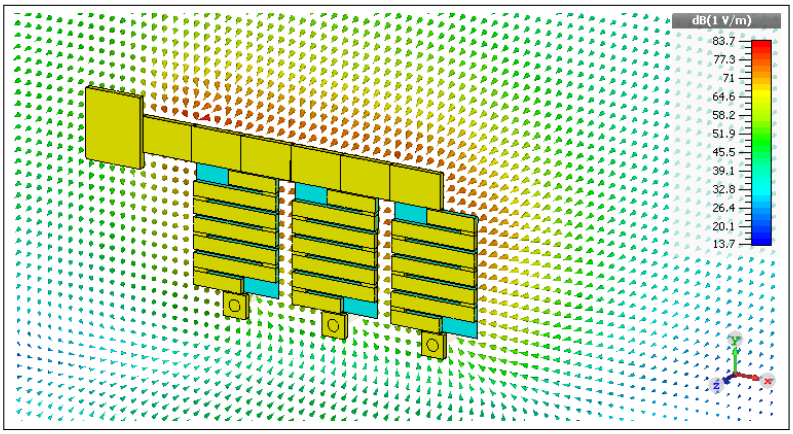

(a)

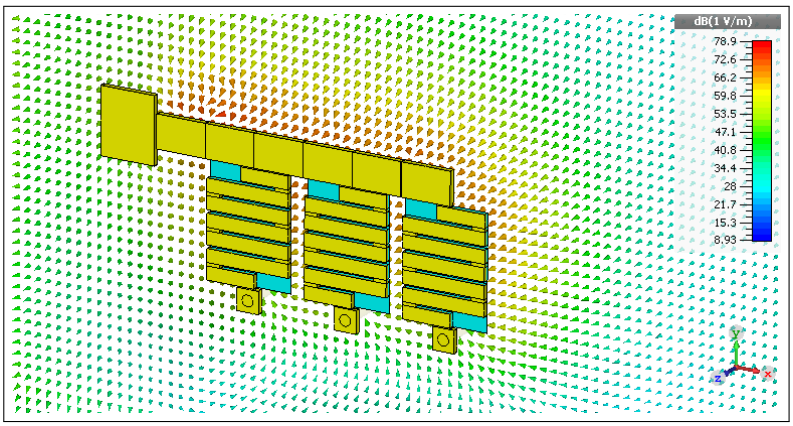

(b)

Figure 6.12: Electric field distribution within the substrate for antenna design 1 at a) 1.8 GHz and b) 2.1 GHz, when the graphene sheets are deactivated and activated respectively.

in the proposed antennas, their zeroth order resonant frequencies can be changed between 1.8 GHz and 2.1 GHz.

The antenna efficiencies computed for the antenna design 1 are 31.6% and 15.8% at 1.8 GHz and 2.1 GHz respectively; and 28.8% and 33.9% at 1.8 GHz and 2.1 GHz respectively for the antenna design 2. For both antenna designs, material losses are dominated by graphene, accounting for around 55% to 95% of the losses due to materials and between 35% and 75% of the total losses in the antenna, causing the antenna efficiency to drop considerably. Ideally, when

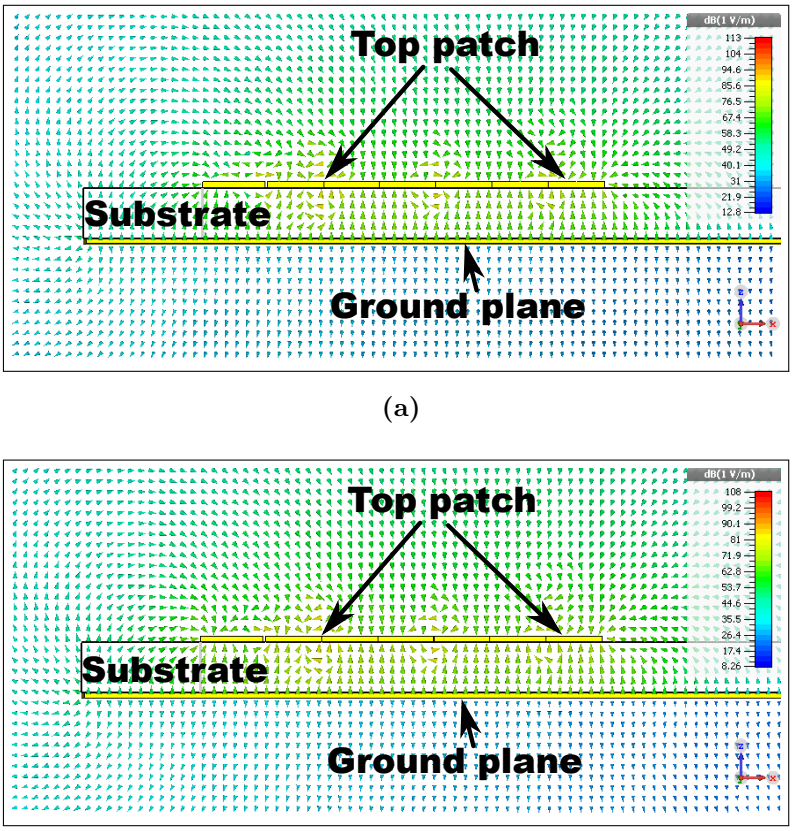

Figure 6.13: Electric field along the plane (X-Z) for antenna design 1 at a) 1.8 GHz and b) 2.1 GHz, when the graphene sheets are deactivated and activated respectively.

graphene is deactivated, its effect should be minimum but the results indicate that there are still some losses due to the presence of graphene. As a result, the addition of graphene does not only affect the antenna efficiency when the graphene sheet is activated but also when it is deactivated, and hence, at both resonant frequencies. In order to reduce the losses in the antennas, it is necessary to increase the surface impedance for the OFF state (Zs_{OFF}) and decrease the surface impedance for the ON state (Zs_{ON}). This could be done by selecting graphene with lower long-ranged charge carrier mobility μ_L and/or lower carrier inhomogeneity density $\tilde{n}$. That should increase the maximum achievable surface impedance Zs_{OFF} for small values of applied DC bias voltage V_b. However, that would also cause an increment of the DC bias voltage V_b needed to achieve a

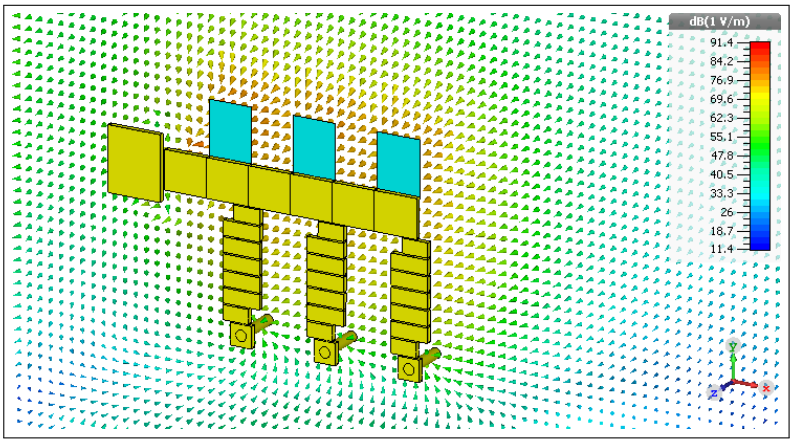

(a)

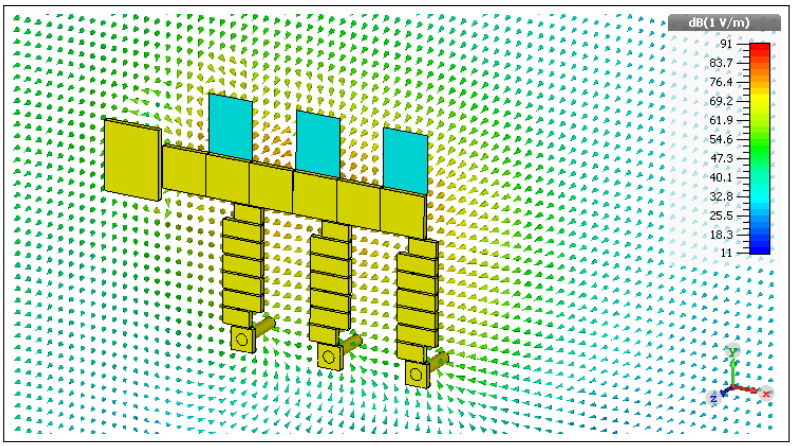

(b)

Figure 6.14: Electric field distribution within the substrate for antenna design 2 at a) 1.8 GHz and b) 2.1 GHz, when the graphene sheets are activated and deactivated respectively.

low Zs_{ON}. Similarly, achieving lower deformation potential D or lowering the operational temperature would allow to reduce the surface impedance of graphene in the ON state. Unfortunately, the deformation potential is still not properly controlled, making it difficult to achieve lower values, as explained in Section 2.2.2 of Chapter 2. In order to demonstrate how the increase of Zs_{OFF} and the decrease of Zs_{ON} should cause the antenna efficiencies to improve, the same two antennas are simulated with the same configuration as before but now with Zs_{ON}

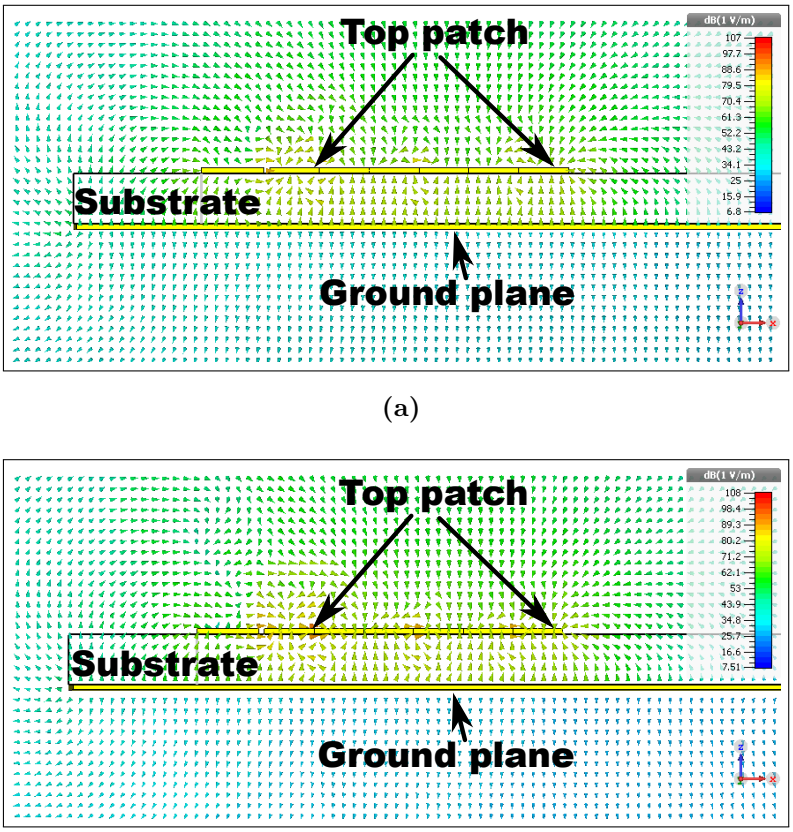

(a)

(b)

Figure 6.15: Electric field along the plane (X-Z) for antenna design 2 at a) 1.8 GHz and b) 2.1 GHz, when the graphene sheets are activated and deactivated respectively.

and Zs_{OFF} taken from set 3 in Table 6.2. Although it is not the aim here to operate at a temperature T=4.2 K, the conditions in set 3 are useful because it has a lower value of Zs_{ON} and a higher value of Zs_{OFF} compared to set 2. The antenna efficiencies now are 31.7% and 33.9% for antenna design 1 at 1.8 GHz and 2.1 GHz respectively; and 56% and 36.6% for antenna design 2 at 1.8 GHz and 2.1 GHz respectively. It can be seen that now all the antenna efficiencies are higher than when the set 2 values are used. Although there is some improvement in the antenna efficiencies when the graphene sheets are in the OFF state, the highest improvement is found when the graphene sheets are in the ON state. This

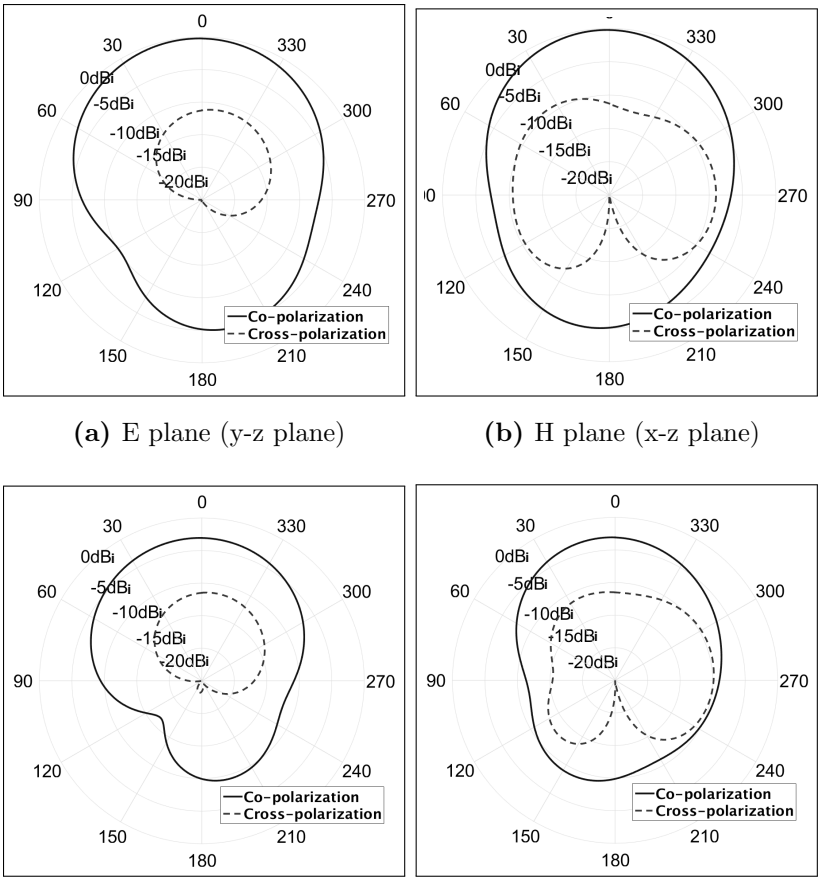

(a) E plane (y-z plane) **(b)** H plane (x-z plane)

(c) E plane (y-z plane) **(d)** H plane (x-z plane)

Figure 6.16: Radiation patterns of the ZOR antenna design 1 at (a)-(b) 1.8 GHz and (c)-(d) 2.1 GHz.

means that, for the two proposed antennas, achieving the lowest possible surface impedance for the ON state is still critical.

6.3.3 SUBSTRATE HEIGHT AND NUMBER OF CELLS EFFECT ON THE ANTENNA EFFICIENCY

The antenna efficiencies obtained in the previous subsection 6.3.2 are mainly dominated by the losses in graphene. However, they are also affected by the

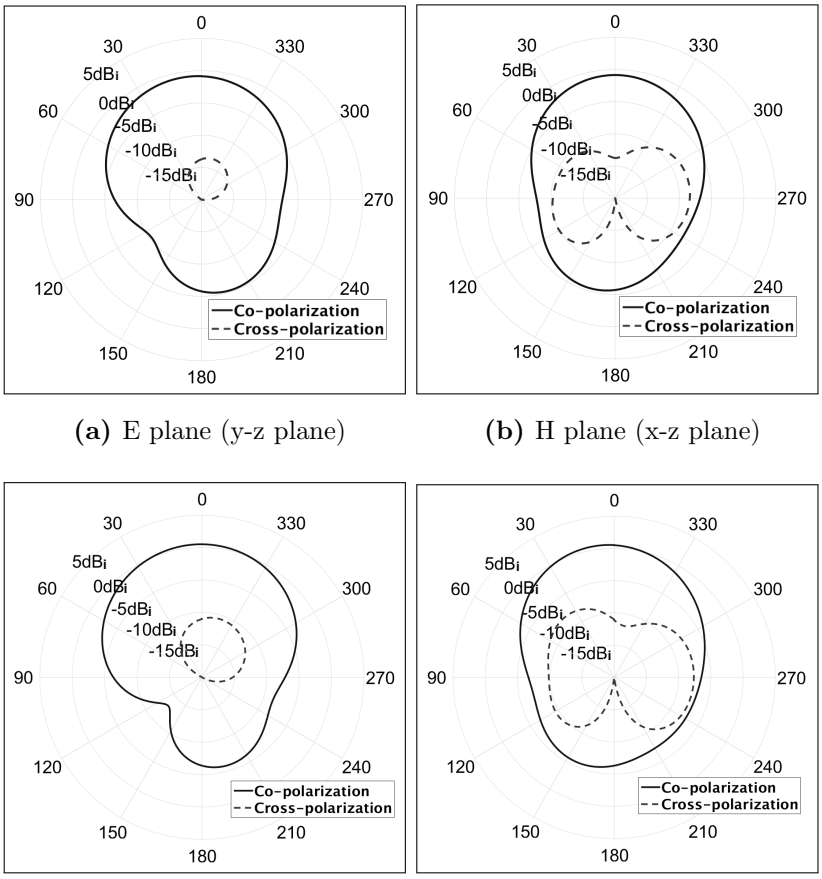

(a) E plane (y-z plane) **(b)** H plane (x-z plane)

(c) E plane (y-z plane) **(d)** H plane (x-z plane)

Figure 6.17: Radiation patterns of the ZOR antenna design 2 at (a)-(b) 1.8 GHz and (c)-(d) 2.1 GHz.

antenna size. Fig. 6.18 displays the trade-off between the height of the antenna substrate H, the length of the antenna L and the antenna efficiency η_t. For both designs, increasing H helps to reduce L and improve η_t. During simulations, when the substrate height was increased, the zeroth order resonance decreased and vice versa. To compensate this effect, the lengths of the two patches, $L1$ and $L2$ in Fig 6.1, were made shorter or longer, resulting in smaller or larger antennas when increasing or decreasing H, respectively. This means that, in the zeroth order resonant frequency, the effect of the vias inductance, L_{vias} in Fig. 6.2, is stronger than the effect of the parallel plate capacitance between the top patches and the

ground plane, C_{patch1} and C_{patch2} in Fig. 6.2. On the other hand, the antenna efficiency is improved for bigger heights H because the antenna occupies a larger volume and radiates more efficiently. However, if the antennas are designed to be implemented in wireless and mobile devices, the available substrate thickness is limited and cannot be further increased.

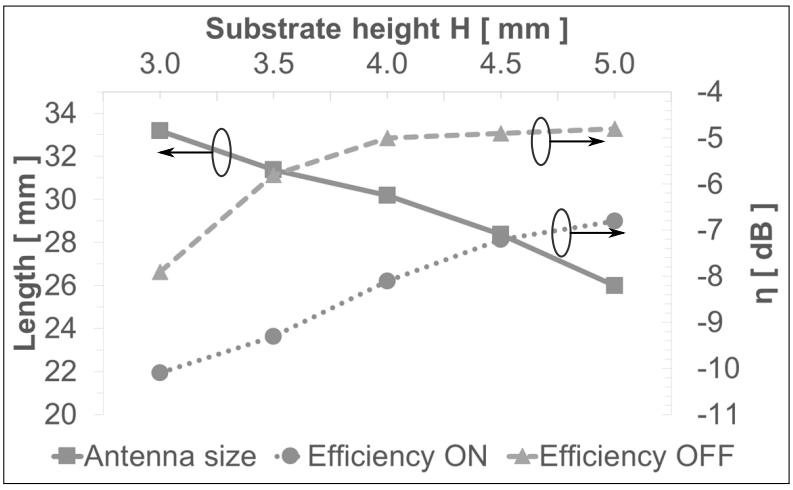

(a)

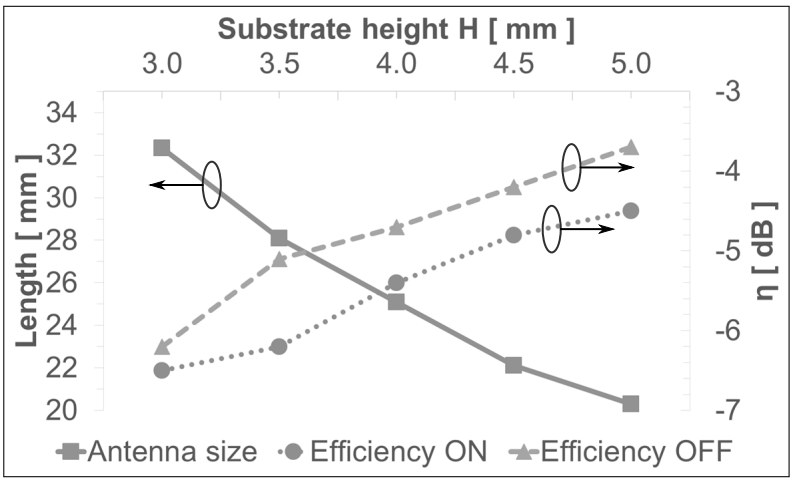

(b)

Figure 6.18: Trade-off between substrate height H, antenna efficiency η_t and antenna length L for a) design 1 and b) design 2.

Likewise, Fig. 6.19 provides the trade-off between the number of cells N, the length of the antenna L and the antenna efficiency η_t. In this case, adding or

removing unit cells increases or decreases the length of the antenna at a linear rate. It also improves or deteriorates the antenna efficiency respectively, but in this case, the rate is not linearly proportional. Consequently, more unit cells do not substantially improve the antenna efficiency. On the other hand, having a larger number of unit cells allows for an easier antenna matching as each additional unit cell drastically reduces the high input impedance of ZOR antennas.

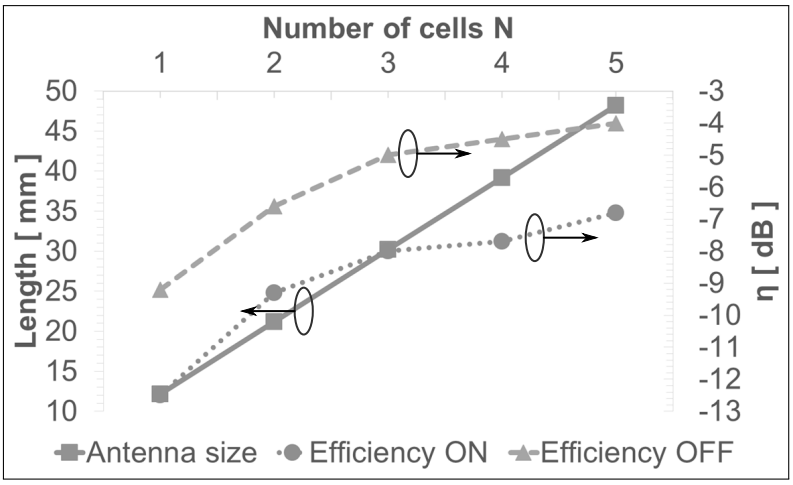

(a)

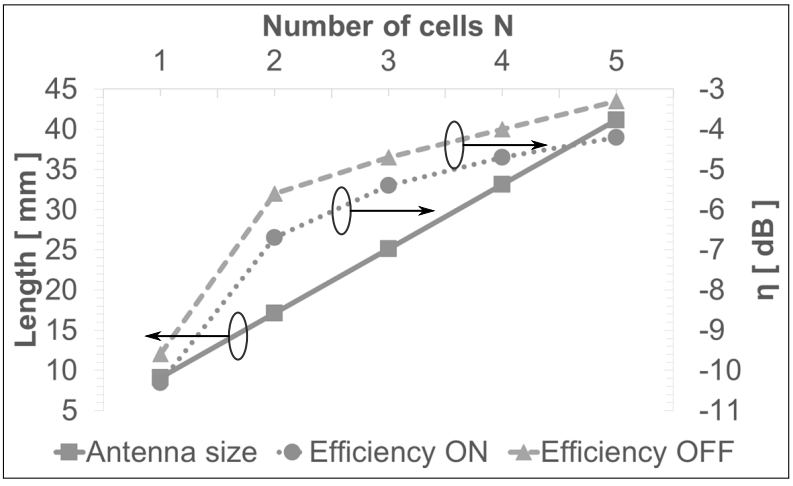

(b)

Figure 6.19: Trade-off between number of cells N, antenna efficiency η_t and antenna length L for a) design 1 and b) design 2.

From these results, it is therefore possible to optimize antenna efficiency of

the proposed ZOR antennas by adjusting the substrate height and the number of unit cells. It is also possible to compensate the efficiencies due to restrictions on thinner substrates by adding more unit cells at the expense of a larger overall antenna size, and vice versa.

6.3.4 ZEROTH ORDER RESONANT FREQUENCY SELECTION

In previous subsections, only two sets of surface impedances, Zs_{ON} and Zs_{OFF}, were used to switch between the two resonant frequencies, 1.8 GHz and 2.1 GHz. However, the surface impedance of graphene can be adjusted to any value between these two impedances. This allows the selection of any intermediate resonant frequency between the two design frequencies. Fig. 6.20 shows the antenna resonant frequencies for different intermediate values of surface resistance Rs for antenna design 2. Note that in these results, only the real part of the surface impedance Rs is changed as the imaginary part Xs has a small effect on the total surface impedance and can hence be neglected. As observed, selecting intermediate surface resistance values permits tuning resonant frequencies in the tuning range. Similar results are obtained for antenna design 1.

Fig. 6.21 shows the change of resonant frequency and antenna efficiency for the antenna design 1 and design 2 when selecting intermediate values of surface resistance Rs. The efficiencies of the intermediate frequencies are lower than the ones obtained for the 1.8 GHz and 2.1 GHz. The reason for this is that as the surface resistance changes, the portion of current propagating on graphene also changes. The current propagating on graphene suffers higher losses because the surface resistance is not at its minimum or maximum value.

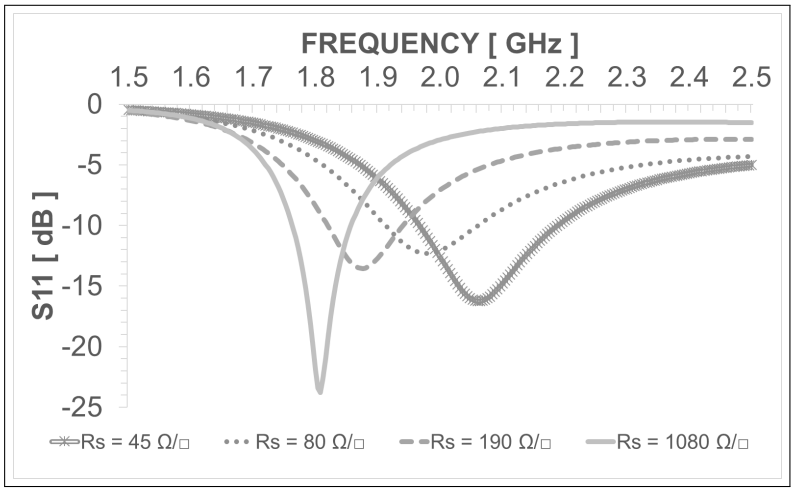

Figure 6.20: Frequency selection in Design 2 by selecting different intermediate surface resistance values of graphene.

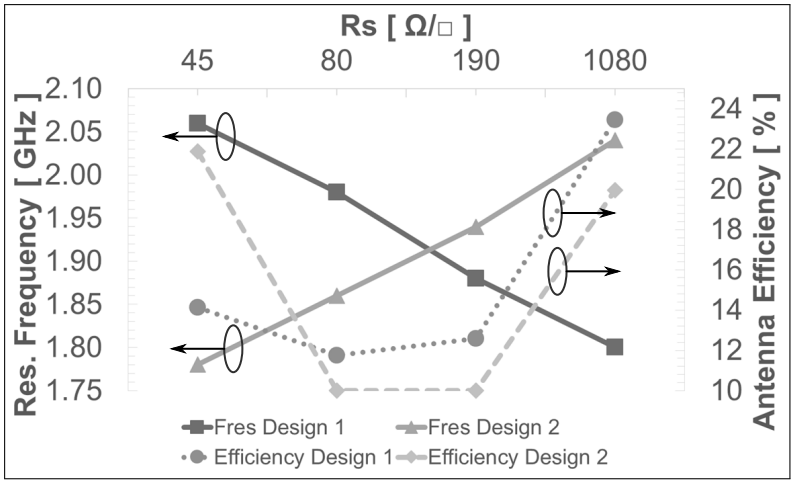

Figure 6.21: Resonant frequency and antenna efficiency variation for intermediate values of Rs.

6.3.5 PERFORMANCE COMPARISON

The results obtained from the proposed frequency reconfigurable ZOR antennas are compared to some other works found in the literature. In [263], a substrate integrated-interdigital capacitor ZOR antenna is reconfigured by integrating varactor diodes. In [264], a ZOR antenna composed by mushroom-like unit cells is able to change its resonant frequency by implementing PIN-diodes in

its integrated spiral slots. In [248], another mushroom-like antenna can switch frequencies by activating and deactivating grounded MEMS. Table 6.5 summarizes the comparison. Note that, λ_0 is calculated in each work from the lowest operating frequency.

Table 6.5: Comparison of different ZOR reconfigurable antennas

Reference	Technology	Electrical Size ($L \times W$)	Frequencies Covered	Antenna Gain
This work: Design 1	Graphene	$0.18\lambda_0 \times 0.09\lambda_0$	1.8GHz and/to 2.1GHz	-0.2dB to -3dB
This work: Design 2	Graphene	$0.15\lambda_0 \times 0.13\lambda_0$	1.8GHz and/to 2.1GHz	-0.8dB to 0.6dB
[263]	Varactor	$0.3\lambda_0 \times 0.3\lambda_0$	4.1GHz to 4.5GHz	2.5dB and 4dB
[264]	PIN-diode	$0.06\lambda_0 \times 0.16\lambda_0$	2.3GHz and 3.1GHz	-6dB and -4.9dB
[248]	MEMS	$0.23\lambda_0 \times 0.28\lambda_0$	4.7GHz and 5GHz	-2.3dB and -2.5dB

As observed from Table 6.5, the two proposed antennas are smaller compared to references [263] and [248] and of similar size to the antenna in reference [264]. It is important to mention that both antennas can be considered to be electrically small antennas as their size is $\sim \lambda_0/2\pi$. The antenna gains obtained for the two proposed antennas here are comparable to those found in other works. Likewise, the range of change in the resonant frequency is within the same proportion as found in the other works. However, the antenna efficiencies for the antennas

proposed in this chapter are expected to be lower than in the other work (antenna efficiencies not provided in the references) as there are large losses attributed to graphene. This is expected as graphene is a technology still in development. Interestingly, implementing graphene in reconfigurable antennas can provide the ON/OFF switching functionality as in PIN diode and MEMS as well as the possibility of continuous frequency selection as in varactors. Finally, graphene can easily operate at higher frequencies (millimetre wave to THz regime) where other switching technologies will struggle to work properly.

6.3.6 SWITCHING POWER CONSUMPTION

Following the same procedure as in Chapters 4 and 5, the power consumed by the proposed antennas is calculated with equation (6.9), see Section 4.2.3 in Chapter 4 for a detailed explanation,

$$P_{peak} = p(0) = \frac{n^2 q^2 dA}{\epsilon_o \epsilon_r^d \tau_{RC}}. \tag{6.9}$$

where the dielectric thickness d, the relative permittivity ϵ_r^d and the time constant τ_{RC} are set using the values in Table 6.1 while the remaining values for the charge carrier densities n are obtained from Table 6.2. The value for the area of graphene A used are from the Table 6.3 and Table 6.4 for the two proposed unit cells and antenna designs. Note that there are as many graphene sheets as number of unit cells in the antennas which are fed individually.

Fig. 6.22 shows the peak power consumed by the proposed unit cells as the size of the graphene sheet length Gl is changed. It is shown that, as expected, the power consumed becomes larger as the graphene sheet area increases. Therefore, it is possible to reduce the power consumption by using graphene sheets smaller but at the expense of reduced reconfigurability, see Fig. 6.7.

Fig. 6.23 presents the peak power consumed by the two proposed antennas for different numbers of unit cells. As expected, the more unit cells are used the larger the power consumed. This trade-off is added to the trade-off between

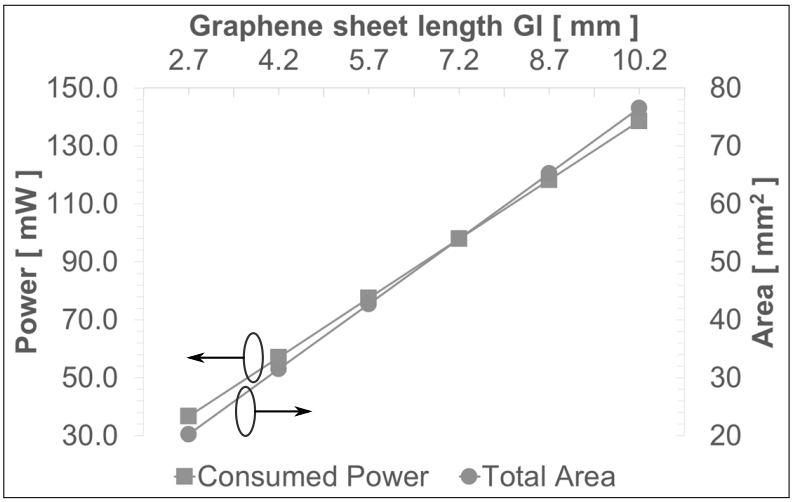

(a)

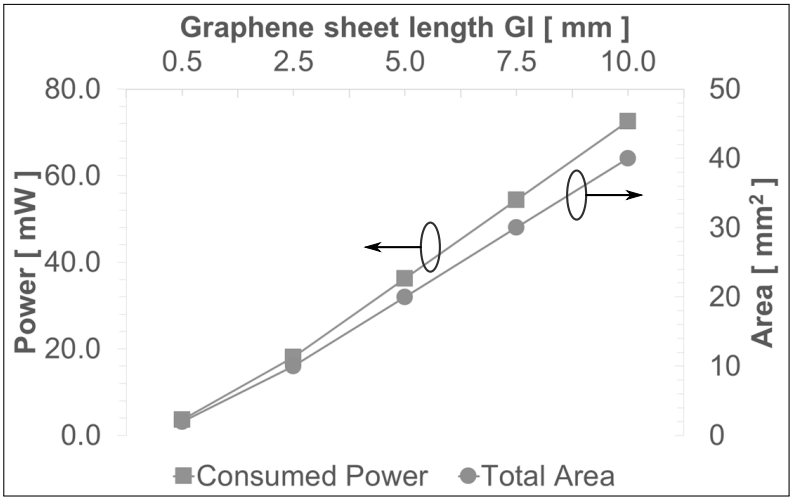

(b)

Figure 6.22: Peak power consumed and graphene area for a) unit cell 1 and b) unit cell 2.

number of unit cells, input impedance and total length of the antenna as seen in Subsection 6.3.3. Although the number of unit cells does not affect the antenna reconfigurability, it is important to find a balance between reducing the high input impedance by adding more unit cells versus reducing the total length of the antenna L by not adding many unit cells N. Therefore, an additional advantage

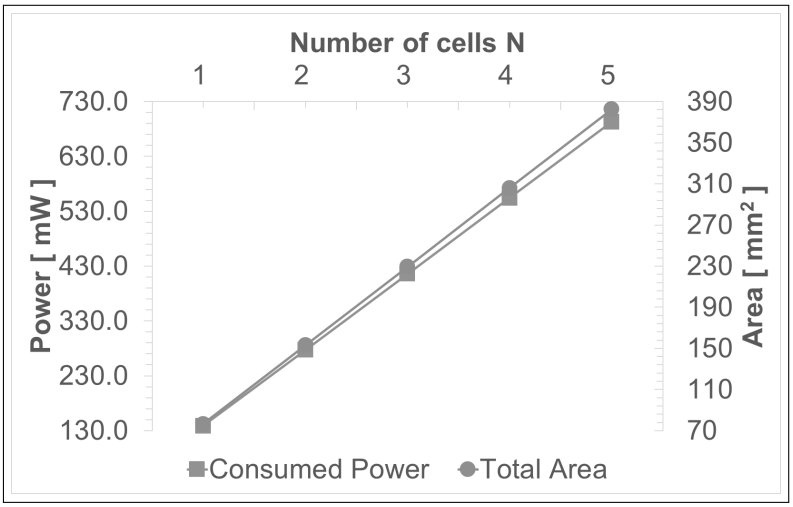

(a)

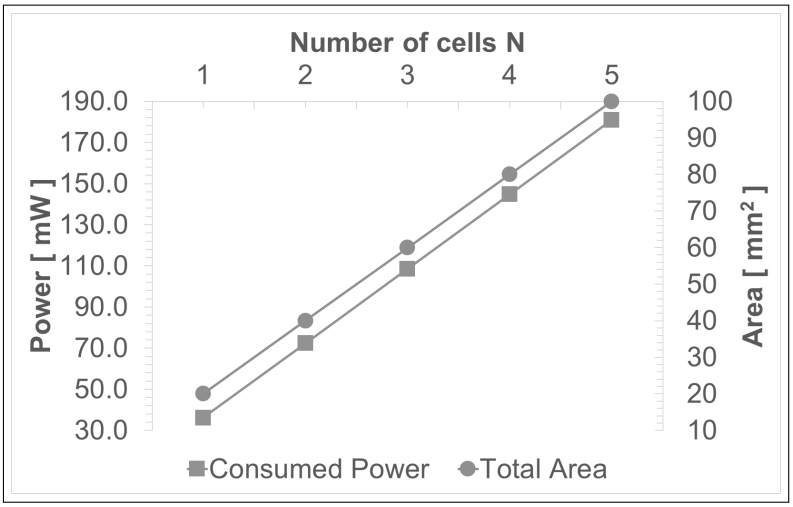

(b)

Figure 6.23: Peak power consumed and graphene area for a) antenna design 1 and b) antenna design 2.

of having a smaller antenna with less unit cells is the low power consumption that can be achieved.

Finally, as seen in Subsection 6.3.4, the proposed antennas can be configured to operate at intermediate resonant frequencies by selecting intermediate surface resistance values for the graphene sheets. In Fig. 6.24 the peak power consumed is calculated when different surface resistance values are selected. It is seen that

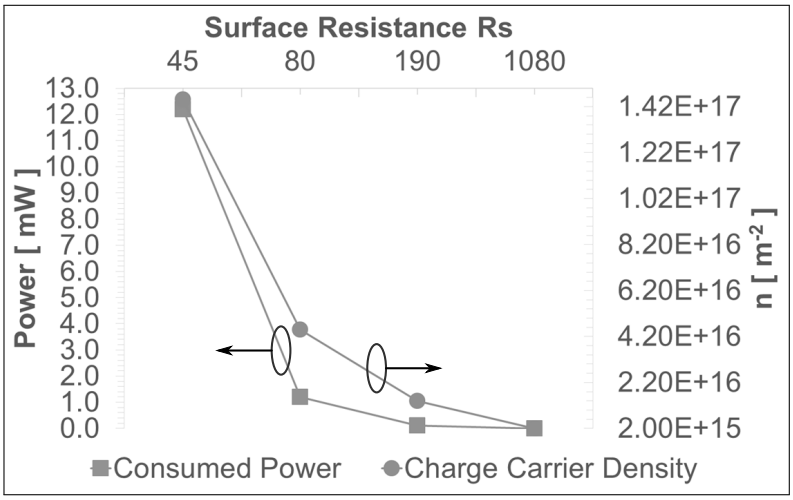

Figure 6.24: Peak power consumed and charge carrier density for antenna design 2 with different surface resistance values.

the power consumed substantially decreases as the values of surface resistance are increased. The reason for this is the low charge carrier density needed to achieve such high surface resistance values and hence to select those intermediate resonant frequencies, see Fig. 6.20. Therefore, the advantage of being able to select intermediate resonant frequencies is also an advantage from the point of view of power consumption.

6.4 CONCLUSIONS

The present chapter has demonstrated that graphene can be used in frequency reconfigurable ZOR antennas for microwave applications. Two unit cells and two antennas formed by these two unit cells have been proposed, analysed, simulated and discussed. The main conclusions obtained from the results are:

- Applying two different surface impedances of graphene, Zs_{ON} and Zs_{OFF}, allows the proposed zeroth order antennas to switch between the LTE bands of 1.8GHz and 2.1GHz as their capacitance and inductance values are changed.

- The two proposed antennas provide reasonable values of antenna efficiency for the size reduction offered.

- Low power consumption is possible due to the use of small graphene sheets.

Additionally, it has been shown that graphene can provide the functionality of selecting intermediate resonant frequencies, between 1.8GHz and 2.1GHz, by selecting different intermediate surface resistances Rs. The obtained antenna efficiencies are mainly affected by the losses in graphene but also by the antenna dimensions and configuration. The antenna design 2 achieves a slightly higher antenna efficiency for the ON state than antenna design 1, 28.8% compared to 15.8%, and similar values to antenna design 1 for the OFF state, 33.9% compared to 31.6%, due to the losses in graphene being lower. The antenna gains obtained for both designs (between -3 dB and 0.6 dB) are better than the ones obtained from other designs found in the literature that use PIN-diodes or MEMS as RF switches. Only the reference that uses varactors performs better in this feature (2.5 dB and 4 dB) but the proposed antenna designs in this chapter are half the size of the antennas in that reference. Finally, the proposed unit cells could be applied in other radio frequency applications such as filters, transmission lines, matching networks and electromagnetic lenses where reconfigurability can be produced as well.

Chapter 7

CONCLUSIONS

This thesis describes research on the application of the extraordinary electrical properties of carbon nanotubes, graphene and metamaterials into the antenna field at microwave frequencies. As a result, a total of five different antennas have been proposed, studied and simulated where advantages, disadvantages and trade-offs have been obtained and established. This chapter contains the main summary and conclusions obtained in this thesis. The chapter is structured as follows; first, a comparison between all the proposed antenna designs in this thesis is provided in section 7.1. Afterwards, the main novelties and contributions of this thesis are listed in section 7.2, followed by the future research lines arising from this thesis in section 7.4. Finally, a last comment is given in section 7.3.

7.1 COMPARISON OF THE PROPOSED ANTENNA DESIGNS

The WIFI and LTE frequency reconfigurable antennas in Chapter 4 presented the lowest antenna efficiencies (between 9.4% and 68%) when compared to polarization reconfigurable antennas in Chapters 5 (between 59.2% and 71.6%) and the frequency reconfigurable ZOR antennas in Chapter 6 (between 15.8% and 33.9%). This is mainly because the change in the antennas in Chapter

Table 7.1: Selected general parameters

Chapter	4		5		6	
Design	WIFI	LTE	1 element	2 element	LTE 1	LTE 2
Switches between	2.4GHz/ 3.6GHz/ 5GHz	1.8GHz/ 2.1GHz/ 2.6GHz/ 3.6GHz	HLP/ RHCP/ LHCP	HLP/ VLP/ RHCP/ LHCP	1.8GHz/ 2.1GHz	1.8GHz/ 2.1GHz
η_t [%]	9.4/68	10/46.8	59.2/61.4	59.3/71.6	15.8/31.6	28.8/33.9
Electrical size [λ_0]	L=0.28 W=0.24	L=0.23 W=0.26	L=0.25 W=0.23	L1=0.3 W1=0.3 L2=0.29 W2=0.3	L=0.18 W=0.09	L=0.15 W=0.13
Power consumed [mW]	330.6	142.6	1.14	0.7	430	110

4 is larger than in the other antennas, so the antenna efficiency suffers from both, large changes in resonant frequency and large areas of graphene. However, the frequency reconfigurable antennas in Chapter 4 provided larger frequency changes (between 2.4 GHz up to 5 GHz or 1.8 GHz up to 3.6 GHz) compared to the frequency reconfigurable ZOR antennas in Chapter 6 (between 1.8 GHz and 2.1 GHz), but the later designs had the lowest antenna size of all the proposed antennas in this thesis as they were effectively electrically small antennas. Finally, the power consumed by the polarization reconfigurable antennas in Chapter 5 was, by far, the lowest of all the antennas (between 0.7 mW and 1.4 mW) mainly because of a much longer time allowed to switch between states ON and OFF, 1

second of switching time in Chapter 5 against just 1 millisecond of switching time in Chapters 4 and 6.

7.2 MAIN NOVELTIES AND CONTRIBUTIONS

The main contributions and novelties of this thesis are summarized here:

- All the proposed antennas provided reasonably good antenna efficiencies because graphene was not the main conductor in the antenna. In fact, the graphene sheets only occupied a fraction of the total area of the antennas which substantially reduced the ohmic losses generated in the antennas. However, the graphene sheets were still able to modify the currents propagating in the antennas, and consequently, have an effect on the antenna behaviour. Therefore, the implementation of graphene provided the desired antenna reconfigurability while copper, as the main conductor, kept the antenna efficiency within acceptable values. This is the main reason for proposing hybrid metal-graphene solutions for microwave applications and this is the main novelty of this thesis.

- All the proposed antennas in this thesis used graphene mainly as a tunable material that can provide ON/OFF states like other switching methods such as MEMS, FET and PIN diodes. However, in the proposed antenna designs of Chapters 4 and 6, selecting intermediate values of the surface impedance of graphene also provided other extra features such as active tuning of the reflection coefficient and operational bandwidth as well as selection of any resonant frequency between two extreme values. This feature is similarly found in reconfigurable antennas where varactors are used for switching. For this reason, graphene could be proposed as an all-in-one switching solution.

- This thesis was the first work to analyse, study and investigate, in the microwave regime, other elements and aspects that are also important in order to obtain a realistic, or as close as possible, performance evaluation of reconfigurable antennas made of graphene. For instance, this thesis provided a formula that relates the power consumed by the tuning structure to some important parameters such as the applied DC voltage bias, the characteristics of the dielectric used in the tuning structure, the switching time between states and the dimensions of the graphene sheets. In addition, it also fully considered, theoretically, the effect of the tuning structure and how it affected the graphene and antenna performance. Furthermore, a deep and detailed study of the graphene scattering mechanisms, which defines the surface admittance of graphene in the microwave regime, was also provided. In doing so, this thesis only considered realistic and realisable values of the surface impedance of graphene when applying reasonable values of the DC bias voltage. Other works found in the literature tend to oversimplify this point.

- Taking advantage of the high transparency of graphene to visible light, this thesis proposed graphene as a solution to provide reconfigurability to antennas that are required to be transparent in order to reduce their visible impact, and hence, footprint. Additionally, this thesis also proposed graphene as a solution in wearable antennas where the flexibility of graphene and the various features of antenna reconfigurability might be useful to compensate for the effects of bending and stretching that the wearable antennas normally experience.

7.3 IMPACT OF GRAPHENE PROPERTIES ON RESEARCH FINDINGS

Some of the proposed antenna designs in this thesis had worse performance when compared to other state-of-the-art frequency and polarization reconfigurable antennas. This is somehow expected as graphene, although being an exceptional conductor, is just one atom thick and therefore its surface impedance cannot be improved by increasing its thickness. This is the main disadvantage of graphene when compared to conventional materials at microwave and millimetre wave frequencies. Moreover, the deformation potential D is still not well defined and heavily depends on the graphene sample and thus can take a wide range of values. This highly affects the true potential of graphene as a high value of D translate into high Zs_{ON} and at the same time into a low antenna efficiency, and vice versa. This is because even if all the long range scattering mechanisms such as defects, substrate induced scatterings, wrinkles, impurities, etc.; were all reduced or completely removed, the interaction between charge carriers and phonons would ultimately limit the lowest surface impedance of graphene, and hence, its performance, at room temperature and at the microwave and millimetre wave regime. Consequently, it would only be possible to define the true potential of antennas made of graphene when the limits of the deformation potential is fully known and controlled, via more research.

7.4 FUTURE WORK

Building prototypes of the proposed antenna designs and carry out experimental measurements will ultimately confirm the correct operation of the proposed antenna designs. That will also provide an insight of some adverse effects that have not been considered in the simulations. These effects might arise from current state-of-the-art graphene samples, the DC feed lines of the tuning structure and

the tuning structure itself. The DC feed lines and the tuning structure are expected to not affect the antenna performance much. However, applying graphene sheets produced by using present technology will definitely impact the antenna performance as, currently, the synthesis, transfer and preparation processes are still under development. More research is needed to define processes that allow pristine-like performance of graphene and to avoid the loss of quality of the graphene sample during the transfer process and when building the rest of the elements in the antenna.

In addition, more research could be done to investigate the performance of implementing graphene in other classes of antennas such as slot, pre-fractal and leaky-wave antennas to provide all sorts of frequency, polarization, radiation pattern, bandwidth and/or matching network reconfigurability. Such work could also consider designs of microstrip and metamaterial antennas that could further increase the antenna efficiencies while keeping or adding more antenna reconfigurability. The ability of controlling the variable surface impedance of graphene might be of particular interest in antenna arrays. This might prove useful for adaptive beam-forming applications.

Moreover, the variable surface impedance of graphene might also be useful in other components of the front-end communication systems such as in matching networks, filters, amplifiers, mixers, splitters, etc. This could result in a sort of smart radio-frequency transmission and reception front-end with dynamic control of all the components involved in the communication process.

Finally, there are other interesting novel materials such as silicene, germanene, nano-cellulose and conductivie inks and textiles that might also provide some other benefits in antennas, and therefore, might be worth to investigate. Perhaps, future antennas for base stations, access points and wireless and mobile devices will benefit from tailor-made designs composed of not just one of these materials but of a multitude of them.

Appendix A: DIPOLE ANTENNAS ENTIRELY MADE OF CARBON NANOTUBES

In this section, the performance of dipole antennas made of SWCNT, MWCNT and bundles is simulated following an equivalent transmission line approximation where the special condition of the admittance of carbon nanotubes is taken into account [102]. Special interest is paid to the radiation efficiency and size reduction trade-offs. First, the initial considerations and the different carbon nanotube configurations are defined in subsection A.1. Later, the simulated results are discussed in subsection A.2.

A.1: EVALUATED ANTENNAS

Taking advantage of the cylindrical nature of the carbon nanotubes, dipole antennas made by single-wall carbon nanotubes, multi-wall carbon nanotubes and bundles of single- and multi- wall carbon nanotubes are evaluated here, see Fig. a.1. It is assumed that the carbon nanotube dipoles are generated by flaring 90° the end section of a parallel transmission line made of carbon nanotubes. Therefore, no contact resistance between the transmission line and the antenna is considered here as both the transmission lines and the dipole antennas are made of the same carbon nanotube. Likewise, the antenna matching to the source is not considered here.

The performance of antennas entirely made of carbon nanotubes is carried

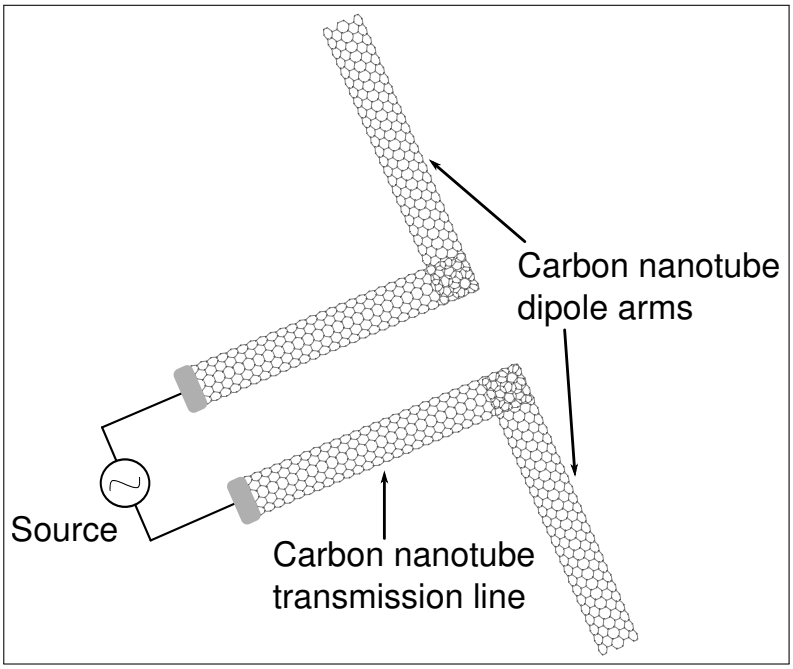

Figure a.1: Graphical representation of a dipole antenna entirely made of carbon nanotubes.

out by analysing the radiation efficiency η_r and the size reduction as the ratio between the plasmon phase constant k_p and the free space phase constant k. The radiation efficiency and plasmon wavenumber are evaluated following a similar process found in [102]. The process determines the antenna efficiency of carbon nanotube dipoles by calculating the power lost as heat in the dipole and the power radiated by the dipole. In order to do so, the large resistance, kinetic inductance and quantum capacitance are introduced in the equations to obtain the current distribution along the dipole antenna. From the resulting current distribution, the radiation power and ohmic power are calculated. In addition, the plasmon wavenumber is calculated by finding the propagation velocity of the wave propagating in the carbon nanotube under the effect of the kinetic inductance and quantum capacitance. The equation used to calculate the radiation efficiency η_r (dB) is, see equation (2.8) in chapter 2 for a detailed analysis,

$$\eta_r = 10 \log \left(\frac{P_{rad}}{P_{rad} + P_{loss}} \right), \qquad \text{(a.1)}$$

where P_{rad} (W) is the power radiated by the carbon nanotube dipole (SWCNT, MWCNT or SWCNT and MWCNT bundle dipole) and P_{loss} (W) is the power lost as heat in the carbon nanotube. The plasmon phase constant k_p is calculated as, see equation (2.87) in chapter 2 for a detailed analysis,

$$k_p = \frac{2\pi f_{res}}{v_p}. \qquad \text{(a.2)}$$

Commonly, the propagation velocity v_p (m/s) of waves in transmission lines and antennas made of conventional metallic materials are very close to the speed of light c. However, due to the large kinetic inductance present in the carbon nanotubes, waves propagating on carbon nanotubes are much slower than when propagating in free space. This is the main cause of the apparence of plasmons in carbon nanotubes.

Equations (2.82) and (a.2) are dependent on setting values for the radius r_{SWCNT} of the SWCNTs, the number of shells N of MWCNT and the number of tubes N_b in the SWCNT and MWCNT bundles. This is because the resulting resistance per unit length R_{CNT}, kinetic inductance per unit length L_K and quantum capacitance per unit length C_Q change for different physical configurations of carbon nanotubes.

RESULTS

In this section, the radiation efficiency η_r and plasmon phase constant k_p are analysed for different values of SWCNT radius r_{SWCNT}, number of shells in MWCNT N and number of tubes for SWCNT and MWCNT bundles N_b at three different resonant frequencies f_{res}=2.45 GHz, f_{res}=60 GHz and f_{res}=110 GHz. For the simulations, the voltage applied to the terminals of the dipole is always $V_{terminals}$=1 V, the separation between the carbon nanotubes is sep=1 mm and the inner radius for the MWCNT case is r_{inner}=0.5 nm. The carbon nanotube dipoles

are assumed to be surrounded by free space, thus ϵ_r=1. Finally, the admittance of the SWCNT σ_{SWCNT} is extracted from equation (2.80) in chapter 2 for radii r_{SWCNT} $\leq$3.4 nm, and from equation (2.78) in chapter 2 for r_{SWCNt} $\geq$3.4 nm and considering that armchair SWCNTs are always used. During the analysis, a value of radiation efficiency that can be considered to be potentially applicable to commercial applications is η_r $\geq$-10 dB. Below this value, the antenna is considered to be excessively lossy and only in very extreme applications might the antenna be used.

Fig. a.2.a shows the radiation efficiency and the ratio between the plasmon phase constant and the free space phase constant of $\lambda/2$ dipole antennas made of single-wall carbon nanotubes with different radii. It can be seen that by increasing the radius of the SWCNT dipoles, the radiation efficiency is improved. However, for any value of the radius, the radiation efficiency is below -10 dB and hence too small for commercial applications. The reason is, although carbon nanotubes have considerably lower resistance per unit lengths R_{CNT} than for other nanotube materials with same dimensions (i.e. copper), the resistance per unit length found in SWCNT is still excessively high for antenna applications. Focusing on the k_p/k ratio, it is confirmed that dipole antennas made of SWCNTs can present substantially larger phase constants, and hence smaller resonant lengths than in free space. This applies for all values of the radius wall but the size reduction advantage is diminished by the exceptionally low efficiencies that results. The size reduction advantage is, at the same time, a disadvantage because small SWCNT dipoles still suffer from the effects of electrically small antennas, and hence, they are naturally inefficient, see section 2.1.3 in chapter 2 regarding electrically small antenna limitations. Therefore, it is concluded that SWCNT dipoles are not acceptable for antenna applications at the frequencies of interest.

Note that, for simplicity, the plasmon resonant frequencies obtained here are assumed to be available at any frequency. However, in reality, plasmon resonances are damped for frequencies lower than the relaxation frequency υ=$1/2\pi\tau$ [32],

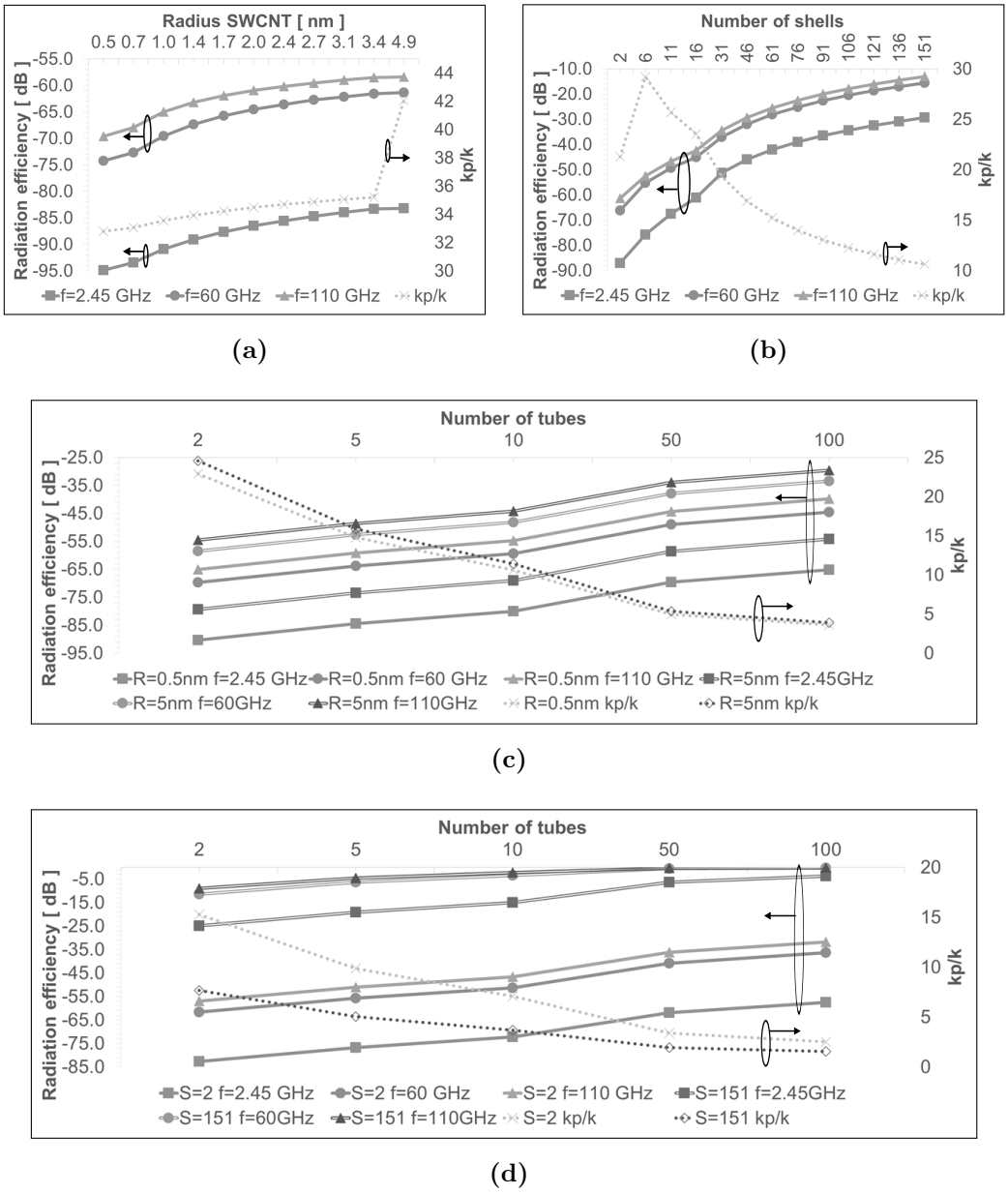

Figure a.2: Radiation efficiency (solid lines) and wavenumber ratio (dashed lines) for (a) SWCNT, (b) MWCNT, (c) SWCNT bundle of SWCNTs with radius 0.5 nm (single solid lines) and 5 nm (double solid lines); and (d) MWCNT bundle of MWCNTs with N=2 (single solid lines) and N=151 (double solid lines).

where τ=$2r_{SWCNT}/\dot{\alpha}T$ depends on the radius of the SWCNT, with $\dot{\alpha}$ ≈9.2 (ms/K). If this condition is accounted for, no plasmon resonance frequencies can

be found at 2.45 GHz because they would be too damped. For the cases of 60 GHz and 110 GHz, the minimum radius that the SWCNT must have is r_{SWCNT} ≈3.4 nm and r_{SWCNT} ≈2 nm for plasmon resonances to be found at 60 GHz and 110 GHz respectively.

Fig. a.2.b presents the results for the radiation efficiency η_r and the phase constant ratio k_p for MWCNT dipoles. Recalling that the total radius for the MWCNT is calculated as r_{MWCNT}=r_{inner}+δN, the simulated radii are from r_{MWCNT}=0.84 nm (N=2 shells) to r_{MWCNT}=51.84 nm (N=151). Similar to the SWCNT dipoles, increasing the number of shells N increases the radiation efficiency because more shells contribute in the conduction of electrons. This is caused by the effect of having more conducting channels in shells with a large radius r_{MWCNT}. On the other hand, when the number of shells increases, the ratio between k_p and k decreases. For the resistance of the MWCNTs dipoles, the more shells contributing to the conduction, the higher the admittance and the lower the kinetic inductance. This increases the speed of the waves v_p propagating in the MWCNTs, which causes v_p to become closer to the value of c and the wavelength is of similar size to its free space equivalent. For a large number of shells and at f_{res}=60 GHz and f_{res}=110 GHz, the radiation efficiencies converge to reasonable values but they are still below the target value of η_r ≥-10 dB. Nevertheless, MWCNTs dipoles might still be considered for antenna applications where some size reduction is desired at the expense of low efficiency.

Fig. a.2.c and Fig. a.2.d give the results of the radiation efficiency and phase constant ratios for antenna dipoles made of bundles of SWCNTs and MWCNTs respectively. Interestingly, Fig. a.2.c shows that even with a large number of SWCNTs in the bundle, the resulting radiation efficiency is still far below the target value of η_r ≥-10 dB. Consequently, there is not a single case where SWCNTs could potentially be used for antenna applications at the frequencies of interest. In contrast, for the MWCNT bundle case, radiation efficiencies of around -10 dB can be achieved with as little as two tubes of MWCNTs with 151 shells

at 60 GHz and 110 GHz, or with fifty tubes of MWCNTs with 151 shells at 2.45 GHz. As a result, it is possible to find an optimum value of N_b for MWCNTs that might satisfy the minimum radiation efficiency of some commercial applications. However, by improving the radiation efficiency, the ratio between k_p and k is drastically reduced and little to no size reduction is obtained when acceptable values of radiation efficiency are achieved. This is an important drawback because one of the main reasons for using carbon nanotubes antennas is the ability to enable significant reduction of the antenna size. Consequently, even in the cases where MWCNTs bundles could be used, it might still not justify the lower antenna performance compared to antennas made of other metallic materials (i.e. copper).

In addition, dipoles made of carbon nanotubes present a very high input impedance (on the order of kΩ) which makes them impossible to match to conventional source impedances of 50 Ω and 75 Ω. Consequently, it is unlikely for them to be of any use at microwave and millimetre wave bands as long as the standard internal impedances of radio-frequency sources are set to 50 Ω or 75 Ω.

Appendix B: PUBLICATIONS

This section provides the four papers published or under review arisen from this thesis:

Alvarez, C. N.; Cheung, R. and Thompson, J. S.; "Graphene reconfigurable antennas for LTE and WIFI Systems", 2014 Loughborough Antennas and Propagation Conference (LAPC 2014), 2014, 434-438.

Alvarez, C. N.; Cheung, R. and Thompson, J. S.; "Polarization Reconfigurable Antennas Using Graphene for Microwave Applications", 2015 IEEE International Conference on Ubiquitous Wireless Broadband (ICUWB 2015), 2015, 1-5.

Nunez-Alvarez, C.; Cheung, R. and Thompson, J. S.; "Performance Analysis Of Hybrid Metal-Graphene Frequency Reconfigurable Antennas For The Microwave Regime", IEEE Transactions on Antennas and Propagation, under third round review.

Nunez-Alvarez, C.; Cheung, R. and Thompson, J. S.; "Performance Analysis Of Hybrid Metal-Graphene Frequency Reconfigurable Zeroth Order Resonant Antennas For Long Term Evolution Applications", IEEE Transactions on Antennas and Propagation, under review.

Graphene Reconfigurable Antennas for LTE and WIFI Systems

Christian Nuñez Alvarez*, Rebecca Cheung† and John S. Thompson*
*Institute of Digital Communications (IDCOM), The University of Edinburgh, Edinburgh EH9 3JL, UK.
e-mail: C.Nunez-Alvarez@sms.ed.ac.uk
†Institute for Integrated Micro- and Nano- Systems, The University of Edinburgh, Edinburgh EH9 3JL, UK.

***Abstract*—This paper presents an initial study of reconfigurable antennas made of graphene for multi-band wireless communications applications. A simple microstrip patch antenna with graphene extensions on its sides has been analysed for Wireless Fidelity (WIFI) operational bands, and another microstrip patch antenna with inset notches filled with graphene strips has been evaluated for Long Term Evolution (LTE) applications. The graphene sheet resistances are changed to activate or deactivate parts of the antenna via DC voltage bias. This changes the effective lengths of the antennas, and therefore, their resonant frequencies.**

I. INTRODUCTION

Future wireless communication systems will need to operate over multiple bands, make use of new spectrum band (mm- and THz wave), adapt to variable communication scenarios and applications, and increase power efficiency. In addition, as science evolves, electronic devices tend to decrease in size. However, size reduction in antennas is not a matter of technology constraint but is limited by the fundamental physics of wave propagation. In order to further shrink a multiband transmitting system, antenna reconfiguration provides an option to colocate multiple radiating elements into a single one, and hence, save space.

A reconfigurable antenna changes its resonance frequency, operational bandwidth, radiation pattern, or polarization by mechanically, electrically or Infrared Light Emitting Diode (IR-LED) switching the current path propagating along the element [1] [2]. Therefore, a single reconfigurable antenna could perform the job of multiple antennas while occupying less space.

Mechanical switching is mostly performed by Micro or Nano Electromechanical systems (MEMS/NEMS) depending on the device scale. Electrical switching is mainly carried out by transistor based technology, such as Metal Semiconductor Field Effect Transistor (MESFET), Pseudomorphic High Electron Mobility transistor (PHEMT); or by diode-based technology, such as the P-type Insulator N-type diode (PIN diode) [**?**]. In this paper we study graphene as an alternative material.

This work was supported by the Engineering and Physical Sciences Research Council (EPSRC) grant no. EP/K503034/1.

With these goals in mind, this paper will analyse the potential use of graphene in reconfigurable antennas for Long Term Evolution (LTE) and Wireless Fidelity (WIFI) applications and is structured as follows: sections 2 will introduce the concept of graphene, with a comparison between switching technologies in section 3. Sections 4 and 5 will describe the scenario evaluated and the results obtained, respectively. Finally, section 6 will present some conclusions and future work.

II. GRAPHENE

Graphene is a mono-atomic layer of carbon atoms distributed in a hexagonal pattern. Graphene was initially a very promising material mainly for nano-electronics due to its extraordinary electrical properties, but because large sheets of graphene have been synthesised recently [3], it can also be used for large scale applications.

Equation (1), e.g. see ref. [4] for more details, shows the frequency-dependency of graphene conductivity.

$$\sigma_s = \frac{-je^2 k_B T}{\pi\hbar^2\left(\omega - j\tau^{-1}\right)}\left(\frac{\mu_c}{k_B T} + 2\ln\left(e^{-\frac{\mu_c}{k_B T}} + 1\right)\right) \quad (1)$$

This approximation is valid for the range of frequencies and the absence of magnetic field assumed here [4]. From the equation, it is possible to observe that there are three parameters that define its conductivity, namely the relaxation time τ, the temperature T, and the chemical potential μ_c. These parameters are related to the quality of the graphene sample, the end application (low, room or high temperatures), and the doping level. In particular, this doping could be active, by bias voltage or electrostatic field, or passive, by addition of chemicals or different substrates. This makes it possible to have very large or very small sheet resistances that could simulate the ON-OFF states in switches. The idea proposed in this paper is to use this effect, via active doping (bias voltage), to control the current passing through selected areas of a patch antenna. This causes a variation in the total length of the path where the current propagates, and hence, a resonant frequency shift. The selected values are Rs=0.5$\Omega/\square$ (corresponding to 30V) and

Rs=430+j1$\Omega/\square$ (corresponding to 0.03V) for the ON and OFF states, respectively. These values are calculated by equation (1) where τ=0.5ps, T=300K, μ_c=4.8e^{-19}eV for the ON state, and μ_c=4.8e^{-21}eV for the OFF state. The absolute values of ON-OFF voltages needed (0.03 V and 30V) could be different in practice as this will depend on the commercial quality of graphene used and the initial chemical potential (here is assumed to be μ_c=0eV), but the difference between ON-OFF would remain the same (around 30V).

III. SWITCHING METHODS

In this section, a brief comparison between today's RF switch technologies is presented along with an analysis of using graphene sheets with DC decoupling capacitors as the switching method in a reconfigurable antenna. Table I shows the comparison between them. The values given for graphene were obtained via simulation or circuit analysis, and all of them are simple theoretical approximations. Experimental measurements will be necessary to provide a confirmation of this analysis.

TABLE I
COMPARISON OF SWITCHING METHODS [1] [5]

Method	Transistor	Diode	MEMS	Graphene
Insertion Loss	0.3-2.5dB	0.3-1.5dB	0.1-5dB	0.3-2dB
Isolation	$\geq$25dB	$\geq$30dB	$\geq$30dB	$\geq$20dB
Power Handling	$\leq$100W	$\leq$50W	$\leq$0.1W	$\leq 1\mu$A/nm
Bias ON/OFF	0V/-5V	0V/-30V	80V/0V	30V/0V
Power Drain	$\leq$0.1mW	$\leq$100mW	$\leq$0.1mW	"Zero"
Switching Time	ns	ns	μs	ns

For the insertion loss and isolation values, a graphene strip with two DC decoupling capacitors was simulated between two ports using the IE3D software from Mentor Graphics. The scenario is presented in Figure 1. The values were obtained while adjusting the width and length of the graphene strip. The insertion loss was calculated from the S12 parameter when the graphene strip was activated, and the isolation was obtained from the S12 parameter when the graphene strip was deactivated. From Figures 2 and 3, it is observed that increasing the width of the graphene band reduced the insertion losses while the isolation value remains constant. On the other hand, increasing the length of the strip augmented the isolation but also the insertion loss. Therefore, there is a trade-off between increasing the length of the graphene sheet in order to increase the isolation value and increasing the width to obtain lower insertion losses.

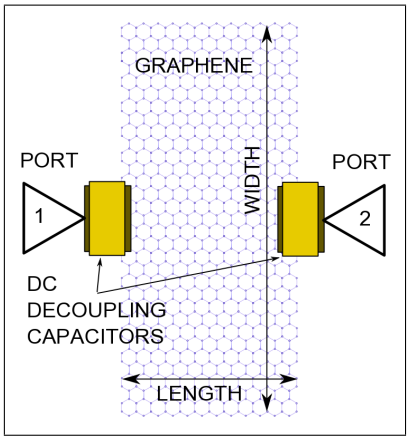

Fig. 1. Switch made of graphene sheet and decoupling capacitors.

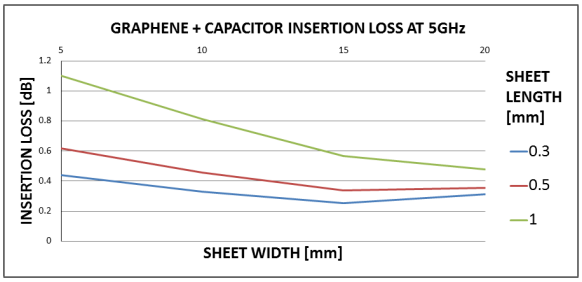

Fig. 2. Insertion loss evolution as length and width are increased.

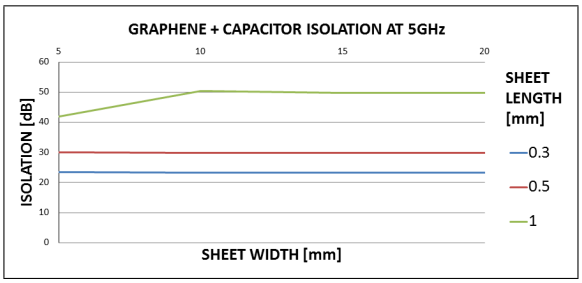

Fig. 3. Isolation values when width and length are increased.

Measurements carried out in [**?**] concluded that graphene sheets can typically handle up to 1μA/nm. Consequently, graphene with DC decoupling capacitors can handle a range of power depending on the dimensions of the sheet and the characteristics of the capacitor used.

The strongest benefit of using graphene is its theoretically zero power consumption as it is approximated as a capacitor when a DC voltage is applied. This will be key for power saving in future devices. However, in practice, there will be a very small leakage current being consumed as the substrate will not be a perfect isolator. Nevertheless, simulations show this leakage current will be on the order of nano Amperes (nA) or less depending on the dimensions of the graphene sheet and the voltage applied.

The switching time has been approximated as the

time that the electric field (or Voltage) on the graphene sheet would take to reach $\sim 66\%$ of the final value. This time, in capacitors, is called the time constant (τ) and depends on capacitance and resistance values. In this case, the capacitance depends on the area of the graphene sheet, the height between this sheet and the ground plane; and the substrate used. Roughly speaking, the capacitance will be on the order of pico Farads (pF) for a substrate with $\epsilon_r = 2 - 10$, height of 1mm and a sheet area of up to 400mm^2. These values are likely to be used in the range of frequencies and applications of interest. The series resistance is the surface resistance (on the order of hundreds of Ω) of graphene if the rest of the DC feed circuit is kept almost lossless. All together, it results in a time constant on the order of nano seconds (ns).

Table II presents different insertion losses and isolation values for different choices of graphene quality (which alters the relaxation time). Results were obtained from the same scenario as Figure 1 at 5GHz and with a 1mmx10mm (length x width) graphene sheet. Using a worse quality graphene (smaller τ) translates into higher sheet resistances for both ON and OFF states. This improves isolation values at the expense of higher insertion losses. In the same manner, better quality graphene (larger τ) reduces both sheet resistance values, which helps to reduce the insertion losses but will adversely affect also the isolation. This could be compensated by augmenting the voltage difference between the ON-OFF states. Therefore, there is another trade-off between selecting the graphene quality and the feed voltages.

TABLE II
COMPARISON OF DIFFERENT GRAPHENE QUALITIES

Relaxation time τ	0.1ps	0.5ps	1ps
Rs ON	2.8Ω/□	0.5Ω/□	0.28Ω/□
Rs OFF	2116+j1Ω/□	430+j1Ω/□	214+j1Ω/□
Insertion Loss	2dB	0.81dB	0.68dB
Isolation	70dB	50dB	35dB

Finally, graphene is transparent and flexible which allows it to be easily integrated in future mobile terminals and devices. In addition, the complexity of producing devices based on graphene promises to be lower than any other method as graphene is a simple atomic layer deposited over a substrate.

IV. NOVEL ANTENNA DESIGNS

Simulations of two simple designs of reconfigurable microstrip patch antennas are evaluated for two different range of frequencies. One set of frequencies (2.4 / 3.6 / 5 GHz) corresponding to WIFI frequency bands, and another set (1.8 / 2.1 / 2.6 / 3.6 GHz) for LTE systems, are simulated using the IE3D software from Mentor Graphics. Two different designs are analysed in order to demonstrate two configurations where graphene could be used in reconfigurable antennas.

The first structure for WIFI is composed by a central rectangular patch with two extensions of graphene added on the sides, see Figure 4. The idea is very similar to the one proposed by [2], but in this scenario, the side bands conductivity are tuned via a DC voltage bias instead of adding a more complex and power consuming IR-LED system. When deactivated, the current stops flowing through the side bands and a resonant frequency (3.6GHz) is defined set by the length of the central patch (22.35mm). When activated, the side bands allow the current to pass through, so it travels a longer distance. This extra distance (35.8mm) changes the resonant frequency to a lower band (2.4GHz). In addition, the width of the antenna (15.4mm) also defines another resonant frequency (5GHz). In this case, this frequency does not change when activating or deactivating the extensions.

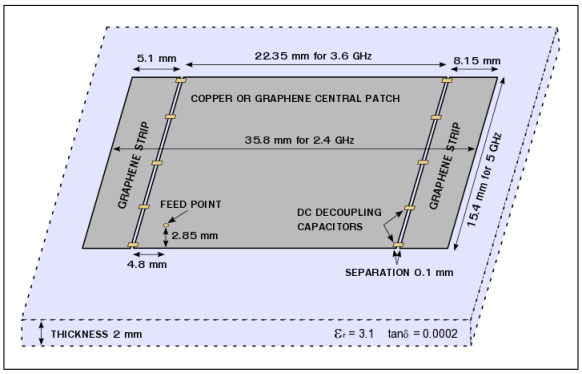

Fig. 4. Graphene reconfigurable antenna for WIFI.

The second structure for LTE is based on a microstrip patch antenna with inset notches on the edges, where graphene strips are added in those spaces, see Figure 5. With a similar function as in the previous design, the graphene strips are activated or deactivated by increasing or reducing their conductivity. When activated, the current is able to travel through the graphene strips and the resonant frequencies (2.1GHz and 3.6GHz) are defined by the length (40.5mm) and width (21.7mm) of the patch, respectively. When the "graphene strip group 1" is deactivated, the graphene bands prevent the current passing through them, and therefore, they acted as notches diverting the current. This causes the current to travel a longer distance and the resonant frequency is changed to a lower band (1.8GHz). Likewise, when the "graphene strip group 2" is deactivated, the resonant frequency moves to (2.6GHz).

In both designs, the strips need to be connected to the central patches via decoupling capacitors in order

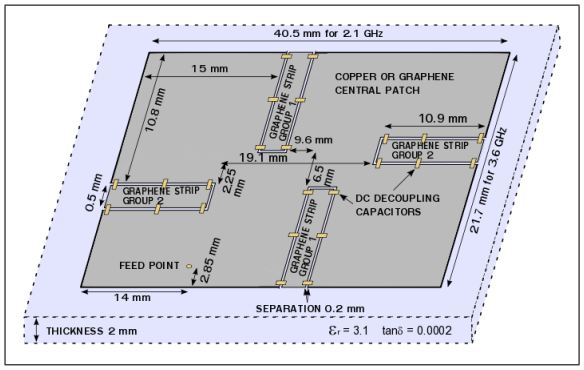

Fig. 5. Graphene reconfigurable antenna for LTE.

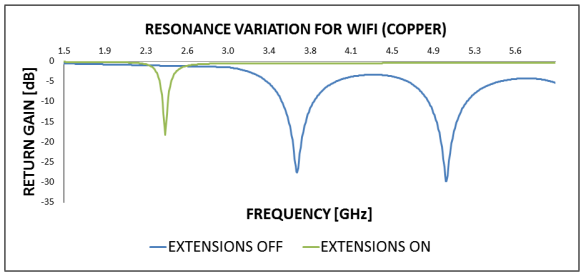

Fig. 6. Resonant frequency shift for WIFI reconfigurable antenna made of copper and graphene bands.

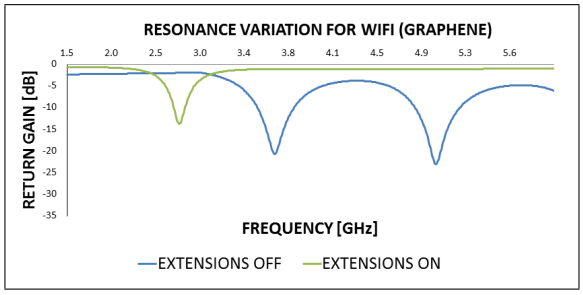

Fig. 7. Resonant frequency shift for WIFI reconfigurable antenna made entirely of graphene.

to isolate each DC bias voltage from the rest. This is important as it was necessary to be able to feed with different voltages to each strip at any moment. The conductors used in the central patches are first set to be copper, and then graphene. The idea is to analyse the performance of the reconfigurable antennas using a very good conductor for normal applications and graphene for potential applications where transparency or flexibility is a requirement. Likewise, polystyrene (PS) is considered for the substrate because of its transparency and flexibility, with a reasonable relative permittivity $\epsilon_r = 3.1$ and loss tangent $\tan\delta = 0.0002$. The conductivity of the graphene bands and strips are individually modified to simulate the variable sheet resistance (Rs) when applying a DC bias voltage to graphene. Furthermore, when graphene is used in the central patch, the conductivity can be changed to any desired value. Finally, the inner area is fed close to a corner so the Transverse Magnetic modes 01 and 10 (TM01 and TM10) are excited.

V. RESULTS

Results presented in this section are divided into data obtained when copper is the conductor for the central patch and the results obtained when graphene is the conductor used instead. Figure 6 shows the WIFI reconfigurable antenna (Figure 4) made of copper and graphene extensions resonating at different frequencies. When the extensions are deactivated, the antenna is in its smallest physical dimension because no current can flow through the graphene bands on the edges. In that case, the two resonant frequencies come from the TM01 and TM10 modes. Then, when the extensions are activated, the current is able to pass, and therefore, the physical dimension is effectively increased allowing the mode TM01 to change its resonant frequency to a lower band. Likewise, Figure 7 presents the same behaviour when using graphene for the central patch.

The main differences between both solutions are the extracted efficiency and bandwidth values, see Table III. When using copper, the antenna efficiency is higher than when using graphene, but using graphene as the conductor for the central patch allows a certain degree of tuning of the return gain and bandwidth of the antenna at the expense of reducing its efficiency. This is achieved by increasing or decreasing the conductivity of the sheet which causes the input impedance to also increase or decrease.

TABLE III
EFFICIENCY AND BANDWIDTH COMPARISON WIFI ANTENNA

Material	Frequency [GHz]	2.4	3.6	5
Copper	Efficiency [dB]	-4.3	-6.9	-3.1
	Bandwidth [MHz]	40	280	350
Graphene	Efficiency [dB]	-8.2	-7.5	-3.8
	Bandwidth [MHz]	90	310	380

As a demonstration, the WIFI reconfigurable antenna made entirely of graphene is analysed for different sheet resistance values of the graphene sheet used for the central patch. Figure 8 demonstrates that changing the Rs allows for a wider or narrower bandwidth and, in certain conditions, a better matching. The initial value of sheet resistance for the central patch is $Rs = 0.5\Omega/\square$. Under this condition, the return gain is around -13dB, but when the conductivity is changed to $Rs = 1\Omega/\square$, the return gain greatly improves to -28dB.

Finally, the same analysis can also be applied to the LTE reconfigurable antenna made of copper/graphene with graphene strips on the notches, see Figure 5. Fig-

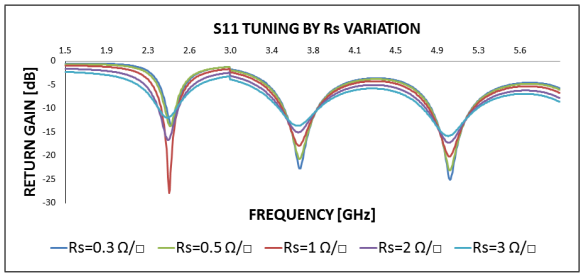

Fig. 8. Return gain (S11) variation by changing the central patch Rs from a reconfigurable antenna made entirely of graphene.

ure 9 shows the shift of the resonant frequencies when activating and deactivating the strips. When activated, the current is able to pass through the graphene strips, and therefore, the electrical size is close to the physical dimensions. The two resonances are due to the TM10 and TM01 modes. When the strips are deactivated, the current travelling through the patch is diverted as it is not able to pass through the graphene strips, and then, the electrical size of the antenna is much larger than the physical size as the current has to travel longer distances. This causes the resonances to move to lower frequencies. Figure 10 shows the same behaviour when graphene is used in the central patch. Again, the main differences are found in the efficiency values and the bandwidths achieved, see Table IV. Radiation efficiencies are higher when copper is the main conductor but bandwidths are larger when graphene is used instead.

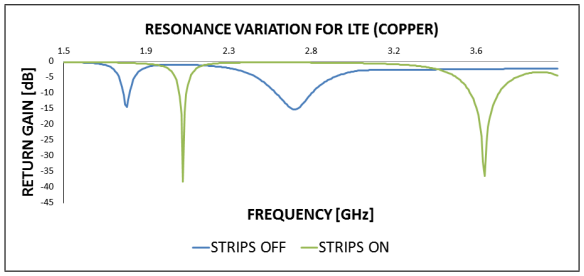

Fig. 9. Resonant frequency shift for LTE reconfigurable antenna made of copper and graphene strips.

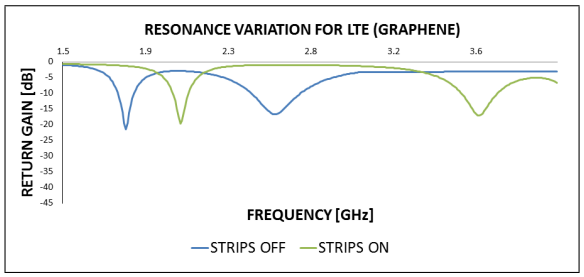

Fig. 10. Resonant frequency shift for LTE reconfigurable antenna made entirely of graphene.

TABLE IV
EFFICIENCY AND BANDWIDTH COMPARISON LTE ANTENNA

Material	Frequency [GHz]	1.8	2.1	2.6	3.6
Copper	Efficiency [dB]	-7.3	-12.8	-4.1	-1.6
	Bandwidth [MHz]	30	35	180	150
Graphene	Efficiency [dB]	-8.2	-13.9	-8	-3.9
	Bandwidth [MHz]	81	80	250	180

VI. CONCLUSIONS

This paper has demonstrated a potential use of graphene in reconfigurable antennas for both LTE and WIFI applications. The results obtained from simulating both antenna designs show that switching the conductivity of the graphene bands and strips between ON and OFF states allows one to modify their resonances. Using copper, or any other conventional metal, as the main conductor for the central patch delivers higher efficiencies than when graphene is considered. However, the option of graphene adds a degree of tuning for the bandwidth and return gain, as well as, a solution for applications where transparency and flexibility are a requirement.

Simulation results from graphene as a switching element suggest that its performance is not far from other state of the art technologies and could save power and complexity in future reconfigurable antennas. Nevertheless, experimental measurements must be performed to show the practical viability of graphene as a switching method. Similarly, prototypes of the antennas proposed here need to be built in order to confirm the feasibility of the designs. Future work will be focus on these matters.

REFERENCES

[1] R. L. Haupt and M. Lanagan. Reconfigurable antennas. *IEEE Antennas Propag. Mag*, 55(1):49–61, 2013.
[2] R. L. Haupt. Reconfigurable patch with switchable conductive edges. *Microw. Opt. Technol. Lett.*, 51(7):1757–1760, 2009.
[3] S. Bae et al. Roll-to-roll production of 30-inch graphene films for transparent electrodes. *Nat. Nanotechnol.*, 5(8):574–578, 2010.
[4] G. W. Hanson. Dyadic Greens functions and guided surface waves for a surface conductivity model of graphene. *J. Appl. Phys.*, 103(6), 2008.
[5] P. Hindle. The state of RF/microwave switches. *Microwave J*, 53(11):20–36, 2010.

Polarization Reconfigurable Antennas using Graphene For Microwave Applications

Christian Nuñez Alvarez*, Rebecca Cheung† and John S. Thompson*
*Institute of Digital Communications (IDCOM), The University of Edinburgh, Edinburgh EH9 3JL, UK.
e-mail: C.Nunez-Alvarez@sms.ed.ac.uk
†Institute for Integrated Micro- and Nano- Systems (IMNS), The University of Edinburgh, Edinburgh EH9 3JL, UK.

***Abstract*—This paper presents a study of using graphene in polarization reconfigurable antennas for wireless communication applications in the microwave regime. Two scenarios are analysed and simulated based on the square patch antenna made of copper or a hybrid transparent film where the truncated corners are replaced by graphene extensions. The graphene extensions are activated or deactivated by applying two different DC bias voltages. This design allows one antenna to switch dynamically between linear and circular polarizations.**

I. INTRODUCTION

Wireless devices are becoming packed with more applications that require an increasing number of communication technologies. Ideally, every communication subsystem should have a dedicated antenna. However, the space available for these elements are conversely being reduced more and more. A potential solution to save space in wireless devices is to use reconfigurable antennas where multiple antennas can be integrated into one. A reconfigurable antenna is able to change actively any of its radiation properties such as resonant frequency, bandwidth, radiation pattern, or polarization. This is commonly achieved by using mechanical or electrical switches, varactors or tunable materials which use a mechanical, electrical, magnetic, light or thermal bias [1]. Polarization in an antenna defines the time varying orientation and relative magnitude of the electric-field vector when the antenna is radiating or receiving electromagnetic waves [2]. The polarization of an antenna can be linear, circular or elliptical. In general, any communication system can operate using any polarization, but in practice, some polarizations are preferred to others for particular applications. In terrestrial broadcasting and mobile communications, linear polarization is widely, but not exclusively, used as the amount of electromagnetic radiation coupled is higher and the position of the antennas are assumed to be known, while circular polarization is mainly used for satellite-to-earth communications due to the Faraday rotation effect present in the ionosphere [3]. However, in multipath environments or when the orientation of the antennas is unknown, circular polarization can be used as it is more robust than linear polarization in such conditions. This paper will analyse the use of the variable conductivity of graphene as a potential method to switch between different polarizations. The proposed antennas are made of copper or a hybrid transparent film where graphene sheets are added to the structure since antennas fully made of graphene are inefficient. The paper is structured as follows: Section II will introduce the concept of the variable conductivity of graphene with a brief description of its limitations. Sections III and IV will describe the scenarios evaluated and present the results obtained, respectively. Finally, Section V will summarise some conclusions and future work.

This work was supported by the Engineering and Physical Sciences Research Council (EPSRC) grant no. EP/K503034/1.

II. CONDUCTIVITY OF GRAPHENE

Graphene is a flat mono-atomic layer of Carbon atoms distributed in a two-dimensional honeycomb-like lattice through sp2 bonding. Recent improvements on material synthesis is allowing the production of large sizes of graphene sheets [4]. This opens the possibility of using graphene for large scale applications in the microwave regime. In this paper, the variable conductivity of graphene is used to switch between linear and circular polarization by using a large sheet resistance in the OFF state (Rs_{OFF}) and a low sheet resistance in the ON state (Rs_{ON}). For the range of frequencies considered in this paper and in the absence of a magnetic field, the graphene conductivity can be approximated following equation (1), e.g. see ref. [5] for more details,

$$\sigma_s = \frac{-jq^2 k_B T}{\pi\hbar^2\left(\omega - j\tau^{-1}\right)}\left(\frac{\mu_c}{k_B T} + 2\ln\left(e^{-\frac{\mu_c}{k_B T}} + 1\right)\right), \quad (1)$$

where T is temperature (K), w is the angular frequency $2\pi f$ (rad/s), τ is the relaxation time (s) and μ_c is the chemical potential (eV). As observed from equation (1), the conductivity, and consequently the sheet resistance of graphene ($Rs = \sigma_s^{-1}$) is dependent on the surrounding temperature T, the quality of the graphene sheet τ and the chemical potential μ_c. In graphene, the chemical potential μ_c is related to the carrier density n (m^{-2}) [6] as shown in equation (2)

$$n \simeq \frac{(\mu_c/\hbar v_f)^2}{\pi}, \tag{2}$$

where $v_f = 1 \times 10^6$ (m/s) is the Fermi velocity in graphene. The carrier density can be dynamically modified via the electric field effect [6] [7] following equation (3)

$$n = \frac{\epsilon_o \epsilon V_b}{de}, \tag{3}$$

where ϵ_o is the vacuum permittivity (F/m), V_b is the DC voltage bias (V), d and ϵ is the thickness (m) and relative permittivity of the dielectric separating the graphene sheet and the back gate material (a p or n doped semiconductor) respectively. Consequently, the conductivity of graphene can be tuned by applying a variable DC bias voltage.

In simple approximations, the relaxation time is assumed to be independent of the chemical potential [7], however, in practice this is not always the case. The number of carriers induced in graphene n directly affects the relaxation time since different scattering mechanisms dominate at different carrier densities [8]. At low carrier densities, the electron mobilities μ in graphene is mainly determined by the defects and impurities present in the material itself and in the substrate supporting the graphene sheet [6]. The relaxation time τ_L due to these long-range scattering mechanisms is related to the electron mobility following equation (4)

$$\sigma = ne\mu_L = \frac{ne^2\tau_L}{m} \simeq \frac{ne^2\tau_L v_f}{\hbar\sqrt{n\pi}}, \tag{4}$$

where σ is the DC conductivity (S/$\square$), μ_L is the electron mobility due to long-range scattering (m^2/Vs) and m is the carrier mass (Kg). Furthermore, the minimum achievable chemical potential $\mu_{c,min}$ is limited by thermally excited carriers [9] and electron-hole puddles caused again by charged impurities [10]. The conductivity equation in (1) already considers the thermally excited carriers since it is temperature dependent. The energy of the electron-hole puddles ε_{puddle} (or the lowest possible chemical doping level) follows equation (5)

TABLE I: Selected sheet resistance values

Set	1		2	
State	ON	OFF	ON	OFF
n [m^{-2}]	5×10^{16}	6×10^{14}	5×10^{17}	6×10^{14}
V_b [V]	22.72	$\sim$0	22.72	$\sim$0
μ_L [m^2/Vs]	2.7		2.7	
D [eV]	4	4	18	18
Rs [$\Omega/\square$]	6+j0.3	2580+j6	34+j0.3	2580+j6

$$\varepsilon_{puddle} = \mu_{c,min} = \hbar v_f \sqrt{\pi \tilde{n}}, \tag{5}$$

where $\tilde{n}$ is the carrier density variations (carrier inhomogeneity density) caused by the electron-hole puddles. This forces the number of carriers to be greater than or equal to this value and therefore the minimum achievable chemical potential $\mu_{c,min}$ used to compute the conductivity in equation (1) is equal to this electron-hole puddle energy ε_{puddle}. On the other hand, at high carrier densities, the longitudinal phonons (LA-phonons) limit the minimum sheet resistance achievable when applying large DC bias voltages [8]. The relaxation time set by the LA phonons follows the equation (6)

$$\tau_{ph} = \tau_S = \frac{4\hbar^2 \rho_m v_{ph}^2 v_f}{\sqrt{n\pi} D^2 k_B T e}, \tag{6}$$

where D is the deformation potential (eV), $\rho_m = 7.6 \times 10^{-7}$ is the two dimensional mass density of graphene (Kg/m^2) and $v_{ph} = 2.1 \times 10^4$ is the sound velocity of LA phonons in graphene (m/s). The precise value of D is still being discussed as it could range between 4 eV and 30 eV, with 18 eV the most common value found in the literature. As a result, the total relaxation time τ_t affected by the different scattering mechanisms can be calculated from the Matthesen rule as [6]

$$\frac{1}{\tau_t} = \left(\frac{1}{\tau_{de}} + \frac{1}{\tau_{im}}\right) + \left(\frac{1}{\tau_{ph}}\right) = \left(\frac{1}{\tau_L}\right) + \left(\frac{1}{\tau_S}\right), \tag{7}$$

where each τ_x is due to a single scattering mechanism such as defects (τ_{de}), impurities (τ_{im}) and phonons (τ_{ph}). The value of τ_t will be later used in equation (1) to compute the conductivity. Table I provides the values for Rs_{ON} and Rs_{OFF} used in this paper.

The values of sheet resistances for the ON and OFF states (Rs_{ON} and Rs_{OFF} respectively) in Table I are obtained from equation (1) where τ is calculated from equation (7). The scalars τ_{de} and τ_{im} are combined into τ_L which is related to μ_L as in equation (4). The value of μ_L is extracted from reference

[11] and $\tau_S = \tau_{ph}$ is obtained from equation (6) setting different deformation potentials D at room temperature 295 K. Specifically, the Rs_{ON} value is found by increasing the charge carrier density n until saturation is reached as the LA phonon scattering becomes dominant and at the same time not too high a DC bias voltage is required. On the other hand, the values for Rs_{OFF} are obtained assuming that the minimum chemical potential is equal to the energy of the electron-hole puddles ($\mu_{c,min} = \varepsilon_{puddle}$) following equation (5) where its carrier density value is extracted from [11] as $\tilde{n}$=6×10^{14} m^{-2}. In addition, V_b values are obtained from equation (3) considering that the graphene sheets are deposited over hexagonal boron nitride (hBN) which has a thickness d=10 nm and a relative permittivity ϵ=4 [12].

III. ANTENNA DESIGNS

Two scenarios are evaluated to introduce a potential use of graphene in polarization reconfigurable antennas. The first scenario evaluates a single polarization reconfigurable antenna based on a square patch antenna with corners truncated to cover Digital Audio Broadcasting (DAB) at 1.45-1.5 GHz and global navigation satellite systems (GNSS) such as Galileo and GPS, at 1.55-1.6 GHz, Fig. 1. The DAB uses linear polarization while the GNSS operates using circular polarization. Graphene extensions are added to substitute the truncated corners. Activating or deactivating these extensions allows one to switch between different polarizations. Linear polarization is achieved when all the extensions are ON. Right-hand circular polarization (RHCP) is set when only extensions 1 and 2 are OFF while left-hand circular polarization (LHCP) is produced when only extensions 3 and 4 are OFF. The first scenario is studied by using two different materials as the conductor for the main patch. Copper is used to provide antenna efficiencies that are mainly affected by the addition of the graphene extensions, while a hybrid transparent conductive film composed of mesoscale and nanoscale silver and copper nanowires (AgNW/Cu) from [13] with Rs=0.36 $\Omega/_{\square}$ and transparency of 92% is used to simulate a full transparent and flexible polarization reconfigurable antenna.

The second scenario analyses a two element array based on the same design as the first scenario to cover any wireless technology such as wireless fidelity (WIFI), radio frequency identification (RFID) or Bluetooth working at 2.4 GHz, Fig. 2. The second system is designed in order to be able to switch between two linear polarizations (vertical and horizontal) and two circular polarizations (right-hand and left-hand). By switching between different linear and circular polarizations, the system is able to work under different link conditions such as known or unknown orientation of the antennas, and in both line of sight (LOS) or non-line of sight (NLOS) cases. If the antennas are aligned on the same axis, linear polarization (either horizontal or vertical) is desired, while when they are not aligned, circular polarization is preferred as it is independent of the antennas' alignment. In NLOS conditions, the multipath effects are reduced by using circular polarization instead of linear polarization, which is more sensitive to depolarization caused by reflections and refractions. As in the first scenario, activating and deactivating the graphene extensions allows one to switch between different polarizations. When all extensions are ON, both antennas produce linear polarization but with opposite orientation as one antenna produces vertical polarization while the other radiates with horizontal polarization. In this manner, both linear polarizations are covered by the system. When extensions 1 and 2 and/or 7 and 8 are OFF, RHCP is achieved in antenna 1 and/or 2 respectively. In contrast, when extensions 3 and 4 and/or 5 and 6 are OFF, LHCP is produced in antenna 1 and/or 2 respectively. This allows the system to cover both circular polarizations.

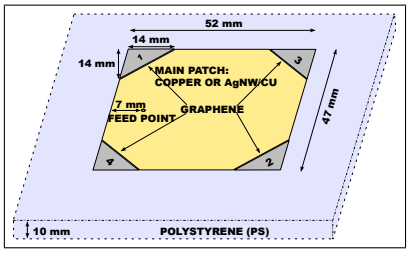

Fig. 1: Square patch antenna made partially of graphene for polarization reconfigurability.

In both scenarios, polystyrene (PS) is always used as the antenna substrate with ϵ_r=3.1 and tanδ=0.0002. Finally, the graphene extensions are referred to be activated or deactivated when the graphene sheet resistance is modelled as Rs_{ON} or Rs_{OFF} (see Table I) in the simulation software, respectively. This would be achieved in a practical scenario by applying one of the two DC bias voltages also defined in Table I.

IV. RESULTS

The results presented in this section are divided into data obtained from the single polarization reconfigurable square patch antenna with graphene extensions in the corners, and the two element array polarization reconfigurable antenna with graphene extensions in the corners. The antennas have been designed in order to

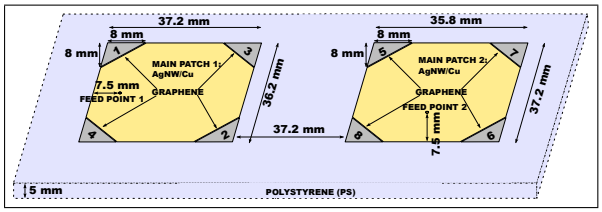

Fig. 2: Array of two square patch antennas made partially by graphene for polarization reconfigurability.

obtain the required polarization for each application. The axial ratio (AR) is used that the proper polarization is achieved. The AR is a figure that represents the ratio between the major and the minor magnitudes of the electric field along each of the x- and y- axis when the electromagnetic wave propagates along the z- axis. It follows equation (8) [2]

$$AR = \frac{Ex}{Ey} \text{ or } \frac{Ey}{Ex}, \tag{8}$$

where Ex and Ey are the electric field components on the x- and y- axis respectively. Ideally, the AR needed for an antenna to radiate with a circular polarization (CP) is AR=0 dB as this corresponds to the two components of the electric field (Ex and Ey) being equal. However, an AR within 3 dB of this value is still accepted as CP. In contrast, linear polarization is achieved when the AR is as high as possible since it means that the electric field is being propagated only on one of the axis.

A. DAB-GNSS SOLUTION

Table II provides the antenna efficiencies (e) and best axial ratios (AR) obtained from the Computer Simulation Technology (CST) solver. The set up column shows what extensions are ON or OFF and what the material is used in the main patch (Copper or AgNW/Cu). The default state of the extensions is ON, unless stated otherwise. From the results shown in Table II, it is observed that switching ON and OFF the extensions allows the change of polarization between horizontal (HORZ) and right-handed and left-handed circular polarization (RCHP and LHCP respectively). The AR obtained for linear polarization is always 40 dB which is the maximum available while the AR extracted for the circular polarizations are within 3 dB of the ideal 0 dB value. The antenna efficiencies obtained are mostly affected by the value of the sheet resistance used for the ON state (Rs_{ON}) as similar results for the antenna efficiency are observed when using copper or AgNW/Cu as the conductor for the main patch. It is important to mention that the

TABLE II: Efficiency and axial ratio results

Comb.	Set up	Pol.	Rs set	e[dB]	AR[dB]
1	1-2 OFF Copper	RHCP	2	-2.25	0.45
2	1-2 OFF AgNW/Cu	RHCP	2	-2.1	0.73
3	1-4 ON Copper	HORZ	2	-2.25	40
4	1-4 ON AgNW/Cu	HORZ	2	-2.55	40
5	1-4 ON Copper	HORZ	1	-1.05	40

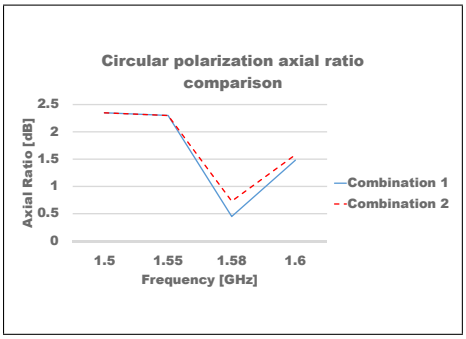

Fig. 3: Axial ratio results for circular polarizations in the DAB-GNSS design.

transparent film losses are not significant as the Rs value is very low. However, if transparent and flexible films with higher Rs values are used it is expected to lead to lower antenna efficiencies. As observed, using the set 1 of Rs_{ON} values from Table I provides a much lower sheet resistance for the ON state than for set 2 and therefore the antenna efficiency is improved by around 1 dB. However, the resulting antenna efficiency is within reasonable range for a patch antenna and only a small improvement is achieved when using much lower sheet resistance.

Fig. 3 shows the axial ratio values for the circular polarization configurations within the required bandwidth for a GNSS application at 1.55 GHz. It is confirmed that the antenna satisfies the condition of having an $AR \leq$3 dB along the GNSS band. It is also observed that changing the conductor of the main patch does not strongly affect the AR value obtained. Note that results for the combination when the extensions 3 and 4 are OFF (LHCP) are not shown as their values are exactly the same as for the ones already shown in Table II and Fig. 3.

B. KNOWN-UNKNOWN ANTENNA ORIENTATION AND LOS-NLOS LINK CONDITION SOLUTION

Table III provides the antenna efficiencies (e) and best axial ratios (AR) obtained from simulations using

TABLE III: Efficiency and axial ratio results

Comb.	Set up	Pol. 1/2	e[dB]	AR[dB]
1	1-2 OFF	RCHP/VERT	-2.45	1.72
2	3-4 OFF	LHCP/VERT	-2.45	1.67
3	5-6 OFF	HORZ/LHCP	-2.25	1.12
4	7-8 OFF	HORZ/RHCP	-2.25	1.53
5-6	1-2 OFF	RHCP/LHCP	-2.45	1.6
	5-6 OFF		-2.25	1.41
7-8	3-4 OFF	LHCP/RHCP	-2.45	1.63
	7-8 OFF		-2.25	1.64
9	1-8 ON	HORZ/VERT	-2.1	40

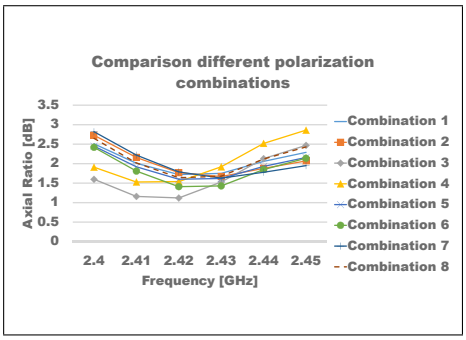

Fig. 4: Axial ratio results for circular polarizations in the two elements array antenna.

CST. The polarization column (Pol. 1/2) gives the polarization being used for antenna 1 and 2 respectively. Again, it is demonstrated that an array of different polarizations is achieved such as horizontal (HORZ), vertical (VERT), right-hand (RHCP) and left-hand (LHCP) circular polarization by switching the graphene extensions between ON and OFF states. As a result, this two element array is able to work effectively with random antenna orientations and with either LOS and NLOS conditions. Likewise, antenna efficiencies are within reasonable values confirming the low impact of using graphene as an alternative method in polarization reconfigurable antennas.

Fig. 4 shows that the achieved axial ratios are always within the 3 dB range along the required bandwidth of a wireless application working at 2.4 GHz.

V. CONCLUSIONS

This paper has demonstrated a potential use of graphene in polarization reconfigurable antennas in two application-oriented scenarios. Results from both scenarios demonstrate that antennas made partially of graphene can switch between the linear polarization required for DAB and the circular polarization required for a GNSS; and to adapt changing environments such us random orientation of the antennas, or when the antennas operate in LOS or NLOS conditions. Antenna efficiency results show that using graphene to switch between polarizations does not strongly affect the performance of the antenna since the area of graphene needed is much smaller than the total area of the antenna. This translates into graphene being a very promising method to provide polarization reconfigurable antennas that at the same time could be integrated in environments where transparency and/or flexibility is a requirement such as car windows or solar panels. In addition, improving the sheet resistance of the ON state from Rs_{ON}=34+j0.3 $\Omega/_{\square}$ to Rs_{ON}=6+j0.3 $\Omega/_{\square}$ only slightly increased the efficiency about 1 dB. Consequently, these antenna designs do not demand very low sheet resistance to work. Finally, the DC voltage bias used in this paper could be reduced if thinner dielectrics, where graphene could be laid, were synthesised with higher relative permittivity ϵ. Future work will be focused on widening designs for reconfigurable antennas that could use graphene while improving the antenna performance by reducing the impact of graphene.

REFERENCES

[1] R. L. Haupt and M. Lanagan, "Reconfigurable antennas," *IEEE Antennas Propag. Mag*, vol. 55, no. 1, pp. 49–61, 2013.

[2] C. A. Balanis, *Antenna theory : analysis and design.* New York ; Chichester : Wiley, 1997.

[3] K.-L. Du and M. N. Swamy, *Wireless communication systems: from RF subsystems to 4G enabling technologies*. Cambridge University Press, 2010.

[4] S. Bae *et al.*, "Roll-to-roll production of 30-inch graphene films for transparent electrodes," *Nat. Nanotechnol.*, vol. 5, no. 8, pp. 574–578, 2010.

[5] G. W. Hanson, "Dyadic Greens functions and guided surface waves for a surface conductivity model of graphene," *J. Appl. Phys.*, vol. 103, no. 6, 2008.

[6] N. M. R. Peres, "*Colloquium* : The transport properties of graphene: An introduction," *Rev. Mod. Phys.*, vol. 82, pp. 2673–2700, Sep 2010.

[7] K. S. Novoselov *et al.*, "Electric field effect in atomically thin carbon films," *Science*, vol. 306, no. 5696, pp. 666–669, 2004.

[8] J. H. Chen *et al.*, "Intrinsic and extrinsic performance limits of graphene devices on SiO_2," *Nat. Nanotechnol.*, vol. 3, no. 4, pp. 206–209, 2008.

[9] T. Fang *et al.*, "Carrier statistics and quantum capacitance of graphene sheets and ribbons," *Appl. Phys. Lett.*, vol. 91, no. 9, p. 092109, 2007.

[10] J. Martin *et al.*, "Observation of electron–hole puddles in graphene using a scanning single-electron transistor," *Nature Phys.*, vol. 4, no. 2, pp. 144–148, 2008.

[11] N. Petrone *et al.*, "Chemical vapor deposition-derived graphene with electrical performance of exfoliated graphene," *Nano Lett.*, vol. 12, no. 6, pp. 2751–2756, 2012.

[12] K. K. Kim *et al.*, "Synthesis and characterization of hexagonal boron nitride film as a dielectric layer for graphene devices," *ACS nano*, vol. 6, no. 10, pp. 8583–8590, 2012.

[13] P. C. Hsu *et al.*, "Performance enhancement of metal nanowire transparent conducting electrodes by mesoscale metal wires," *Nat. Commun.*, vol. 4, 2013.

Performance Analysis Of Hybrid Metal-Graphene Frequency Reconfigurable Antennas For The Microwave Regime

Christian Nuñez Alvarez, Rebecca Cheung and John S. Thompson

***Abstract*—This paper analyses the potential application of graphene in microwave frequency reconfigurable antennas. Two multi-band designs, one for wireless local area networks (WIFI), covering the frequency bands of 2.4 GHz, 3.6 GHz and 5 GHz; and another for the cellular long term evolution (LTE) system, operating the frequency bands of 1.8 GHz, 2.5 GHz, 2.6 GHz and 3.6 GHz; are evaluated to demonstrate the working principle and the performance trade-offs. The designs are made mostly of copper with some parts made of graphene to enable reconfigurable behaviour. The graphene material's surface impedance is tuned by applying a DC bias voltage which allows to obtain one of two extreme values that emulate the ON and OFF states of common switches such as Micro Electromechanical Switches (MEMS), Field effect transistor (FET) and P-type Insulator N-type (PIN) diode, or continuous values to mimic reconfigurable antennas loaded by varactors. This material switching modifies the electrical length of the current propagating through the antenna and consequently switches the resonant frequencies. Additionally, results show that hybrid metal-graphene frequency reconfigurable antennas can, at the same time, provide tunable bandwidth and antenna matching.**

***Index Terms*—Microstrip antennas, microwave antennas, multifrequency antennas, switching frequency.**

I. INTRODUCTION

Future wireless devices will incorporate multiple wireless services operating over a wide frequency spectrum such as 3^{rd} (3G) and 4^{th} (4G) mobile generation and beyond at 700-800 MHz, 1.8-2.6 GHz and 3.6 GHz; wireless fidelity (WIFI) at 2.4 GHz, 3.6 GHz and 5 GHz. In order to shrink a multi-radio transmitting system, antenna reconfiguration provides an option to integrate multiple radiating elements at different frequencies into a single physical antenna, and hence, save space.

A reconfigurable antenna is designed in a manner that it is possible to manually or automatically (via software) change its resonant frequency, operational bandwidth, radiation pattern, and/or polarization to adapt to different services, system requirements and the environment. This is most commonly done with Micro or Nano Electromechanical systems (MEMS or NEMS) [1], [2], electrical RF switches such as Metal Semiconductor Field Effect Transistor (MESFET) and Pseudomorphic High Electron Mobility transistor (PHEMT) [3], [4], diode-based technology such as the P-type Insulator N-type diode (PIN diode) [5], [6], varactors [7], [8] or tunable materials [9]; via applying a mechanical, electrical, magnetic, light or thermal bias [10]. Alternatively, the variable surface impedance of graphene can also be used as tunable material in reconfigurable antennas.

Graphene is a flat mono-atomic layer of Carbon atoms distributed in a two-dimensional honeycomb-like lattice [11]. In addition, an unbiased pristine single layer of graphene (SLG) only absorbs 2.3% [12] of visible light and supports breaking forces of up to 42 N/m with a Young's modulus of 1 TPa and an intrinsic strength of 130 GPa [13] while also being extremely light (0.77 mg/m^2). As a result, a reconfigurable antenna made of graphene could also be transparent, flexible and light weight. Importantly, the admittance of graphene can be tuned by a DC voltage bias and hence high and low impedances can be set to mimic the ON and OFF states found in switches. This effect is used in the present paper to affect the currents propagating in the antenna, and consequently, change the resonant frequency. However, graphene is not only an alternative option to a conventional RF switch, it can be used for fabricating the radiating antenna itself.

Graphene reconfigurable antennas are being mostly studied for infra-red and THz frequencies as graphene can significantly reduce size and provide high antenna reconfigurability at such frequencies [14]–[21]. Since antennas fully made of graphene are expected to have low antenna efficiencies with very little reconfigurability at microwave frequencies [15], [22], the antenna designs proposed here are hybrid metal-graphene frequency reconfigurable antennas where the impact of the high ohmic losses of graphene is reduced while providing

This work was supported by the Engineering and Physical Sciences Research Council (EPSRC) grant no. EP/K503034/1.

substantial antenna reconfigurability. In [23], the concept and analysis of hybrid metal-graphene antennas were introduced for THz frequencies. However, as large area samples of graphene grown by chemical vapour deposition (CVD) have been successfully synthesised [24], this paper carries out a feasibility study of using this novel material as a potential solution for hybrid metal-graphene antennas in the microwave regime. An early work containing similar designs had been presented in [25]. In this paper, a deeper and more detailed analysis on related hybrid metal-graphene frequency reconfigurable antenna designs is presented.

The novel contributions of this paper can be summarized as follows:

- Analyse and simulate two possible hybrid metal-graphene reconfigurable antenna designs to cover WIFI (2.4 GHz, 3.6 GHz and 5 GHz) and LTE (1.8 GHz , 2.1 GHz , 2.6 GHz and 3.6 GHz) frequency bands.
- Present the advantages and disadvantages of using graphene in reconfigurable antennas at microwave frequencies as well as system limitations such as the selection of suitable dielectric-semiconductor layers for the DC voltage bias and the power consumption.

The paper is structured as follows, sections II and III will introduce the admittance of graphene and system limitations, then, section IV will define the proposed antenna designs and the system set up. Afterwards, the simulation results are presented and discussed in section V. Finally, section VI will finish the paper with key conclusions.

II. ADMITTANCE PROPERTIES OF GRAPHENE

For the range of frequencies considered in this paper and in the absence of magnetic field B, the graphene's dynamic, or alternating current (AC), surface admittance can be evaluated in a Kubo-like form in equation (1) [26], [27]

$$\sigma_{AC} \approx \frac{-jq^2 k_B T}{\pi\hbar^2(\omega - j\tau_t^{-1})}\left(\frac{\mu_c}{k_B T} + 2\ln(e^{-\frac{\mu_c}{k_B T}} + 1)\right), \tag{1}$$

where ω is the angular frequency $2\pi f$ (rad/s), f is the operating frequency (Hz), μ_c is the chemical potential (J), τ_t is the relaxation time (s) which is assumed to be independent of the energy ε [27], T is the temperature (K), q is the elementary charge (C), $\hbar$ is the reduced Planck's constant (Js) and k_B is the Boltzmann constant (J/K). In graphene, the chemical potential μ_c is related

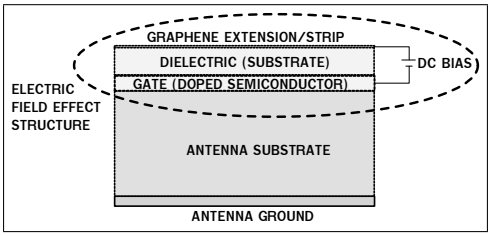

Fig. 1: Example of an electric field effect structure added to a patch antenna.

to the carrier density n (m^{-2}) as shown in equation (2) [11], [28]

$$\mu_c \simeq \hbar v_f \sqrt{n\pi}, \tag{2}$$

where $v_f = 1 \times 10^6$ is the Fermi velocity (m/s) in graphene. n can be dynamically modified via the electric field effect shown in Fig. 1, where a direct current (DC) voltage is applied between a graphene sheet and a heavily doped semiconductor to induce an increment or decrement of the number of charge carriers n in the graphene sheet. In this paper, this electric field effect structure is integrated on the antenna substrate. The change of n follows equation (3) [28], [29]

$$n = \frac{\epsilon_o \epsilon V_b}{dq}, \tag{3}$$

where ϵ_o is the vacuum permittivity (F/m), V_b is the DC voltage bias (V), d is the thickness (m) and ϵ is the relative permittivity of the dielectric separating the graphene sheet and the back gate material (a p or n doped semiconductor).

The total relaxation time τ_t in equation (1) depends on different scattering mechanisms at different carrier densities and temperatures [11], [30]. The Matthiessen rule, equation (4), determines the overall relaxation time τ_t for any carrier density n and temperature T [28],

$$\frac{1}{\tau_t} = \left(\frac{1}{\tau_L}\right) + \left(\frac{1}{\tau_S}\right), \tag{4}$$

where τ_L is due to long range scattering mechanisms such as defects and inpurities, and τ_S is due to short range scattering mechanisms such as phonon and carrier-carrier interactions. Finally, at room temperature (295 K), the minimum achievable chemical potential μ_{min} is limited by electron-hole puddles caused by charged impurities [31] and can be calculated as follows

$$\varepsilon_{puddle} = \mu_{c,min} = \hbar v_f \sqrt{\pi \tilde{n}}, \tag{5}$$

where $\tilde{n}$ is the carrier density variations - carrier inhomogeneity density - caused by the electron-hole puddles (m^{-2}) which forces the minimum carrier density n to be greater than or equal to this value $n_{min} \geq \tilde{n}$.

III. SYSTEM LIMITATIONS

In this section, three critical issues are discussed related to the implementation of graphene, and the field-effect structure, in antennas for frequency reconfigurability. In subsection III-A, there is a discussion of the trade-offs between suspending graphene on air or laying it on a dielectric/substrate, see Fig. 1, and in case of depositing graphene on a substrate, to select a suitable dielectric/substrate material that could provide the best performance. Afterwards, a brief analysis of the effect of adding the heavily doped semiconductor to the antenna structure is found in subsection III-B. Finally, the instantaneous power consumption expression, when a graphene sheet is switched between large or small surface impedances, is derived in subsection III-C. These points are important for supporting later the selection of the parameters in section IV as well as the power consumed by the proposed antennas in section V.

A. SUSPEND GRAPHENE IN AIR OR LAY IT ON A SUBSTRATE?

Suspending graphene in air provides better performance than over substrates [32]. However, large electric fields and narrow distances d between the gate semiconductor and graphene sheet, see Fig. 1, are needed to induce high carrier density n values with reasonably low voltages V_b values. This might not be possible to achieve for suspended graphene without compromising its structural integrity [13], [32]. Consequently, only graphene laid on a substrate acting as a dielectric (Fig. 1) is considered from now on.

Recently, CVD grown graphene has also been successfully transferred to hexagonal boron nitride (hBN) substrates providing qualities close to exfoliated graphene and mobilities similar to suspended graphene [33]. Therefore, in this paper, it is assumed that a large area of graphene sheet could be deposited onto hBN substrates following, for instance, the dry method described in [33] in the near future.

B. DOPED SEMICONDUCTOR EFFECT

Heavily doped semiconductors can potentially provide reasonably good values of conductivity, specially in the microwave regime. From the general Drude's formula of conductivity, the conductivity of a doped semiconductor σ_{DS} (S/m) is

$$\sigma_{DS} = n_{DS} q \mu_{DS}, \tag{6}$$

where q is the electron charge (C), n_{DS} (m^{-3}) and μ_{DS} (m^{-2}/Vs) are the free carrier density and mobility of the doped semiconductor respectively. Therefore, by substantially raising the free carrier density n_{DS} (assuming the electron mobility μ_{DS} is kept the same) the conductivity of the doped semiconductor is also highly increased. To compensate this effect, a low carrier mobility μ_{DS} should be selected. As shown later in this paper in Table II, the number of free carrier densities needed in graphene are n_{ON}=5·10^{17} m^{-2} for the ON state and n_{OFF}=6·10^{14} m^{-2} for the OFF state. Consequently, the required free carrier density n_{DS} in the doped semiconductor can be obtained as

$$n_{DS} \geq \frac{(n_{ON} - n_{OFF})}{t_{DS}}, \tag{7}$$

where t_{DS} (m) is the thickness of the doped semiconductor layer. Note that, to reach this relation, the length l (m) and the width w (m) of both, the graphene layer and the doped semiconductor, are assumed to be the same. From equations (6) and (7), the total resistance of the doped semiconductor R_{DS} can be calculated as

$$R_{DS} \leq (\sigma_{DC})^{-1} \frac{l}{w t_{DS}} = \frac{l}{(n_{ON} - n_{OFF})\, w q \mu_{DS}}. \tag{8}$$

For the size of the graphene sheets considered in this paper, see Tables III and IV, and to obtain resistances R_{DS} on the order of kΩ or larger, the required electron mobility should be $\mu_{DS} \leq$0.02 m^{-2}/Vs. Heavily doped silicon carbride (SiC) [34] or hydrogenated amorphous silicon (a-Si:H) [35] can meet these requirements and be used as heavily doped semiconductors in Fig. 1 without a noticable impact on the antenna performance. Alternatively, the graphene layer could be self-biased. In [36], the authors produced a field-effect structure composed by two doped graphene monolayers at THz frequencies. There, the authors applied one or two DC voltage bias to control independently the conductivity of each of the doped graphene layers. Applying a similar procedure here but at microwave frequencies would allow one to substitute the doped semicondcutor in Fig. 1 for a doped graphene layer. It is important that this second graphene layer should present low quality (low electron mobility) and hence reduce undesired effects on the antenna performance.

C. DC INSTANTANEOUS POWER IN BIASED GRAPHENE

Finally, another important system limitation is set by the power consumed. In the field effect configuration, Fig. 1, the graphene sheet and the heavily doped semiconductor might be modelled as a parallel plate capacitor. The capacitance C (F) created is defined as

$$C = \frac{\epsilon \epsilon_o A}{d}, \tag{9}$$

where A is the area of the graphene sheet and the doped semiconductor ($l \times w$, assumed to be the same) (m^2). Hence, the resulting capacitance C is dictated, in one hand, by the parameters ϵ and d in equation (3) as low V_b values are desired, and on the other hand, by the dimensions of the graphene sheets used. Although the DC power consumption in capacitors is negligible due to electrical isolation, there is still movement of induced charges between the plates every time the DC bias voltage V_b is changed. This movement of charges creates a temporary current that charges the capacitor and therefore power is dissipated in any resistance present in the circuit. The peak power is the dynamic power (W) consumed by the circuit at t=0 and depends on the transitional current and the voltage on the resistance R present in the circuit - $i_R(t)$ and $v_R(t)$ - as equation (10) shows

$$p(t) = v_R(t) i_R(t) = \frac{V_b^2}{R} e^{\frac{-2t}{\tau_{RC}}}\Big|_{t=0} = \frac{n^2 q^2 dA}{\epsilon_o \epsilon \tau_{RC}}. \tag{10}$$

where $\tau_{RC} = RC$ and V_b is obtained from equation (3). This is the maximum power that the circuit might consume at the instant of changing the value of V_b. As observed, a fast switching time causes a large current in the system and more power is consumed during a short amount of time. In contrast, a longer waiting time reduces the maximum power consumed during the charging-discharging time. The value at P_{peak} can be further decreased by using a larger ϵ or reducing the thickness d of the dielectric. This would additionally reduce the required V_b. However, these parameters are not easily modified as ϵ depends on the properties of the target dielectric substrate and d on current technology constraints.

IV. PROPOSED ANTENNA DESIGNS

In order to demonstrate the use of graphene in frequency reconfigurable antennas, two main designs are studied:

- A rectangular microstrip antenna with extensions made of graphene added at the edges, Fig. 2a.
- A rectangular microstrip antenna with inserted strips made of graphene, Fig. 2b.

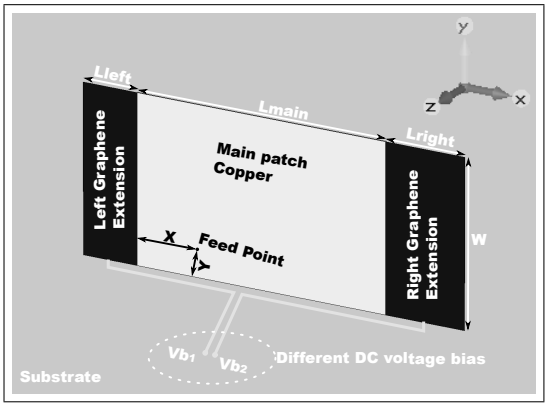

(a)

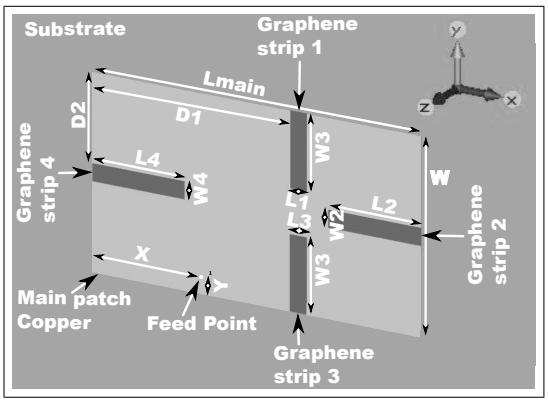

(b)

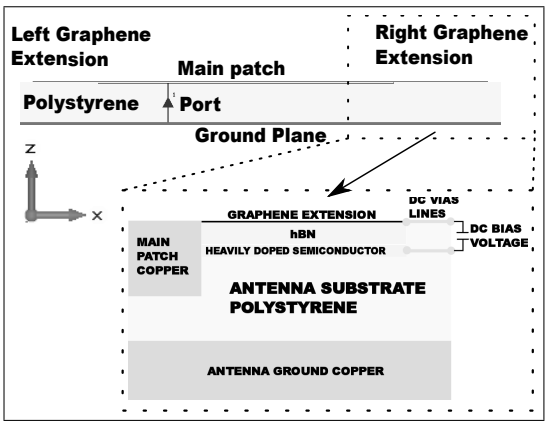

(c)

Fig. 2: Graphical representation of the frequency reconfigurable antennas for a) WIFI applications, b) LTE applications and c) zoomed view of the tuning structure for WIFI design (x-z plane) in a).

The first design (Fig. 2a) aims to increase or decrease the physical length of the structure in the ON or OFF

TABLE I: Selected general parameters

τ_{RC} [ms]	1
Switching time [ms]	1.6
d [nm]	10
ϵ for hBN	4

state respectively, while the second one (Fig. 2b) diverts the current propagating along the antenna so the effective length is larger or shorter than the physical length in the OFF or ON state respectively. The DC voltage bias (V_b) could be applied directly through the feeding port if a common value of V_b is desired for all the graphene extensions/strips so that it activates and deactivates them all at the same time. That would save the necessity of adding a DC bias circuit. However, inserting a gap between the main patch and the extensions/strips provides a solution to avoid a common DC bias voltage throughout the antenna and allows individual control to activate and deactivate single extensions/strips. Consequently, different DC voltage bias (i.e. Vb_1 and Vb_2) should be applied through individual DC vias lines to each of the required graphene sheets. Figs. 2a and 2c include an example of how the DC vias lines can be implemented. Note that both the DC vias lines in Fig. 2a and the field-effect structure in Fig. 2c have not been included in the simulations due to their extremely small thicknesses (in the nanometre scale). The values of Zs_{ON}, Zs_{OFF} and the general set up values for the simulations are defined next.

A. ELECTRIC FIELD EFFECT CONFIGURATION

For the values shown in Table I, it is firstly assumed that the time between switching from one operating frequency to another does not have to be fast (on the order of 1 millisecond). This is within a reasonable assumption considering handover interruption times in LTE-advanced (60 ms) [37]. The switching time is defined as the time needed for the voltage between the graphene sheet and the semiconductor to rise from 50% of the final value to the 90% [10]. Secondly, the thickness d of the dielectric can be reduced up to a few nanometres which is technologically available nowadays [38]. Finally, the ϵ for hBN is obtained from [38].

B. SIMULATED Zs_{ON} AND Zs_{OFF} VALUES

In order to obtain practical values of the ON and OFF state surface impedances Zs_{ON} and Zs_{OFF}, realistic values of τ_S, τ_L and $\tilde{n}$ are needed. Additionally, a high OFF/ON ratio (Zs_{OFF}/Zs_{ON}) is also desired. The values of surface impedance for the ON and OFF states, Zs_{ON} and Zs_{OFF} respectively, in Table II are obtained from equation (11), which is a slightly modified version of equation (1) which includes the relaxation time effect in equation (4),

$$Zs \approx \frac{j\pi\hbar^2(2\pi f(\tau_L\tau_S) - j(\tau_L + \tau_S))}{q^2(\tau_L\tau_S)[\mu_c + 2k_BT\ln(e^{-\frac{\mu_c}{k_BT}} + 1)]}, \quad (11)$$

where τ_L accounts for all the long range scattering effects and can be calculated as [11], [29], [39]

$$\tau_L = \frac{\mu_L m*}{q} \simeq \frac{\mu_L\hbar\sqrt{n\pi}}{qv_f}, \quad (12)$$

where μ_L is the electron mobility (m^2/Vs) and $m*$ is the carrier mass (Kg) in graphene. The value of τ_S is calculated as in equation (13) by just considering the LA phonon contribution, considered in this paper to be the dominant scattering mechanism at room temperature [30], [40], [41],

$$\tau_S = \frac{\mu_p\hbar\sqrt{n\pi}}{qv_f} = \frac{4\hbar^2\rho_m v_{ph}^2 v_f}{\sqrt{n\pi}D^2k_BT}, \quad (13)$$

where D is the deformation potential (eV), $\rho_m = 7.6 \times 10^{-7}$ is the two dimensional mass density of graphene (Kg/m^2) and $v_{ph} = 2.1 \times 10^4$ is the sound velocity of LA phonons in graphene (m/s). The precise deformation potential D value is still discussed, but some experimental values have been obtained in the literature and D ~18 eV seems to be a common and accepted value for graphene over a substrate [30]. However, it might theoretically have a large range of possible values between 4 eV and 30 eV as found in graphite and carbon nanotube materials [42]. The value of μ_c is directly obtained by substituting equation (2) into equation (3).

The Zs_{ON} value is found by increasing the charge carrier density n until saturation is reached as LA phonon scattering becomes dominant and at the same time the voltage V_b is not too high (22.7 V). On the other hand, the value for Zs_{OFF} is obtained by setting the minimum achievable chemical potential equal to the energy of the electron-hole puddles ($\mu_{c,min} = \varepsilon_{puddle}$) - equation (5). The carrier inhomogeneity density $\tilde{n}$=6×10^{14} m^{-2} is obtained from [33]. The value of μ_L is also extracted from reference [33]. V_b values are calculated using equation (3) by considering selected values of ϵ and d in Table I, and n values in Table II. Although the resulting V_b values might be too large for implementation in low voltage devices, e.g. mobile phones, the values can be reduced in the future by using thinner dielectrics with higher relative permittivity once the technology is available. For the OFF state, the

TABLE II: Selected surface impedance Zs values

Set	1		2	
State	ON	OFF	ON	OFF
n [m^{-2}]	$5{\cdot}10^{17}$	$6{\cdot}10^{14}$	$5{\cdot}10^{17}$	$6{\cdot}10^{14}$
V_b [V]	22.72	$\sim$0	22.72	$\sim$0
μ_L [m^2/Vs]	2.7		2.7	
D [eV]	4		18	
T [K]	295		295	
Zs [$\Omega/\square$]	6 + j0.3	2580 + j6	34 + j0.3	2580 + j6

TABLE III: Set up parameters for WIFI scenario, see Fig. 2a

$Lmain$ [mm]	W [mm]	$Lleft$ [mm]	$Lright$ [mm]	X [mm]	Y [mm]
23	14.7	5	7.3	5.5	2

resulting V_b values are near 0 V due to having very low inhomogeneity density $\tilde{n}$.

Finally, for all the scenarios evaluated in Section V the antenna substrate selected is Polystyrene (PS) with ϵ_r=2.4 and tanδ=0.0002 [43]. The antenna substrate thickness (H) is set to 2.1 mm as the space available in mobile devices is very limited. In the next section, the proposed antenna designs are simulated and analysed.

V. RESULTS

The results here are obtained from the transient solver (time domain solver) in the CST Microwave Studio 2015. The graphene sheets have been defined as solid sheets with thickness equal to zero and simulated as ohmic sheet surface impedances. The excitation is a discrete port with 50 Ω port impedance. The efficiencies calculated from CST follow equation (14);

$$\eta_t = \left(\frac{P_{rad}}{P_{sim}}\right) \times 100 \qquad (14)$$

where η_t is the total antenna efficiency (%), P_{rad} is the power being radiated by the antenna (W) and P_{sim}=0.5 W is the power generated by the excitation signal.

A. WIFI SCENARIO

The following scenario evaluates the first design to cover three bands in WIFI (2.4 GHz, 3.6 GHz and 5 GHz), see Fig. 2a. The extensions are activated and deactivated to change the resonant frequencies between 2.4 GHz and 3.6 GHz. In this scenario, the TM_{110} mode is used as the antenna is fed in a corner which allows an extra resonance at 5 GHz by adjusting the width of the main patch W. See Table III for the antenna dimensions.

Fig. 3 provides the reflection coefficient ($S11$) parameters for the WIFI scenario. When the extensions are deactivated (OFF state), the resonant frequencies are found

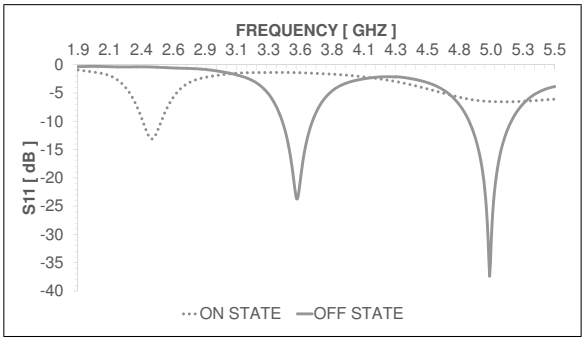

Fig. 3: Reflection coefficient for the WIFI design with the extensions activated (dotted line) and with the extensions deactivated (solid line).

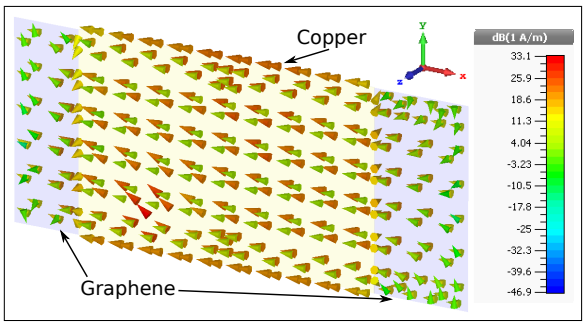

(a)

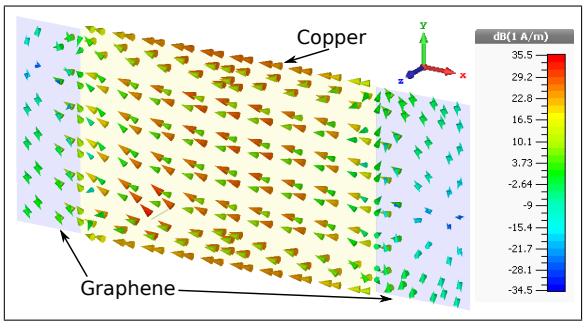

(b)

Fig. 4: Surface current density on the WIFI antenna at (a) 2.4 GHz and (b) 3.6 GHz.

at 3.6 GHz and 5 GHz. On the other hand, when the extensions are activated (ON state), the lower resonant frequency changes from 3.6 GHz to 2.4 GHz. Thus the activation and deactivation of the extensions is required to switch between these two resonant frequencies.

In order to confirm that the activation/deactivation of the graphene extensions do change the antenna behaviour, Fig. 4 provides the surface current distribution along the main patch and the graphene extensions for

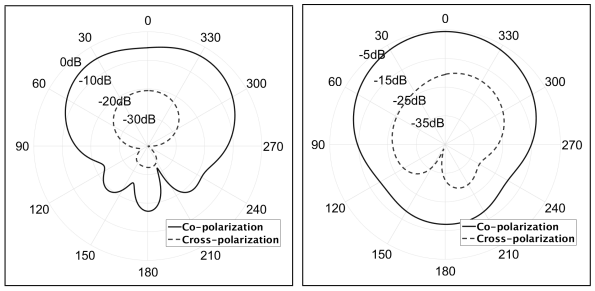

(a) E Plane (x-z plane)

(b) H plane (y-z plane)

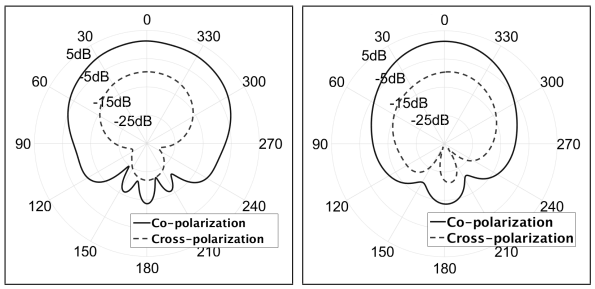

(c) E Plane (x-z plane)

(d) H plane (y-z plane)

Fig. 5: Radiation patterns of the WIFI antenna at (a)-(b) 2.4 GHz and (c)-(d) 3.6 GHz.

frequencies 2.4 GHz and 3.6 GHz, when the graphene extensions are either activated or deactivated respectively. As expected, when the graphene extensions are on the OFF state - at 3.6 GHz, little current is allowed to propagate along the extensions. In contrast, when the graphene extensions are in the ON state - at 2.4 GHz, substantially more current is able to propagate along the extensions and contribute to the electromagnetic radiation. This effectively changes the resonant length of the antenna and hence its resonant frequency.

Fig. 5 shows the radiation patterns at 2.4 GHz and 3.6 GHz, when the graphene extensions are activated and deactivated respectively. As observed, all the radiation patterns are similar in shape and close to the characteristics for a typical square patch antenna, showing that the graphene extensions have little effect on the shape of the radiation pattern. The results for the surface current and radiation pattern at 5 GHz are not included here, however, the same conclusions apply at that frequency. The obtained antenna gains are -3.4dB, 1.3 dB and 5.2 dB at 2.4 GHz, 3.6 GHz and 5 GHz respectively.

The antenna efficiencies extracted from the WIFI design are summarized in Fig. 6. The antenna efficiencies η_t show that when the antenna radiates at 2.6 GHz, η_t is lower than at any of the other two frequencies because

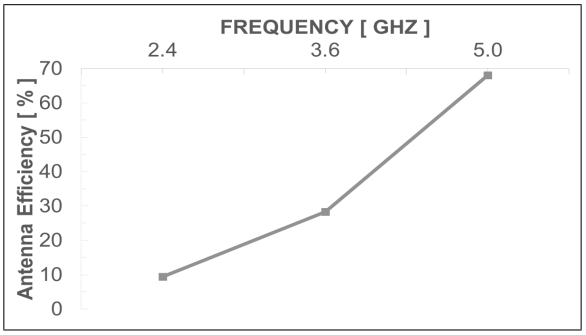

Fig. 6: Antenna efficiencies of the WIFI design.

of the graphene extensions attenuating the currents that contribute to radiation at that frequency. The power lost on graphene is about 337 mW which is a 67% of the total loss. When the graphene extensions are deactivated, in theory, the presence of the graphene extensions should affect equally at 3.6 GHz and 5 GHz, but their respective antenna efficiencies are not the same. An explanation might be that at 3.6 GHz, the graphene sheet must stop as much as possible any current propagating to the extensions. The better the graphene extensions achieve that, the less power is lost in graphene and the more is radiated. On the contrary, at 5 GHz whether currents are attenuated or not does not strongly affect the antenna efficiency but the antenna matching at that frequency, see Fig. 3. In general, it is demonstrated that the WIFI design proposed here is able to cover the target bands but the antenna efficiency at 2.4 GHz might be too low.

To demonstrate the impact of the surface impedance on the ON state (2.4 GHz), the same antenna is evaluated but now Zs_{ON}=6+j0.3 $\Omega/\square$ (set 1 in Table II) instead of Zs_{ON}=34+j0.3 $\Omega/\square$ (set 2 in Table II) by assuming that the deformation potential D is improved from D=18 eV to D=4 eV. The resulting value of η_t changes from 9.4% to 35.5% as the the power lost in graphene has been reduced from 337 mW to 253 mW at 2.4 GHz. This shows how important is to reduce the graphene surface impedance for the ON state Zs_{ON} in order to have reasonable antenna efficiencies. Unfortunately, the lower limit of Zs_{ON} depends on the deformation potential D which is yet not fully determined from experimental studies, and consequently, variations when defining this parameter strongly affects the final performance.

1) TUNABLE BANDWIDTH AND ANTENNA MATCHING: Here, the antenna matching and operational bandwidth is studied when different surface resistances Rs are selected. Note that by changing the Rs, the surface reactance Xs of the surface impedance - $Zs = Rs + jXs$ - is also slightly

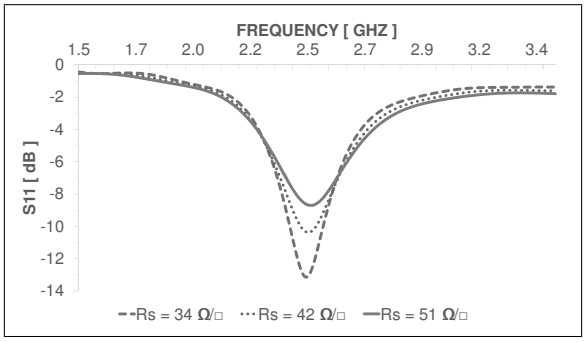

(a)

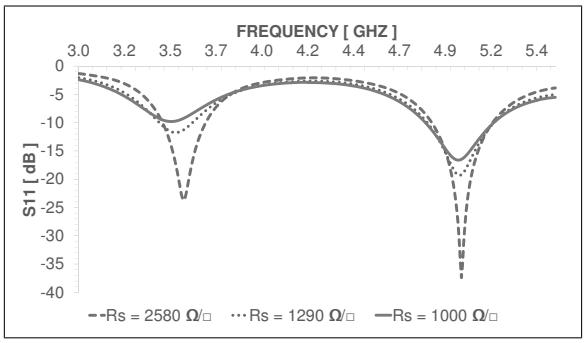

(b)

Fig. 7: Reflection coefficient for the WIFI antenna with variable BW for the (a) ON state and (b) OFF state.

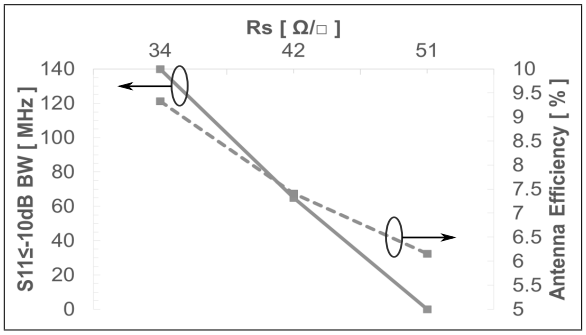

(a)

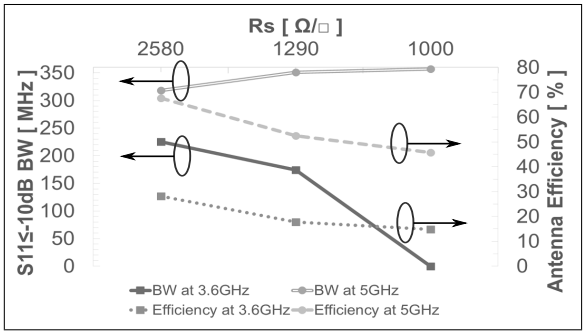

(b)

Fig. 8: Bandwidth and antenna efficiency variation for different values of Rs at a) 2.4 GHz and b) 3.6 GHz and 5 GHz.

changed but has no impact on the final result. As observed in Fig. 7, this allows to improve the antenna matching and tune the operational bandwidth BW. For instance, at 2.4 GHz, the value of the reflection coefficient goes from -8.7 dB to -13.2 dB by just selecting Rs=51 $\Omega/_{\square}$ or Rs=31 $\Omega/_{\square}$ respectively, see Fig. 8. This effect this is also reproduced for the 3.6 GHz and 5 GHz frequencies. The operational bandwidth can be tuned from a maximum all the way down to 0 MHz, which means not having the condition $S11 \leq$10 dB, by again selecting a proper Rs. This might help to reduce the complexity of the antenna matching network in future reconfigurable antennas made partially of graphene. The resulting antenna efficiencies are close to each other, however, the best efficiencies are again found when both Rs_{ON} and Rs_{OFF} are minimum and maximum respectively.

2) TUNABLE RESONANT FREQUENCY: Since intermediate values of the graphene surface impedance between Zs_{ON} and Zs_{OFF} can be selected, it is theoretically possible to select any resonant frequency between the two edge frequencies limited by these values. To show an example of this, Fig. 9 shows the reflection coefficient of the WIFI antenna design, Fig. 2a, for four different values of Rs. Both extension lengths have been shrunk to L_{left}=L_{right}=3 mm to keep a good matching of the antenna over the range of operating frequencies. In this case, the four different values of Rs provide four different resonant frequencies, see Fig. 10. Interestingly, the antenna efficiency η_t for the two extreme values Rs=70 $\Omega/_{\square}$ and Rs=2580 $\Omega/_{\square}$ are now better than the ones obtained in the WIFI scenario for Rs_{ON}=34 $\Omega/_{\square}$ and Rs_{OFF}=2580 $\Omega/_{\square}$, see section V-A. Clearly, shorter graphene extensions cause less ohmic losses but smaller changes in the resonant frequencies since now the lower resonant frequency is 3 GHz instead of 2.4 GHz. For the intermediate resonant frequencies, the antenna efficiencies are worse compared to the two edge frequencies. The cause is that as more and more current is allowed to propagate to the extensions (by reducing the Rs), the current is being substantially attenuated due to large values of Rs. The ability to select any resonant frequency within a specific range might prove very useful in wearable applications, where streching and bending affects the resonant frequency of the antenna among

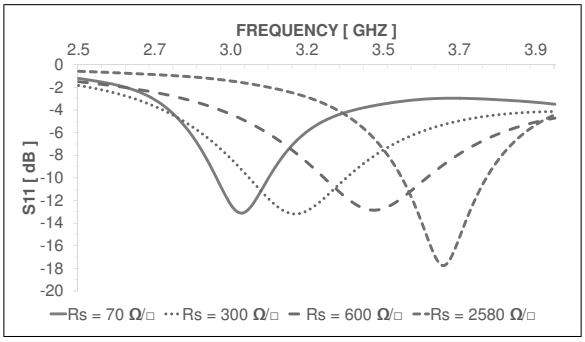

Fig. 9: Reflection coefficient for the WIFI design with intermediate Rs values selected.

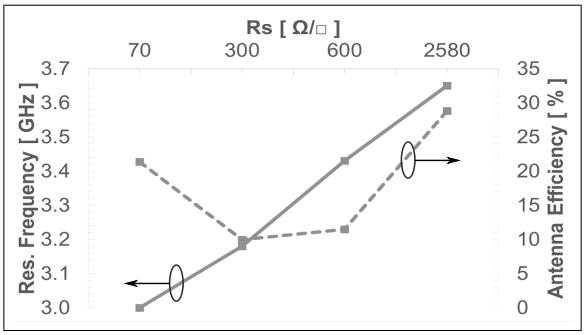

Fig. 10: Resonant frequency and antenna efficiency variation as Rs changes.

other parameters.

In [44], the authors studied the performance of wearable antennas made of graphene ink from 1 GHz to 5 GHz. Their obtained gains, between 0.2 dB and -1 dB, were similar or lower to the ones obtained here. The resonant frequency, bandwidth and gain of the antennas under their study were slightly affected at different bending and twisting cases. Because the graphene ink cannot provide reconfigurability by itself, the proposed antennas in this paper might produce enough reconfigurability to compensate for the side effects observed in the graphene ink case.

B. LTE SCENARIO

The second design, Fig. 2b, covers four bands of LTE (1.8 GHz, 2.1 GHz, 2.6 GHz and 3.6 GHz) by switching ON and OFF different graphene strips. This scenario also uses the TM_{110} mode for radiating. The values of Zs_{ON} and Zs_{OFF} are assigned from the Set 2 in Table II. See Table IV for the structure dimensions.

Fig. 11 provides the $S11$ parameters for the LTE scenario. When all four graphene strips are activated,

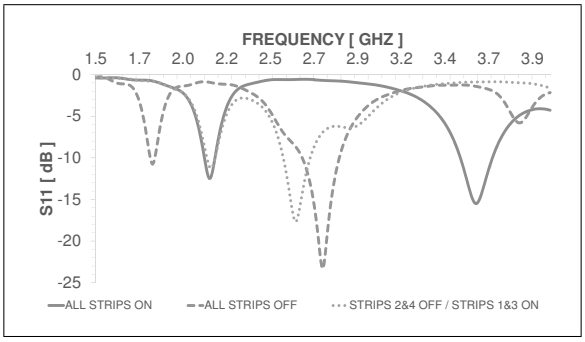

Fig. 11: Reflection coefficient for the LTE design with all strips activated (solid line), all strips deactivated (dashed line), and with strips 2 and 4 deactivated and strips 1 and 3 activated (dotted line).

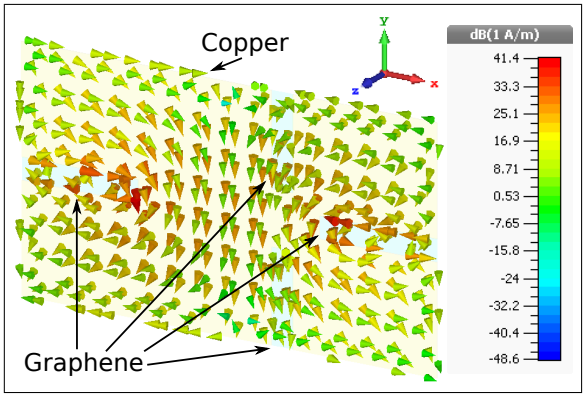

(a)

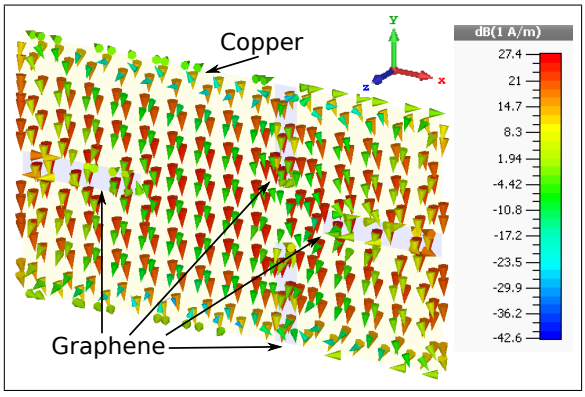

(b)

Fig. 12: Surface current density in the LTE antenna at (a) 2.6 GHz and (b) 3.6 GHz.

the antenna operates efficiently at 2.1 GHz and 3.6 GHz. Conversely, when all four strips are deactivated, the antenna switches now to 1.8 GHz operation. Finally,

TABLE IV: Set up parameters for LTE scenario, see Fig. 2b

$Lmain$ [mm]	W [mm]	$L1$ [mm]	$W1$ [mm]	$L2$ [mm]	$W2$ [mm]	$L3$ [mm]	$W3$ [mm]	$L4$ [mm]	$W4$ [mm]	$D1$ [mm]	$D2$ [mm]	X [mm]	Y [mm]
39	22	2	8.5	11	2	2	8.5	11	2	23.5	10	12.5	1

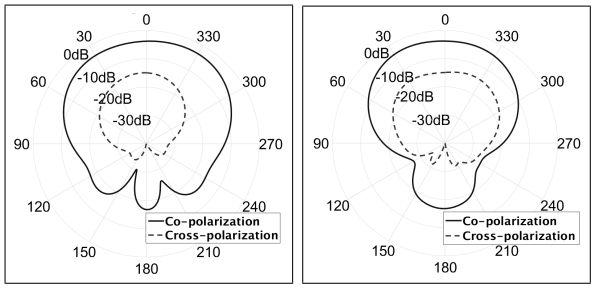

(a) E plane (y-z plane) (b) H plane (x-z plane)

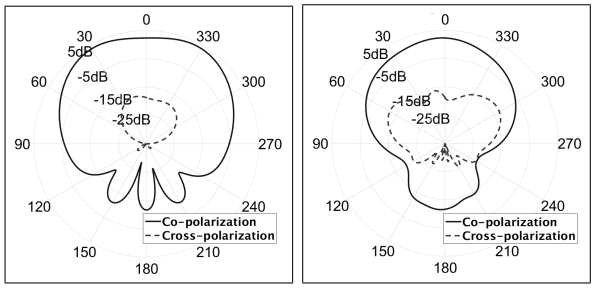

(c) E plane (y-z plane) (d) H plane (x-z plane)

Fig. 13: Radiation patterns of the LTE antenna at (a)-(b) 2.6 GHz and (c)-(d) 3.6 GHz.

when strips 2 and 4 are OFF and strips 1 and 3 are ON, the antenna achieves good matching at 2.6 GHz. Ideally, the antenna should switch between the four desired bands by switching ON or OFF all four strips at the same time. Unfortunately, when the four strips are deactivated the secondary frequency is found to be slightly over 2.6 GHz. This is because deactivating strips 1 and 3 affects the resonance at 2.6 GHz.

The surface current densities have been simulated to show the effect of the graphene strips on the behaviour of the antenna. Fig. 12 shows the current distributions along the main patch and the graphene strips at 2.6 GHz and 3.6 GHz, where graphene strips 2 and 4 (Fig. 2b) are activated and deactivated. When the graphene strips are set to the ON state, Fig. 12b, the current is allowed to propagate through the strips. However, when the graphene strips are set to the OFF state, Fig. 12a, the currents are not allowed to propagate through the strips but are diverted around them. That makes the currents

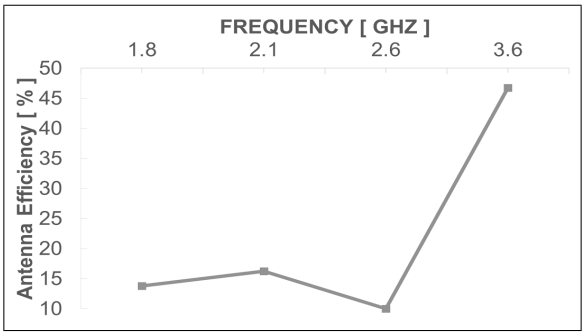

Fig. 14: Antenna efficiencies of the LTE design.

travel longer paths and therefore the antenna resonance is found at a lower frequency. Similar behaviour is found at 1.8 GHz and 2.1 GHz.

Fig. 13 shows the radiation patterns at 2.6 GHz and 3.6 GHz, where again graphene strips 2 and 4 are activated and deactivated. The resulting radiation patterns are again similar in shape and close to a typical square patch antenna, as previously observed in the WIFI scenario. Thus, the addition of the graphene strips seems to not strongly affect the shape of the radiation pattern. The radiation patterns for the remaining resonant frequencies, 1.8 GHz and 2.1 GHz, are very similar to the ones at 2.6 GHz and 3.6 GHz and therefore are not shown here. The resulting antenna gains are -1.6 dB, -0.7 dB, -3.3 dB and 3.9 dB at 1.8 GHz, 2.1 GHz, 2.6 GHz and 3.6 GHz respectively.

The efficiency results obtained are shown in Fig. 14. The worst efficiency is found at 2.6 GHz due to a large change of frequency being forced - from 3.6 GHz to 2.6 GHz.

1) INDIVIDUAL GRAPHENE STRIP SWITCHING: In the LTE design, in order to change the resonant frequencies, pairs of strips are accordingly switched ON and OFF. However, it could be possible to individually activated or deactivate any of strips independently and hence achieve intermediate resonant frequencies. Fig. 15 presents the results for individually switching graphene strips 1 and 3, where the widths of strips 1 and 3 were changed from $W1$=$W3$=8.5 mm to $W1$=9.5 mm and $W3$=7.5 mm. As shown, if both graphene strips are on the ON state, the antenna is radiating at 2.1 GHz, as in the previous LTE configuration. But, if strip 1 is now

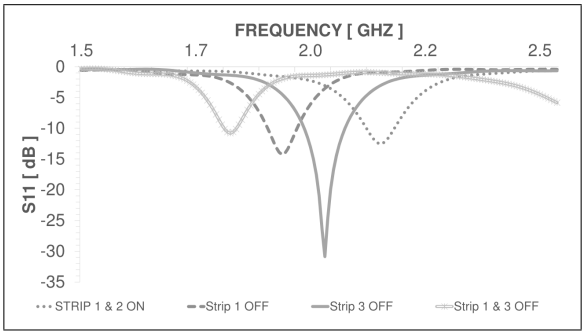

Fig. 15: Reflection coefficient for the LTE design with strips 1 and 3 activated (dotted line), strip 1 deactivated and strip 3 activated (dashed line), strip 2 deactivated and 1 activated (solid line) and strip 1 and 3 deactivated (double solid line).

individually changed to the OFF state while strip 3 is kept on the ON state, the resonance changes to 1.92 GHz. On the contrary, if strip 3 is the one changed to the OFF state and the strip 1 is kept on the ON state, the obtained resonant frequency is now 2.01 GHz. Finally, if both are switched to the OFF state, then the antenna resonates to 1.8 GHz as in the previous scenario. The efficiencies for the two extra resonant frequencies achieved here - 1.92 GHz and 2.01 GHz - are found to be 11% and 15.5% respectively, in the same order as for 1.8 GHz. Therefore, frequency reconfigurable antennas made partially of graphene extensions/strips could provide as many resonant frequencies as combinations of activating/deactivating graphene sheets without causing a drop in the the antenna efficiency.

C. PERFORMANCE COMPARISON

Here, the results obtained from the proposed WIFI and LTE antennas are compared to some other planar frequency reconfigurable antennas found in the literature. In [2], an anular slot antenna is configured to switch between two operating frequencies by integrating MEMS. In [6], a planar inverted-F antenna (PIFA) covers some commercial mobile phone bands by implementing multiple PIN-diodes. In [8], a patch antenna with a varactor loaded slot can operate at any frequency within a specific range by applying different DC voltages. Table V summarizes the comparison.

As observed from Table V, the antenna efficiencies obtained when using graphene are lower compared to any of the other switching technologies in the low and high limits. This is expected as graphene is still a material under developement. Moreover, graphene is used here as part of the radiating structure which does not add extra weight or space. However, in the other papers, the RF switches are elements added to the structure that do not contribute to radiation and increase the weight and volume of the antenna. As shown in this section, implementing graphene in antennas can provide the ON/OFF behaviour similar to MEMS and PIN-diode switches. In addition, it provides the continous frequency selection found in antennas loaded with varactors with the extra feature of bandwidth selection. Therefore, using graphene converges multiple modes of operation into a single solution. Additionally, substituting some metallic parts of the structure with graphene would allow for reconfigurable antennas where transparency and/or flexibility is desired. The remaining metallic part would also require to be a transparent and/or flexible low resistive conductor such as transparent thin films, eTextiles or conductive inks. Finally, graphene can easily operate at mm-wave and THz regime where conventional switches will perform poorly or even not work at all.

D. SWITCHING POWER CONSUMPTION

Table VI and VII provide the peak power consumed (P_{peak}) for all the scenarios evaluated in this paper when switching from one operating frequency to another due to the change of required values of charge carrier density n. For example, when switching between 2.4 GHz and 3.6 GHz in the WIFI design as the graphene extensions are activated or deactivated respectively. It is important to highlight here that the power consumption happens during a very short period of time - t $\ll$ switching time - and quickly drops to zero. So in normal use, hybrid metal-graphene reconfigurable antennas have very low power consumption. The total power shown is calculated by using equation (10) where the dielectric thickness d, the relative permittivity ϵ and the time constant τ_{RC} are set using the values in Table I. Specific values such as the charge carrier density n and the physical area of graphene A are extracted from Tables II, III and IV. Note that, in the evaluated scenarios there are from two to four graphene sheets being fed and the total power consumed is the addition of the power consumed by each individual sheet as it switches ON or OFF.

From Table VI and VII it is observed that the peak power consumption substantially decreases as the physical dimensions of the graphene sheets reduce. For example, when the area of the extensions of the WIFI design is reduced from 180.8 mm^2 to 88.2 mm^2, or when only strips 1 and 3 are turned ON - total area of 34 mm^2 - instead of all the strips ON - total area 78 mm^2 - in the LTE design, the value of P_{peak} is reduced. This is another reason for implementing graphene in

TABLE V: Comparison of different reconfigurable antennas

Reference	Technology	Frequencies Covered	Antenna Efficiency
This work WIFI design	Graphene	2.4GHz, 3.6GHz and 5GHz	9.4%(D=18eV) 35%(D=4eV) to 68%
This work LTE design	Graphene	1.8GHz, 2.1GHz, 2.6GHz and 3.6GHz	10% to 46.8%
[2]	MEMS	2.4GHz and 5.2GHz	90% to 92%
[6]	PIN-diode	0.7GHz, 0.85/0.9GHz, 1.8/1.9GHz and 2.3/2.5GHz	52.1% to 85.4%
[8]	Varactor	continuous from 3.24GHz to 4.35GHz	38% to 90%

TABLE VI: P_{peak} values for WIFI based designs

WIFI (Section V-A)	n [m^{-2}]	A [mm^2]	P_{peak} [mW]
Zs_{ON}= 34+j0.3 [$\Omega/\square$]	$5{\cdot}10^{17}$	180.8	330.6
Zs_{ON}= 6+j0.3 [$\Omega/\square$]	$5{\cdot}10^{17}$	180.8	330.6
Tunable BW and $S11$ (Section V-A1)	n [m^{-2}]	A [mm^2]	P_{peak} [mW]
Rs_{ON}= 34 [$\Omega/\square$]	$5{\cdot}10^{17}$	180.8	330.6
Rs_{ON}= 42 [$\Omega/\square$]	$1.8{\cdot}10^{17}$	180.8	42.8
Rs_{ON}= 51 [$\Omega/\square$]	$1.05{\cdot}10^{17}$	180.8	14.6
Tunable $f_{resonant}$ (section V-A2)	n [m^{-2}]	A [mm^2]	P_{peak} [mW]
Rs_{ON}= 70 [$\Omega/\square$]	$5.7{\cdot}10^{16}$	88.2	2.1
Rs_{ON}= 300 [$\Omega/\square$]	$8.5{\cdot}10^{15}$	88.2	0.0466
Rs_{ON}= 600 [$\Omega/\square$]	$3.9{\cdot}10^{15}$	88.2	0.0098

TABLE VII: P_{peak} values for LTE based designs

LTE scenario (V-B)	n [m^{-2}]	A [mm^2]	P_{peak} [mW]
All Zs_{ON}= 34+j0.3 [$\Omega/\square$]	$5{\cdot}10^{17}$	78	142.6
Strips 1-3 Zs_{ON}= 34+j0.3 [$\Omega/\square$]	$5{\cdot}10^{17}$	34	62.2
Individual Strip V-B1)	n [m^{-2}]	A [mm^2]	P_{peak} [mW]
Strip 1 Zs_{ON}= 34+j0.3 [$\Omega/\square$]	$5{\cdot}10^{17}$	19	34.7
Strip 3 Zs_{ON}= 34+j0.3 [$\Omega/\square$]	$5{\cdot}10^{17}$	15	27.4

hybrid metal-graphene antennas instead of full graphene antennas. Likewise, low values of charge carrier density n also help to reduce the power consumed. Interesting results are obtained for the tunable resonant frequency scenario in Table VI (Subsection V-A2) where very low peak power consumptions are obtained - 2.1 mW, 46.6 μW and 9.8 μW - for changes in the resonant frequency of up to 650 MHz. Likewise, relaxing the values for the ON state surface impedance (Zs_{ON}) seems to be also beneficial on the point of view of power consumption. For example, in the tunable bandwidth and matching scenario, selecting the Rs_{ON}=51 $\Omega/\square$ instead of Rs_{ON}=34 $\Omega/\square$ reduces the neccessary carrier density significantly and hence the peak power consumption drops by more than 20 times, from 330.6 mW to 14.6 mW.

It is also worth to analyse the impact of the deformation potential D value in the power consumption. As seen in the WIFI section, see section V-A, the antenna efficiency can be greatly improved by assuming Zs_{ON}=6+j0.3 $\Omega/\square$ due to a much better achievable deformation potential D=4 eV. However, if instead of dropping the value of Zs so much, it is enough to have Zs_{ON}=34+j0.3 (assuming that the antenna efficiency obtained is acceptable), then, the required charge carrier density n to achieve that value would be n=7$\times 10^{16}$ m^{-2} instead of n=5$\times 10^{17}$ m^{-2} (an order of magnitude lower). This reduction in the n would cause a reduction of the peak power consumption from 330.6 mW to just 6.6 mW, a factor of 50 times less. As a result, there is a trade off between in one hand a required antenna performance, such as achievable frequency reconfigurability and/or antenna efficiency; and on the other hand, the allowed switching power consumption. It is possible to greatly improve one aspect at the expense of increasing the other.

VI. CONCLUSIONS

This paper has analysed the performance of using graphene in frequency reconfigurable antennas in the microwave regime via the simulation of two hybrid metal-graphene antennas for WIFI and LTE applications. Implementing graphene as a material with tunable surface impedance allowed large frequency reconfigurability - up to 1.2 GHz change - with additional tunability of the antenna matching - up to 20 dB improvement - and bandwidth - up to 225 MHz increase. Although very low power consumption is achieved during normal operation, moderate values of the instantaneous peak power ($\leq$ 330.6 mW) are present during the switching process which only occurs during very short time periods ($\leq$ 1.6 ms). The proposed antennas can achieve high reconfigurability degree in terms of changing operational frequency but at the expense of lower antenna efficiencies - between 9.4% and 68%. To mitigate this effect, the losses due to the presence of graphene must be reduced

while still keeping the necessary reconfigurability. This might drive to study other types of antennas where small graphene sheets can be integrated without compromising the antenna performance. To ultimately confirm the feasibility of the proposed designs, prototypes should be built and measured. Its physical study will include effects not considered in this paper such as the contact resistance, the possible parasitic effects of the DC bias circuit (if needed) and the impact of adding the electric field effect structure between the radiating patch and the ground.

REFERENCES

[1] C. W. Jung, M. J. Lee, G. P. Li, and F. De Flaviis, "Reconfigurable scan-beam single-arm spiral antenna integrated with RF-MEMS switches," *IEEE Trans. Antennas Propag.*, vol. 54, no. 2, pp. 455–463, 2006.

[2] B. A. Cetiner and G. Roqueta Crusats and L. Jofre and N. Biyikli, "RF MEMS Integrated Frequency Reconfigurable Annular Slot Antenna," *IEEE Trans. Antennas Propag.*, vol. 58, no. 3, pp. 626–632, March 2010.

[3] L. N. Pringle *et al.*, "A reconfigurable aperture antenna based on switched links between electrically small metallic patches," *IEEE Trans. Antennas Propag.*, vol. 52, no. 6, pp. 1434–1445, 2004.

[4] T. Aboufoul, A. Alomainy, and C. Parini, "Reconfiguring UWB monopole antenna for cognitive radio applications using GaAs FET switches," *IEEE Antennas Wireless Propag. Lett*, vol. 11, pp. 392–394, 2012.

[5] D. Peroulis, K. Sarabandi, and L. P. B. Katehi, "Design of reconfigurable slot antennas," *IEEE Trans. Antennas Propag.*, vol. 53, no. 2, pp. 645–654, 2005.

[6] S. W. Lee and Y. Sung, "Compact Frequency Reconfigurable Antenna for LTE/WWAN Mobile Handset Applications," *IEEE Trans. Antennas Propag.*, vol. 63, no. 10, pp. 4572–4577, Oct 2015.

[7] C. R. White and G. M. Rebeiz, "Single-and dual-polarized tunable slot-ring antennas," *IEEE Trans. Antennas Propag.*, vol. 57, no. 1, pp. 19–26, 2009.

[8] A. Khidre and F. Yang and A. Z. Elsherbeni, "A Patch Antenna With a Varactor-Loaded Slot for Reconfigurable Dual-Band Operation," *IEEE Trans. Antennas Propag.*, vol. 63, no. 2, pp. 755–760, 2015.

[9] R. L. Haupt, "Reconfigurable patch with switchable conductive edges," *Microw. Opt. Technol. Lett.*, vol. 51, no. 7, pp. 1757–1760, 2009.

[10] R. L. Haupt and M. Lanagan, "Reconfigurable antennas," *IEEE Antennas Propag. Mag*, vol. 55, no. 1, pp. 49–61, 2013.

[11] A. H. N. Castro, F. Guinea, N. M. R. Peres, K. Novoselov, and A. Geim, "The electronic properties of graphene," *Rev. Mod. Phys.*, vol. 81, pp. 109–162, Jan 2009.

[12] F. Bonaccorso, Z. Sun, T. Hasan, and A. C. Ferrari, "Graphene photonics and optoelectronics," *Nature Photon.*, vol. 4, no. 9, pp. 611–622, 2010.

[13] C. Lee, X. Wei, J. W. Kysar, and J. Hone, "Measurement of the elastic properties and intrinsic strength of monolayer graphene," *Science*, vol. 321, no. 5887, pp. 385–388, 2008.

[14] Dragoman, M. and Muller, A. A. and Dragoman, D. and Coccetti, F. and Plana, R., "Terahertz antenna based on graphene," *J. Appl. Phys.*, vol. 107, no. 10, p. 104313, 2010.

[15] J. S. Gomez-Diaz and J. Perruisseau-Carrier, "Microwave to THz properties of graphene and potential antenna applications," in *2012 Int. Symp. on Antennas and Propagation (ISAP)*. IEEE, 2012, pp. 239–242.

[16] M. Tamagnone, J. S. Gomez-Diaz, J. R. Mosig, and J. Perruisseau-Carrier, "Analysis and design of terahertz antennas based on plasmonic resonant graphene sheets," *J. Appl. Phys.*, vol. 112, no. 11, p. 114915, 2012.

[17] M. Tamagnone, J. Gomez-Diaz, J. R. Mosig, and J. Perruisseau-Carrier, "Reconfigurable terahertz plasmonic antenna concept using a graphene stack," *Appl. Phys. Lett.*, vol. 101, no. 21, p. 214102, 2012.

[18] Y. Yao, M. A. Kats, P. Genevet, N. Yu, Y. Song, J. Kong, and F. Capasso, "Broad electrical tuning of graphene-loaded plasmonic antennas," *Nano Lett.*, vol. 13, no. 3, pp. 1257–1264, 2013.

[19] J. M. Jornet and I. F. Akyildiz, "Graphene-based Plasmonic Nano-Antenna for Terahertz Band Communication in Nanonetworks," *IEEE J. Sel. Areas Commun*, vol. 31, no. 12, pp. 685–694, December 2013.

[20] M. Esquius-Morote and J. S. Gmez-Daz and J. Perruisseau-Carrier, "Sinusoidally Modulated Graphene Leaky-Wave Antenna for Electronic Beamscanning at THz," *IEEE Trans. THz Sci. Technol.*, vol. 4, no. 1, pp. 116–122, Jan 2014.

[21] Eduardo Carrasco and Michele Tamagnone and Juan R Mosig and Tony Low and Julien Perruisseau-Carrier, "Gate-controlled mid-infrared light bending with aperiodic graphene nanoribbons array," *Nanotechnology*, vol. 26, no. 13, p. 134002, 2015.

[22] J. Perruisseau-Carrier and M. Tamagnone and J. S. Gomez-Diaz and E. Carrasco, "Graphene antennas: Can integration and reconfigurability compensate for the loss?" in *2013 European Microwave Conf. (EuMC)*, Oct 2013, pp. 369–372.

[23] M. Tamagnone and J. S. G. Diaz and J. Mosig and J. Perruisseau-Carrier, "Hybrid graphene-metal reconfigurable terahertz antenna," in *2013 IEEE MTT-S Int. Microwave Symp. Dig. (IMS)*, June 2013, pp. 1–3.

[24] S. Bae *et al.*, "Roll-to-roll production of 30-inch graphene films for transparent electrodes," *Nat. Nanotechnol.*, vol. 5, no. 8, pp. 574–578, 2010.

[25] C. N. Alvarez and R. Cheung and J. S. Thompson, "Graphene reconfigurable antennas for LTE and WIFI Systems," in *2014 Antennas and Propagation Conf. (LAPC 2014)*, Nov 2014, pp. 434–438.

[26] V P Gusynin and S G Sharapov and J P Carbotte, "Magneto-optical conductivity in graphene," *J. Phys.: Condens. Matter*, vol. 19, no. 2, p. 026222, 2007.

[27] G. W. Hanson, "Dyadic Greens functions and guided surface waves for a surface conductivity model of graphene," *J. Appl. Phys.*, vol. 103, no. 6, 2008.

[28] N. M. R. Peres, "*Colloquium* : The transport properties of graphene: An introduction," *Rev. Mod. Phys.*, vol. 82, pp. 2673–2700, Sep 2010.

[29] K. S. Novoselov *et al.*, "Electric field effect in atomically thin carbon films," *Science*, vol. 306, no. 5696, pp. 666–669, 2004.

[30] J. H. Chen, C. Jang, S. Xiao, M. Ishigami, and M. S. Fuhrer, "Intrinsic and extrinsic performance limits of graphene devices on SiO_2," *Nat. Nanotechnol.*, vol. 3, no. 4, pp. 206–209, 2008.

[31] J. Martin *et al.*, "Observation of electron–hole puddles in graphene using a scanning single-electron transistor," *Nature Phys.*, vol. 4, no. 2, pp. 144–148, 2008.

[32] K. I. Bolotin *et al.*, "Ultrahigh electron mobility in suspended graphene," *Solid State Commun.*, vol. 146, no. 9, pp. 351–355, 2008.

[33] N. Petrone *et al.*, "Chemical vapor deposition-derived graphene with electrical performance of exfoliated graphene," *Nano Lett.*, vol. 12, no. 6, pp. 2751–2756, 2012, pMID: 22582828.

[34] M. Roschke and F. Schwierz, "Electron mobility models for 4H, 6H, and 3C SiC [MESFETs]," *IEEE Trans. Electron Devices*, vol. 48, no. 7, pp. 1442–1447, Jul 2001.

[35] Street, R. A. and Kakalios, J. and Hack, M., "Electron drift mobility in doped amorphous silicon," *Phys. Rev. B*, vol. 38, pp. 5603–5609, Sep 1988.

[36] Gomez-Diaz, JS and Moldovan, C and Capdevila, S and Romeu, J and Bernard, LS and Magrez, A and Ionescu, AM and Perruisseau-Carrier, Julien, "Self-biased reconfigurable graphene stacks for terahertz plasmonics," *Nat. Commun.*, vol. 6, 2015.
[37] ITUR, "M. 2134. requirements related to technical performance for imt-advanced radio interface (s)," Technical Report, 3GPP, Tech. Rep., 2008.
[38] K. K. Kim *et al.*, "Synthesis and characterization of hexagonal boron nitride film as a dielectric layer for graphene devices," *ACS nano*, vol. 6, no. 10, pp. 8583–8590, 2012.
[39] V. Ariel and A. Natan, "Electron effective mass in graphene," in *2013 Int. Conf. on Electromagnetics in Advanced Applications (ICEAA)*, Sept 2013, pp. 696–698.
[40] S. V. Morozov *et al.*, "Giant intrinsic carrier mobilities in graphene and its bilayer," *Phys. Rev. Lett.*, vol. 100, p. 016602, Jan 2008.
[41] V. N. Kotov, B. Uchoa, V. M. Pereira, F. Guinea, and A. H. C. Neto, "Electron-electron interactions in graphene: Current status and perspectives," *Rev. Mod. Phys.*, vol. 84, no. 3, p. 1067, 2012.
[42] L. M. Woods and G. D. Mahan, "Electron-phonon effects in graphene and armchair (10, 10) single-wall carbon nanotubes," *Phys. Rev. B*, vol. 61, no. 16, p. 10651, 2000.
[43] F. Cardarelli, *Materials handbook: a concise desktop reference*. London : Springer, 2008.
[44] Huang, X., and others, "Highly Flexible and Conductive Printed Graphene for Wireless Wearable Communications Applications," *Scientific reports*, vol. 5, 2015.

Performance Analysis Of Hybrid Metal-Graphene Frequency Reconfigurable Zeroth Order Resonant Antennas For Long Term Evolution Applications

Christian Nuñez-Alvarez, Rebecca Cheung and John S. Thompson

***Abstract*—This paper presents a study of implementing graphene into frequency reconfigurable zeroth order resonant antennas. Two antenna designs made of copper with integrated graphene sheets are presented, simulated and discussed here. The proposed antennas are designed to cover two Long Term Evolution bands, 1.8GHz and 2.1GHz. The results confirm that by tuning the surface impedance of graphene the zeroth order resonant frequencies of the two proposed antennas are successfully switched between the two bands. Changing the surface impedance of graphene between a high and low value can provide the ON/OFF switching functionality found in reconfigurable antennas with integrated Micro Electromechanical Systems (MEMS), Field-Effect Transistors (FET) or P-type and N-type Diode switches. Moreover, selecting intermediate values of surface resistance of graphene also allows for the selection of intermediate resonant frequencies. This provides, in theory, the possibility of selecting any resonant frequency between the two operational bands. Trade-offs between the graphene dimensions, substrate thickness, number of cells, antenna size and antenna efficiency are also provided in this paper. As expected, the larger the dimension of the graphene sheet, the larger the shift in the resonant frequency that can be achieved but with reduced antenna efficiencies.**

***Index Terms*—reconfigurable antennas, microwave antennas, frequency control, electrically small antennas.**

I. INTRODUCTION

Increasingly, the regular addition of new communication systems to wireless and mobile devices as well as the steady desire for reducing their size is limiting the available space for antennas. In addition, the implementation of multiple-input multiple-output (MIMO) technology is further highlighting the necessity of finding alternative solutions to antennas where their size determines their operational frequency. In order to overcome such space constraints, reconfigurable metamaterial antennas might be a potential solution for future wireless devices.

This work was supported by the Engineering and Physical Sciences Research Council (EPSRC) grant no. EP/K503034/1.

Reconfigurable antennas are radiating structures that can dynamically change any of their properties such as the radiation pattern, the resonant frequency, the operational bandwidth and/or the polarization to operate on different applications or adapt to diverse conditions. Consequently, reconfigurable antennas can perform the job of more than one antenna and hence save space in devices. Antenna reconfigurability is most commonly done with Micro or Nano Electromechanical systems (MEMS or NEMS) [1] [2], electrical radio frequency (RF) field-effect transistor (FET) switches [3] [4], diode-based technology such as the P-type Insulator N-type diode (PIN diode) [5] [6], varactors [7] [8] or tunable materials [9]; via applying a mechanical, electrical, magnetic, light or thermal bias [10].

Metamaterials (MTM) are artificial materials composed of a repetition of elements that present unusual electromagnetic properties not found in nature such as simultaneous negative permittivity ϵ and permeability μ [11]. Interestingly, metamaterials can be used in antennas as additional elements to improve the performance in electrically small antennas, reduce surface wave propagation and provide zero reflection phase [12]–[15]; and as electromagnetic resonators based on the composite right/left-handed transmission line (CRLH TL). The CRLH TL based antenna is characterised by presenting simultaneous left-hand (L_L and C_L) and right-hand (L_R and C_R) inductive and capacitive behaviour that supports negative, zeroth and positive order resonant modes [11]. Here, the zeroth order resonance of the CRLH TL antenna is studied, also called the zeroth order resonant (ZOR) antenna. ZOR antennas are size independent of the resonant frequency and hence can substantially save space in wireless and mobile devices. For instance, in [16] the ZOR structure is formed by microstrip interdigital capacitors and meander lines while in [17] mushroom-like structures are used as unit cells. Additionally, ZOR antennas can be made reconfigurable

if their inductive and capacitive components can be actively tuned. Frequency reconfigurable ZOR antennas have been achieved by using varactors [18], PIN diodes [19] and MEMS [20]. In this paper, the variable surface impedance of graphene is utilized to create frequency reconfigurable ZOR antennas.

Graphene is a flat mono-atomic layer of Carbon atoms distributed in a two-dimensional honeycomb-like lattice [21]. The conductivity of graphene can be tuned by applying an electrostatic field via a direct current (DC) voltage bias. Furthermore, an unbiased pristine single layer of graphene (SLG) only absorbs 2.3% [22] of visible light and supports breaking forces of up to 42 N/m with a Young's modulus of 1 TPa and an intrinsic strength of 130 GPa [23] while also being extremely light (0.77 mg/m^2). As a result, graphene could be implemented into transparent and/or flexible antenna designs.

Graphene reconfigurable antennas are being mostly studied for the infrared and terahertz (THz) band as graphene can significantly reduce size and provide high antenna reconfigurability at such frequencies [24]–[26]. However, since large area samples of graphene have been successfully synthesised [27], this paper carries out a feasibility study of using this novel material as a potential solution for frequency reconfigurable ZOR antennas in the microwave regime. At microwave frequencies, graphene presents moderate to high surface impedances compared to conventional metals [28] and hence the proposed designs are hybrid metal-graphene structures. The concept of hybrid metal-graphene reconfigurable antennas was introduced in [29] for the THz band. Some previous work in hybrid metal-graphene reconfigurable antennas in the microwave regime has been already carried out where frequency [30] [31] and polarization [32] reconfigurability was achieved. Additional designs have been proposed in [33] where graphene is used as a switch for frequency reconfigurability, or in [34] for radiation pattern tunability. In the present paper, the variable surface impedance of graphene is applied to modify the inductive and capacitive components of the ZOR antenna so that the zeroth-order resonant frequency is changed.

The novel contributions of this paper can be summarized as follows:

- Investigate the use of the variable surface impedance of graphene to tune the capacitive and inductive components of ZOR antennas in the microwave regime.
- Analyse and simulate two possible hybrid metal-graphene frequency reconfigurable ZOR antenna designs to cover LTE (1.8 GHz and 2.1 GHz) frequency bands.
- Provide design trade-offs between graphene sheet dimensions, reconfigurability and antenna efficiency in frequency reconfigurable ZOR antennas.

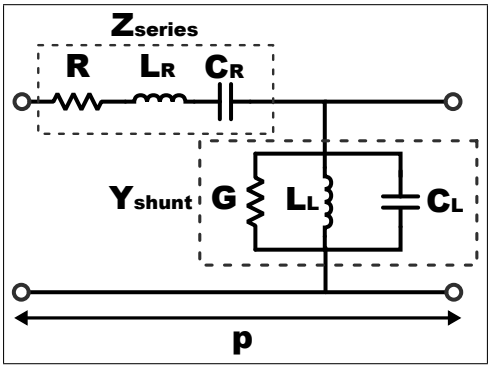

Fig. 1: Circuit model of a CRLH TL unit cell.

The paper is structured as follows, sections II and III will introduce the ZOR antenna theory and the variable surface impedance of graphene, then, section IV will define the proposed antenna designs followed by the simulation results in section V. Finally, section VI will close the paper with some conclusions.

II. ZEROTH ORDER RESONANT ANTENNA THEORY

The CRLH TL antenna can be modelled using a unit cell equivalence formed by a resistance R (Ω) and a conductance G (S) representing the losses in the antenna, a right-hand inductance L_R (L), a right-handed capacitance C_R (F), a left-handed inductance L_L (L) and a left-handed capacitance C_L (F) as shown in Fig. 1 [11]. Additionally, the same unit cell can also be modelled as a series impedance Z_{series} (Ω) and a shunt conductance Y_{shunt} (S)

$$Z_{series} = R + j\left(\omega L_R - \frac{1}{\omega C_L}\right), \tag{1}$$

$$Y_{shunt} = G + j\left(\omega C_R - \frac{1}{\omega L_L}\right), \tag{2}$$

where ω is the operational angular frequency (rad/s). Consequently, the dispersion relation $\beta(\omega)$ (rad/m) of a CRLH TL antenna can be extracted by applying the periodic boundary conditions (PBCs) related to the Bloch-Floquet theorem [11]

$$\beta(\omega) = \frac{1}{p}\cos^{-1}\left(1 - \frac{1}{2}\left(Z_{series}Y_{shunt}\right)\right) = \frac{1}{p}\cos^{-1}\left(1 - \frac{1}{2}\left(\frac{\omega_L^2}{\omega^2} + \frac{\omega^2}{\omega_R^2} - \frac{\omega_L^2}{\omega_{se}^2} - \frac{\omega_L^2}{\omega_{sh}^2}\right)\right), \quad (3)$$

where p is the length of the unit cell (m) and

$$\omega_L = \frac{1}{\sqrt{C_L L_L}}, \quad \omega_R = \frac{1}{\sqrt{C_R L_R}}, \quad (4)$$

$$\omega_{se} = \frac{1}{\sqrt{C_L L_R}}, \quad \omega_{sh} = \frac{1}{\sqrt{C_R L_L}}, \quad (5)$$

are the resonances due to the right-handed ω_R, the left-handed ω_L, the series ω_{se} and the shunt ω_{sh} contributions respectively. From the dispersion relation of the CRLH TL antenna in equation (3), an open- or short-ended resonator based on the CRLH TL presents resonances whenever the following condition is satisfied [35]

$$\beta_n(\omega) = \frac{n\pi}{l} = \frac{n\pi}{Np} \qquad \text{for } n\text{=}0,\pm1,\pm2,...,(N\text{-}1); \quad (6)$$

where n is the resonant mode, l is the total length of the CRLH TL structure (m) and N is the number of cascaded unit cells. Therefore, the higher the number of unit cells placed in cascade the higher the number of negative and positive resonances. When solving equations (3) and (6) for n=0 (zeroth order), there are two possible solutions that fulfil the condition, or in other words, there are two possible values for the zeroth order resonant frequency. In such a case, the zeroth order resonant frequency is calculated from equation (5) by either the series resonant frequency ω_{se} if the structure is left short-ended, or the shunt resonant frequency ω_{sh} if left open-ended. Importantly, when n=0, the zeroth order resonant frequency becomes independent of the physical length of the antenna and it is only determined by the values of the C_L and L_R in the case of the short-ended case or C_R and L_L in the case of the open-ended case. Although the ZOR antenna centre frequency is independent of the size of the structure, in practice, it is limited by the space p required by the components C_R, C_L, L_R and L_L. These capacitances and inductances can be implemented by using surface mounted technology (SMT) chip components or distributed components [11], such as microstrip interdigital capacitors, parallel plate capacitors, meander lines, among others. Interestingly, actively changing the inductive and/or capacitive behaviour of the antenna effectively changes its resonant frequency.

III. VARIABLE SURFACE IMPEDANCE OF GRAPHENE

For the range of frequencies considered in this paper and in the absence of a magnetic field, the surface impedance Zs ($\Omega/\square$) of graphene is defined in a Kubo-like form as [36]

$$Zs = \frac{j\pi\hbar^2(2\pi f - j\tau_t^{-1})}{q^2[\mu_c + 2k_BT\ln(e^{-\frac{\mu_c}{k_BT}} + 1)]}, \quad (7)$$

where f is the operating frequency (Hz), μ_c is the chemical potential (J), τ_t is the total relaxation time (s) assumed to be independent of the energy ε [36], T is the temperature (K), q is the elementary charge (C), $\hbar$ is the reduced Planck's constant (Js) and k_B is the Boltzmann constant (J/K). It can be seen that, the surface impedance of graphene depends on T, τ_t and μ_c. Changing any of these parameters will alter the surface impedance of graphene. The chemical potential μ_c can be controlled in a field effect configuration as shown in Fig. 2 by applying a direct current (DC) voltage. The chemical potential μ_c is related to the carrier density n (m^{-2}) as [21]

$$\mu_c \simeq \hbar v_f \sqrt{n\pi}, \quad (8)$$

where $v_f = 1 \times 10^6$ is the Fermi velocity (m/s) in graphene. Additionally, the charge carrier density n is related to the DC bias voltage as [37]

$$n = \frac{\epsilon_o \epsilon V_b}{dq}, \quad (9)$$

where ϵ_o is the vacuum permittivity (F/m), V_b is the DC voltage bias (V), d is the thickness (m) and ϵ is the relative permittivity of the dielectric separating the graphene sheet and the back gate material [37]. Consequently, by combining equations (8) and (9), the chemical potential μ_c can be expressed in terms of V_b as

$$\mu_c \simeq \hbar v_f \sqrt{\frac{\epsilon_o \epsilon V_b}{dq}\pi}, \quad (10)$$

which shows that the surface impedance of graphene can be tuned by applying a DC voltage bias.

The total scattering time τ_t is defined by the dominant scattering time at any charge carrier density n and can be calculated by applying Matthiessen's rule [37], [38]

$$\frac{1}{\tau_t} = \left(\frac{1}{\tau_L}\right) + \left(\frac{1}{\tau_S}\right), \quad (11)$$

where τ_L is the scattering mechanism due to long-range mechanisms such as defects and impurities (τ_i) and τ_S is the scattering mechanisms due to short-range

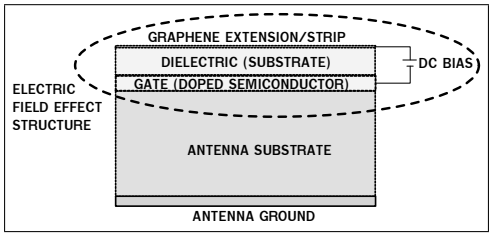

Fig. 2: Example of an electric field effect structure added to a plannar antenna.

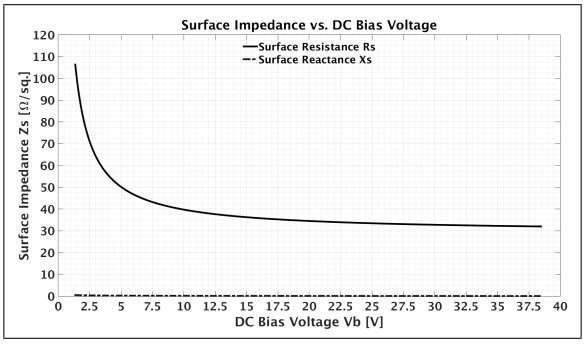

Fig. 3: Surface impedance of graphene Zs dependency in the applied DC bias voltage V_b at 2GHz with μ_L=2.7m^2/Vs and D=18eV.

mechanisms such as carrier-phonon and carrier-carrier interactions [21], [37], [38].

In the present paper, the selected surface impedance Zs values are obtained from equation (7). The value of τ_S is obtained from [38]

$$\tau_S = \tau_p = \frac{4\hbar^2\rho_m v_{ph}^2 v_f}{\sqrt{n\pi}D^2 k_B T} = \frac{4\hbar^2\rho_m v_{ph}^2 v_f}{\sqrt{\frac{\epsilon_o \epsilon V_b}{dq}\pi}D^2 k_B T}, \quad (12)$$

where τ_p is the relaxation time due to phonon-carrier interactions, D is the deformation potential (eV), $\rho_m = 7.6 \times 10^{-7}$ is the two dimensional mass density of graphene (Kg/m^2) and $v_{ph} = 2.1 \times 10^4$ is the sound velocity of LA phonons in graphene (m/s). The selected deformation potential is set to D=18eV as this is the most commonly measured value in graphene. However, the deformation potential can have a range of values between 4 eV and 30 eV as found in graphite and carbon nanotube materials [39]. The value of τ_L is calculated from equation (13) by applying the special carrier mass equation in graphene to Drude's DC conductivity model [21],

$$\tau_L = \frac{\mu_L \hbar\sqrt{n\pi}}{q v_f} = \frac{\mu_L \hbar\sqrt{\frac{\epsilon_o \epsilon V_b}{dq}\pi}}{q v_f}, \quad (13)$$

where μ_L is the long-range charge carrier mobility achieved in graphene due to defects and impurities. The chosen value of μ_L is extracted from reference [40], where the authors achieved a high electron mobility (μ=2.7m^2/Vs) by placing graphene on top of hexagonal Boron Nitride (hBN) and using chemical vapour deposition (CVD). hBN is an excellent substrate for graphene as it is flat, possesses a similar crystal structure to graphite (reduced lattice mismatch) and provides large optical phonon energies and band gap [41], however, at the time of writing, hBN/graphene sheets of only a few micrometres have been succesfully manufactured. Nevertheless, it is here assumed that, in the near future, improvements in the chemical vapour deposition process in reference [40] will support large area of graphene sheets on hBN. Therefore, the graphene sheet is assumed here to be placed on top of a hBN dielectric in a field effect like configuration as shown in Fig. 2. The thickness and relative permittivity of hBN is set to d=10nm and ϵ_r=4 [42], respectively. Finally, the operational temperature T is set to be the same as the room temperature T=295K. Therefore, the selected set up allows one different values of Zs to be obtained when different V_b voltages are applied, see Fig. 3.

As observed in Fig. 3, low values of surface impedance Zs converge to a point where increasing V_b does not substantially improve the surface impedance values. Consequently, the maximum voltage considered here is set to be V_b=22.72V with a surface impedance equivalent value of Zs=34+j0.3 $\Omega/\square$. This provides a good surface impedance for a reasonable voltage value. This surface impedance is set as an equivalent ON state impedance Zs_{ON}. On the other hand, the surface impedance drastically changes for small changes of DC bias voltage values. The maximum surface impedance of graphene is limited by the carrier density variations, or carrier inhomogeneity density, $\tilde{n}$ (m^{-2}) caused by the electron-hole puddles. This carrier inhomogeneity density $\tilde{n}$ limits the lowest possible chemical potential $\mu_{c,min}$ due to mainly impurities [43] and is defined as

$$\varepsilon_{puddle} = \mu_{c,min} = \hbar v_f \sqrt{\pi\tilde{n}}. \quad (14)$$

The selected carrier inhomogeneity density $\tilde{n}$=6$\cdot$10^{14} m^{-2} is also extracted from reference [40], which gives a maximum surface impedance of Zs=2580+j6 $\Omega/\square$ and sets an equivalent OFF state surface impedance Zs_{OFF} with V_b=0.027V. Table I provides a summary of the selected parameters for simulations.

TABLE I: Selected surface impedance Zs values

State	ON	OFF
n [m^{-2}]	$5{\cdot}10^{17}$	$6{\cdot}10^{14}$
V_b [V]	22.72	0.027
μ_L [m^2/Vs]	2.7	
D [eV]	18	
T [K]	295	
Zs [$\Omega/\square$]	34 + j0.3	2580 + j6

TABLE II: Unit cells dimensions, in millimetre (mm)

Unit cell 1, Fig. 4a			
$W1 = W2 = 3$	$L1 = L2 = 4.5$	$l0 = 4.35$	$l1 = 1.2$
$l2 = 0.3$	$l3 = 1.2$	$l4 = 7.5$	$l5$=0.1
$Gap = 0.01$	$r = 0.5$	$W3 = 10.2$	p=12.16
Unit cell 2, Fig. 4b			
$W1 = W2 = 3.6$	$L1 = L2 = 4$	$l0 = 2.425$	$l1 = 1.35$
$l2 = 0.15$	$l3 = 1.35$	$l4 = 3.5$	$l5$=0.1
$Gap = 0.01$	$r = 0.5$	$W3 = 5$	p=9.08

IV. PROPOSED ANTENNA DESIGNS

As mentioned in Section II, the zeroth order resonant frequency f_{ZOR} of an open-ended ZOR antenna is determined by the values of the right-handed capacitance C_R and the left-handed inductance L_L, see ω_{sh} in equation (5). Consequently, in order to change the resonant frequency, either or both of these two components must be actively tuned. For this reason, in the proposed antenna designs, the selected surface impedance values of graphene are used to dynamically change the values of L_L or C_R and hence change the zeroth order resonant frequency ω_{sh}. The two proposed ZOR antennas are constructed from the two unit cells shown in Fig. 4 and Fig. 5 with dimensions presented in Table II.

The proposed unit cells are based on microstrip distributed capacitances and inductances where two microstrip patches are separated by a gap and followed by a meander line connected to ground via a cylindrical solid bias. The values C_{pat1}, C_{pat2}, L_{pat1} and L_{pat2} are the capacitances generated between the two top patches and the ground plane, and the inductances present in the two top patches, respectively. Additionally, R_{pat1} and R_{pat2} are the losses in the conductors forming the top patches. C_{gap}, C_{dis1} and C_{dis2} are the capacitances generated by the discontinuity (or separation) between the two top patches. L_{mea}, C_{mea} and R_{mea} are the inductance, capacitance and resistance of the meander line. L_{vias} is the inductance of the solid vias, where the resistance of the bias is assumed to be negligible. Finally, the G_{sub} is the conductance of the substrate. In the first unit cell design, Fig. 4a, a graphene sheet is laid under the meander line, while in the second design, Fig. 4b, a graphene sheet is laid next to one of the microstrip patches. The two unit cells achieve tunable C_R and L_L values by changing the surface impedance Zs of graphene which causes the inductive behaviour of the meander line in Fig. 5a and the capacitive behaviour in Fig. 5b to change. However, the variation of the surface impedance of the graphene sheets also affects the capacitive C_{mea} and resistive R_{mea} contributions of the meander line, the inductive L_{pat2} and resistive R_{pat2} contributions of the parallel plate, and the capacitances C_{gap} and C_{dis2} of the

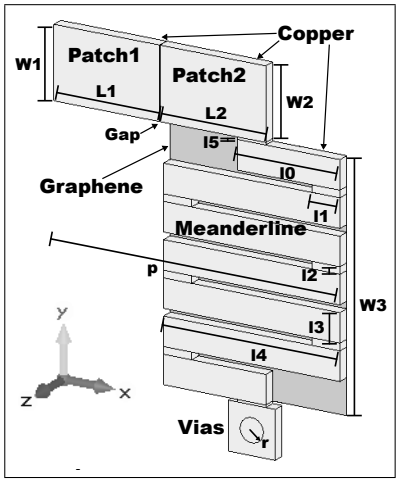

(a)

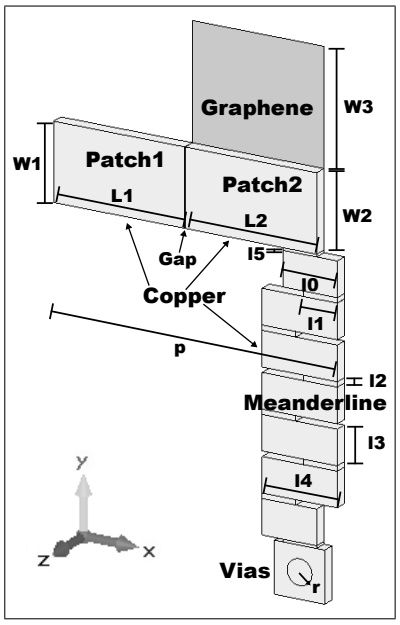

(b)

Fig. 4: The two proposed unit cell designs, a) Unit cell 1: graphene laid under the meander line, b) Unit cell 2: graphene laid next to patch 2.

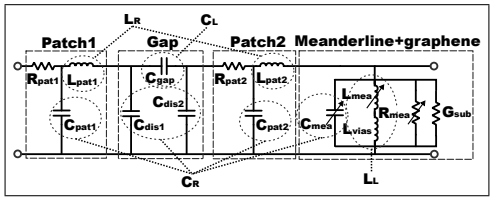

(a)

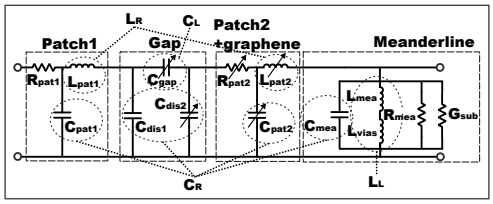

(b)

Fig. 5: Equivalent electrical circuit of the two proposed unit cell designs, a) Unit cell 1: graphene laid under the meander line, b) Unit cell 2: graphene laid next to patch 2.

gap between the patches. Consequently, the theoretical variable ZOR resonant frequency f_{ZOR} (Hz) for the unit cells are calculated as

$$f_{ZOR} = \frac{\omega_{sh}}{2\pi} = \frac{1}{2\pi\sqrt{C_R L_L}}, \tag{15}$$

where

$$C_R = C_{pat1} + C_{pat2} + C_{dis1} + C_{dis2} + C_{mea}, \tag{16}$$

and

$$L_L = L_{mea} + L_{vias}. \tag{17}$$

The two proposed ZOR antenna designs are shown in Fig. 6. They are composed of 3 unit cells (N=3) each. Antenna design 1 is formed by the unit cell 1 with graphene laid under the meander line, and antenna design 2 is formed by the unit cell 2 with graphene laid next to the patch 2. Additionally in Fig. 6c, there is a proposed method to bias the graphene sheets in the proposed antennas. Note that the field-effect structure shown in Fig. 6c is not simulated here as the thickness of the hBN and doped semiconductor layers are extremely small (in the order of nanometres). The antenna dimensions are shown in Table III. The substrate used is the Rogers RT5880 with a relative permittivity ϵ_r=2.2 and a loss tangent tanδ=0.0009 [44]. The thickness H of the substrate is chosen to optimise the ratio between size reduction and efficiency of the antenna, and at the same time, can still

TABLE III: Antenna dimensions, in millimetre (mm)

Common for both designs			
H = 4	t = 0.5	W_{feed} = 6	L_{feed} = 5
Design 1, Fig. 6a			
W = 15.4	L = 30.18	G_{feed} = 0.2	
Design 2, Fig. 6b			
W = 21.15	L = 25.1	G_{feed} = 0.45	

fit into current mobile and wireless devices, e.g. mobile phones, tablets, etc. Note that, the antennas are fed by proximity coupling to a microstrip section to reduce the inherent high input impedances of the ZOR antennas for a wide range of frequencies. This generates additional series, $C_{feed,gap}$, and parallel, $C_{feed,dis1}$ and $C_{feed,dis2}$, capacitances between the feed antennas. Particularly important are the additional $C_{feed,dis1}$ and $C_{feed,dis2}$ capacitances as they slightly modify the ZOR resonant frequency f_{ZOR} when added into equation (16). In the simulations, the excitation is modelled as a discrete port with an internal impedance of Z=50Ω. The graphene sheets are modelled as ohmic sheet surfaces with real and imaginary impedances.

V. RESULTS

The results section is structured as follows, first, in Subsection V-A, the impact of graphene on the unit cells is computed. Second, in Subsection V-B, the two proposed antenna designs shown in Fig. 6 are evaluated. In Subsection V-C, some antenna design trade-offs are analysed. In Subsection V-D, some intermediate values of Zs are simulated for frequency selection. Finally, in Subsection V-E, a performance comparison is made to other designs found in the literature.

The simulation results are obtained from the computer simulation technology (CST) microwave studio 2015. In the simulations, the excitation is modelled as a discrete port with an internal impedance of Z=50Ω. The graphene sheets are modelled as ohmic sheet surface impedance with real and imaginary impedances. The antenna efficiency η (%) provided is calculated as

$$\eta = \left(\frac{P_{rad}}{P_{sim}}\right) \times 100, \tag{18}$$

where P_{rad} is the power radiated by the antenna and P_{sim} is the power simulated (500mW). Therefore, the antenna efficiency also considers the mismatch losses between the feed and the antenna.

A. IMPACT OF GRAPHENE ON THE MEANDER LINE AND TOP PATCHES

As shown in Fig. 5, it is expected that changing the surface impedance of graphene should change the

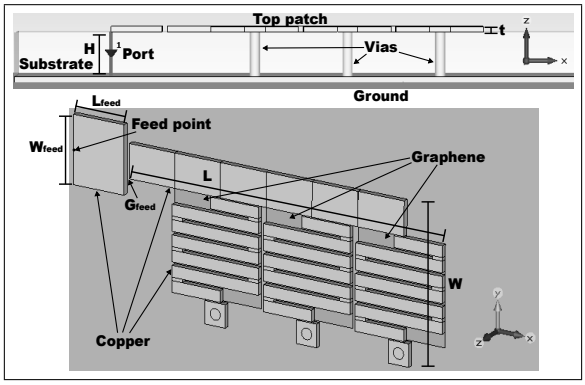

(a)

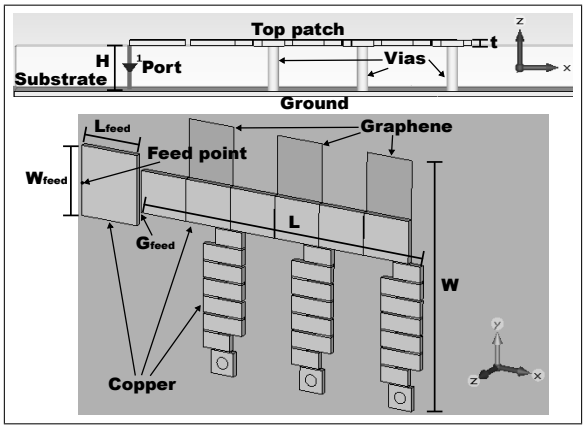

(b)

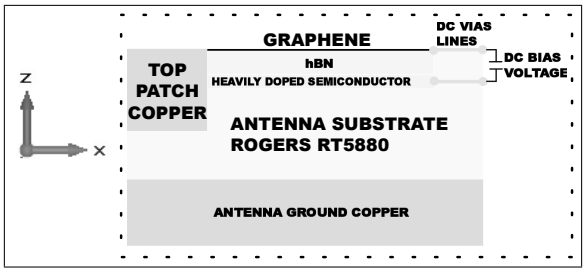

(c)

Fig. 6: Frequency reconfigurable ZOR antenna designs, a) Design 1: plan and 3D views of graphene laid under the meander line, b) Design 2: plan and 3D views of graphene laid next to patch 2, and c) an example of a possible bias structure

inductive and capacitive behaviour of some of the elements that compose the unit cells. Fig. 7 shows the two configurations used to compute the inductance and capacitance variation when Zs is changed for different lengths of the graphene sheets. The inductance and

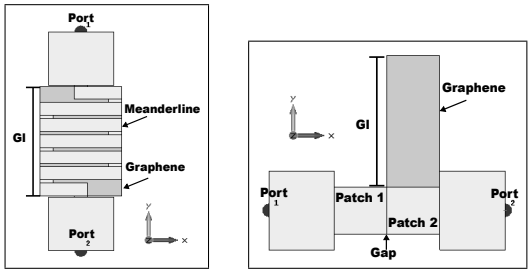

(a) (b)

Fig. 7: Inductance and capacitance computation of a) graphene under the meander line and b) graphene next to the second patch.

capacitance values are obtained from network analysis by modifying the graphene sheet lengths, Gl in Fig. 7, when it is activated (ON) and deactivated (OFF).

The results in Fig. 8 shows the difference between the variation in the inductance ΔL and capacitance ΔC values when the graphene sheets are activated (ON) and deactivated (OFF). Both values ΔL and ΔC are calculated as the difference between the inductance and capacitance values generated when the graphene sheet is deactivated and the inductance and capacitance values generated when the graphene sheet is activated. These inductance and capacitance variations between ON/OFF states will cause the antenna resonant frequency to change as they change the values of the left-handed inductance L_L and the right-handed capacitance C_R. In the case where graphene is laid under the meander line, the result in Fig. 8a indicates that both components, ΔL and ΔC, change when the length of the graphene sheet is varied. Specifically, when the graphene sheet becomes longer, from Gl=2.7mm to Gl=10.2mm, ΔL increases from ΔL=-0.27nH to ΔL=0.96nH. The reason is that, ideally when the graphene sheet is deactivated, most of the current must propagate through the meander line and consequently it has a large inductance. However, when the graphene sheet is activated, the current is diverted to propagate through the graphene sheet instead of going all the way through the meander line. As the inductance of a meander line depends on the number of turns and the length of the turns (among other parameters), the longer the graphene sheet is the shorter the path of the current that needs to propagate through the meander line, and consequently, the lower the resulting inductance. On the contrary, the difference on the capacitance values ΔC decreases, from ΔC=0.15pF to ΔC=0.02pF, becoming almost negligible for the longest graphene sheet. As a result, as the graphene sheet becomes longer, the change in the resonant frequency becomes dominated by the

change of its inductance instead of the capacitance. Note that, the ΔC values are not large enough to provide a substantial change in the resonant frequency, and hence, it is necessary to base the change of the resonant frequency on the modification of the inductance values ΔL.

In the second case, Fig. 8b shows the results when the graphene sheet is attached to the second patch. As the graphene sheet becomes larger, from Gl=0.5mm to Gl=10mm, the capacitance difference ΔC also becomes larger, from ΔC=-0.11pF to ΔC=-0.43pF. The reason is that when the graphene sheet is deactivated, negligible current propagates through the graphene sheet and therefore it does not contribute to the parallel capacitance between the top patches and the ground plane. Consequently, it does not matter how large the graphene sheet is. However, when the graphene sheet is activated, some current propagates through the graphene sheet which then contributes to the total capacitance. Thus, the larger the area of the graphene is, the larger the capacitance it generates. In this case, the variation of the capacitance is negative because the capacitance generated when the graphene sheet is deactivated is lower than when the graphene sheet is activated. Regarding the inductance change, it does not follow a perfect linear change but it can be seen that in general the difference also decreases for longer graphene sheets. Nevertheless, in this case, the inductance change is not important as it only contributes to the right-handed inductance L_R and consequently it does not change the resonant frequency, see equation (15). Therefore, the main contribution to the change in the ZOR frequency comes from the capacitance variations ΔC as this affects the right-handed capacitance.

From the inductance and capacitance results it seems that large changes in resonant frequencies are possible by implementing long graphene sheets. However, it is also important to consider the losses. In Fig. 9 the losses due to the presence of graphene when it is activated (ON) and deactivated (OFF) are shown for both cases. Unfortunately, it indicates that the longer the graphene sheet is, the larger the losses are. Consequently, there is a trade-off between the maximum resonant frequency switch and the maximum acceptable losses due to the use of graphene. Additionally, comparing both designs, using a graphene sheet under the meander line when activated provides lower ohmic losses for long lengths of graphene sheets - 29.2mW as compared to 66.8mW for graphene next to the second patch. On the other hand, when the length of the graphene sheet is shorter, as well as when the graphene sheet is deactivated (OFF), both designs perform similarly.

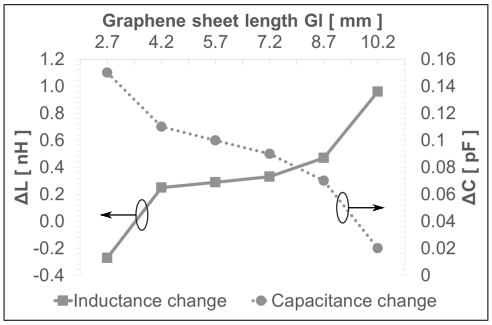

(a)

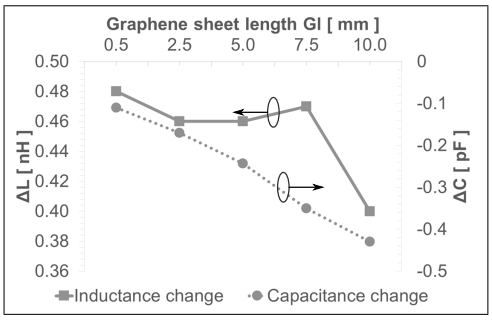

(b)

Fig. 8: Inductance and capacitance variations of a) graphene under the meander line and b) graphene next to the patch 2.

B. PERFORMANCE OF THE FREQUENCY RECONFIGURABLE ZOR ANTENNAS

Fig. 10 shows the reflection coefficient values of the two antennas when graphene is activated (ON) and deactivated (OFF). In the Design 1, when graphene is activated, the resonant frequency is set to 2.1GHz while when deactivated it changes to 1.8GHz. Likewise, in Design 2, when graphene is activated, the resonant frequency is found at 1.8GHz while when deactivated it moves to 2.1GHz. Additionally, Fig. 11 and 12 show the surface current distribution on the two antennas when the graphene sheets are activated and deactivated. In the case of the design 1, Fig. 11, the change in how the current propagates is difficult to appreciate due to the overlap of the meander line on the graphene sheet. However, it is still possible to note how the current follows the turns of the meander line when the graphene sheet is OFF, Fig. 11a, and how it follows a more straight path when the graphene sheet is ON, Fig. 11b. For the design 2, when the graphene sheets are deactivated, little current propagates. In contrast, when the graphene sheets are activated some current now propagates on the graphene sheets which effectively changes the inductive

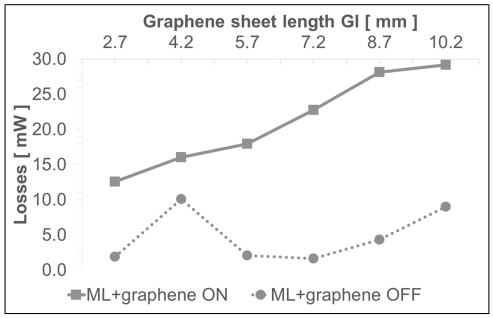

(a)

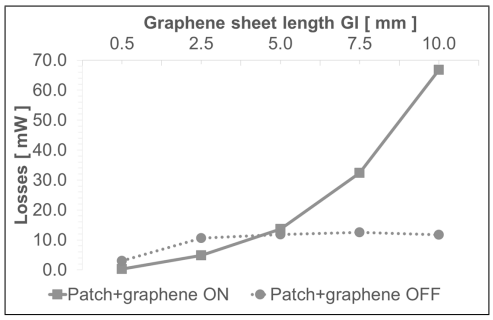

(b)

Fig. 9: Losses due to graphene in a) graphene under the meander line (ML+graphene) and b) graphene next to the patch 2 (Patch+graphene).

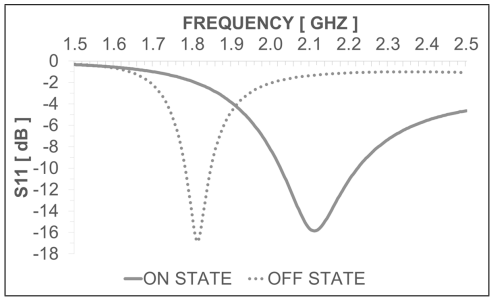

(a)

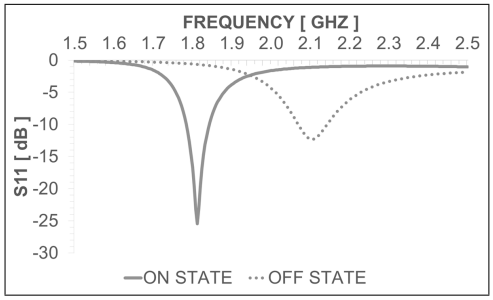

(b)

Fig. 10: Reflection coefficients for the ON and OFF states, a) Design 1 b) Design 2.

and capacitive behaviour of the antenna.

In a CRLH TL based antenna, the order of resonance is identified by looking into the electric field distribution at the particular frequencies of interest. When the CRLH TL based antenna is operating in its zeroth order resonance, the electric field lines in the enclosed volume that surrounds the antenna are all pointing to the same direction as the wavelength is infinite. This condition is recognized for both designs at both resonant frequencies as Fig. 13 demonstrates. Specifically, in Fig. 13 the electric field lines between the ground plane and the top patch are uniformly all pointing to the same direction (upwards). The same behaviour is found in the antenna Design 2.

Furthermore, the radiation patterns obtained in Fig. 14 are of similar shape of a common microstrip antenna and switching ON and OFF the graphene sheets seems to not strongly affect the resulting radiation patterns. Very similar radiation patterns are obtained for antenna Design 2. The extracted gains for Design 1 are -0.2dB and -3dB at 1.8GHz and 2.1GHz respectively; and -0.8dB and 0.6dB at 1.8GHz and 2.1GHz respectively for Design 2. All the presented results confirm that by switching the surface impedance of the graphene sheets in the proposed antennas, their zeroth order resonant frequencies can be changed between 1.8GHz and 2.1GHz.

The antenna efficiencies computed for Design 1 are 31.6% and 15.8% at 1.8GHz and 2.1GHz respectively; and 28.8% and 33.9% at 1.8GHz and 2.1GHz respectively for Design 2. For both antenna designs, material losses are dominated by graphene, accounting for around 55% to 95% of the losses due to materials and between 35% and 75% of the total losses in the antenna, causing the antenna efficiency to drop considerably. Ideally, when graphene is deactivated, its effect should be minimum but the results indicate that there are still some losses due to the presence of graphene. As a result, the addition of graphene does not only affect the antenna efficiency when the graphene sheet is activated but also when it is deactivated, and hence, at both resonant frequencies. In order to reduce the losses in the antennas, it is necessary to increase the surface impedance for the OFF state (Zs_{OFF}) and decrease the surface impedance for the ON state (Zs_{ON}). This could be done by selecting graphene with lower long-ranged charge carrier mobility μ_L and/or lower carrier inhomogeneity density $\tilde{n}$. That should increase the maximum achievable surface impedance Zs_{OFF} for small values of applied DC bias

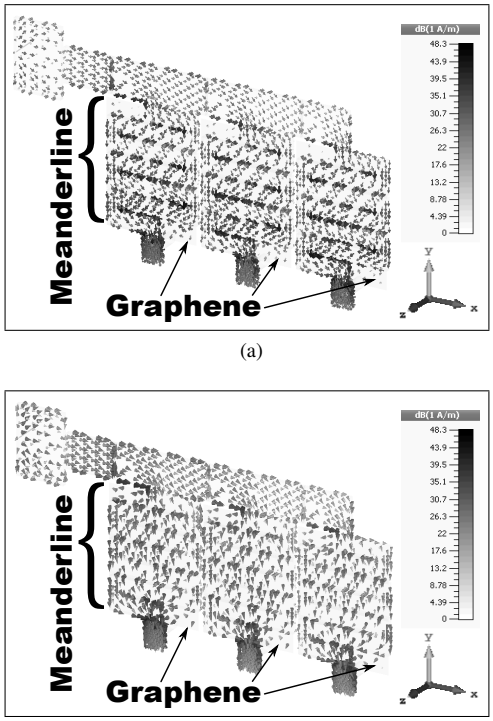

(a)

(b)

Fig. 11: Surface current distribution for antenna design 1 at a) 1.8 GHz and b) 2.1 GHz.

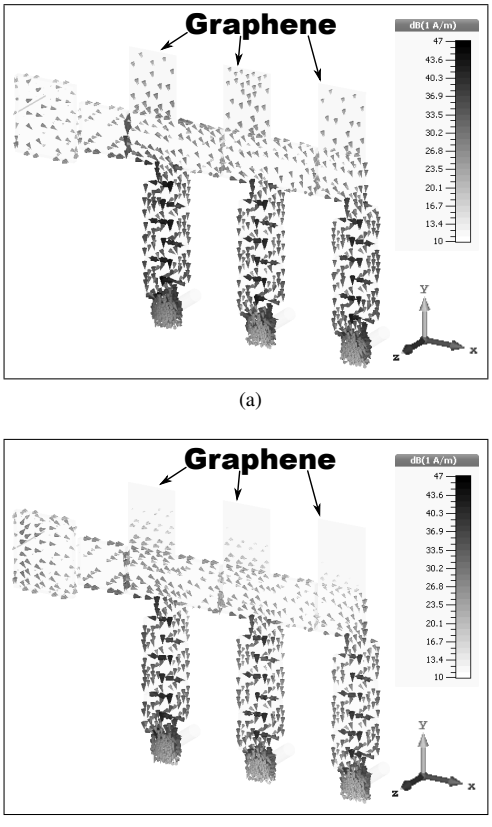

(a)

(b)

Fig. 12: Surface current distribution for antenna design 2 at a) 1.8 GHz and b) 2.1 GHz.

voltage V_b. However, that would also cause an increment of the DC bias voltage V_b needed to achieve a low Zs_{ON}. Similarly, achieving lower deformation potential D or lowering the operational temperature would allow to reduce the surface impedance of graphene in the ON state. Unfortunately, the deformation potential is still not properly controlled, making it difficult to achieve lower values, as explained in section III.

C. SUBSTRATE HEIGHT AND NUMBER OF CELLS EFFECT ON THE ANTENNA EFFICIENCY

The antenna efficiencies obtained in the previous subsection V-B are mainly dominated by the losses in graphene. However, they are also affected by the antenna size. Fig. 15 displays the trade-off between the height of the antenna substrate H, the length of the antenna L and the antenna efficiency η. For both designs, increasing H helps to reduce L and improve η. During simulations, when the substrate height was increased, the zeroth order resonance decreased and vice versa. To compensate this effect, the lengths of the two patches, $L1$ and $L2$ in Fig 4, were made shorter or longer, resulting in smaller or larger antennas when increasing or decreasing H, respectively. This means that, in the zeroth order resonant frequency, the effect of the vias inductance, L_{vias} in Fig. 5, is stronger than the effect of the parallel plate capacitance between the top patches and the ground plane, C_{patch1} and C_{patch2} in Fig. 5. On the other hand, the antenna efficiency is improved for bigger heights H because the antenna occupies a larger volume and radiates more efficiently. However, if the antennas are designed to be implemented in wireless and mobile devices, the available substrate thickness is limited and cannot be further increased.

Likewise, Fig. 16 provides the trade-off between the number of cells N, the length of the antenna L and the antenna efficiency η. In this case, adding or removing unit cells increases or decreases the length of the antenna at a linear rate. It also improves or deteriorates the antenna efficiency respectively, but in this case, the rate is not linearly proportional. Consequently, more unit cells do not substantially improve the antenna efficiency. On the other hand, having a larger number of unit cells

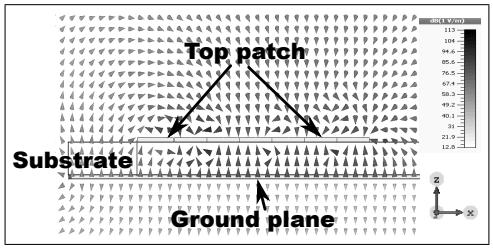

(a)

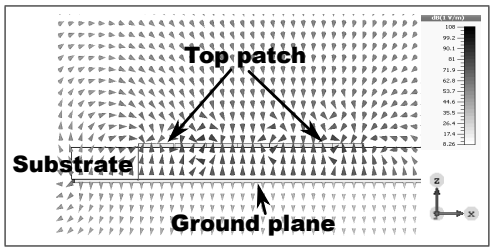

(b)

Fig. 13: Electric field along the plane (x-z) for antenna design 1 at a) 1.8 GHz and b) 2.1 GHz.

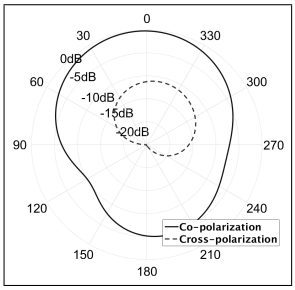

(a) E plane (y-z plane)

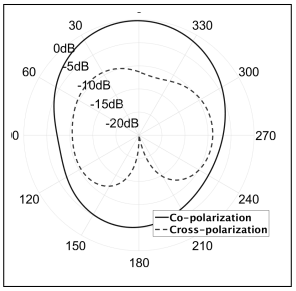

(b) H plane (x-z plane)

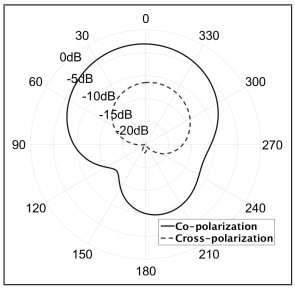

(c) E plane (y-z plane)

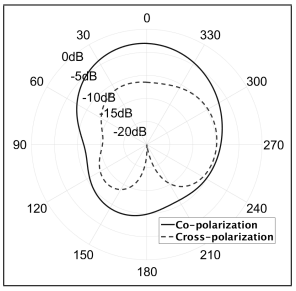

(d) H plane (x-z plane)

Fig. 14: Radiation patterns of the ZOR antenna design 1 at (a)-(b) 1.8 GHz and (c)-(d) 2.1 GHz.

allows for an easier antenna matching as each additional unit cell drastically reduces the high input impedance of ZOR antennas.

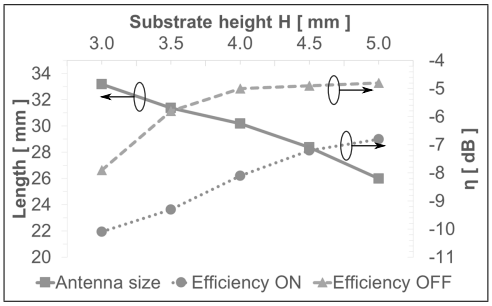

(a)

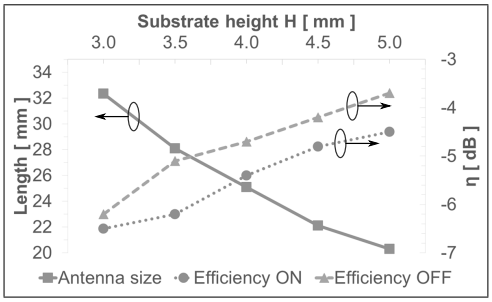

(b)

Fig. 15: Trade-off between substrate height H, antenna efficiency η and antenna length L for a) design 1 and b) design 2.

From these results, it is therefore possible to optimize antenna efficiency of the proposed ZOR antennas by adjusting the substrate height and the number of unit cells. It is also possible to compensate the efficiencies due to restrictions on thinner substrates by adding more unit cells at the expense of a larger overall antenna size, and vice versa.

D. ZEROTH ORDER RESONANT FREQUENCY SELECTION

In previous subsections, only two sets of surface impedances, Zs_{ON} and Zs_{OFF}, were used to switch between the two resonant frequencies, 1.8GHz and 2.1GHz. However, the surface impedance of graphene can be adjusted to any value between these two impedances. This allows the selection of any intermediate resonant frequency between the two design frequencies. Fig. 17 shows the antenna resonant frequencies for different intermediate values of surface resistance Rs for antenna Design 2. Note that in these results, only the real part of the surface impedance Rs is changed as the imaginary part Xs has a small effect on the total surface impedance and can hence be neglected. As observed, selecting intermediate surface resistance values permits

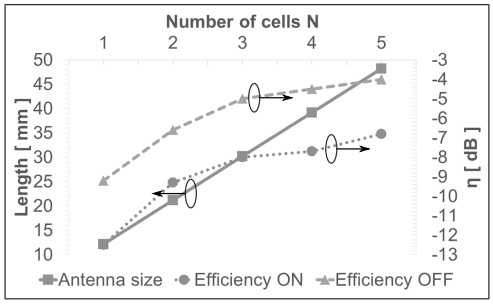

(a)

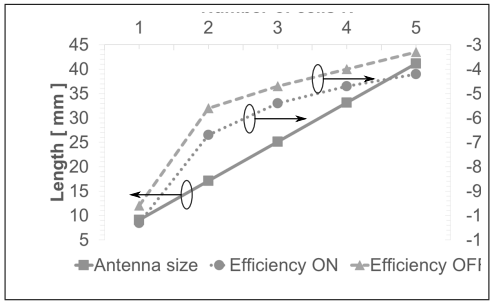

(b)

Fig. 16: Trade-off between number of cells N, antenna efficiency η and antenna length L for a) design 1 and b) design 2.

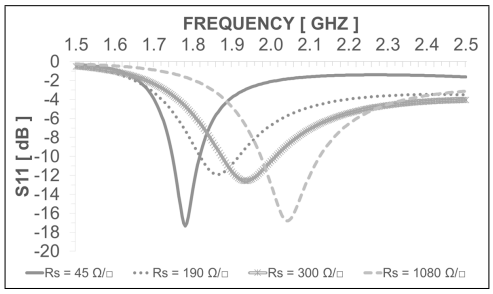

(a)

Fig. 17: Frequency selection in Design 2.

tuning resonant frequencies in the tuning range. Similar results are obtained for antenna Desing 1.

Fig. 18 shows the change of resonant frequency and antenna efficiency for Design 1 and Design 2 when selecting intermediate values of surface resistance Rs. The efficiencies of the intermediate frequencies are lower than the ones obtained for the 1.8GHz and 2.1GHz. The reason for this is that as the surface resistance changes, the portion of current propagating on graphene also changes. The current propagating on graphene suffers higher losses because the surface resistance is not at its minimum or maximum value.

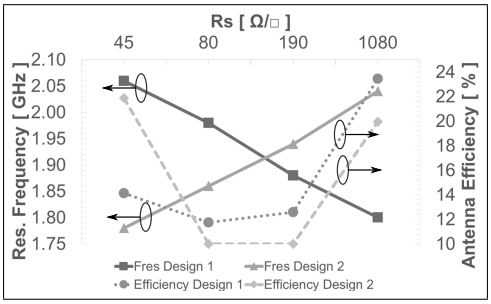

Fig. 18: Resonant frequency and antenna efficiency variation for intermediate values of Rs.

E. PERFORMANCE COMPARISON

The results obtained from the proposed frequency reconfigurable ZOR antennas are compared to some other works found in the literature. In [18], a substrate integrated-interdigital capacitor ZOR antenna is reconfigured by integrating varactor diodes. In [19], a ZOR antenna composed by mushroom-like unit cells is able to change its resonant frequency by implementing PIN-diodes in its integrated spiral slots. In [20], another mushroom-like antenna can switch frequencies by activating and deactivating grounded MEMS. Table IV summarizes the comparison. Note that, λ_0 is calculated in each work from the lowest operating frequency.

As observed from Table IV, the antenna gains obtained for the two proposed antennas here are comparable to those found in other works. Likewise, the range of change in the resonant frequency is within the same proportion as found in the other works. However, the antenna efficiencies for the antennas proposed in this paper are expected to be lower than in the other works (antenna efficiencies not provided in the references) as there are large losses atributed to graphene. This is expected as graphene is a technology still in development. Interestingly, implementing graphene in reconfigurable antennas can provide the ON/OFF switching functionality as in PIN diode and MEMS as well as the possibility of continuous frequency selection as in varactors. Finally, graphene can easily operate at higher frequencies (millimetre wave to THz regime) where other switching technologies will struggle to work properly.

VI. CONCLUSIONS

The present paper has demonstrated that graphene can be used in frequency reconfigurable ZOR antennas. The two proposed antenna designs switch between the

TABLE IV: Comparison of different ZOR reconfigurable antennas

Reference	Technology	Electrical Size ($L \times W$)	Frequencies Covered	Antenna Gain
This work: Design 1	Graphene	$0.18\lambda_0 \times 0.09\lambda_0$	1.8GHz and/to 2.1GHz	-0.2dB to -3dB
This work: Design 2	Graphene	$0.15\lambda_0 \times 0.13\lambda_0$	1.8GHz and/to 2.1GHz	-0.8dB to 0.6dB
[18]	Varactor	$0.3\lambda_0 \times 0.3\lambda_0$	4.1GHz to 4.5GHz	2.5dB and 4dB
[19]	PIN-diode	$0.06\lambda_0 \times 0.16\lambda_0$	2.3GHz and 3.1GHz	-6dB and -4.9dB
[20]	MEMS	$0.23\lambda_0 \times 0.28\lambda_0$	4.7GHz and 5GHz	-2.3dB and -2.5dB

LTE bands of 1.8GHz and 2.1GHz by applying different surface impedances of graphene Zs. Additionally, it has been shown that graphene can provide the functionality of selecting intermediate resonant frequencies, between 1.8GHz and 2.1GHz, by selecting different intermediate surface resistances Rs. Some design trade-offs such as graphene dimensions, substrate height, number of cells, antenna dimensions and antenna efficiency have also been described. The obtained antenna efficiencies are mainly affected by the losses in graphene but also by the antenna dimensions and configuration. The antenna Design 2 achieves a slightly higher antenna efficiency for both states than Design 1, 28.8% compared to 15.8% in the ON state and 33.9% compared to 31.6% in the OFF state, due to the losses in graphene being lower. The antenna gains obtained for both designs (-0.2 dB, -3 dB, -0.8 dB and 0.6 dB) are better than the ones obtained from other designs found in the literature that use PIN-diodes (-6 dB and -4.9 dB) or MEMS (-2.3 dB and -2.5 dB) as RF switches. Only the reference that uses varactors performs better in this feature (2.5 dB and 4 dB) but the proposed antenna designs in this paper are half the size of the one in that reference. In order to confirm the feasibility of using graphene in frequency reconfigurable antennas, physical prototypes of the proposed antennas need to be produced and measured in future work. This work will also analyse the effect of different methods that can be used to feed the DC voltage bias to the graphene sheets.

REFERENCES

[1] S. Nikolaou *et al.*, "UWB elliptical monopoles with a reconfigurable band notch using MEMS switches actuated without bias lines," *IEEE Trans. Antennas Propag.*, vol. 57, no. 8, pp. 2242–2251, 2009.

[2] G. H. Huff and J. T. Bernhard, "Integration of packaged RF MEMS switches with radiation pattern reconfigurable square spiral microstrip antennas," *IEEE Trans. Antennas Propag.*, vol. 54, no. 2, pp. 464–469, 2006.

[3] M. Y. Chen *et al.*, "Conformal ink-jet printed C-band phased-array antenna incorporating carbon nanotube field-effect transistor based reconfigurable true-time delay lines," *IEEE Trans. Microw. Theory Techn*, vol. 60, no. 1, pp. 179–184, Jan 2012.

[4] X. L. Yang *et al.*, "Frequency reconfigurable antenna for wireless communications using GaAs FET switch," *IEEE Antennas Wireless Propag. Lett*, vol. 14, pp. 807–810, Dec 2015.

[5] B. Kim *et al.*, "A novel single-feed circular microstrip antenna with reconfigurable polarization capability," *IEEE Trans. Antennas Propag.*, vol. 56, no. 3, pp. 630–638, 2008.

[6] C. Zhang *et al.*, "A low-profile branched monopole laptop reconfigurable multiband antenna for wireless applications," *IEEE Antennas Wireless Propag. Lett*, vol. 8, pp. 216–219, 2009.

[7] C. Yoon *et al.*, "A reconfigurable antenna using varactor diode for LTE MIMO applications," *Microw. Opt. Technol. Lett.*, vol. 55, no. 5, pp. 1141–1145, 2013.

[8] M. W. Young, S. Yong, and J. T. Bernhard, "A miniaturized frequency reconfigurable antenna with single bias, dual varactor tuning," *IEEE Trans. Antennas Propag.*, vol. 63, no. 3, pp. 946–951, March 2015.

[9] R. L. Haupt, "Reconfigurable patch with switchable conductive edges," *Microw. Opt. Technol. Lett.*, vol. 51, no. 7, pp. 1757–1760, 2009.

[10] R. L. Haupt and M. Lanagan, "Reconfigurable antennas," *IEEE Antennas Propag. Mag*, vol. 55, no. 1, pp. 49–61, 2013.

[11] C. Caloz and T. Itoh, *Electromagnetic metamaterials: transmission line theory and microwave applications*. John Wiley & Sons, 2005.

[12] F. Yang and Y. Rahmat-Samii, "Microstrip antennas integrated with electromagnetic band-gap (EBG) structures: a low mutual coupling design for array applications," *IEEE Trans. Antennas Propag.*, vol. 51, no. 10, pp. 2936–2946, Oct 2003.

[13] H. Mosallaei and K. Sarabandi, "Antenna miniaturization and bandwidth enhancement using a reactive impedance substrate," *IEEE Trans. Antennas Propag.*, vol. 52, no. 9, pp. 2403–2414, Sept 2004.

[14] F. Bilotti, A. Alu, and L. Vegni, "Design of miniaturized metamaterial patch antennas with μ-negative loading," *IEEE Trans. Antennas Propag.*, vol. 56, no. 6, pp. 1640–1647, June 2008.

[15] W. Yang *et al.*, "A wideband and high-gain edge-fed patch antenna and array using artificial magnetic conductor structures," *IEEE Antennas Wireless Propag. Lett*, vol. 12, pp. 769–772, 2013.

[16] A. Sanada *et al.*, "A planar zeroth-order resonator antenna using a left-handed transmission line," in *34th European Microwave Conf. (EuMC 2004)*, vol. 3, Oct 2004, pp. 1341–1344.

[17] A. Lai, K. M. K. H. Leong, and T. Itoh, "Infinite wavelength resonant antennas with monopolar radiation pattern based on periodic structures," *IEEE Trans. Antennas Propag.*, vol. 55, no. 3, pp. 868–876, March 2007.

[18] S. Sam, H. Kang, and S. Lim, "Frequency reconfigurable and miniaturized substrate integrated waveguide interdigital capacitor (SIW-IDC) antenna," *IEEE Trans. Antennas Propag.*, vol. 62, no. 3, pp. 1039–1045, March 2014.

[19] J. Choi and S. Lim, "Frequency and radiation pattern reconfigurable small metamaterial antenna using its extraordinary zeroth-order resonance," *J. Electromagnet. Wave*, vol. 24, no. 14-15, pp. 2119–2127, 2010.

[20] Y. Jang, J. Choi, and S. Lim, "Frequency reconfigurable zeroth-order resonant antenna using RF MEMS switch," *Microw. Opt. Technol. Lett.*, vol. 54, no. 5, pp. 1266–1269, 2012.

[21] A. H. N. Castro *et al.*, "The electronic properties of graphene," *Rev. Mod. Phys.*, vol. 81, pp. 109–162, Jan 2009.

[22] F. Bonaccorso *et al.*, "Graphene photonics and optoelectronics," *Nature Photon.*, vol. 4, no. 9, pp. 611–622, 2010.

[23] C. Lee *et al.*, "Measurement of the elastic properties and intrinsic strength of monolayer graphene," *Science*, vol. 321, no. 5887, pp. 385–388, 2008.
[24] Y. Yao *et al.*, "Broad electrical tuning of graphene-loaded plasmonic antennas," *Nano Lett.*, vol. 13, no. 3, pp. 1257–1264, 2013.
[25] Z. Xu, X. Dong, and J. Bornemann, "Design of a reconfigurable MIMO system for THz communications based on graphene antennas," *IEEE Trans. THz Sci. Technol.*, vol. 4, no. 5, pp. 609–617, Sept 2014.
[26] E. Carrasco *et al.*, "Gate-controlled mid-infrared light bending with aperiodic graphene nanoribbons array," *Nanotechnology*, vol. 26, no. 13, p. 134002, 2015.
[27] S. Bae *et al.*, "Roll-to-roll production of 30-inch graphene films for transparent electrodes," *Nat. Nanotechnol.*, vol. 5, no. 8, pp. 574–578, 2010.
[28] J. Perruisseau-Carrier *et al.*, "Graphene antennas: Can integration and reconfigurability compensate for the loss?" in *2013 European Microwave Conf. (EuMC)*, Oct 2013, pp. 369–372.
[29] M. Tamagnone *et al.*, "Hybrid graphene-metal reconfigurable terahertz antenna," in *2013 IEEE MTT-S Int. Microwave Symp. Dig. (IMS)*, June 2013, pp. 1–3.
[30] C. N. Alvarez, R. Cheung, and J. S. Thompson, "Graphene reconfigurable antennas for LTE and WIFI systems," in *2014 Antennas and Propagation Conf. (LAPC 2014)*, Nov 2014, pp. 434–438.
[31] X. Zhang *et al.*, "Graphene reconfigurable coplanar waveguide (CPW)-fed circular slot antenna," in *2015 IEEE Int. Symp. Antennas and Propagation USNC/URSI Nat. Radio Science Meeting (APS/URSI 2015)*, July 2015, pp. 2293–2294.
[32] C. N. Alvarez, R. Cheung, and J. S. Thompson, "Polarization reconfigurable antennas using graphene for microwave applications," in *2015 IEEE Int. Conf. Ubiquitous Wireless Broadband (ICUWB 2015)*, Oct 2015, pp. 1–5.
[33] T. Leng *et al.*, "Reconfigurable dipole antenna design using graphene based switich," in *2015 IEEE Int. Symp. Antennas and Propagation USNC/URSI Nat. Radio Science Meeting (APS/URSI 2015)*, July 2015, pp. 2295–2296.
[34] M. Aldrigo, M. Dragoman, and D. Dragoman, "Smart antennas based on graphene," *J. Appl. Phys.*, vol. 116, no. 11, 2014.
[35] A. Sanada, C. Caloz, and T. Itoh, "Novel zeroth-order resonance in composite right/left-handed transmission line resonators," in *Proc. Asia-Pacific Microwave Conf*, vol. 3, 2003, pp. 1588–1591.
[36] G. W. Hanson, "Dyadic Greens functions and guided surface waves for a surface conductivity model of graphene," *J. Appl. Phys.*, vol. 103, no. 6, 2008.
[37] N. M. R. Peres, "*Colloquium* : The transport properties of graphene: An introduction," *Rev. Mod. Phys.*, vol. 82, pp. 2673–2700, Sep 2010.
[38] J. H. Chen *et al.*, "Intrinsic and extrinsic performance limits of graphene devices on SiO_2," *Nat. Nanotechnol.*, vol. 3, no. 4, pp. 206–209, 2008.
[39] L. M. Woods and G. D. Mahan, "Electron-phonon effects in graphene and armchair (10, 10) single-wall carbon nanotubes," *Phys. Rev. B*, vol. 61, no. 16, p. 10651, 2000.
[40] N. Petrone *et al.*, "Chemical vapor deposition-derived graphene with electrical performance of exfoliated graphene," *Nano Lett.*, vol. 12, no. 6, pp. 2751–2756, 2012, pMID: 22582828.
[41] K. H. Lee *et al.*, "Large-scale synthesis of high-quality hexagonal boron nitride nanosheets for large-area graphene electronics," *Nano Lett.*, vol. 12, no. 2, pp. 714–718, 2012.
[42] K. K. Kim *et al.*, "Synthesis and characterization of hexagonal boron nitride film as a dielectric layer for graphene devices," *ACS nano*, vol. 6, no. 10, pp. 8583–8590, 2012.
[43] J. Martin *et al.*, "Observation of electron–hole puddles in graphene using a scanning single-electron transistor," *Nature Phys.*, vol. 4, no. 2, pp. 144–148, 2008.
[44] *RT/duroid 5870 /5880 High Frequency Laminates*, Rogers Corporation, 2016. [Online]. Available: https://www.rogerscorp.com/documents/606/acm/RT-duroid-5870-5880-Data-Sheet.pdf

Bibliography

[1] W. Roh, "5G mobile communications for 2020 and beyond-vision and key enabling technologies," *Key note: at IEEE WCNC*, 2014.

[2] S. Mann. Wearable computing in "the encyclopedia of human-computer interaction, 2nd ed.". Interaction Design Foundation. [Online]. Available: https://www.interaction-design.org/literature/book/the-encyclopedia-of-human-computer-interaction-2nd-ed/wearable-computing

[3] J. McCann and D. Bryson, *Smart clothes and wearable technology*. Elsevier, 2009.

[4] J. P. Conti, "The internet of things," *Communications Engineer*, vol. 4, no. 6, pp. 20–25, 2006.

[5] P. Demestichas *et al.*, "5G on the horizon: Key challenges for the radio-access network," *IEEE Vehicular Technology Magazine*, vol. 8, no. 3, pp. 47–53, Sept 2013.

[6] F. Boccardi *et al.*, "Five disruptive technology directions for 5G," *IEEE Commun. Mag.*, vol. 52, no. 2, pp. 74–80, February 2014.

[7] W. H. Chin, Z. Fan, and R. Haines, "Emerging technologies and research challenges for 5G wireless networks," *IEEE Wireless Communications Magazine*, vol. 21, no. 2, pp. 106–112, April 2014.

[8] P. Corcoran, "The internet of things: Why now, and what's next?" *IEEE Consumer Electronics Magazine*, vol. 5, no. 1, pp. 63–68, Jan 2016.

[9] D. Soldani and A. Manzalini, "Horizon 2020 and beyond: On the 5G operating system for a true digital society," *IEEE Vehicular Technology Magazine*, vol. 10, no. 1, pp. 32–42, March 2015.

[10] S. Greengard, *The Internet of Things*. MIT Press, 2015.

[11] P. Smulders, "Exploiting the 60 GHz band for local wireless multimedia access: prospects and future directions," *IEEE Commun. Mag.*, vol. 40, no. 1, pp. 140–147, 2002.

[12] T. S. Rappaport *et al.*, "Millimeter wave mobile communications for 5G cellular: It will work!" *IEEE Access*, vol. 1, pp. 335–349, 2013.

[13] C. X. Wang *et al.*, "Cellular architecture and key technologies for 5G wireless communication networks," *IEEE Commun. Mag.*, vol. 52, no. 2, pp. 122–130, February 2014.

[14] J. Karjalainen *et al.*, "Challenges and opportunities of mm-wave communication in 5G networks," in *2014 9th International Conference on Cognitive Radio Oriented Wireless Networks and Communications (CROWNCOM)*, June 2014, pp. 372–376.

[15] J. G. Andrews *et al.*, "What will 5G be?" *IEEE J. Sel. Areas Commun*, vol. 32, no. 6, pp. 1065–1082, June 2014.

[16] S. Iijima *et al.*, "Helical microtubules of graphitic carbon," *Nature*, vol. 354, no. 6348, pp. 56–58, 1991.

[17] R. A. Shelby, D. R. Smith, and S. Schultz, "Experimental verification of a negative index of refraction," *Science*, vol. 292, no. 5514, pp. 77–79, 2001.

[18] K. S. Novoselov *et al.*, "Electric field effect in atomically thin carbon films," *Science*, vol. 306, no. 5696, pp. 666–669, 2004.

[19] V. G. Veselago, "The electrodynamics of substances with simultaneously negative values of ϵ and μ," *Soviet Physics Uspekhi*, vol. 10, no. 4, p. 509, 1968.

[20] R. E. Smalley, M. S. Dresselhaus, G. Dresselhaus, and P. Avouris, *Carbon nanotubes: synthesis, structure, properties, and applications*. Springer Science & Business Media, 2003, vol. 80.

[21] A. Lai, T. Itoh, and C. Caloz, "Composite right/left-handed transmission line metamaterials," *IEEE Microw. Mag.*, vol. 5, no. 3, pp. 34–50, 2004.

[22] A. H. N. Castro *et al.*, "The electronic properties of graphene," *Rev. Mod. Phys.*, vol. 81, pp. 109–162, Jan 2009.

[23] L. Pierantoni and F. Coccetti, "Radio-frequency nanoelectronics: A new paradigm in electronic systems design," in *2010 Asia-Pacific Microwave Conference*. IEEE, 2010, pp. 1007–1014.

[24] N. M. R. Peres, "*Colloquium* : The transport properties of graphene: An introduction," *Rev. Mod. Phys.*, vol. 82, pp. 2673–2700, Sep 2010.

[25] S. Das Sarma, S. Adam, E. H. Hwang, and E. Rossi, "Electronic transport in two-dimensional graphene," *Rev. Mod. Phys.*, vol. 83, pp. 407–470, May 2011.

[26] A. D. Franklin *et al.*, "Sub-10 nm carbon nanotube transistor," *Nano Lett.*, vol. 12, no. 2, pp. 758–762, 2012.

[27] M. Voutilainen, E. T. Seppala, P. Pasanen, and M. Oksanen, "Graphene and carbon nanotube applications in mobile devices," *IEEE Trans. Electron Devices*, vol. 59, no. 11, pp. 2876–2887, Nov 2012.

[28] R. Saito *et al.*, *Physical properties of carbon nanotubes*. World Scientific, 1998, vol. 35.

[29] N. Engheta and R. W. Ziolkowski, *Metamaterials: physics and engineering explorations*. John Wiley & Sons, 2006.

[30] C. Caloz and T. Itoh, *Electromagnetic metamaterials: transmission line theory and microwave applications*. John Wiley & Sons, 2005.

[31] P. Poncharal, C. Berger, Y. Yi, Z. Wang, and W. A. de Heer, "Room temperature ballistic conduction in carbon nanotubes," *The Journal of Physical Chemistry B*, vol. 106, no. 47, pp. 12 104–12 118, 2002.

[32] G. W. Hanson, "Fundamental transmitting properties of carbon nanotube antennas," *IEEE Trans. Antennas Propag.*, vol. 53, no. 11, pp. 3426–3435, Nov 2005.

[33] "IEEE standard for definitions of terms for antennas," *IEEE Std 145-2013 (Revision of IEEE Std 145-1993)*, pp. 1–50, March 2014.

[34] C. A. Balanis, *Antenna theory : analysis and design.*, 2nd ed. New York ; Chichester : Wiley, 1997.

[35] R. E. Collin, *Antennas and Radiowave Propagation*. New York: McGraw-Hill Series in Electrical Engineering, 1985.

[36] R. Johnson, *Antenna engineering handbook.*, 3rd ed. New York ; London : McGraw-Hill, 1993.

[37] D. M. Pozar, *Microwave Engineering.*, 2nd ed. New York ; Chichester : Wiley, 1998.

[38] L. Jofre, M. Martínez-Vázquez, R. Serrano, and G. Roqueta, Eds., *Handbook on Small Antennas*, 1st ed. EurAAP Technical Working Group on Compact Antennas, 2012.

[39] L. J. Chu, "Physical limitations of omnidirectional antennas," *J. Appl. Phys.*, vol. 19, no. 12, pp. 1163–1175, 1948.

[40] J. S. McLean, "A re-examination of the fundamental limits on the radiation Q of electrically small antennas," *IEEE Trans. Antennas Propag.*, vol. 44, no. 5, pp. 672–, May 1996.

[41] H. A. Wheeler, "Fundamental limitations of small antennas," *Proceedings of the IRE*, vol. 35, no. 12, pp. 1479–1484, Dec 1947.

[42] ——, "The radiansphere around a small antenna," *Proceedings of the IRE*, vol. 47, no. 8, pp. 1325–1331, Aug 1959.

[43] R. Harrington, "On the gain and beamwidth of directional antennas," *IRE Transactions on Antennas and Propagation*, vol. 6, no. 3, pp. 219–225, July 1958.

[44] A. D. Yaghjian and S. R. Best, "Impedance, bandwidth, and Q of antennas," *IEEE Trans. Antennas Propag.*, vol. 53, no. 4, pp. 1298–1324, April 2005.

[45] A. R. Lopez, "Wheeler and fano impedance matching [antenna designer's notebook]," *IEEE Antennas Propag. Mag*, vol. 49, no. 4, pp. 116–119, Aug 2007.

[46] R. L. Haupt and M. Lanagan, "Reconfigurable antennas," *IEEE Antennas Propag. Mag*, vol. 55, no. 1, pp. 49–61, 2013.

[47] C. G. Christodoulou, Y. Tawk, S. A. Lane, and S. R. Erwin, "Reconfigurable antennas for wireless and space applications," *Proc. IEEE*, vol. 100, no. 7, pp. 2250–2261, 2012.

[48] A. Geim and K. Novoselov, "The rise of graphene," *Nat. Mater.*, vol. 6, no. 3, pp. 183–191, 2007.

[49] V. Skákalová and A. B. Kaiser, Eds., *"Electronic transport in graphene: towards high mobility",in Graphene : properties, preparation, characterisation and devices [electronic resource].* Elsevier, 2014.

[50] J. H. Warner, A. Bachmatiuk, M. Rummeli and, and F. Schaffel, Eds., *"Properties of graphene",in Graphene. [electronic resource] : fundamentals and emergent applications.* Elsevier, 2013.

[51] R. Murali, Ed., *Graphene nanoelectronics: from materials to circuits.* Springer, 2012.

[52] S. Bae *et al.*, "Roll-to-roll production of 30-inch graphene films for transparent electrodes," *Nat. Nanotechnol.*, vol. 5, no. 8, pp. 574–578, 2010.

[53] P. R. Wallace, "The band theory of graphite," *Phys. Rev.*, vol. 71, pp. 622–634, May 1947.

[54] A. B. Kuzmenko, E. Van Heumen, F. Carbone, and D. Van Der Marel, "Universal optical conductance of graphite," *Phys. Rev. Lett.*, vol. 100, no. 11, p. 117401, 2008.

[55] F. Bonaccorso *et al.*, "Graphene photonics and optoelectronics," *Nature Photon.*, vol. 4, no. 9, pp. 611–622, 2010.

[56] C. Lee *et al.*, "Measurement of the elastic properties and intrinsic strength of monolayer graphene," *Science*, vol. 321, no. 5887, pp. 385–388, 2008.

[57] G. Burns, Ed., *Solid State Physics.* Academic Press, 1985.

[58] P. Hofmann, Ed., *Solid State Physics : An Introduction [e-book].* Wiley-VCH, 2008.

[59] M. Dressel and G. Grüner, *"Metals" in Electrodynamics of Solids.* Cambridge University Press, 2002, cambridge Books Online.

[60] V. P. Gusynin, S. G. Sharapov, and J. P. Carbotte, "Magneto-optical conductivity in graphene," *J. Phys.: Condens. Matter*, vol. 19, no. 2, p. 026222, 2007.

[61] G. W. Hanson, "Dyadic Greens functions and guided surface waves for a surface conductivity model of graphene," *J. Appl. Phys.*, vol. 103, no. 6, 2008.

[62] J. H. Chen *et al.*, "Intrinsic and extrinsic performance limits of graphene devices on SiO_2," *Nat. Nanotechnol.*, vol. 3, no. 4, pp. 206–209, 2008.

[63] K. S. Novoselov *et al.*, "Two-dimensional gas of massless Dirac fermions in graphene," *Nature*, vol. 438, no. 7065, pp. 197–200, 2005.

[64] Y. Zhang, Y. W. Tan, H. L. Stormer, and P. Kim, "Experimental observation of the quantum Hall effect and Berry's phase in graphene," *Nature*, vol. 438, no. 7065, pp. 201–204, 2005.

[65] V. Ariel and A. Natan, "Electron effective mass in graphene," in *2013 Int. Conf. on Electromagnetics in Advanced Applications (ICEAA)*, Sept 2013, pp. 696–698.

[66] M. Jablan, H. Buljan, and M. Soljačić, "Plasmonics in graphene at infrared frequencies," *Phys. Rev. B*, vol. 80, p. 245435, Dec 2009.

[67] F. Banhart, J. Kotakoski, and A. V. Krasheninnikov, "Structural defects in graphene," *ACS nano*, vol. 5, no. 1, pp. 26–41, 2010.

[68] T. Stauber, N. M. R. Peres, and F. Guinea, "Electronic transport in graphene: A semiclassical approach including midgap states," *Phys. Rev. B*, vol. 76, p. 205423, Nov 2007.

[69] A. Ferreira *et al.*, "Transport properties of graphene with one-dimensional charge defects," *EPL (Europhysics Letters)*, vol. 94, no. 2, p. 28003, 2011.

[70] L. G. Canado *et al.*, "Quantifying defects in graphene via raman spectroscopy at different excitation energies," *Nano Letters*, vol. 11, no. 8, pp. 3190–3196, 2011.

[71] E. H. Hwang, S. Adam, and S. Das Sarma, "Carrier transport in two-dimensional graphene layers," *Phys. Rev. Lett.*, vol. 98, p. 186806, May 2007.

[72] D. Teweldebrhan and A. A. Balandin, "Modification of graphene properties due to electron-beam irradiation," *Appl. Phys. Lett.*, vol. 94, no. 1, p. 013101, 2009.

[73] Z. H. Ni *et al.*, "On resonant scatterers as a factor limiting carrier mobility in graphene," *Nano Lett.*, vol. 10, no. 10, pp. 3868–3872, 2010.

[74] P. Y. Huang *et al.*, "Grains and grain boundaries in single-layer graphene atomic patchwork quilts," *Nature*, vol. 469, no. 7330, pp. 389–392, 2011.

[75] W. Gannett *et al.*, "Boron nitride substrates for high mobility chemical vapor deposited graphene," *Appl. Phys. Lett.*, vol. 98, no. 24, 2011.

[76] N. Petrone *et al.*, "Chemical vapor deposition-derived graphene with electrical performance of exfoliated graphene," *Nano Lett.*, vol. 12, no. 6, pp. 2751–2756, 2012, pMID: 22582828.

[77] J. Moser, A. Barreiro, and A. Bachtold, "Current-induced cleaning of graphene," *Appl. Phys. Lett.*, vol. 91, no. 16, p. 163513, 2007.

[78] K. I. Bolotin *et al.*, "Ultrahigh electron mobility in suspended graphene," *Solid State Commun.*, vol. 146, no. 9, pp. 351–355, 2008.

[79] D. Jena and A. Konar, "Enhancement of carrier mobility in semiconductor nanostructures by dielectric engineering," *Phys. Rev. Lett.*, vol. 98, p. 136805, Mar 2007.

[80] X. Hong, A. Posadas, K. Zou, C. H. Ahn, and J. Zhu, "High-mobility few-layer graphene field effect transistors fabricated on epitaxial ferroelectric gate oxides," *Phys. Rev. Lett.*, vol. 102, no. 13, p. 136808, 2009.

[81] C. R. Dean *et al.*, "Boron nitride substrates for high-quality graphene electronics," *Nat. Nanotechnol.*, vol. 5, no. 10, pp. 722–726, 2010.

[82] W. Bao *et al.*, "Lithography-free fabrication of high quality substrate-supported and freestanding graphene devices," *Nano Res.*, vol. 3, no. 2, pp. 98–102, 2010.

[83] A. S. Mayorov *et al.*, "Micrometer-scale ballistic transport in encapsulated graphene at room temperature," *Nano Lett.*, vol. 11, no. 6, pp. 2396–2399, 2011.

[84] P. J. Zomer, S. P. Dash, N. Tombros, and B. J. van Wees, "A transfer technique for high mobility graphene devices on commercially available hexagonal boron nitride," *Appl. Phys. Lett.*, vol. 99, no. 23, 2011.

[85] Y. C. Lin *et al.*, "Graphene annealing: how clean can it be?" *Nano Lett.*, vol. 12, no. 1, pp. 414–419, 2011.

[86] C. Kittel, Ed., *Introduction to Solid State Physics*. Wiley, 2005.

[87] S. Piscanec, M. Lazzeri, F. Mauri, and A. C. Ferrari, "Optical phonons of graphene and nanotubes," *Eur. Phys. J.*, vol. 148, no. 1, pp. 159–170, 2007.

[88] S. V. Morozov *et al.*, "Giant intrinsic carrier mobilities in graphene and its bilayer," *Phys. Rev. Lett.*, vol. 100, p. 016602, Jan 2008.

[89] V. N. Kotov, B. Uchoa, V. M. Pereira, F. Guinea, and A. H. C. Neto, "Electron-electron interactions in graphene: Current status and perspectives," *Rev. Mod. Phys.*, vol. 84, no. 3, p. 1067, 2012.

[90] T. Fang, A. Konar, H. Xing, and D. Jena, "Carrier statistics and quantum capacitance of graphene sheets and ribbons," *Appl. Phys. Lett.*, vol. 91, no. 9, p. 092109, 2007.

[91] J. Martin *et al.*, "Observation of electron–hole puddles in graphene using a scanning single-electron transistor," *Nature Phys.*, vol. 4, no. 2, pp. 144–148, 2008.

[92] R. Bancroft, *Microstrip and printed antenna design.*, 2nd ed. Raleigh, N.C. : SciTech Pub, 2009.

[93] J. Prasek *et al.*, "Methods for carbon nanotubes synthesis-review," *J. Mater. Chem.*, vol. 21, pp. 15 872–15 884, 2011.

[94] X. Zhao, Y. Liu, S. Inoue, T. Suzuki, R. O. Jones, and Y. Ando, "Smallest carbon nanotube is 3$\AA$ in diameter," *Phys. Rev. Lett.*, vol. 92, p. 125502, Mar 2004.

[95] X. Wang *et al.*, "Fabrication of ultralong and electrically uniform single-walled carbon nanotubes on clean substrates," *Nano Lett.*, vol. 9, no. 9, pp. 3137–3141, 2009.

[96] C. T. White and T. N. Todorov, "Carbon nanotubes as long ballistic conductors," *Nature*, vol. 393, no. 6682, pp. 240–242, 1998.

[97] M. J. Treacy, T. Ebbesen, and J. Gibson, "Exceptionally high Young's modulus observed for individual carbon nanotubes," *Nature*, 1996.

[98] E. W. Wong, P. E. Sheehan, and C. M. Lieber, "Nanobeam mechanics: elasticity, strength, and toughness of nanorods and nanotubes," *Science*, vol. 277, no. 5334, pp. 1971–1975, 1997.

[99] G. Y. Slepyan, S. Maksimenko, A. Lakhtakia, O. Yevtushenko, and A. Gusakov, "Electrodynamics of carbon nanotubes: Dynamic conductiv-

ity, impedance boundary conditions, and surface wave propagation," *Phys. Rev. B*, vol. 60, no. 24, p. 17136, 1999.

[100] M. Lin and K. W.-K. Shung, "Plasmons and optical properties of carbon nanotubes," *Phys. Rev. B*, vol. 50, no. 23, p. 17744, 1994.

[101] O. N. Singh and A. Lakhtakia, *Electromagnetic fields in unconventional materials and structures*. Wiley-Interscience, 2000, vol. 119.

[102] P. J. Burke, S. Li, and Z. Yu, "Quantitative theory of nanowire and nanotube antenna performance," *IEEE Trans. Nanotechnol.*, vol. 5, no. 4, pp. 314–334, July 2006.

[103] M. S. Sarto and A. Tamburrano, "Single-conductor transmission-line model of multiwall carbon nanotubes," *IEEE Trans. Nanotechnol.*, vol. 9, no. 1, pp. 82–92, Jan 2010.

[104] G. W. Hanson, "Radiation efficiency of nano-radius dipole antennas in the microwave and far-infrared regimes," *IEEE Antennas Propag. Mag*, vol. 50, no. 3, pp. 66–77, June 2008.

[105] H. Tang, X. Ding, and Q. Wu, "Transmission-line modeling characterization for multi-wall carbon nanotube antenna radiation," in *2012 5th Global Symposium on Millimeter Waves (GSMM)*, May 2012, pp. 549–553.

[106] J. J. Plombon, K. P. OBrien, F. Gstrein, V. M. Dubin, and Y. Jiao, "High-frequency electrical properties of individual and bundled carbon nanotubes," *Appl. Phys. Lett.*, vol. 90, no. 6, 2007.

[107] C. Rutherglen, D. Jain, and P. Burke, "RF resistance and inductance of massively parallel single walled carbon nanotubes: Direct, broadband measurements and near perfect 50 impedance matching," *Appl. Phys. Lett.*, vol. 93, no. 8, p. 83119, 2008.

[108] D. Sievenpiper *et al.*, "High-impedance electromagnetic surfaces with a forbidden frequency band," *IEEE Trans. Microw. Theory Techn*, vol. 47, no. 11, pp. 2059–2074, Nov 1999.

[109] A. Sanada, C. Caloz, and T. Itoh, "Novel zeroth-order resonance in composite right/left-handed transmission line resonators," in *Proc. Asia-Pacific Microwave Conf*, vol. 3, 2003, pp. 1588–1591.

[110] P. J. Burke, "Luttinger liquid theory as a model of the gigahertz electrical properties of carbon nanotubes," *IEEE Trans. Nanotechnol.*, vol. 1, no. 3, pp. 129–144, Sep 2002.

[111] Y. Wang *et al.*, "Receiving and transmitting light-like radio waves: Antenna effect in arrays of aligned carbon nanotubes," *Appl. Phys. Lett.*, vol. 85, no. 13, pp. 2607–2609, 2004.

[112] K. Kempa *et al.*, "Carbon nanotubes as optical antennae," *Advanced Materials*, vol. 19, no. 3, pp. 421–426, 2007.

[113] A. Naeemi and J. D. Meindl, "Performance modeling for single-and multi-wall carbon nanotubes as signal and power interconnects in gigascale systems," *IEEE Trans. Electron Devices*, vol. 55, no. 10, pp. 2574–2582, 2008.

[114] W. Yue, W. Qun, H. Xun-Jun, Z. Shao-Qing, and Z. Lei-Lei, "Terahertz radiation from armchair carbon nanotube dipole antenna," *Chinese Physics B*, vol. 18, no. 5, p. 1801, 2009.

[115] M. V. Shuba, G. Y. Slepyan, S. A. Maksimenko, C. Thomsen, and A. Lakhtakia, "Theory of multiwall carbon nanotubes as waveguides and antennas in the infrared and the visible regimes," *Phys. Rev. B*, vol. 79, p. 155403, Apr 2009.

[116] J. M. Jornet and I. F. Akyildiz, "Graphene-based nano-antennas for electromagnetic nanocommunications in the terahertz band," in *2010 Proceedings*

of the Fourth European Conference on Antennas and Propagation (EuCAP). IEEE, 2010, pp. 1–5.

[117] S. Choi and K. Sarabandi, "Performance assessment of bundled carbon nanotube for antenna applications at terahertz frequencies and higher," *IEEE Trans. Antennas Propag.*, vol. 59, no. 3, pp. 802–809, March 2011.

[118] I. Llatser *et al.*, "Graphene-based nano-patch antenna for terahertz radiation," *Photonics and Nanostructures - Fundamentals and Applications*, vol. 10, no. 4, pp. 353 – 358, 2012, taCoNa-Photonics 2011.

[119] J. Perruisseau-Carrier, "Graphene for antenna applications: Opportunities and challenges from microwaves to THz," in *2012 Loughborough Antennas and Propagation Conf. (LAPC)*, Nov 2012, pp. 1–4.

[120] J. M. Jornet and I. F. Akyildiz, "Graphene-based plasmonic nano-antenna for terahertz band communication in nanonetworks," *IEEE J. Sel. Areas Commun*, vol. 31, no. 12, pp. 685–694, December 2013.

[121] J. Perruisseau-Carrier *et al.*, "Graphene antennas: Can integration and reconfigurability compensate for the loss?" in *2013 European Microwave Conf. (EuMC)*, Oct 2013, pp. 369–372.

[122] M. Tamagnone and J. Perruisseau-Carrier, "Predicting input impedance and efficiency of graphene reconfigurable dipoles using a simple circuit model," *IEEE Antennas Wireless Propag. Lett*, vol. 13, pp. 313–316, 2014.

[123] F. Cardarelli, *Materials handbook: a concise desktop reference*. London : Springer, 2008.

[124] D. Peroulis, K. Sarabandi, and L. P. B. Katehi, "Design of reconfigurable slot antennas," *IEEE Trans. Antennas Propag.*, vol. 53, no. 2, pp. 645–654, 2005.

[125] N. Behdad and K. Sarabandi, "A varactor-tuned dual-band slot antenna," *IEEE Trans. Antennas Propag.*, vol. 54, no. 2, pp. 401–408, 2006.

[126] C. J. Panagamuwa, A. Chauraya, and J. C. Vardaxoglou, "Frequency and beam reconfigurable antenna using photoconducting switches," *IEEE Trans. Antennas Propag.*, vol. 54, no. 2, pp. 449–454, 2006.

[127] K. R. Boyle and P. G. Steeneken, "A five-band reconfigurable PIFA for mobile phones," *IEEE Trans. Antennas Propag.*, vol. 55, no. 11, p. 3300, 2007.

[128] E. Erdil, K. Topalli, M. Unlu, O. A. Civi, and T. Akin, "Frequency tunable microstrip patch antenna using RF MEMS technology," *IEEE Trans. Antennas Propag.*, vol. 55, no. 4, pp. 1193–1196, April 2007.

[129] S. L. S. Yang, A. A. Kishk, and K. F. Lee, "Frequency reconfigurable U-slot microstrip patch antenna," *IEEE Antennas Wireless Propag. Lett*, vol. 7, pp. 127–129, 2008.

[130] C. R. White and G. M. Rebeiz, "Single-and dual-polarized tunable slot-ring antennas," *IEEE Trans. Antennas Propag.*, vol. 57, no. 1, pp. 19–26, 2009.

[131] R. L. Haupt, "Reconfigurable patch with switchable conductive edges," *Microw. Opt. Technol. Lett.*, vol. 51, no. 7, pp. 1757–1760, 2009.

[132] C. Zhang *et al.*, "A low-profile branched monopole laptop reconfigurable multiband antenna for wireless applications," *IEEE Antennas Wireless Propag. Lett*, vol. 8, pp. 216–219, 2009.

[133] B. A. Cetiner, G. R. Crusats, L. Jofre, and N. Biyikli, "RF MEMS integrated frequency reconfigurable annular slot antenna," *IEEE Trans. Antennas Propag.*, vol. 58, no. 3, pp. 626–632, March 2010.

[134] T. Aboufoul, A. Alomainy, and C. Parini, "Reconfiguring UWB monopole antenna for cognitive radio applications using GaAs FET switches," *IEEE Antennas Wireless Propag. Lett*, vol. 11, pp. 392–394, 2012.

[135] L. Huitema *et al.*, "Frequency tunable antenna using a magneto-dielectric material for DVB-H application," *IEEE Trans. Antennas Propag.*, vol. 61, no. 9, pp. 4456–4466, Sept 2013.

[136] H. A. Majid, M. K. A. Rahim, M. R. Hamid, N. A. Murad, and M. F. Ismail, "Frequency-reconfigurable microstrip patch-slot antenna," *IEEE Antennas Wireless Propag. Lett*, vol. 12, pp. 218–220, 2013.

[137] S. Pendharker, R. K. Shevgaonkar, and A. N. Chandorkar, "Optically controlled frequency-reconfigurable microstrip antenna with low photoconductivity," *IEEE Antennas Wireless Propag. Lett*, vol. 13, pp. 99–102, 2014.

[138] S. W. Lee and Y. Sung, "Compact frequency reconfigurable antenna for LTE/WWAN mobile handset applications," *IEEE Trans. Antennas Propag.*, vol. 63, no. 10, pp. 4572–4577, Oct 2015.

[139] A. Khidre, F. Yang, and A. Z. Elsherbeni, "A patch antenna with a varactor-loaded slot for reconfigurable dual-band operation," *IEEE Trans. Antennas Propag.*, vol. 63, no. 2, pp. 755–760, 2015.

[140] M. Borhani, P. Rezaei, and A. Valizade, "Design of a reconfigurable miniaturized microstrip antenna for switchable multiband systems," *IEEE Antennas Wireless Propag. Lett*, vol. 15, pp. 822–825, 2016.

[141] S. Hage-Ali, N. Tiercelin, P. Coquet, R. Sauleau, V. Preobrazhensky, and P. Pernod, "A millimeter-wave inflatable frequency-agile elastomeric antenna," *IEEE Antennas Wireless Propag. Lett*, vol. 9, pp. 1131–1134, 2010.

[142] P. Y. Qin, A. R. Weily, Y. J. Guo, and C. H. Liang, "Millimeter wave frequency reconfigurable quasi-Yagi antenna," in *2010 Asia-Pacific Microwave Conf.*, Dec 2010, pp. 642–645.

[143] Y. Yang, Y. Cai, K. Y. Chan, R. Ramer, and Y. J. Guo, "MEMS-loaded millimeter wave frequency reconfigurable quasi-Yagi dipole antenna," in *Asia-Pacific Microwave Conf. 2011*, Dec 2011, pp. 1318–1321.

[144] Y. Orlic *et al.*, "Frequency agile mechanical antenna for low-cost millimeter-wave applications," in *Proc. of the 2012 IEEE Int. Symp. on Antennas and Propagation*, July 2012, pp. 1–2.

[145] Z. Jiang, S. M. Rahman, J. L. Hesler, P. Fay, and L. Liu, "Design and characterisation of a 200 GHz tunable lens-coupled annular-slot antenna with a 50 GHz tuning range," *IET Microwaves, Antennas Propagation*, vol. 8, no. 11, pp. 842–848, August 2014.

[146] S. F. Jilani, S. M. Abbas, K. P. Esselle, and A. Alomainy, "Millimeter-wave frequency reconfigurable T-shaped antenna for 5G networks," in *2015 IEEE 11th Int. Conf. on Wireless and Mobile Computing, Networking and Communications (WiMob)*, Oct 2015, pp. 100–102.

[147] H. Ito, T. Yoshimatsu, H. Yamamoto, and T. Ishibashi, "Widely frequency tunable terahertz-wave emitter integrating uni-traveling-carrier photodiode and extended bowtie antenna," *Applied Physics Express*, vol. 6, no. 6, p. 064101, 2013.

[148] M. Unlu, A. Yilmaz, and C. Yilmaz, "Frequency and impedance reconfigurable antennas for terahertz photomixers," in *General Assembly and Scientific Symposium (URSI GASS), 2014 XXXIth URSI*, Aug 2014, pp. 1–4.

[149] A.-K. U. Michel *et al.*, "Using low-loss phase-change materials for mid-infrared antenna resonance tuning," *Nano Lett.*, vol. 13, no. 8, pp. 3470–3475, 2013.

[150] ——, "Reversible optical switching of infrared antenna resonances with ultrathin phase-change layers using femtosecond laser pulses," *ACS Photonics*, vol. 1, no. 9, pp. 833–839, 2014.

[151] T. Atay, J.-H. Song, and A. V. Nurmikko, "Strongly interacting plasmon nanoparticle pairs: from dipole-dipole interaction to conductively coupled regime," *Nano Lett.*, vol. 4, no. 9, pp. 1627–1631, 2004.

[152] A. Alu and N. Engheta, "Tuning the scattering response of optical nanoantennas with nanocircuit loads," *Nature Photon.*, vol. 2, no. 5, pp. 307–310, 2008.

[153] N. Large, M. Abb, J. Aizpurua, and O. L. Muskens, "Photoconductively loaded plasmonic nanoantenna as building block for ultracompact optical switches," *Nano Lett.*, vol. 10, no. 5, pp. 1741–1746, 2010.

[154] N. Liu, F. Wen, Y. Zhao, Y. Wang, P. Nordlander, N. J. Halas, and A. Alu, "Individual nanoantennas loaded with three-dimensional optical nanocircuits," *Nano Lett.*, vol. 13, no. 1, pp. 142–147, 2012.

[155] K. Chen *et al.*, "Electromechanically tunable suspended optical nanoantenna," *Nano Lett.*, vol. 16, no. 4, pp. 2680–2685, 2016.

[156] T. B. Hoang and M. H. Mikkelsen, "Broad electrical tuning of plasmonic nanoantennas at visible frequencies," *Appl. Phys. Lett.*, vol. 108, no. 18, 2016.

[157] J. S. Gomez-Diaz and J. Perruisseau-Carrier, "Microwave to THz properties of graphene and potential antenna applications," in *2012 Int. Symp. on Antennas and Propagation (ISAP)*. IEEE, 2012, pp. 239–242.

[158] M. Tamagnone, J. Gomez-Diaz, J. R. Mosig, and J. Perruisseau-Carrier, "Reconfigurable terahertz plasmonic antenna concept using a graphene stack," *Appl. Phys. Lett.*, vol. 101, no. 21, p. 214102, 2012.

[159] P. Liu *et al.*, "Tunable terahertz optical antennas based on graphene ring structures," *Appl. Phys. Lett.*, vol. 100, no. 15, 2012.

[160] Y. Yao *et al.*, "Broad electrical tuning of graphene-loaded plasmonic antennas," *Nano Lett.*, vol. 13, no. 3, pp. 1257–1264, 2013.

[161] J. Perruisseau-Carrier *et al.*, "Resonant and leaky-wave reconfigurable antennas based on graphene plasmonics," in *2013 IEEE Antennas and Propagation Society Int. Symp. (APSURSI)*, July 2013, pp. 136–137.

[162] M. Tamagnone, J. S. G. Diaz, J. Perruisseau-Carrier, and J. R. Mosig, "High-impedance frequency-agile THz dipole antennas using graphene," in *2013 7th European Conf. on Antennas and Propagation (EuCAP)*, April 2013, pp. 533–536.

[163] S. M. Raeis-Zadeh, M. Haghtalab, and S. Safavi-Naeini, "Graphene-based controllable antenna for terahertz photomixer sources," in *2014 IEEE Antennas and Propagation Society Int. Symp. (APSURSI)*, July 2014, pp. 862–863.

[164] F. Zangeneh-Nejad and R. Safian, "Graphene-based archimedean spiral thz antenna," in *2014 Third Conf. on Millimeter-Wave and Terahertz Technologies (MMWATT)*, Dec 2014, pp. 1–4.

[165] A. Cabellos-Aparicio, I. Llatser, E. Alarcn, A. Hsu, and T. Palacios, "Use of terahertz photoconductive sources to characterize tunable graphene RF plasmonic antennas," *IEEE Trans. Nanotechnol.*, vol. 14, no. 2, pp. 390–396, March 2015.

[166] M. Tamagnone *et al.*, "Hybrid graphene-metal reconfigurable terahertz antenna," in *2013 IEEE MTT-S Int. Microwave Symp. Dig. (IMS)*, June 2013, pp. 1–3.

[167] X. Zhang *et al.*, "Graphene reconfigurable coplanar waveguide (CPW)-fed circular slot antenna," in *2015 IEEE Int. Symp. Antennas and Propagation USNC/URSI Nat. Radio Science Meeting (APS/URSI 2015)*, July 2015, pp. 2293–2294.

[168] T. Leng, X. Huang, X. Zhang, and Z. Hu, "Reconfigurable dipole antenna design using graphene based switich," in *2015 IEEE Int. Symp. Antennas and Propagation USNC/URSI Nat. Radio Science Meeting (APS/URSI 2015)*, July 2015, pp. 2295–2296.

[169] A. Bunea, D. Neculoiu, M. Dragoman, G. Konstantinidis, and G. Deligeorgis, "X band tunable slot antenna with graphene patch," in *2015 European Microwave Conf. (EuMC)*. IEEE, 2015, pp. 614–617.

[170] C. Mias *et al.*, "Optically transparent microstrip antennas," in *IEE Colloq. on Antennas for Automotives*, 2000, pp. 8/1–8/6.

[171] G. Clasen and R. Langley, "Meshed patch antennas," *IEEE Trans. Antennas Propag.*, vol. 52, no. 6, pp. 1412–1416, 2004.

[172] F. Colombel, X. Castel, M. Himdi, G. Legeay, S. Vigneron, and E. M. Cruz, "Ultrathin metal layer, ITO film and ITO/Cu/ITO multilayer towards transparent antenna," *IET Sci. Meas. Technol.*, vol. 3, no. 3, pp. 229–234, 2009.

[173] T. W. Turpin and R. Baktur, "Meshed patch antennas integrated on solar cells," *IEEE Antennas Wireless Propag. Lett*, vol. 8, pp. 693–696, 2009.

[174] J. Hautcoeur, F. Colombel, X. Castel, M. Himdi, and E. M. Cruz, "Optically transparent monopole antenna with high radiation efficiency manufactured

with silver grid layer (AgGL)," *Electron. Lett*, vol. 45, no. 20, pp. 1014–1016, 2009.

[175] T. Yasin, R. Baktur, and C. Furse, "A study on the efficiency of transparent patch antennas designed from conductive oxide films," in *2011 IEEE Int. Symp. on Antennas and Propagation (APSURSI)*, 2011, pp. 3085–3087.

[176] M. J. Roo-Ons, S. V. Shynu, M. J. Ammann, S. J. McCormack, and B. Norton, "Transparent patch antenna on a-Si thin-film glass solar module," *Electronics Letters*, vol. 47, no. 2, pp. 85–86, January 2011.

[177] J. R. Saberin and C. Furse, "Challenges with optically transparent patch antennas," *IEEE Antennas Propag. Mag*, vol. 54, no. 3, pp. 10–16, 2012.

[178] J. Hautcoeur, L. Talbi, and K. Hettak, "Feasibility study of optically transparent CPW-fed monopole antenna at 60-GHz ISM bands," *IEEE Trans. Antennas Propag.*, vol. 61, no. 4, pp. 1651–1657, 2013.

[179] J. Hautcoeur, F. Colombel, M. Himdi, X. Castel, and E. M. Cruz, "Large and optically transparent multilayer for broadband H-shaped slot antenna," *IEEE Antennas Wireless Propag. Lett*, vol. 12, pp. 933–936, 2013.

[180] S. Hakimi, S. K. A. Rahim, M. Abedian, S. M. Noghabaei, and M. Khalily, "CPW-fed transparent antenna for extended ultrawideband applications," *IEEE Antennas Wireless Propag. Lett*, vol. 13, pp. 1251–1254, 2014.

[181] Y. Xu, E. P. Li, and X. C. Wei, "Modeling and design of multifunctional nanomaterial based flexible antenna," in *2014 XXXIth URSI General Assembly and Scientific Symp. (URSI GASS)*, Aug 2014, pp. 1–4.

[182] B. Wu and Y. Hao, "Material region division and antenna application of monolayer and multilayer graphene," in *The 8th European Conf. on Antennas and Propagation (EuCAP 2014)*, April 2014, pp. 497–498.

[183] K. H. Lee *et al.*, "Large-scale synthesis of high-quality hexagonal boron nitride nanosheets for large-area graphene electronics," *Nano Lett.*, vol. 12, no. 2, pp. 714–718, 2012.

[184] M. Roschke and F. Schwierz, "Electron mobility models for 4H, 6H, and 3C SiC [MESFETs]," *IEEE Trans. Electron Devices*, vol. 48, no. 7, pp. 1442–1447, Jul 2001.

[185] R. A. Street, J. Kakalios, and M. Hack, "Electron drift mobility in doped amorphous silicon," *Phys. Rev. B*, vol. 38, pp. 5603–5609, Sep 1988.

[186] J. Gomez-Diaz, C. Moldovan, S. Capdevila, J. Romeu, L. Bernard, A. Magrez, A. Ionescu, and J. Perruisseau-Carrier, "Self-biased reconfigurable graphene stacks for terahertz plasmonics," *Nat. Commun.*, vol. 6, 2015.

[187] T. L. Floyd, *"Capacitors",in Principles of electric circuits.* Maxwell Macmillan International, 1993.

[188] ITUR, "M. 2134. requirements related to technical performance for imt-advanced radio interface (s)," Technical Report, 3GPP, Tech. Rep., 2008.

[189] K. K. Kim *et al.*, "Synthesis and characterization of hexagonal boron nitride film as a dielectric layer for graphene devices," *ACS nano*, vol. 6, no. 10, pp. 8583–8590, 2012.

[190] L. M. Woods and G. D. Mahan, "Electron-phonon effects in graphene and armchair (10, 10) single-wall carbon nanotubes," *Phys. Rev. B*, vol. 61, no. 16, p. 10651, 2000.

[191] K. Technologies. (2017) E3634a 200w power supply, 25v, 7a or 50v, 4a. [Online]. Available: http://www.keysight.com/en/pd-836423-pn-E3634A/200w-power-supply-25v-7a-or-50v-4a?nid=-35690.384003.00&cc=GB&lc=eng

[192] X. Huang *et al.*, "Highly flexible and conductive printed graphene for wireless wearable communications applications," *Scientific reports*, vol. 5, 2015.

[193] P. C. Hsu *et al.*, "Performance enhancement of metal nanowire transparent conducting electrodes by mesoscale metal wires," *Nat. Commun.*, vol. 4, 2013.

[194] K.-L. Du and M. N. Swamy, *Wireless communication systems: from RF subsystems to 4G enabling technologies*. Cambridge University Press, 2010.

[195] A. M. D. Turkmani and other, "An experimental evaluation of the performance of two-branch space and polarization diversity schemes at 1800 MHz," *IEEE Trans. Veh. Technol*, vol. 44, no. 2, pp. 318–326, May 1995.

[196] B. A. Cetiner *et al.*, "Multifunctional reconfigurable MEMS integrated antennas for adaptive MIMO systems," *IEEE Commun. Mag.*, vol. 42, no. 12, pp. 62–70, 2004.

[197] K. T. Wong, S. L. A. Chan, and R. P. Torres, "Fast-polarization-hopping transmission diversity to mitigate prolonged deep fades in indoor wireless communications," *IEEE Antennas Propag. Mag*, vol. 48, no. 3, pp. 20–27, June 2006.

[198] P. Y. Qin, Y. J. Guo, and C. H. Liang, "Effect of antenna polarization diversity on MIMO system capacity," *IEEE Antennas Wireless Propag. Lett*, vol. 9, pp. 1092–1095, 2010.

[199] J. Balcells, Y. Damgaci, B. A. Cetiner, J. Romeu, and L. Jofre, "Polarization reconfigurable MEMS-CPW antenna for mm-wave applications," in *Proc. of the Fourth European Conf. on Antennas and Propagation*, April 2010, pp. 1–5.

[200] T. J. Jung, I. J. Hyeon, C. W. Baek, and S. Lim, "Circular/linear polarization reconfigurable antenna on simplified RF-MEMS packaging platform in K-band," *IEEE Trans. Antennas Propag.*, vol. 60, no. 11, pp. 5039–5045, Nov 2012.

[201] J. Ouyang, F. Yang, and S. Yang, "A novel reconfigurable circular polarization patch antenna," *Microw. Opt. Technol. Lett.*, vol. 50, no. 7, pp. 1921–1923, 2008.

[202] W.-J. Liao, S.-J. You, and H.-T. Chou, "Polarization reconfigurable patch array antenna," in *2010 IEEE Int.l Conf. on Wireless Information Technology and Systems (ICWITS)*, Aug 2010, pp. 1–4.

[203] W. Lin and H. Wong, "Polarization reconfigurable aperture-fed patch antenna and array," *IEEE Access*, vol. 4, pp. 1510–1517, 2016.

[204] Y. J. Sung, T. U. Jang, and Y. S. Kim, "A reconfigurable microstrip antenna for switchable polarization," *IEEE Microw. Compon. Lett.*, vol. 14, no. 11, pp. 534–536, Nov 2004.

[205] Y. F. Wu, C. H. Wu, D. Y. Lai, and F. C. Chen, "A reconfigurable quadri-polarization diversity aperture-coupled patch antenna," *IEEE Trans. Antennas Propag.*, vol. 55, no. 3, pp. 1009–1012, March 2007.

[206] D. Piazza, P. Mookiah, M. D'Amico, and K. R. Dandekar, "Experimental analysis of pattern and polarization reconfigurable circular patch antennas for MIMO systems," *IEEE Trans. Veh. Technol*, vol. 59, no. 5, pp. 2352–2362, Jun 2010.

[207] R. H. Chen and J. S. Row, "Single-fed microstrip patch antenna with switchable polarization," *IEEE Trans. Antennas Propag.*, vol. 56, no. 4, pp. 922–926, April 2008.

[208] Y. Li, Z. Zhang, J. Zheng, and Z. Feng, "Channel capacity study of polarization reconfigurable slot antenna for indoor MIMO system," *Microw. Opt. Technol. Lett.*, vol. 53, no. 6, pp. 1209–1213, 2011.

[209] X. X. Yang, B. C. Shao, F. Yang, A. Z. Elsherbeni, and B. Gong, "A polarization reconfigurable patch antenna with loop slots on the ground plane," *IEEE Antennas Wireless Propag. Lett*, vol. 11, pp. 69–72, 2012.

[210] X. X. Yang, B. Gong, F. Yang, and A. Z. Elsherbeni, "A reconfigurable patch antenna with quadri-polarization states using dual feed ports," in *Proc. of the 2012 IEEE Int.Symp. on Antennas and Propagation*, July 2012, pp. 1–2.

[211] P. Y. Qin, Y. J. Guo, and C. Ding, "A dual-band polarization reconfigurable antenna for WLAN systems," *IEEE Trans. Antennas Propag.*, vol. 61, no. 11, pp. 5706–5713, Nov 2013.

[212] J. S. Row and M. J. Hou, "Design of polarization diversity patch antenna based on a compact reconfigurable feeding network," *IEEE Trans. Antennas Propag.*, vol. 62, no. 10, pp. 5349–5352, Oct 2014.

[213] W. Lin and H. Wong, "Wideband circular polarization reconfigurable antenna," *IEEE Trans. Antennas Propag.*, vol. 63, no. 12, pp. 5938–5944, Dec 2015.

[214] Y. Cao, S. W. Cheung, and T. I. Yuk, "A simple planar polarization reconfigurable monopole antenna for GNSS/PCS," *IEEE Trans. Antennas Propag.*, vol. 63, no. 2, pp. 500–507, Feb 2015.

[215] S. W. Lee and Y. J. Sung, "Simple polarization-reconfigurable antenna with T-shaped feed," *IEEE Antennas Wireless Propag. Lett*, vol. 15, pp. 114–117, 2016.

[216] S. Y. Lin, Y. C. Lin, C. Y. Li, and Y. M. Lee, "Patch antenna with reconfigurable polarization," in *Asia-Pacific Microwave Conference 2011*, Dec 2011, pp. 634–637.

[217] T.-Y. Han, C. Jiashih Shih, and J.-S. Row, "Polarization reconfigurable microstrip patch antenna," *Microw. Opt. Technol. Lett.*, vol. 55, no. 3, pp. 471–474, 2013.

[218] J. D. Barrera and G. H. Huff, "A fluidic loading mechanism in a polarization reconfigurable antenna with a comparison to solid state approaches," *IEEE Trans. Antennas Propag.*, vol. 62, no. 8, pp. 4008–4014, Aug 2014.

[219] J. Winters, "On the capacity of radio communication systems with diversity in a Rayleigh fading environment," *IEEE J. Sel. Areas Commun*, vol. 5, no. 5, pp. 871–878, Jun 1987.

[220] A. Sabharwal *et al.*, "In-band full-duplex wireless: Challenges and opportunities," *IEEE J. Sel. Areas Commun*, vol. 32, no. 9, pp. 1637–1652, Sept 2014.

[221] Y. Dong and T. Itoh, "Metamaterial-based antennas," *Proc. IEEE*, vol. 100, no. 7, pp. 2271–2285, July 2012.

[222] R. W. Ziolkowski and A. Erentok, "Metamaterial-based efficient electrically small antennas," *IEEE Trans. Antennas Propag.*, vol. 54, no. 7, pp. 2113–2130, 2006.

[223] A. Erentok and R. W. Ziolkowski, "Metamaterial-inspired efficient electrically small antennas," *IEEE Trans. Antennas Propag.*, vol. 56, no. 3, pp. 691–707, March 2008.

[224] R. W. Ziolkowski *et al.*, "Experimental verification of Z antennas at UHF frequencies," *IEEE Antennas Wireless Propag. Lett*, vol. 8, pp. 1329–1333, 2009.

[225] A. Ahmadi, S. Saadat, and H. Mosallaei, "Resonance and Q performance of ellipsoidal ENG subwavelength radiators," *IEEE Trans. Antennas Propag.*, vol. 59, no. 3, pp. 706–713, March 2011.

[226] F. Bilotti, A. Alu, and L. Vegni, "Design of miniaturized metamaterial patch antennas with μ-negative loading," *IEEE Trans. Antennas Propag.*, vol. 56, no. 6, pp. 1640–1647, June 2008.

[227] S. Ghadarghadr, A. Ahmadi, and H. Mosallaei, "Negative permeability-based electrically small antennas," *IEEE Antennas Wireless Propag. Lett*, vol. 7, pp. 13–17, 2008.

[228] P. Jin and R. W. Ziolkowski, "Multi-frequency, linear and circular polarized, metamaterial-inspired, near-field resonant parasitic antennas," *IEEE Trans. Antennas Propag.*, vol. 59, no. 5, pp. 1446–1459, May 2011.

[229] Z. G. Liu and Y. X. Guo, "Compact low-profile dual band metamaterial antenna for body centric communications," *IEEE Antennas Wireless Propag. Lett*, vol. 14, pp. 863–866, Dec 2015.

[230] R. W. Ziolkowski and A. D. Kipple, "Application of double negative materials to increase the power radiated by electrically small antennas," *IEEE Trans. Antennas Propag.*, vol. 51, no. 10, pp. 2626–2640, Oct 2003.

[231] Q. Wu, M.-F. Wu, F.-Y. Meng, J. Wu, and L.-W. Li, "A novel broadband double negative medium substrate design for microstrip antenna miniaturization," in *2006 IEEE Antennas and Propagation Society Int. Symp.*, July 2006, pp. 39–42.

[232] T. L. Pu and K. M. Huang, "A novel double negative substrate for miniature patch antenna," in *2008 IEEE MTT-S Int. Microwave Workshop Series on Art of Miniaturizing RF and Microwave Passive Components*, Dec 2008, pp. 201–204.

[233] C. Torbitt, J. Venkataraman, and Z. Lu, "Gain enhancement using DOE lens and DNG lens," in *2013 IEEE Antennas and Propagation Society International Symposium (APSURSI)*, July 2013, pp. 1550–1551.

[234] Y. Zhang, J. von Hagen, M. Younis, C. Fischer, and W. Wiesbeck, "Planar artificial magnetic conductors and patch antennas," *IEEE Trans. Antennas Propag.*, vol. 51, no. 10, pp. 2704–2712, Oct 2003.

[235] F. Yang and Y. Rahmat-Samii, "Reflection phase characterizations of the EBG ground plane for low profile wire antenna applications," *IEEE Trans. Antennas Propag.*, vol. 51, no. 10, pp. 2691–2703, Oct 2003.

[236] ——, "Microstrip antennas integrated with electromagnetic band-gap (EBG) structures: a low mutual coupling design for array applications," *IEEE Trans. Antennas Propag.*, vol. 51, no. 10, pp. 2936–2946, Oct 2003.

[237] H. Mosallaei and K. Sarabandi, "Antenna miniaturization and bandwidth enhancement using a reactive impedance substrate," *IEEE Trans. Antennas Propag.*, vol. 52, no. 9, pp. 2403–2414, Sept 2004.

[238] A. P. Feresidis, G. Goussetis, S. Wang, and J. C. Vardaxoglou, "Artificial magnetic conductor surfaces and their application to low-profile high-gain planar antennas," *IEEE Trans. Antennas Propag.*, vol. 53, no. 1, pp. 209–215, Jan 2005.

[239] Y. Dong, H. Toyao, and T. Itoh, "Design and characterization of miniaturized patch antennas loaded with complementary split-ring resonators," *IEEE Trans. Antennas Propag.*, vol. 60, no. 2, pp. 772–785, Feb 2012.

[240] W. Yang *et al.*, "A wideband and high-gain edge-fed patch antenna and array using artificial magnetic conductor structures," *IEEE Antennas Wireless Propag. Lett*, vol. 12, pp. 769–772, 2013.

[241] S. Lim, C. Caloz, and T. Itoh, "Metamaterial-based electronically controlled transmission-line structure as a novel leaky-wave antenna with tunable radiation angle and beamwidth," *IEEE Trans. Microw. Theory Techn*, vol. 52, no. 12, pp. 2678–2690, 2004.

[242] S. Paulotto, P. Baccarelli, F. Frezza, and D. R. Jackson, "Full-wave modal dispersion analysis and broadside optimization for a class of microstrip CRLH leaky-wave antennas," *IEEE Trans. Microw. Theory Techn*, vol. 56, no. 12, pp. 2826–2837, Dec 2008.

[243] T. Ueda, N. Michishita, M. Akiyama, and T. Itoh, "Dielectric-resonator-based composite right/left-handed transmission lines and their application to leaky wave antenna," *IEEE Transactions on Microwave Theory and Techniques*, vol. 56, no. 10, pp. 2259–2269, Oct 2008.

[244] Y. Dong and T. Itoh, "Composite right/left-handed substrate integrated waveguide and half mode substrate integrated waveguide leaky-wave structures," *IEEE Trans. Antennas Propag.*, vol. 59, no. 3, pp. 767–775, March 2011.

[245] Y. Luo *et al.*, "Programmable leaky-wave antenna with periodic J-shaped metamaterial patches," *Electronics Letters*, vol. 51, no. 10, pp. 733–734, 2015.

[246] A. Sanada *et al.*, "A planar zeroth-order resonator antenna using a left-handed transmission line," in *34th European Microwave Conf. (EuMC 2004)*, vol. 3, Oct 2004, pp. 1341–1344.

[247] S. W. Lee and J. H. Lee, "Electrically small MNG ZOR antenna with multilayered conductor," *IEEE Antennas Wireless Propag. Lett*, vol. 9, pp. 724–727, 2010.

[248] T. Jang, J. Choi, and S. Lim, "Compact coplanar waveguide (CPW)-fed zeroth-order resonant antennas with extended bandwidth and high efficiency

on vialess single layer," *IEEE Trans. Antennas Propag.*, vol. 59, no. 2, pp. 363–372, Feb 2011.

[249] H. M. Lee, "A compact zeroth-order resonant antenna employing novel composite right/left-handed transmission-line unit-cells structure," *IEEE Antennas Wireless Propag. Lett*, vol. 10, pp. 1377–1380, 2011.

[250] C. P. Lai, S. C. Chiu, H. J. Li, and S. Y. Chen, "Zeroth-order resonator antennas using inductor-loaded and capacitor-loaded CPWs," *IEEE Trans. Antennas Propag.*, vol. 59, no. 9, pp. 3448–3453, Sept 2011.

[251] S. Y. Yang and M. N. M. Kehn, "A bisected miniaturized ZOR antenna with increased bandwidth and radiation efficiency," *IEEE Antennas Wireless Propag. Lett*, vol. 12, pp. 159–162, 2013.

[252] M. S. Majedi and A. R. Attari, "A compact and broadband metamaterial-inspired antenna," *IEEE Antennas Wireless Propag. Lett*, vol. 12, pp. 345–348, 2013.

[253] P. L. Chi and Y. S. Shih, "Compact and bandwidth-enhanced zeroth-order resonant antenna," *IEEE Antennas Wireless Propag. Lett*, vol. 14, pp. 285–288, 2015.

[254] A. Lai, K. M. K. H. Leong, and T. Itoh, "Infinite wavelength resonant antennas with monopolar radiation pattern based on periodic structures," *IEEE Trans. Antennas Propag.*, vol. 55, no. 3, pp. 868–876, March 2007.

[255] J. G. Lee and J. H. Lee, "Zeroth order resonance loop antenna," *IEEE Trans. Antennas Propag.*, vol. 55, no. 3, pp. 994–997, March 2007.

[256] J. H. Park, Y. H. Ryu, J. G. Lee, and J. H. Lee, "Epsilon negative zeroth-order resonator antenna," *IEEE Trans. Antennas Propag.*, vol. 55, no. 12, pp. 3710–3712, Dec 2007.

[257] S. T. Ko and J. H. Lee, "Wideband folded mushroom zeroth-order resonance antenna," *IET Microwaves, Antennas Propagation*, vol. 7, no. 2, pp. 79–84, January 2013.

[258] S. Yan and G. A. E. Vandenbosch, "Zeroth-order resonant circular patch antenna based on periodic structures," *IET Microwaves, Antennas Propagation*, vol. 8, no. 15, pp. 1432–1439, 2014.

[259] T. J. Jung, J. H. Kwon, and S. Lim, "Flexible zeroth-order resonant antenna independent of substrate deformation," *Electron. Lett*, vol. 46, no. 11, pp. 740–742, 2010.

[260] J. Ha, K. Kwon, and J. Choi, "Compact zeroth-order resonance antenna for implantable biomedical service applications," *Electronics Letters*, vol. 47, no. 23, pp. 1267–1269, November 2011.

[261] J. Kim, G. Kim, W. Seong, and J. Choi, "A tunable internal antenna with an epsilon negative zeroth order resonator for DVB-H service," *IEEE Trans. Antennas Propag.*, vol. 57, no. 12, pp. 4014–4017, Dec 2009.

[262] T. Jang, S. Lim, and T. Itoh, "Tunable compact asymmetric coplanar waveguide zeroth-order resonant antenna," *Journal of Electromagnetic Waves and Applications*, vol. 25, no. 17-18, pp. 2379–2388, 2011.

[263] S. Sam, H. Kang, and S. Lim, "Frequency reconfigurable and miniaturized substrate integrated waveguide interdigital capacitor (SIW-IDC) antenna," *IEEE Trans. Antennas Propag.*, vol. 62, no. 3, pp. 1039–1045, March 2014.

[264] J. Choi and S. Lim, "Frequency and radiation pattern reconfigurable small metamaterial antenna using its extraordinary zeroth-order resonance," *J. Electromagnet. Wave*, vol. 24, no. 14-15, pp. 2119–2127, 2010.

[265] I. Lim and S. Lim, "CPW-fed arbitrary frequency-switchable antenna using CRLH transmission line," *ETRI Journal*, vol. 36, no. 1, pp. 151–154, 2014.

[266] Y. Peng, J. W. Li, Y. H. Ran, and X. L. Jing, "A compact frequency-reconfigurable antenna empolying novel composite right/left-handed transmission-line structure," in *2015 16th International Conference on Electronic Packaging Technology (ICEPT)*, Aug 2015, pp. 1416–1418.

[267] Y. Jang, J. Choi, and S. Lim, "Frequency reconfigurable zeroth-order resonant antenna using RF MEMS switch," *Microw. Opt. Technol. Lett.*, vol. 54, no. 5, pp. 1266–1269, 2012.

[268] *RT/duroid 5870 /5880 High Frequency Laminates*, Rogers Corporation, 2016. [Online]. Available: https://www.rogerscorp.com/documents/606/acm/RT-duroid-5870-5880-Data-Sheet.pdf